Multiscale biomechanics of skin: experimental investigation of the role of the collagen microstructure

Barbara Lynch

To cite this version:

Barbara Lynch. Multiscale biomechanics of skin: experimental investigation of the role of the collagen microstructure. Biomechanics [physics.med-ph]. Ecole Doctorale Polytechnique, 2015. English. NNT : . tel-01237007

HAL Id: tel-01237007
https://pastel.hal.science/tel-01237007v1

Submitted on 2 Dec 2015

Thèse présentée pour l'obtention du titre de

DOCTEUR DE L'ÉCOLE POLYTECHNIQUE

Spécialité : Mécanique

par

BARBARA LYNCH

Sujet de thèse

Multiscale biomechanics of skin: experimental investigation of the role of the collagen microstructure

Soutenue le 7 Septembre 2015 devant le jury composé de :

Karine BRUYÈRE-GARNIER	IFSTTAR	*Rapporteure*
Valérie DEPLANO	IRPHE, Aix-Marseille Université	*Rapporteure*
Edoardo MAZZA	ETH Zürich	*Examinateur*
Marie-Claire SCHANNE-KLEIN	LOB, École Polytechnique	*Examinatrice*
Claude VERDIER	LIPhy, Université Joseph Fournier	*Examinateur*
Jean-Marc ALLAIN	LMS, École Polytechnique	*Directeur de thèse*

Remerciements

Je tiens en premier lieu à remercier les membres de mon jury, Karine Bruyère-Garnier, Valérie Deplano, Edoardo Mazza et Claude Verdier, de m'avoir fait l'honneur d'évaluer mon travail de thèse.
J'aimerai également remercier Patrick Le Tallec de m'avoir accueillie au sein du Laboratoire de Mécanique des Solides, ainsi que l'École Polytechnique pour le financement de cette thèse.

Je remercie chaleureusement Jean-Marc Allain de m'avoir encadrée en qualité de directeur de thèse durant ces trois années. Merci pour ta disponibilité, ta confiance et ton enthousiasme (même quand on avait "pas de peau").
J'adresse ma sincère gratitude à Marie-Claire Schanne-Klein du Laboratoire Optique et Biosciences, qui m'a également beaucoup guidée pendant ce travail. Merci pour toutes nos discussions bilingues optique-mécanique, toujours très enrichissantes.

Un grand merci à ceux avec qui j'ai eu le plaisir de réaliser les manips tout au long de ces 3 ans : Stéphane Bancelin, Guillaume Ducourthial et Sotiris Psilodimitrakopoulos. Je remercie aussi Aurélie Benoit qui a guidé mes premiers pas sur les essais multi-échelles et qui m'a initiée à la corrélation d'images.
Merci à nos collaboratrices de l'Institut de Génomique Fonctionnelle de Lyon, Florence Ruggiero, Christelle Bonod-Bidaud et Ruth Rubio Amador, qui nous ont fourni les peaux de souris. Je les remercie également pour leur détermination à mettre la biologie à la portée des physiciens et pour nos nombreux échanges fructueux.
Je souhaite une longue vie à cette belle collaboration grâce à laquelle j'ai beaucoup appris, et j'adresse mes meilleurs vœux de succès à Jean-Sébastien, Guillaume et Florent, qui en poursuivent les projets.

Pouvoir construire sa machine d'expérimentation sur mesure est un luxe, et je souhaite remercier ceux grâce à qui cela a été possible : François Lelong pour l'usinage des mors et Vincent de Greef pour la gestion du (capricieux) boîtier de commande.

Je tiens également à remercier les personnes avec qui j'ai eu l'opportunité de collaborer sur divers projets annexes à mon travail de thèse principal, en particulier Gervaise Mosser et Aurélien Tidu pour la mécanique des matrices de collagène ainsi que William Parnell, Tom Shearer et Riccardo de Pascalis pour la modélisation du tendon.

Entre mon bureau au bâtiment 65, le LMS et la salle de manip au LOB, j'ai eu la chance de côtoyer pendant 3 ans de nombreuses personnes d'horizons très variés : je les remercie d'avoir contribué chacune à leur manière à rendre ces années sur le plateau très agréables.

Je tiens à remercier les doctorants, post-doctorants et stagiaires du LMS qui ont partagé mon quotidien. Merci à Jessica, David, Gwenaël, Clément, Christelle, Raphaël, Guilia, Kokou, Nicolas, Luka, Laurent... Merci, et bravo, à mes chers co-thésards : Armel, Dennis et Dimitri.
Je remercie également l'ensemble du secrétariat du LMS : Alexandra, Anna, Christiane, Valérie et Danielle, pour leur disponibilité et leur aide précieuse.

Je remercie l'ensemble du personnel du LOB de m'avoir toujours réservé un accueil chaleureux pendant nos si longues journées de manip. Merci en particulier aux doctorants : Claire, Mouna, Nelly, Marianne, Kamel.

J'aimerai remercier enfin toutes les personnes avec qui j'ai eu l'occasion de partager le bâtiment 65. Toute ma reconnaissance va en particulier à mes co-bureaux successifs : Franz, Cécile, François et Manon. Je remercie ici également Avin Babataheri qui nous permet d'effectuer nos expérimentations dans des conditions optimales en gérant efficacement les stocks du laboratoire et le L2.

Merci à mes amis pour leur oreille toujours attentive et leur bienveillance. Merci à Olivier, MH, Clément, Catherine, Célia, Natacha, Béa, Tristan, Manu, Charles & Charles.

A sincere thank you to Maggie and Kip for proofreading this document and for their continued support. Mes plus profonds remerciements à mes parents, pour leur soutien sans faille et leurs encouragements au cours de ces (presque) 25 années d'étude.

Enfin, un immense merci à Alexis, pour son soutien inébranlable.

Table of Contents

General introduction

At first sight, materials from biological origin, whether animals or plants, appear very diverse. What do wood, bone, skin and sponges have in common ? The diversity of biological materials illustrates admirably the variety of tasks they serve and the diverse mechanical environments they need to accommodate.

Most of these materials fulfil more than one function, amongst which one is generally intrinsically mechanical: to provide stiffness, elasticity, resilience, etc. Yet, natural materials are extremely efficient, in the sense that they are composed of a relatively small number of structural building blocks. Consequently, almost all natural materials are composites: adaptation of shape, geometry, size and orientation in a structural block arrangement is nature's preferred strategy to optimise mechanical properties of biological materials to fulfil the complex requirements imposed by plants and animals.

Biomechanics is the application of methods and tools from mechanics to study biological systems. Mechanics offers a complementary approach to understand complex biological systems at various scales, from environment probing at the scale of a single cell to whole body locomotion. It has already enabled significant advances in medicine in multiple fields, *e.g.* diagnosis, surgery, prosthetics, tissue engineering. When understanding the mechanical principles behind the normal function of cells and organs, it becomes possible to foresee outcomes of pathological modifications and conceive new ways to address them.

Material sciences find a particularly straightforward field of application in the investigation of tissue biomechanics. In particular, the application of an upscaling scheme, like the theory of homogeneisation, allows for the deduction of macroscale laws and constitutive relationships from knowledge on microscale behaviours.

This PhD dissertation is the result of a project aimed at multiscale experimental characterisation of skin. Skin belongs to the category of connective tissues, one of the four principal types of animal tissue, together with nervous, epithelial and muscle tissues. Connective tissues are responsible for support and cohesion. Skin is the largest organ of the human body and serves several crucial tasks, such as protection against external aggressions (mechanical, chemical, bacteriological, radiation, etc.), temperature balance, hormonal excretions, sense of touch and appearance. The use of chemicals, the ageing process, wounds and some pathologies are some of the many factors that can influence the properties of skin, including mechanical characteristics. Understanding the complex properties of skin, and in particular how microstructure impacts the macroscopic mechanical behaviour, will be beneficial in a number of domains, ranging from tissue engineering to cosmetics, robotic surgery or car crash predictive assessment.

Skin is a multilayered composite structure: its thickest layer, and the most important from a mechanical point of view, is the dermis. It consists mostly of collagen fibres embedded in a host structure. A scaling up methodology requires precise information on the interplay between components at different scales during mechanical stimulation. Micromechanical experiments are however difficult to implement, as they require precise knowledge on multiple techniques and careful sample preparation.
We developed, optimised and validated a multiphysics and multiscale protocol to perform mechanical experiments while simultaneously assessing microstructural reorganisation. Using Second Harmonic Generation imaging we observed the reorganisation of the collagen network inside the dermis while performing a uniaxial tensile test.

The first chapter introduces useful notions for the understanding of this work. We first present the family of soft connective tissues, skin in particular, from the microscopic scale. We are mostly interested in the structural components and microstructural organisation. We also briefly review in this section the imaging tools available for the investigation of tissues micro-architecture. Then we take a look at the macroscopic mechanical properties of skin: the characterisation methods are introduced, and skin's complex mechanical properties (non-linear elasticity, anisotropy, viscoelasticity, etc.) are detailed. Finally we show the context of existent multiscale works within which this PhD work falls.

Chapter II develops the multiphysics experimental protocol we implemented for this study. The sample preparation and mechanical tensile test protocols are described. We then define the quantitative parameters that were developed for the needs of this work. Firstly we review the parameters used for the assessment of skin's macroscopic mechanical properties. Secondly we introduce the information that were retrieved from the microscopic images obtained with Second Harmonic Generation imaging, in terms of local stretch and fibre orientation assessment in particular.

Chapter III reviews the multiscale results on control mice skin. The experiments were first carried out on one-month-old mice from a control strain. The results yield information on the macroscopic mechanical properties and microscopic evolution of skin. On the one hand they allow us to validate our experimental protocol, while on the other hand the correlation between mechanical behaviour and collagen network reorientation gives unexpected results. These are remarkably different from those expected from the literature on microscopic models of soft collagenous tissues. This inadequacy is discussed, and possible microstructural mechanisms are suggested.

Chapter IV reports the changes in multiscale properties observed in mice that have a mutation affecting skin's microstructure. We studied two mice strains created in the context of studying a pathology that affects all collagenous tissues' mechanical properties: Ehlers-Danlos syndrome. One of the main features of Ehlers-Danlos syndrome is hyperelastic skin. In both mice strains we tested, the microstructure of the dermis is modified, at different levels and various severities. Testing these mice strains with our protocol, we observed how these changes affect microstructural reorganisation and ultimately macroscopic mechanical properties. This is an opportunity to test the conclusions we obtained on control mice skin to various levels of microstructural alteration.

The last chapter addresses the impact of age on multiscale properties of skin. We carried out our multiscale experiments on mice skin aged 15 and 19 months old, both control and with a genetic mutation. The ageing process impacts deeply the microstructural composition and organisation of the dermis, which results in modifications of mechanical properties. We can characterise those alterations with the quantitative parameters developed, at both macroscopic and microscopic scales. Once more, we also evaluated the adequacy of the hypothetic microstructural mechanisms suggested before on an actual perturbation of the dermis' microstructure.

This work illustrates that the link between microstructure and mechanical properties in soft collagenous tissues may not be as simple as initially infered. Small changes in the microstructure can deeply impact the mechanical behaviour, while contradictory effects of more generalised modifications lead to unexpected results. In the end, the aim is to get a better idea of how to approach the development of an effective multiscale model of skin.

Chapter I

Introduction

The purpose of this introductory chapter is to demonstrate the need for precise microstructural investigation of skin behaviour under mechanical stimulation.

The first section is dedicated to skin from a microscopic perspective, from its most fundamental component, collagen, to its structural organisation. The second part considers the tissue from the macroscopic scale, and focuses on the complex mechanical properties of skin. After reviewing the usual mechanical modelling of skin and in particular how it takes microstructure into account, we eventually present the rationale of this PhD work and its novelty in the field.

I.1 Microscopic scale: from collagen to skin

In this section we examine skin from a microscopic point of view. First we introduce collagen and the family of tissues called connective, or "collagen-rich", tissues. Then we review the anatomy and structure of skin more precisely, as well as the experimental methods that can be used to investigate the architecture of collagen-rich tissues at the microscopic level.

I.1.1 Collagen

Proteins are macromolecules formed by one or more long chains of amino acids. They play a crucial role in many biological interactions *in vivo*, including response to stimuli, replication of DNA, transport of molecules or catalysis of metabolic reactions. The specific 3D structure of each protein is of the utmost importance in all of these tasks: if the right binding site is not well presented or if steric effect prevents contact, no interaction is possible.

The main structural proteins in animal life form are the collagens, forming the collagen family. Collagen is ubiquitous in animals, and represents around 30% of the total mass of proteins in vertebrates. It can be found in a number of different molecular forms, as well as presenting various microstructural organisations, including fibres. Collagen also exists in invertebrates, for example in the byssus threads through which mussels attach themselves to rocks.

In vertebrates, collagen is one of the basic bricks composing what is called "collagen-rich" tissues, also called connective or collagenous tissues. Connective tissues are, in most animals, the most abundant and most widely distributed type of tissues, as opposed to the 3 other basic types of tissue, *i.e.* epithelial, muscle and nervous tissue. Connective tissues include fat tissues, dense fibrous tissue, cartilage, bone, blood, etc. Their common purpose is to provide support and protection. Connective tissues only encompass a few cells. The remaining material is called "extracellular matrix", and is mainly composed of collagen.

I.1.1.a The collagen family

At least 28 different collagens are known in vertebrates [1]. The most important and abundant collagen type in collagen-rich tissues is collagen I: it is responsible for most of their structural properties. However, less abundant collagens can also affect the microstructure: it is the case for collagen type V for instance, which will be of particular relevance to our study.

The collagens are classified with roman numbers, I-XXVIII, some also have common names. The size, function, role and abundance in tissues vary considerably from one collagen to another. In terms of structure, some form fibrils, others form 2D networks, and some remain disorganised, for example in basement membranes, the specific layer of extracellular matrix that connects cellular and connective tissues in many organs.

There is no firm and commonly agreed upon definition of what qualifies as a collagen. In general, all proteins that assemble into triple helices (or present triple helical domains) that also fulfil support or assembly functions in tissues are regardered as collagen.

A triple helix is made by binding three amino acid chains, called α-chains, together, in what is called a tropocollagen. A tropocollagen triple helix is represented schematically in figure I.1. The α-chains are numbered with arabic numerals. The chain called α_1 in one collagen type is not identical to the α_1 chain in another collagen type. A triple helix is called homotrimeric when all three α-chains are identical and heterotrimeric when one chain differs from the other two or all three α-chains are different. Most collagens exist in more than one stable form, although one is generally much more abundant than the others.

Table I.1 summarises the 28 different types of collagen, with their preferred structural organisation and distribution in tissues in the human body. There also exists a larger group of so-called "collagen-like proteins".

Collagen I is the most abundant collagen: 90% of collagen in vertebrates is type I collagen. While most collagen can present interruptions in their triple helical regions, collagen I triple helix shows no imperfection [1]. Collagen I forms fibrils, that combine into bigger entities to ensure the struc-

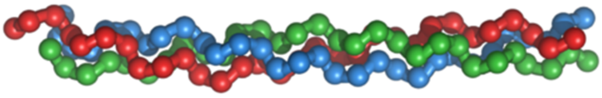

Figure I.1 – Tropocollagen triple helix binding 3 α-chains together.

tural integrity of tissues.

I.1.1.b Collagen's hierarchical structure

Like skin, many biological tissues are fibre composites with a multiscale hierarchical structure. This includes animal tissues, but also wood for instance, which is a composite of cellulose fibres. This structural organisation is one of nature's most common strategy to customise mechanical properties adapted to mechanical stimulation while ensuring tissue integrity. For a larger view of nature's hierarchical materials, see [2, 3].

In some tissues, such as bone or dentine, the stiffness can be tuned notably by the addition of mineralized elements. This is not suitable for soft tissues, such as skin, tendon, ligaments, cornea or arteries, that have to undergo large and multiaxial deformations. In these cases, the mechanical resistance is obtained mostly by a modification of the many levels of collagen hierarchical structure.

This organisation is summarised in figure I.2: α-chains assemble in tropocollagens, that assemble into fibrils, that congregate to form fibres, which organise in turn into a microstructure specific to each tissue [4, 5]. It should be noted that while triple helices assemble inside cells, all other assembling processes take place outside the cells after excretion.

When describing the structure of a protein, four forms are generally distinguinshed. The primary form is the sequence of amino acids. The secondary and tertiary forms are respectively the local organisation and spatial arrangement of a single polypeptidic chain. In the case of collagen, the secondary and tertiary forms are the same and correspond to the organisation in α-chains. α-chains are coiled upon themselves in an helix.

The quaternary form describes how different polypeptidic chains assemble with regards to one another to form the protein. In the case of collagen, it is the triple helical tropocollagen. The stability of the triple helix is ensured by hydrogen bonds between specific amino acids of different α-chains. In fibrillar collagens, the triple helix domain is continuous, while in non fibrillar collagens, the triple helix can be interrupted by non collagenous sequences [1].

Tropocollagens have a diameter of the ordre of 1.5 nm and are approximately 300 nm long for collagen type I.

In fibrillar collagens, such as collagen I, tropocollagens aggregate into collagen fibrils. The struc-

Collagen type	Structural organisation	Distribution in tissues
I	Fibril-forming	Non-cartilaginous connective tissues: tendon, ligament, cornea, bone, skin...
II	Thin fibril-forming	Cartilage, vitreous humour
III	Fibril-forming	Co-distributes with collagen I, especially in skin and vassal walls
IV	Network-forming	Basal membranes
V	Fibril-forming	Co-distributes with collagen I, in skin, cornea and embryonic tissues
VI	Beaded-filament-forming	Widespread, especially muscle, skin
VII	Anchroring fibrils	Epidermis-dermis junction
VIII	Network-forming	Descement's membrane in cornea
IX	FACIT	Co-distributes with collagen II, cartilage, vitrous humour
X	Network-forming	Hypertrophic cartilage
XI	Fibril-forming	Co-distributes with collagen II
XII	FACIT	Found with collagen I
XIII	Transmembrane	Neuromuscular junctions, skin
XIV	FACIT	Found with collagen I
XV	Endostatins	Eye, muscles, microvessels
XVI	FACIT	Integrated into collagen fibrils
XVII	Transmembrane	Epidermis-dermis junction
XVIII	Endostatins	Basement membranes
XIX	FACIT	Basement membranes, muscles
XX	FACIT	Widespread distribution, corneal epithelium
XXI	FACIT	Widespread distribution
XXII	FACIT	Tissue junctions, e.g. hair follicle-dermis
XXIII	Transmembrane	Tissue junctions
XXIV	Fibril-forming	Developing cornea and bone
XXV	Transmembrane	Associated with type I
XXVI	Beaded-filament-forming	
XXVII	Fibril-forming	Embryonic cartilage, developing dermis, cornea, heart, cartilage
XXVIII	Beaded-filament-forming	Basement membranes

Table I.1 – The collagen family: 28 collagen types, with preferred structural organisation and distribution in tissues in the human body. FACIT stands for Fibril-Associated Collagen with Interrupted Triple helices. Endostatins stand for endostatins-producing collagens. Table adapted from [1].

ture of collagen fibrils has been investigated for quite a long time using X-rays and electronic microscopy [4].

The most remarkable characteristic of collagen fibrils is the arrangement of tropocollagens in overlapping and gap zones, as shown in figure I.3 a. This arrangement appears as a result of two tropocollagens bonding through a covalent link between specific amino acids, called lysines. The cross-links formation depends deeply on the specific alignment of amino acids in the tropocollagens, through the maximisation of apolar and ionic interactions [4]. This specific bonding leads to 20 nm long overlapping zones and 47 nm gap zones, and thus to a characteristic periodic arrangement with a period of 67 nm, commonly called D. This shifting period is considered the watermark of fibrillar collagens. In transmission electronic microscopy (TEM) it is revealed by a characteristic alternation of light and dark bands [1]. An example can be seen in a TEM image from lung tissue in figure I.4.

Collagen fibrils have diameters ranging from 12 nm to over 500 nm, and their length vary greatly depending on the tissue and stage of development considered, from several micrometers to millimeters [6].

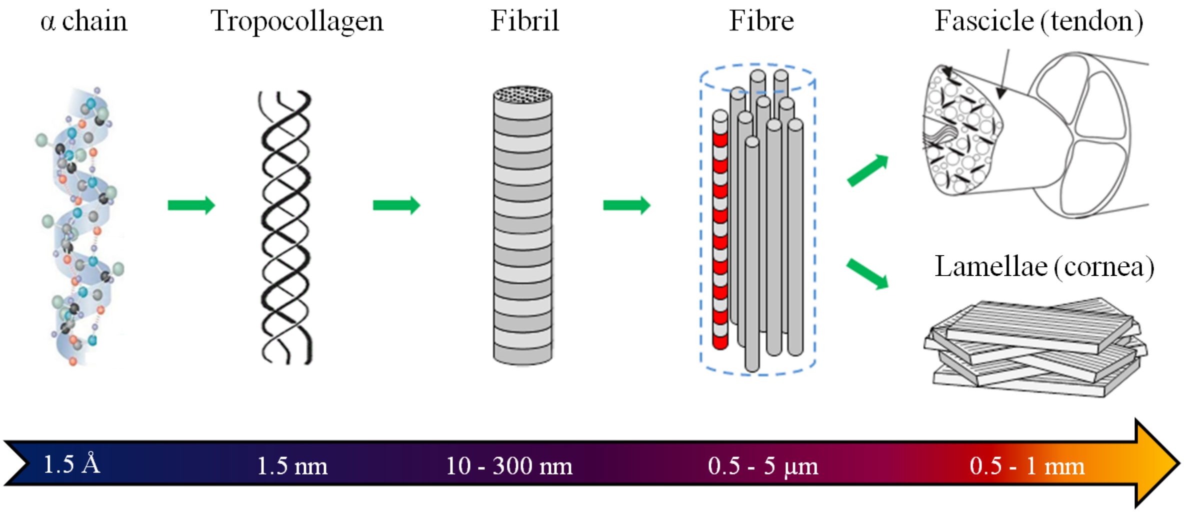

Figure I.2 – Structural organisation of fibrillar collagen from collagen α-chain to tropocollagen, to fibril, to fibre and finally to tissue-specific microstructure, with corresponding scale. Figure adapted from [7].

Fibrils assemble in turn to form collagen fibres. This process is not yet well understood, but seems to depend strongly on the tissue involved. In soft connective tissues such as tendon, cornea or skin, the fibrils are embedded in an environment called "ground substance", composed mostly of water. Ground substance and non-collagenous elements of the extracellular matrix, such as elastin in skin for instance, appear to have a deep impact on the adherence of fibrils together [4].

Some studies demonstrated that the ground substance is not as randomly organised as was first believed. For instance, proteins called proteoglycans (described in section I.1.2.3) extend radially

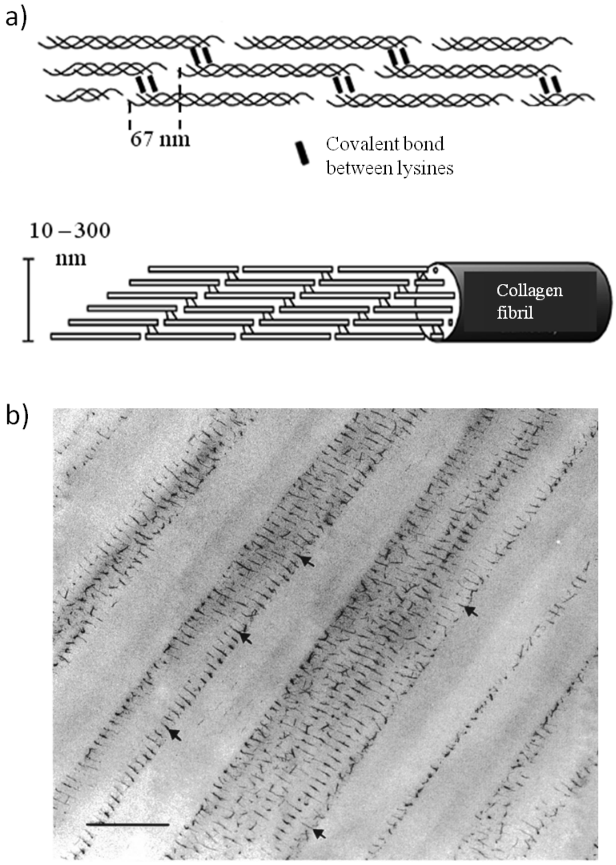

Figure I.3 – Exemples of cohesive strategies between collagenous sub-units: a) Covalent bonds between tropocollagen hold the fibrils together. The longitudinal gap creates overlapping regions with a length of 67 nm, characteristic for fibrillar collagen. Image adapted from [7]. b) TEM image of a 10-week-old rat tail tendon stained with cupromeronic blue. Collagen fibrils can be seen, with proteoglycans filaments (arrowed) extending from one fibril to another. Scale bar is 500 nm. Image from [8].

from one collagen fibril to another and seem to contribute to hold the whole network together [8]. This is shown in figure I.3 b in the case of a rat tail tendon specifically stained to show proteoglycans.
Collagen fibres can extend up to a few millimeters in length and a few micrometers in diameter.

Since the initial investigations of Fung [9], many experimental studies have been aiming for an accurate description of the fibres arrangement in specific biological composite structures, tissues and plants. Some of these studies start from the fibrillogenesis process and focus on cross-links [10] or interactions between fibrils and the rest of the matrix [11]. The dynamic interplay of subunits during a mechanical assay (such as sliding) has been examined very little up to now [12], and will be discussed later in this chapter.
Fibres assemble in a tissue-specific manner, adapting the microstructural organisation to ensure

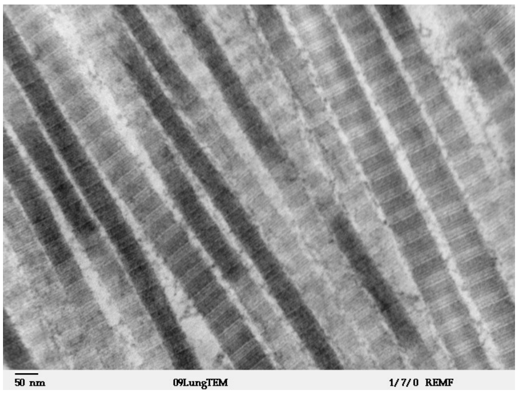

Figure I.4 – TEM image of lung tissue. Collagen type I fibrils can be seen, with characteristic periodic arrangement revealed through the alternance of dark and light bands. Image by L. Howard, Dartmouth College.

the particular functions of the tissue, such as resistance to the mechanical environment.

I.1.1.c Soft collagenous tissues

Soft collagenous tissues such as tendons, ligaments, skin and cornea are all made of the same simple building blocks: fibrillar collagen, a tissue-dependent proportion of elastin fibrils, and a surrounding substance composed mainly of water, proteins, and a few cells. From this relatively simple recipe originate tissues that are very different in terms of aspect, function and properties.

Soft collagenous tissues can be submitted to various mechanical environments. Tendons transmit displacement from muscle to bone: they need to be resilient, but do not sustain large displacements. Furthermore, most tendons are solicited in only one direction (with a few exceptions, such as shoulder tendons). Cornea on the other hand must sustain the inner pressure of the eye, but also respond to a very specific need: transparency. Finally, skin is solicited in various directions and its primary protective function requires a large extensibility.
To adapt to this wide range of mechanical environments while having simple building blocks common to all tissues, the microstructural organisation has to be optimised.

Figure I.5 shows images of cornea, tendon, and skin obtained with Transmission Electron Microscopy (TEM).
In the case of cornea the collagen fibrils organise in lamellae, stacked onto one another. They are also deposited in an hexagonal arrangement, as seen in the insert in figure I.5 a. This organisation is believed to be crucial for the transparency of the cornea [13].
Tendons also present a very organised microstructure, shown in figure I.5 b: fibres are unidirectionnal, parallel, aligned with the direction of mechanical stimulation. When observed with polarised light microscopy, the collagen fibres show a periodic waveform configuration, commonly called crimp, as shown in figure I.6 [14]. This crimp structure is believed to be intended as a safety

margin: the tendon can extend for a few percent, during which the crimp disappears, with no effect on fibres themselves [15].

Skin on the other hand, as seen in figure I.5 c, presents a very disorganised tangle of fibres. The fibres are often coiled or wavy. No preferred direction of alignment stands out at this scale. This organisation is ideal to allow the skin to sustain mechanical stimulation in any direction.

The fibre orientation is always closely related to the direction or directions in which the tissue is mechanically sollicited. When no direction is preferred, the fibres are randomly oriented, as in the vitreous humour for instance.

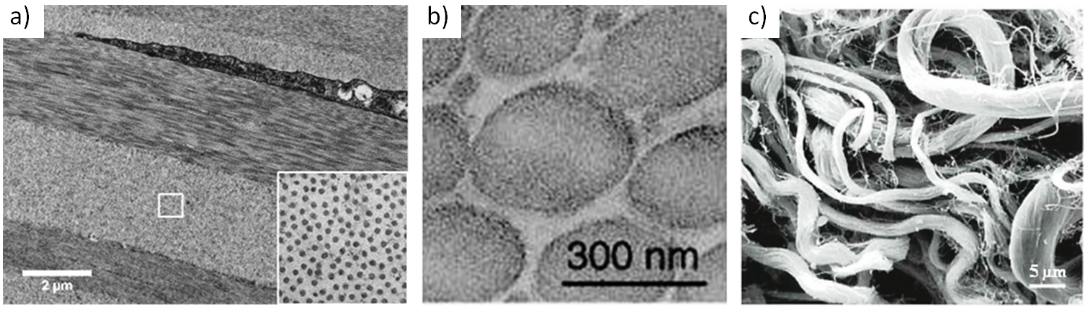

Figure I.5 – Variety of microstructure in functionally different tissues, TEM images from: a) Cornea (transversal cut). The fibrils are organised in lamellae stacked onto one another, in an hexagonal arrangement (insert). Image from Michèle Salvodelli, Hôpital de l'Hôtel-Dieu. b) Tendon (transversal cut). The fibres are unidirectionnal, parallel, aligned in the main direction. Image from [16]. c) Skin (horizontal cut). The fibres are coiled and form thick disorganised bundles. Image from [17].

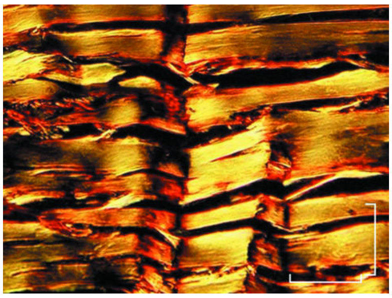

Figure I.6 – Polarised light image of collagen fibre bundles from relaxed rat tendon. Crimps appear as triangles of different length and with variable width of the top angle. Scale bar is 200 μm. Image from [14].

The fibre orientation is not the only property that can be tuned to respond to different mechanical stimuli. For instance the collagen content, the cross-links between fibrils and the fibre diameter distribution can have crucial roles, as well as the properties of the rest of the extracellular matrix. It has been demonstrated for instance that the fibre diameter distribution alone could explain a number of differences in the mechanical properties of collagenous tissues [18]. Indeed, numerous small fibrils, such as in the cornea for instance, present a large surface to the matrix, which promotes shear. On the other hand, large fibres, such as in tendons, sustain a larger number of lateral cross-links between fibres, which enhances the tensile properties.

I.1.1.d Mechanical properties of collagen

To understand how collagen-based networks confer elasticity and resilience to connective tissues, the investigation of the mechanical properties of each of the hierarchical sub-structures and their interplay can be valuable.

Many studies have been conducted in the past decade to determine the mechanical properties of isolated α-chains, collagen triple-helices, fibrils and fibres, either experimentally, theoretically or numerically [5, 18, 19, 20, 21, 22].

The main conclusion of these studies is that the average Young's modulus is divided by approximately 6 from the molecular level (≈ 6 GPa) to the fibrillar scale (≈ 0.9 GPa). The viscoelasticity on the contrary seems to be several orders of magnitude higher in fibrils (characteristic relaxation time from 10 to 100 s) than in collagen molecules (characteristic relaxation time ≈ 0.5 ns). This indicates that the viscous properties of the collagenous tissues cannot be attributed to collagen as a material alone, but also results from other mechanisms, such as sliding and slipping at different length scales [5] and from the properties of the surrounding matrix.

Isolated collagen fibrils have been investigated relatively extensively both experimentally and theoretically. Collagen fibrils, as any slender structure, are anisotropic in the mechanical sense. While collagen fibrils have little strength in flexion or torsion, they exhibit a high tensile strength in their main direction, attributed to the intermolecular covalent cross-links. To test isolated collagen fibrils mechanically, Atomic Force Microscopy (AFM) [20, 21], MicroElectroMechanical Systems (MEMS) [5, 19] and Optical Tweezers [22] are the most commonly used experimental devices. The results highlight the influence of hydration even at the fibrillar level, and show the intrinsic viscoelastic nature of collagen fibrils, illustrated in figure I.7 by the hysteresis that occurs during cyclic loading on a single fibril [21]. This viscoelasticity is however at a time scale an order of magnitude lower than the time scale of the whole tissue viscoelasticity.

Taking advantage of recent technical improvements in tissue engineering, some studies have been focusing on investigating the mechanical properties of specifically engineered collagen gels [23, 24]. These allow for customisation of the tissue morphological characteristics, and can help identify the microstructural parameters relevant to the macroscopic mechanical properties. They can however mimic the real organs only as well as we know the actual tissue's microstructure.

A lot remains unknown as to how to integrate mechanical properties and spatial organisation of

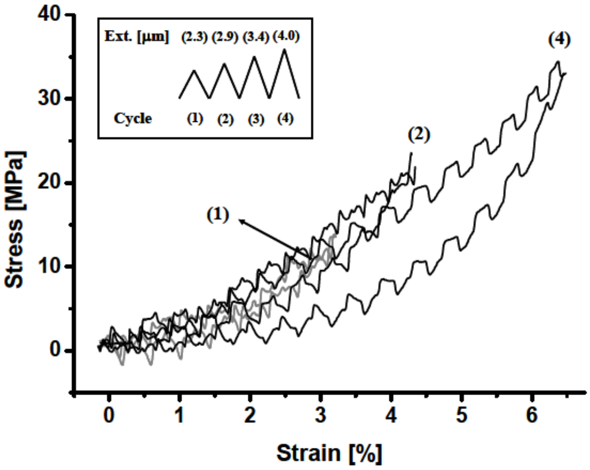

Figure I.7 – Stress/strain curve for a cyclic loading (loading path shown in insert) on a single collagen fibril using AFM: the hysteresis reveals the viscoelasticity of collagen fibrils. Figure from [21].

collagenous sub-elements in a scaling-up process to get a comprehensive view of the mechanics of macroscopic structures. Adequate micromechanical experiments are necessary to comprehend the behaviour of the microstructure under mechanical stimulation.

I.1.2 Skin

Most studies of skin have been conducted on humans, and therefore all information from this chapter addresses the properties of human skin. It is generally accepted that murine skin is similar to human skin with only scale changes. The similarities between human and murine skin is evidenced for instance by the fact that it is possible to perform xenografts of human skin on mice, as illustrated in figure I.8. It is however possible that some differences exist between the two species, either microstructural, macroscopic or both.

Skin is the largest organ in the human body. It has an average surface of 1.5 - 2.0 m^2 and weighs 3.5 - 4 kg in an average adult. It is a complex organ with multiple functions, reviewed in the first section below, and a variety of components, summarised in the second section. The third section focuses on the dermis, the most important layer for mechanical properties and the one we are most interested in.

I.1.2.a Properties and functions

The primary function of skin is one of protection and regulation. Skin plays an important role of structural support and protection from mechanical impacts and outer pressure. To this effect the mechanical strength of skin is crucial.

Skin protects the inner organs from outer radiations, especially UVs from the sun, an important

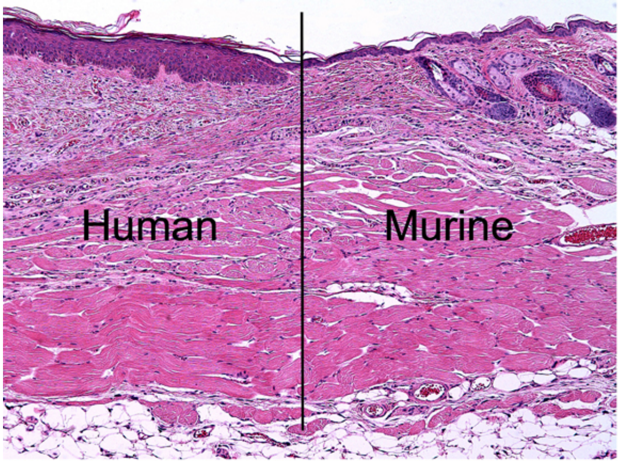

Figure I.8 – Histological section of skin after a xenograft (human skin transplanted onto immunodeficient mice) at junction site, coloured with hematoxylin and eosin (H&E) stain. H&E stain colours cell nuclei dark blue and proteins pink. Image from Fuhlbrigge Lab, Harvard.

factor of cancer development. When it has sustained a burn, the protective function of skin against UVs is impaired.

Skin is however not impermeable: it is an important exchange area. Through perspiration and muscle activation in goose bumps, skin contributes actively in the regulation of body temperature. The precise control of body temperature is of the utmost importance: below 32 ° C and above 41.6 ° C body temperature a human being is considered in mortal danger. Perspiration also regulates body fluid balance. Some chemicals such as hormones can also be released through skin when needed.
Skin is our first barrier against micro-organisms and outer chemicals. In addition to a passive physical barrier, some elements of the immune systems, both innate and adaptative, are fully integrated in the skin. For example, Langherhans cells' in the epidermis capture antigens and present them to the T-lymphocytes to engage the chain of immune reaction.

Finally, skin is our primary organ for the touch sense. An extensive network of nervous cells can detect and relay touch, heat, cold and pain. Alteration of this function is extremely imparing in everyday life and can lead to an increased risk of severe injuries.

I.1.2.b Global structure

Skin is a complex multilayered organ. It encompasses cells, fibres, complex molecules, sweat and sebaceous glands, hairs, nerves, blood vessels, etc. Figure I.9 presents a simplified representation of skin's structure.

The outermost layer of skin is the epidermis. Its thickness can range from 0.05 mm, on the eye-

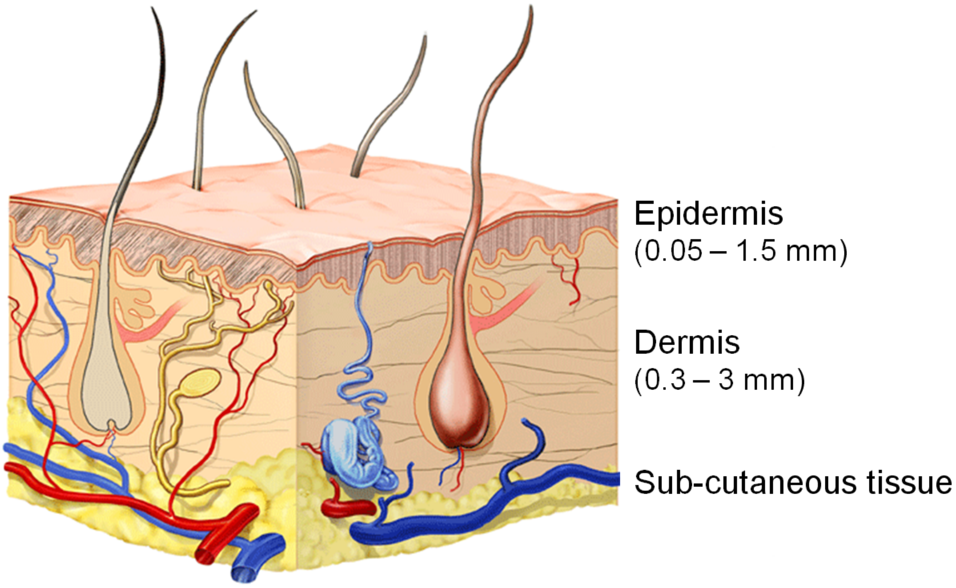

Figure I.9 – Schematic representation of skin's multilayered structure. Three layers are distinguished, from top to bottom: epidermis, dermis and sub-cutaneous tissue. Image adapted from *dermnetnz.org*.

lids, to 1.5 mm on soles and palms. The epidermis is made of layers of cells, called keratinocytes, stacked onto each other. The epidermal cells can be seen coloured in dark blue in the histological section presented in figure I.10.

The cells originate from the junction between the epidermis and the dermis, called basal layer. This is where melanin is added to the keratinocytes by cells called melanocytes. No blood vessel goes through the epidermis. Some immune cells, such as the Langerhans' cells, migrate through the epidermis to detect antigens.

The epidermal cells migrate from the basal membrane to the skin's surface while filling with keratin, a very resistant fibrous protein. The outermost layer of the epidermis is called the stratum corneum, and is entirely composed of dead cells glued together with lipidic cement. The cells from the stratum corneum detach progressively with friction and cleansing, leaving space for new cells. The mean turnover time of the epidermis, required to renew the cells completely, is roughly 39 days [25]. This time can be affected by various diseases, psoriasis for instance.

Under the epidermis lays the dermis. The epidermis-dermis junction presents finger-like waves, visible in figure I.10, to facilitate both adhesion and exchange of nutrients. The cohesion between the two layers is ensured by anchoring filaments of proteins: proteoglycans (called hemidesmosomes) and type VII collagen fibrils.

The dermis is the thickest and most important layer of the skin for structure and mechanical resistance. A few cells, called fibroblasts, can be found in the dermis. Their role is to synthetise the components of the extracellular matrix which constitutes the greater part of the dermis. These components are collagen fibres of different types (I, III, V, VI, XII, XIV, XVI), elastin fibres and

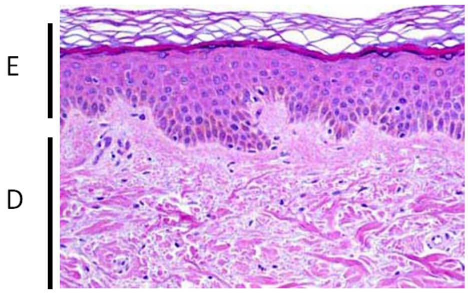

Figure I.10 – Histological section of skin at the epidermis-dermis junction, coloured with H&E stain (transversal cut). H&E stain colours cell nuclei dark blue and proteins pink. E identifies the epidermis, D the dermis. Image adapted from *mrcophth.com*.

ground substance. The ground substance encompasses everything in the extracellular matrix that are not fibres, including, but not limited to, proteoglycans. The main component of the ground substance and of the dermis in general is water, which represents 64% of the whole skin. The exact microstructure of the dermis is detailed in the next section.
Sebaceous and sweat glands lay in the dermis. Small blood vessels run through the dermis and especially at the epidermis-dermis junction, to bring nutrients to the epidermal basal cells.

Under the dermis lays the hypodermis, the deepest layer of the skin, also called "sub-cutaneous" tissue. It is composed of fat cells and is often interconnected with the fat layers underneath. The hair follicules initiate there, and blood vessels run through the hypodermis. The two main roles of the hypodermis are energy storage and shock absorption.

I.1.2.c Microstructure of the dermis

The dermis is a collagenous tissue in the general sense described earlier: it is a heterogenous structure made of a few cells and extracellular matrix. In our study, the cells of the dermis can generally be neglected, as their impact on the mechanical properties is considered negligible at the time scale we explore. It is however possible that dying cells, going through apoptosis, produce substances that can affect the extracellular network organisation.

The dermis is a composite structure in the mechanical sense of the term: a combination of collagen fibres, elastin fibrils and a host structure.
More than 70% of the dermis' dry weight is attributable to collagen. The most abundant type is collagen I, that accounts of approximately 80% of total amount of collagen in the dermis. Collagen I forms long and large fibres, that are arranged in a tight network. The dermis is separated in two parts, based on morphology of the collagen network: the papillary dermis and the reticular dermis. Figure I.11 shows scanning electron microscope (SEM) images of the dermis and collagen types location, demonstrating the differences in structure and composition between papillary and reticular dermis.

The dermis layer that is closest to the epidermis is called papillary dermis, and owes that name to the finger-like structures of the epidermis-dermis junction, called papillae. The papillary dermis consists of fairly small fibres, curled and crimped, that are quite loosely arranged. It is commonly believed to be responsible for skin's extensibility.
The deepest layer of the dermis is called reticular dermis. It consists of fibres that are arranged in thick bundles stacked densely onto one another. The fibres are straighter and thicker than in the papillary dermis. The reticular dermis is believed to be responsible for skin's resilience.
The papillary dermis is much thinner than the reticular dermis, with a ratio of approximately 0.2/0.8.

There are other types of collagen present in skin in lesser amounts. Collagen type III is the second most abundant collagen type in skin (approximately 20% of all collagen in adult skin). Other collagen types (type V, VI, XII, XIV, XVI) are much more scarce and represent only a few percent. Some of these collagen types (type III, type V) are fibrillar. The roles of these other collagens, not always well understood, are very diverse, from fibrillogenesis to adhesion. This is reflected in their uneven repartition in the two dermises, shown in figure I.11.

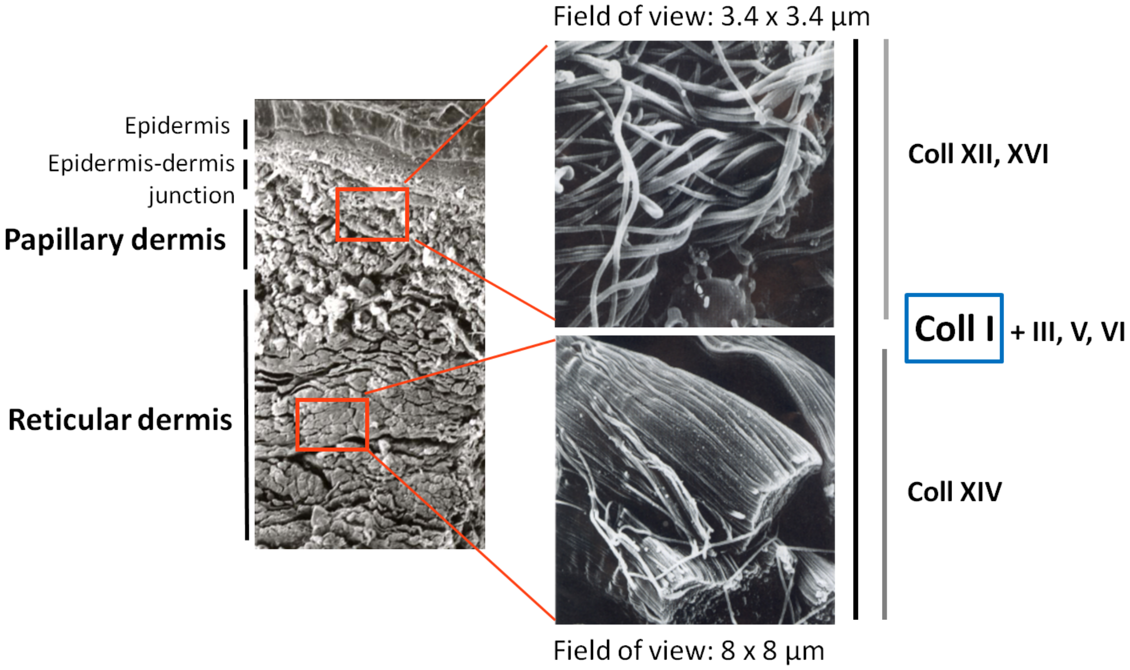

Figure I.11 – SEM images of the two dermises, papillary and reticular, and respective repartition of collagen types (type I, III, V, VI, XII, XIV, XVI). The papillary dermis consists of fairly small fibres, curled and crimped, loosely arranged, while the reticular dermis consists of thick bundles of fibres stacked densely onto one another. Image adapted from [26].

The host structure, which encompasses anything that is not collagen I fibre, is called in this work "extrafibrillar matrix". The extrafibrillar matrix includes a variety of elements. One of its most important component are proteoglycans. These complex molecules make for only about 0.2% of skin's dry weight, but their primary function is of the utmost importance: they retain water, in amounts of up to 1000 times their own volume.

Proteoglycans are complex proteins that consists of a "core protein" with one or more covalently attached glycoaminoglycan chains (GAGs). Figure I.12 shows a schematic representation of a proteoglycan. GAGs consist of a long-chain, aminated polysaccharides. The most common GAGs in the dermis are hyaluronic acid and dermatan sulfate. Proteoglycans are categorised depending upon the nature of their GAGs chains. They also are usually categorised by size in atomic mass units, that can vary between 30 kDa (kiloDaltons) and 500 kDa.

Proteoglycans are visible when coloured with a specific stain, such as alcian blue. Using this technique, Scott and coworkers [27, 28] demonstrated that there is structure in the extrafibrillar matrix. Indeed, in most connective tissues, such as skin, the proteoglycans attach to collagen fibres at regular intervals, and extend perpendicularly from fibre to fibre. They are thus believed to be important structural components of the dermis, that contribute to force transmission.

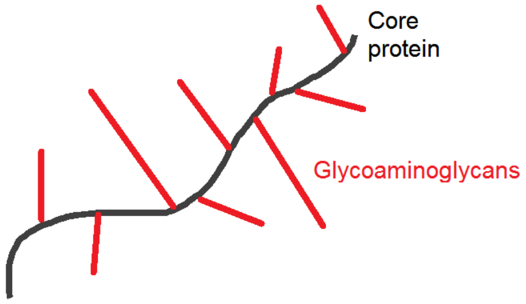

Figure I.12 – Schematic representation of a proteoglycan: a core protein with covalently attached glycoaminoglycan chains (GAGs).

Another major component of the matrix is elastic fibres, the most important of which being elastin. Elastin is a protein that forms small fibres, much thinner than collagen fibres, as shown in figure I.13. Elastin is often presented as providing "elasticity" to skin [29]. In skin, elastin fibres are believed to be wrapped around collagenous fibres, but their exact role and mechanism of action remains unclear [30, 31].

The embryogenesis of the dermis is a complex process, during which even collagen types that are present in small amounts can play an important role. Pathologies of collagen fibrillogenesis have very serious effects on skin and other collagenous tissues, which remain generally poorly understood. One of these pathologies, Ehlers-Danlos syndrome, is particularly relevant to our study and is described in Chapter IV.

The next section focuses on imaging methods enabling the investigation of the microstructural architecture of soft collagenous tissues.

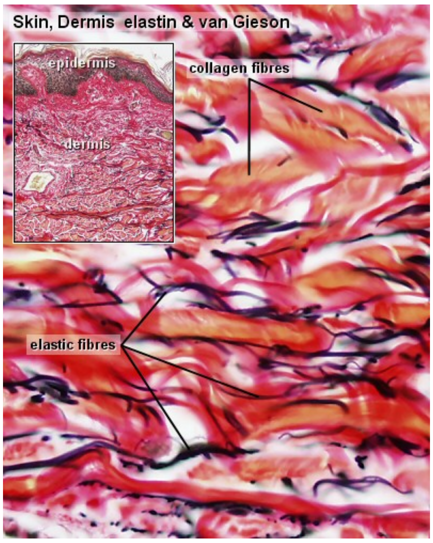

Figure I.13 – Histological section of skin (transversal cut) coloured with van Gieson's stain. Van Gieson's stain colours collagen pink and elastic fibres violet. Image from the School of Anatomy and Human Biology, University of Western Australia.

I.1.3 Imaging the architecture of soft collagenous tissues

When describing a tissue, whether to characterise it (biologically or mechanically speaking) or to diagnose a pathology, the examination of inner structure is valuable. This section will briefly introduce some imaging techniques available to investigate the architecture of soft collagenous tissues. Some allow *in vivo* imaging, whereas other necessitate to take a cut of the tissue, some are destructive, some not.

We will primarily consider optical imaging techniques: they are particularly appropriate for dynamic imaging of soft tissues during a mechanical test, for reasons discussed later. Nevertheless, other imaging techniques, briefly presented in the following section, can be used to unravel the microscopic architecture of soft collagenous tissues.

I.1.3.a Non-optical imaging

A prime example is electron microscopy, Transmission Electron Microscopy (TEM) or Scanning Electron Microscopy (SEM), mostly. Electron microscopy gives access to very small scales with a very good resolution, of about a nanometer or less, over a small field of view. These imaging techniques require a careful preparation of the sample in thin cuts, that need to be resistant both to vacuum and electronic beams. A SEM image of the dermis is shown in figure I.14 a. SEM has been applied to the investigation of fibre reorganisation during a mechanical tensile test on skin by Brown [32] and later by Belkoff and Haut [33]. However, as it is a destructive method, a different sample had to be observed at each deformation step.

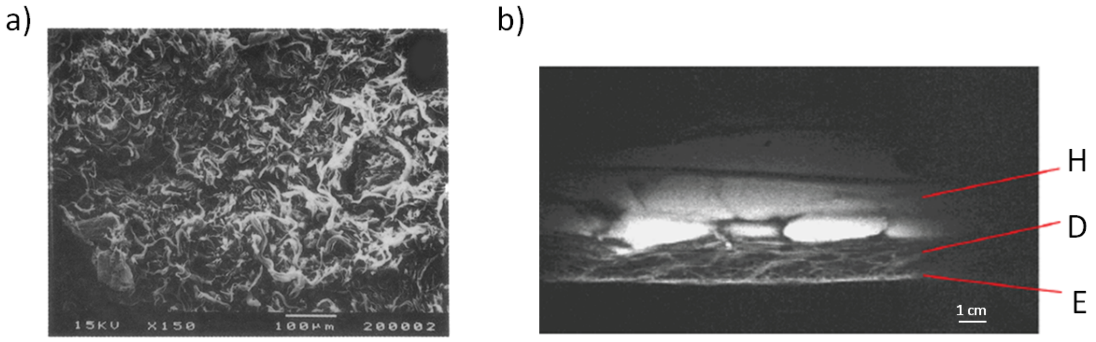

Figure I.14 – Imaging skin with non-optical imaging: a) SEM image of rat skin dermis. Scale bar is 100 μm. Image from [33]. b) MRI image of *in vivo* human skin. H indicates the hypodermis, D the dermis and E the epidermis. Image from [34].

X-ray diffraction techniques, such as Small-Angle X-ray Scattering (SAXS), allow specific imaging of organised tissues, such as the tendon [35] or the cornea [36]. Figure I.15 shows an example of fibre bundle orientation map obtained from a human cornea with X-ray diffraction. The resolution of X-ray imaging ranges between 0.1 and 0.5 mm. This technique is intrinsically limited to a few types of tissue, and damage has been observed when imaging tissues for a long time.

Finally, other imaging techniques are commonly used in *in vivo* imaging for diagnosis purposes, such as ultrasounds (using sound waves) and Magnetic Resonance Imaging (MRI, using magnetic fields and radio waves). They are non invasive and fairly easy to use, although requiring specific equipment. The images, such as the one seen in figure I.14 b for human skin, cover a large spatial field of view, but have a low resolution ($\approx$ 0.1 mm at best) and are sometimes difficult to interpret due to non-specific imaging.

I.1.3.b Optical imaging

Optical imaging techniques are valuable for imaging soft collagenous tissues with relatively large fields of view, good resolutions, light sample preparation and reasonably short imaging times. Depending on the technique used, the lateral resolution can reach 0.2 to 0.5 μm. When 3D imaging is possible, the axial resolution ranges from 1 to 5 μm. These advantages makes optical imaging ideal for microscopic observations of tissues during a mechanical test.
Optical imaging techniques can be classified based on the sources of contrast they depend upon, relying on various types of interaction between light and matter.

One of the most common ways to examine the microstructure of a tissue is to do an histological section. A biopsy of the tissue is embedded in paraffin, and very thin slices of the tissue are cut (a few micrometers thick). The sections are then deparaffinised, coloured with a chosen stain specific to the components sought and observed under an optical microscope (widefield imaging with

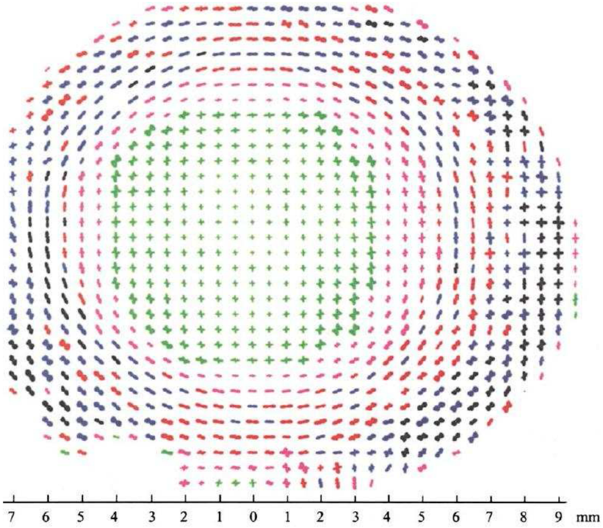

Figure I.15 – Map of fibre bundle orientation in human cornea obtained with X-ray diffraction. Image from [36].

white light). One of the most classical stain for skin is H&E, hematoxylin and eosin, in which cell nuclei are stained purple and proteins (such as collagen) are stained pink. Figure I.16 a shows an histological section of skin stained with H&E.

It is also possible to stain proteins, carbohydrates or lipids with specific antibodies: this technique is called immunohistochemistry. Antibodies can, theoretically, be obtained for any antigen: it is then possible to stain only a specific type of collagen for example.

Histological and immunohistochemical analyses allow for a precise and relatively immediate identification of a sample's components, as they are coloured with respects to their nature. Although time consuming, a 3D observation of the tissue is possible with successive sections. These analyses are however very invasive and inherently destructive. They only allow for a local characterisation of a whole organ. Furthermore, it remains mostly a qualitative analysis of the microstructure.

With a similar principle, it is possible to use polarised light instead of or in combination with specific staining to observe microstructures in the sample. An example of polarised light imaging of tendon without stain was shown earlier in this chapter, see figure I.6.

Reflectance can also be used as a source of contrast in soft collagenous tissues. Examples of imaging techniques making use of reflected light are Optical Coherence Tomography (OCT) or reflectance confocal microscopy.

Optical Coherence Tomography is based on low-coherence interferometry [39], typically employing near-infrared light to enhance penetration in biological tissues, mostly made of water. Depending on the system used, the micrometer resolution can be obtained, and the images, such as the one seen in figure I.16 b, can scan large regions of the tissue.

The advantages of OCT imaging are numerous: no sample preparation, 3D imaging is possible and the imaging time is very short (up to a few images *per* second). This imaging technique requires

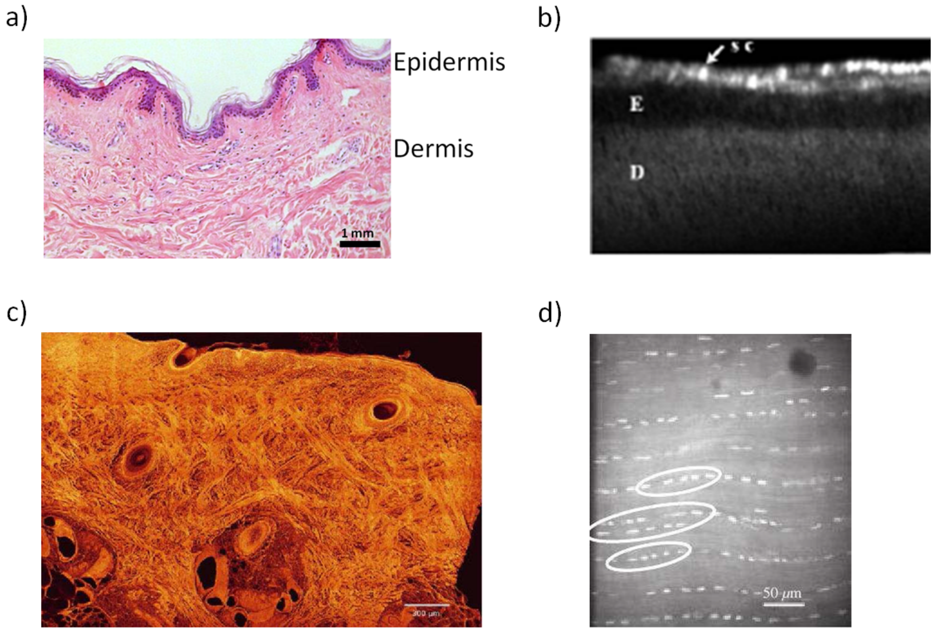

Figure I.16 – Optical imaging of soft collagenous tissues: a) Histological vertical section of skin stained with H&E. Scale bar is 1 mm. b) OCT image of *in vivo* skin. Image size is 1.5 × 0.6 mm^2. E identifies the epidermis, D the dermis and sc the stratum corneum. Image from [37]. c) Sagittal section of porcine skin stained with picrosirius red and observed with confocal microscopy. Scale bar is 300 μm. Image from [38]. d) Tendon observed in confocal microscopy, cell nuclei are stained using acridine orange. Scale bar is 50 μm. Image from [12].

however a tissue with optical interfaces (different refractive indices), and its main drawback is the complete lack of imaging specificity.

Finally, fluorescence has been used more and more extensively in the past decades as a source of contrast to image soft collagenous tissues. Most of the time, imaging techniques based on fluorescence require the introduction of exogenous fluorophores to induce contrast, but they can also rely on endogenous signals. The tissues are then imaged either with widefield microscopy, confocal microscopy or multiphoton microscopy.

Figure I.16 c shows an example of porcine skin imaged with confocal microscopy. This imaging technique was also used for micromechanical experiments by Screen and colleagues: they monitored the displacements of stained cell nuclei in tendons submitted to uniaxial tensile tests, to compare local and global strains [12]. A typical image with a group of nuclei identified is shown in figure I.16 d. Their results will be further discussed in relation with our results in Chapter III. For these techniques, no sample cutting is required, which means that delicate or deep tissues can be examined, sometimes even *in vivo*. The resolution is good (usually sub-micrometric), with a relatively large field of view (up to 1 mm). These techniques are however limited by nature by the small penetration of light in tissues: except for the cornea (which is transparent), the scattering of light greatly limits the penetration. Furthermore, especially when using exogenous signals, the

outcoming signal decreases with exposure time, which limits the possibility of observing a long-time effect such as microstructural reorganisation in tissues. This effect is called photobleaching. Notably, photobleaching can also be used to create patterns in the depth of the tissue, which can be monitored during mechanical loading to compute local stretches [40, 41].
In skin, there is a strong endogenous fluorescence signal from cells, epithelial cells for example, and from keratin in the hair. Melanin absorbs but does not re-emit light.

Confocal microscopy remains the most commonly used optical imaging method to image biological tissues. It allows for 3D imaging, with light sample preparation, a large field of view and good resolution. Collagen fibres in particular can be observed using their intrinsic fluorescence, which is however extremely weak, non specific and difficult to distinguish from fluorescence arising from other components.
In the following section we present fairly recent optical imaging techniques: non-linear microscopy, and in particular 2-photon excitation fluorescence and Second Harmonic Generation. These techniques are more difficult to implement than confocal microscopy, but can solve two major drawbacks of this technique: the small tissue penetration (maximum 30 μm) and the lack of specifity in the absence of exogenous signal (which require sample preparation).

I.1.3.c Non-linear microscopy: 2PEF and SHG imaging

Multiphoton microscopy regroups imaging techniques using non-linear optical effects as a source of contrast in biological samples. Multiphoton microscopy techniques, such as 2-photon excitation fluorescence (2PEF), Second Harmonic Generation (SHG), Third Harmonic Generation (THG) or non-linear Raman imaging, rely on the recombination of two or more photons into one photon by the tissue, hence the term “non-linear”.
Figure I.17 a shows simplified electronic states diagrams (Jablonski diagrams) for conventional (linear) fluorescence (i) and non-linear imaging: 2-photon excitation fluorescence and Second Harmonic Generation (ii). In the case of 2-photon excitation fluorescence the principle is the following: a molecule absorbs two photons and access an excitated state, then reemits one photon while going back to its original energy level.

The probability of occurance of non-linear processes is greater in areas with more photons, that is to say the focal volume (the probability is in N^2 for 2PEF or SHG). In linear imaging techniques, the probability of emission is proportional to the number of photons. This spatial specificity in photon emission is essential in non-linear microscopy: a non-linear excitation will lead to an outcome signal intrinsically localised. This property is illustrated in figure I.17 b. When a fluorescein solution is excited with an excitation wavelength corresponding to linear fluorescence, the signal is extended to an excitation cone (i), whereas with a non-linear effect the signal is intrinsically localised to a point in the focal plane (ii). To image the whole sample in 3D, one just needs to scan the sample by moving the focal point. A thick sample can be imaged by optical sectioning, *i.e.* by changing the focal plane.

Overall, multiphoton microscopy and confocal microscopy have comparable resolutions. However, the unique property of intrinsic signal localisation in multiphoton microscopy optimises the signal-to-noise ratio, and enhances the tissue depth available to imaging in highly scattering tissues, such as soft collagenous tissues.

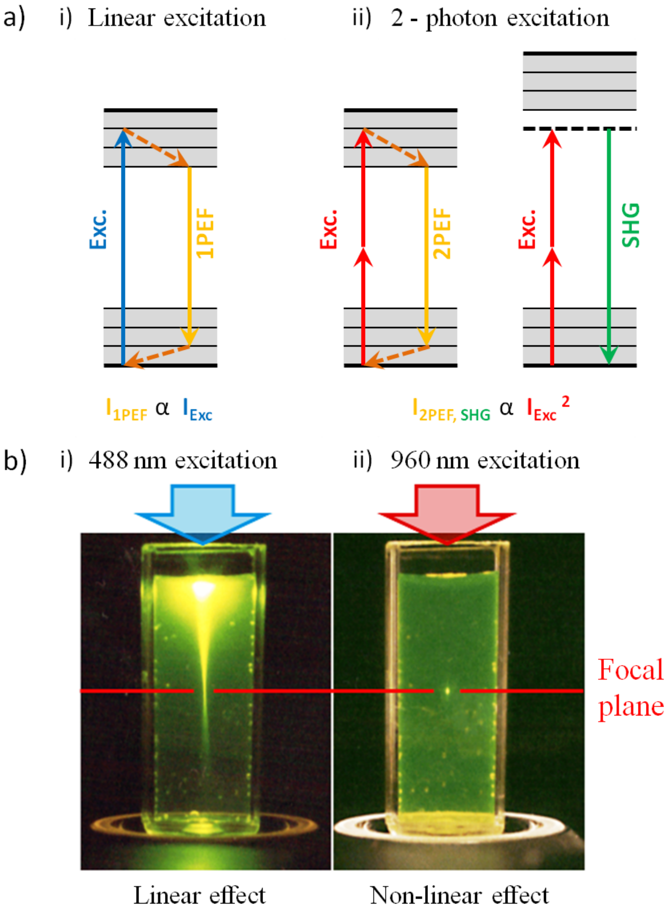

Figure I.17 – Non-linear imaging: a) simplified Jablonski diagrams for i) 1-photon and ii) 2-photon excitation signals (2PEF and SHG): two photons are recombined into a single photon, b) spatial resolution for i) linear and ii) non-linear fluorescence of a fluorescein solution. Non-linear fluorescence is intrinsically localised, whereas in linear fluorescence the excitation is generalised to a cone. Images adapted from [7].

Non-linear imaging techniques can be combined, together or with other imaging techniques, as long as one can distinguish the different signals from their wavelengths.

Multiphoton microscopy has a lot of applications in neurosciences and developmental biology. They have indeed the intrinsic advantages of small invasiveness, deep penetration and ability to rely on endogenous signals. They require however a large laser power to exploit the rare non-linear effects in tissues. This can be obtained with pulsed lasers (femtosecond lasers), that allow for a large peak power with a small mean power, and do not deteriorate the tissue.

Second Harmonic Generation (SHG) imaging is a non-linear imaging technique: the signal results from the combination of two photons of the same wavelength into a photon of halved wavelength. SHG is a coherent effect, meaning that the phase of the emitted photon is strictly related to the phase of the excitation photons. This means that the signal is amplified by constructive interferences if the local environment is organised. In a disorganised, random structure, destructive interferences annihilate the signal. This particularity is summarised schematically in figure I.18 a. Thus, for the same basic SHG-emitting material, the signal can only be seen in organised enough structures, such as fibres. This specificity is illustrated by examples of materials that can be observed using SHG, *e.g.* fibrillar collagens, cellulose fibres, some crystalline polymers.

In all proteins, the SHG signal comes from peptidic chains in amino acids. All collagen molecules that present a triple helical domain emit a small SHG signal. However, only fibrillar collagens emit significant SHG signals, *i.e.* detectable with a microscope. In figure I.18 b, we can see a combined SHG/2PEF image of a kidney with fibrosis. SHG signal, in green, emerges from type I collagen, which is a fibrillar collagen. No SHG signal can be observed in the glomerulus, where immunochemical labelling reveal however the presence of non fibrillar collagen IV.

Further details on the non-linear optical microscopy techniques used in this study can be found for example in [7].

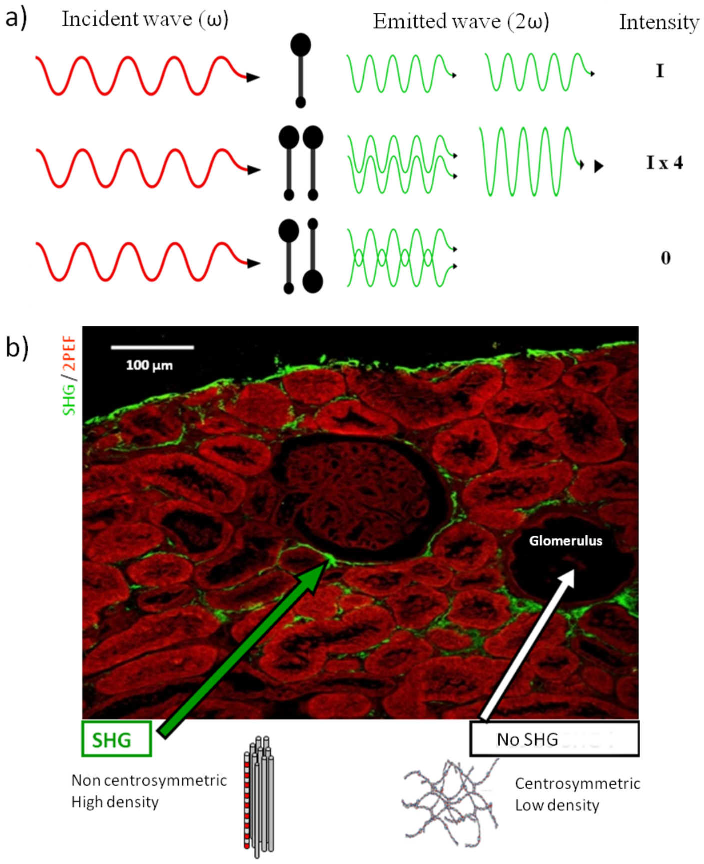

Figure I.18 – Conditions on microstructural organisation for SHG observation: a) generation of SHG signal by parallel molecules leads to constructive interferences, while anti-parallel molecules produce destructive interferences, b) SHG/2PEF image of a human kidney with fibrosis. SHG (green) reveals fibrillar collagen (type I). No SHG signal can be seen in the glomerulus, where non fibrillar collagen IV is known to be present. Images from [7].

I.2 Macroscopic scale: skin's mechanical properties

Skin's mechanical properties are of great importance in many clinical and cosmetical applications. They have hence been studied experimentally both *ex vivo* and *in vivo* for a long time [42]. This section first reviews the techniques allowing for skin's mechanical characterisation, *ex vivo* and *in vivo*. We then detail the complex mechanical properties of skin.

I.2.1 Mechanical characterisation

I.2.1.a *Ex vivo characterisation*

Ex vivo tests have the benefit of allowing for the exploration of a wide range of parameters. Skin can be isolated from fat, muscles and bone to characterise only the properties of skin, and not of an ensemble of tissues. While with *in vivo* analysis, only the top layers of the skin are accessible, *ex vivo* analysis allow the whole depth of the tissue to be tested. Layers of skin can also be isolated to test independently. The failure mechanisms can be evaluated through destructive tests not available *in vivo*.

Finally, another key advantage of *ex vivo* testing is that samples can be modified using chemicals to evaluate separately the contribution of each component, for instance collagenase breaks the peptide bonds in collagen. This method has been used to vary the proportions of collagen [43], elastin [44] and proteoglycans [45].

The *ex vivo* results can also serve as database to compare real tissues and their tissue-engineered imitations.

The tensile properties of skin have been extensively studied. Uniaxial, biaxial and multiaxial tests have been performed. For reviews, see [30, 46, 47]. Figure I.19 shows some examples of set-ups for these tests.

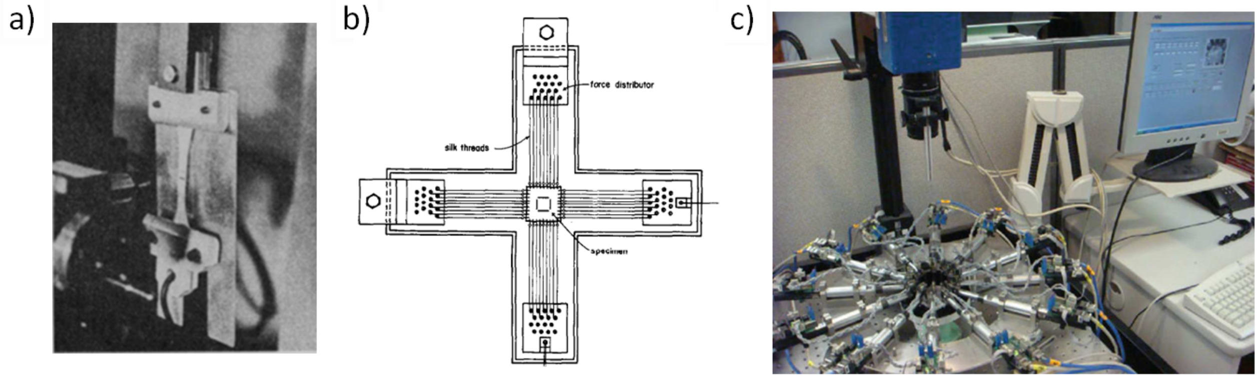

Figure I.19 – Tensile tests on *ex vivo* skin: a) uniaxial test (1970, image from [48]), b) biaxial test (1974, image from [49]), c) multiaxial test with 12 automated motor axes and camera mounted above the testing region for Digital Image Correlation (2011, image from [38]).

Inflation tests can also be used to test for skin tensile multiaxial properties [50]. Compression, torsion and shear tests have also been carried out. Finally, some studies test the epidermis-dermis cohesion with delamination tests. Examples of set-ups for these methods are shown in figure I.20.

The great variety of experimental protocols should however encourage us to be careful when comparing two studies or matching model to experiment. Indeed, many variables can influence the results, such as:

- Animal tested: *e.g.* human [53], rat [43, 45], dog [54], pig [55, 56], cat [48].
- Age of the animal: *e.g.* neonatal, adult, aged.
- Site and orientation: *e.g.* rib, rump, forehead, abdomen, back.
- Sample preparation: *e.g.* tested right after excision, frozen, with layers and/or hairs removed.
- Hydration method: *e.g.* immerged, sprayed, covered in gel, no hydration.
- Clamping method: *e.g.* grips, clips with sandpaper, sewed with silk threads.

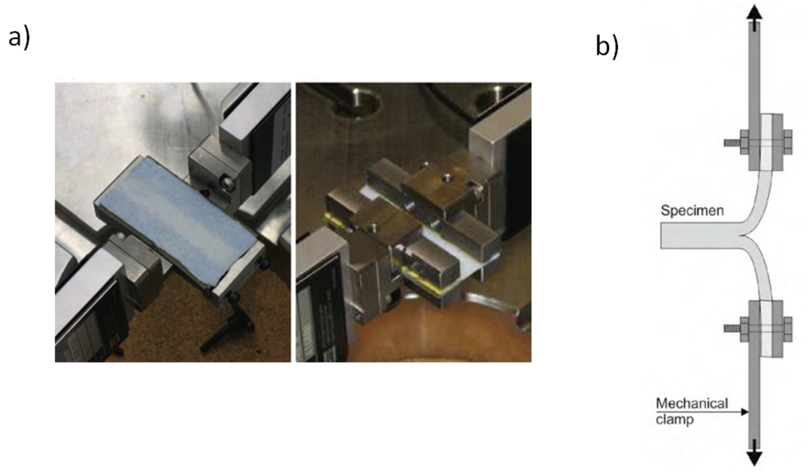

Figure I.20 – Examples of other possible mechanical set-ups on *ex vivo* skin: a) Set-up for pure shear test. Image from [51]. b) Delamination test between epidermis and dermis. Image from [52].

– Loading path: *e.g.* preconditioning or not, strain rate, cycling, maximum stretch ratio.

One of the main differences between mechanical test protocols is the method used for displacement measurements. In recent years, contact extensometers have been supplemented by non-contact methods, such as Digital Image Correlation (DIC), which will be used in the present work.
Digital Image Correlation is a post-processing technique now frequently used in mechanics. The principle is to identify in a deformed image the displacements of a pattern from the reference image. The matching of the two images makes use of a similarity criterium, called correlation coefficient, which relies on the hypothesis of conservation of local contrast in the immediate surroundings of the point sought.
This technique gives a point-by-point displacement field at the local scale, that can be compared with the imposed displacement to correct for slippage or unfolding of the tissue. Digital Image Correlation is generally used in 2D only, but 3D DIC is also available. Details on DIC and its applications to biological materials can be found in [57, 58, 59].

However, *ex vivo* tests have two main drawbacks. As mentioned before, they isolate the tissue from its natural environment. This eases the identification of skin properties, but removes the natural prestress and hydration control. Furthermore, the preparation of the tissue is an inevitable source of damage: from extraction to potential preparation (such as layer separation), the tissue can become deteriorated. This inevitably results in mechanical characterics different from those measured with *in vivo* analysis.

I.2.1.b *In vivo characterisation*

In vivo tests evaluate skin's properties in natural prestress and hydration state. Experiments have mostly been implemented on humans. Obviously, only low loads can be applied with *in* *vivo* analysis. Testing can either be carried out in plane or perpendicular to the surface. Four main categories of *in vivo* tests can be identified: torsion, tension, suction and indentation. For reviews, see [60, 61]. Some set-ups for *in vivo* assessment of skin mechanics are shown in figure I.21.

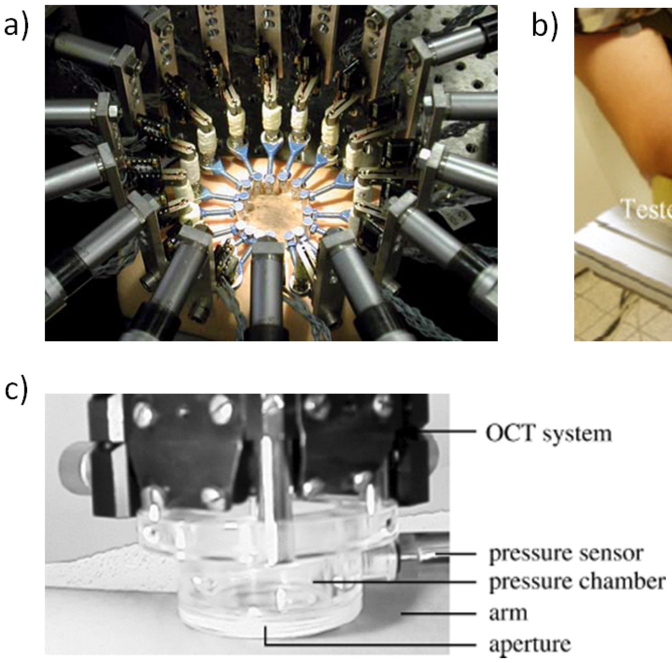

Figure I.21 – *In vivo* tests of skin biomechanical properties: a) Multiaxial tensile test on a subject's arm. Image from [62]. b) Indentation test. Image from [63]. c) Suction device set-up combining suction experiments and OCT imaging. Image from [64].

To test the skin in its surface plane, torsion tests and tensile tests can be carried out. These tests rely mostly on the properties of epidermis and upper dermis [61]. The torsion test consists in the application of a disc to the skin's surface, which is rotated with a prescribed torque. Tensile tests consist in attaching two (for uniaxial tests) or more (for multiaxial tests) tabs to the skin and imposing a displacement.

Suction and indentation measurements evaluate skin's biomechanical properties perpendicularly to the surface. In suction tests a vacuum is applied to the skin's surface, which deforms due to the decrease in pressure. The deformation of the tissue can be related to its mechanical properties. Indentation is a commonly used technique in materials science: a rigid indenter is pressed to the skin's surface. The measured loads and displacements can be linked to the material properties. In these techniques, the lower layers of the skin contribute to the mechanical properties measured as well as the upper layers [61].

I.2.2 Skin's mechanical properties

Skin is a complex multifunctional organ that has to meet numerous specifications. It must be very resilient, flexible in all directions, and able to return to its original state in any circumstances. This leads to a complicated range of mechanical properties, described in this section.

I.2.2.a Non-linear elasticity

The non-linear elasticity of skin, and more generally of all soft collagenous tissues, can be illustrated by the typical stress/stretch curve shown in figure I.22. It is commonly described as a four regions curve. Region 1 is called toe region: strain causes no augmentation in stress. Region 2 is the heel region: it is a transition phase, in which stress builds up. Region 3 is a linear region. Region 4 marks the beginning of tissue failure, with a force plateau followed by progressive rupture. Skin can usually withstand a very large elongation, up to a stretch ratio of 1.6.
In skin, the non-linear elasticity has been intuited by Langer in 1861, and demonstrated in 1966 by Daly [65].

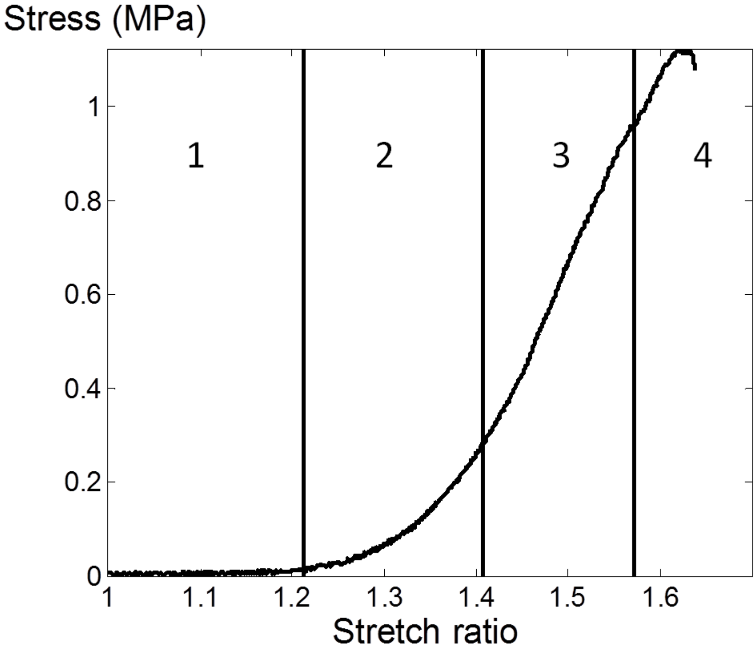

Figure I.22 – Typical stress/stretch curve for skin. Four regions are generally identified: the toe (1), heel (2), and linear (3) regions and the progressive rupture (4). All soft collagenous tissues show similar non-linear stress/stretch curves.

The non-linear stiffening is usually interpreted as a way for soft collagenous tissues to respond to two contradictory needs. Indeed, at relatively small strain, the remodelling of the material should be easy, while at larger strains the tissue should be stiff enough to ensure cell and tissue integrity. The non-linear behaviour of soft collagenous tissues has been studied fairly extensively recently, either with phenomenological [48, 66, 67] or structural approaches [33, 68, 69, 70]. The classic microstructural explanation for this non-linearity is presented in section I.2.3, as well as the commonly used mechanical models.

I.2.2.b Prestress and anisotropy

In vivo, skin is subjected to a prestress, which was described as early as 1861 by Austrian anatomist Karl Langer. He discovered that by puncturing holes in a cadaver's skin with a circular-shaped tip, the resulting holes were ellipsoidal, revealing the existence of a prestressed state. By puncturing several holes close to one another, he was able to delimit pretension lines, known as Langer's lines, schematised in figure I.23. Even if prestress does exist in mouse skin (skin retracts a little when cut out from the mouse's back) and it is likely that so does anisotropy, Langer's line have not been characterised for mice.

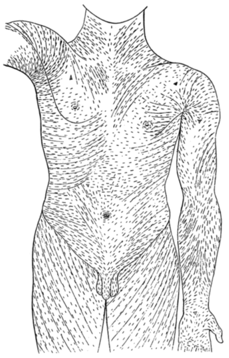

Fig. 838.
Die Spaltrichtungen der Haut. (C. Langer.)

Figure I.23 – Skin's natural pretension lines, called Langers' lines. Image from [71].

Growing in a prestressed environment, skin develops a natural microstructural anisotropy, which reflects on its mechanical properties. Figure I.24 shows the superposition of two stress/stretch curves from tensile tests carried out in directions perpendicular to each other, which demonstrates skin's highly anisotropic mechanical behaviour [72].

I.2.2.c Viscoelasticity

All soft collagenous tissues are viscoelastic materials: they exhibit both elastic and viscous characterics. The viscoelasticity of skin can be attributed to several factors, such as liquid flows, viscoelasticity of the ground substance, viscoelasticity of collagen fibres, rearrangement of the meshwork, etc. It is likely that different structural levels contribute to viscoelasticity at one or more time scales [5, 42].

Examples of behaviour that can be attributed to skin's viscoelasticity include:
- Creep and relaxation. If the stress is held constant, the strain increases with time (creep) and if the strain is held constant, the stress decreases with time (relaxation) [42]. Relaxation

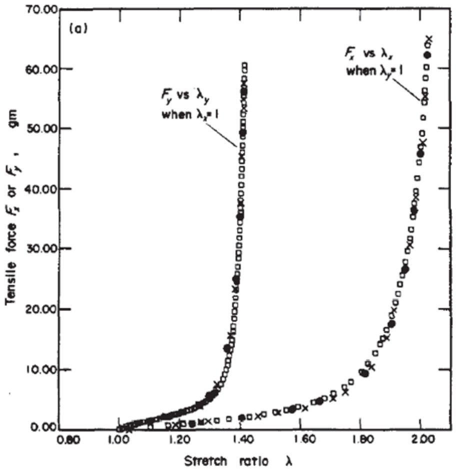

Figure I.24 – Stress/stretch curves from tensile tests carried out on *ex vivo* rabbit abdominal skin in directions perpendicular to each other reveal skin's highly anisotropic mechanical properties. Figure from [72].

experiments are shown in figure I.25 a.

- Cyclic loadings, and in particular the presence of hysteresis [73]. An example is shown in figure I.25 b.
- Dependency of the mechanical properties on strain rate [55], as shown in figure I.25 c.
- Dependency of the mechanical properties on loading history [55]. In particular, it is possible to do a preconditioning, with repeated cycles at a given small strain: after a few cycles, the stress/strain curve converges towards a single cycle, as shown in figure I.25 b. That effect is close to the Mullins effect observed in elastomers [74].

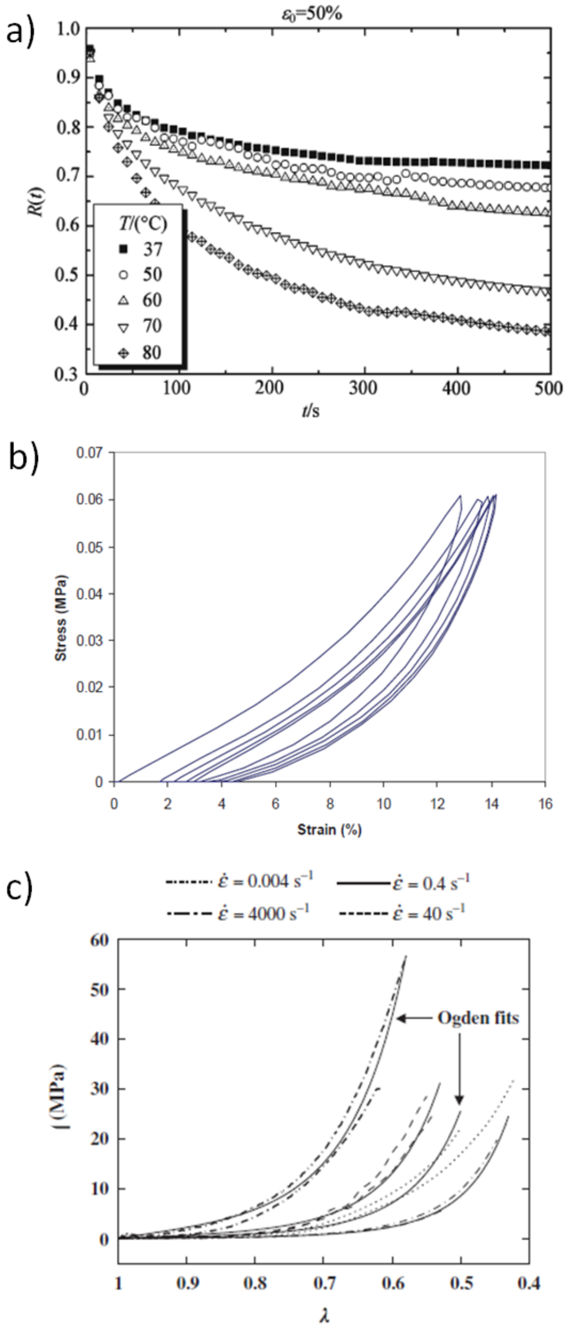

Figure I.25 – Mechanical tests reveal skin viscoelastic properties: a) Relaxation experiments. When the strain is held constant, the stress relaxes. Figure from [42]. b) Cycles. The loading and unloading curves are different (hysteresis), and the cycles converge towards a single curve after a few cycles (preconditioning). Figure from [73]. c) Strain-rate dependency. The faster the sample is stretched the stiffer it appears. Figure from [55].

I.2.3 Soft tissues mechanical modelling

All soft collagenous tissues are made of the same basic components. It seems then reasonable to think that knowing the properties of these basic components and the microstructure of each tissue is sufficient to model every possible tissue. A lot of studies have been carried out recently in an attempt to optimise a model that could account for all types of soft tissues, over a large strain range with reasonable accuracy. These works have been inspired by models of fibre-reinforced composite structures [75].

Soft tissues are highly non-linear, anisotropic, viscoelastic, compressible at least to some extent, fully three dimensional and can undergo very large strains. Simplifications are often needed to reach an effective model. Most models neglect long-term changes and remodelling (due to age or disease), as well as failure mechanisms, which can be physically relevant in clinical procedures. They also consider isolated soft tissues, and in particular neglect active components, such as contracting elements.

Identification of a Strain Energy Function (SEF) is by far the preferred method for characterising the complex material properties of soft tissues and identifying a constitutive equation. Models based on SEF were first phenomelogical models only, but since the crucial role of the microstructure in the mechanical behaviour of soft tissues has been demonstrated, more and more models have included microstructural elements. A recent comprehensive review of continuum modelling of soft biological tissues biomechanics can be found in [76].

I.2.3.a Phenomenological models

A solid is called hyperelastic if its elastic potential energy can be expressed with a scalar valued strain energy function W such that:

$$\mathbf{S} = \frac{\partial W}{\partial \mathbf{F}}(\mathbf{F})$$

where $\mathbf{S}$ is the nominal stress tensor and $\mathbf{F}$ is the deformation gradient tensor.

The most simple strain energy function is the neo-Hookean: $W = \frac{\mu}{2}(I_1 - 3)$, where I_1 is the first invariant of the right Cauchy-Green deformation tensor. It involves a single parameter and provides a simple model for non-linear deformation.

With his pioneering experimental work on skin, Fung was the first to demonstrate both the highly non-linear elasticity of skin and the preconditioning effect [77]. To model the stress/strain relationship, Fung developed a strain energy function with two parameters that is still widely used to this day [72].

Many other strain energy functions have been developed to improve data-fitting and in particular extend the models to large strains and compressible materials. A comprehensive review of strain energy functions used to describe non-linear elasticity of rubber-like materials can be found in [78]. An example of mechanical modelling with different strain energy functions is shown in figure I.26.

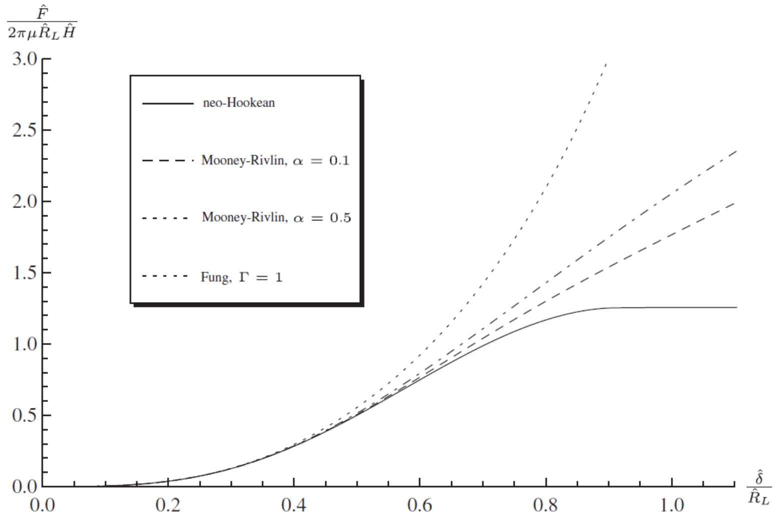

Figure I.26 – Hyperelastic models: force/indentation curves for a spherical indenter on a flat membrane, modelled using three strain energy functions: neo-Hookean, Mooney-Rivlin and Fung. Figure from [79].

Non-linear hyperelastic models are commonly used to describe the mechanical behaviour of soft collagenous tissues: many are available in finite element modelling softwares. They generally fit the data well on simple experiments, but the parameters are difficult to interpret physically. Furthermore, they are limited in range of strain, strain rates and diversity of tissues modelled. This is the reason microstructural models were developed using new data on microstructural architecture of soft collagenous tissues.

I.2.3.b Microstructural models

Microstructural models of soft tissues have been greatly inspired by the classical interpretation of the non-linear stress/strain curve in the case of tendons.

Based on early observations of the periodic waviness of collagen fibres in tendons (or crimps) [15, 80], Kastelic and coworkers developed a microstructural model called "Sequential Straightening and Loading" [81]. In this model, wavy fibres do not contribute to the stress, and get taut progressively when the tendon is stretched, depending on their crimp wavelengths. When straightened, the fibres are linearly elastic. In concrete terms, the strain imposed on the whole tendon first straightens the fibres, and the stress rises only when they become straight and start to be pulled on. The progressive recruitment of linearly elastic fibres results in the well known J-shaped stress/strain cruve.

This simple and effective model has been extended considerably, with different distributions of fibre wavelengths, mechanical properties of fibres, cross-links, extrafibrillar matrix properties, etc. It has been applied to tendons, arteries and other tissues [38, 40, 82, 83].

On skin, this classical interpretation is supported by early observations of Brown in 1973 [32], and later Belkoff and Haut [33]. In these studies, scanning electron microscopy was used to image different skin samples at various deformations. The progressive alignment of fibres was observed, before the fibres appeared straight on SEM images. The images were attributed to the different phases of the stress/strain curve, as seen in figure I.27, and the fibres were supposed to undergo elongation during the linear region.

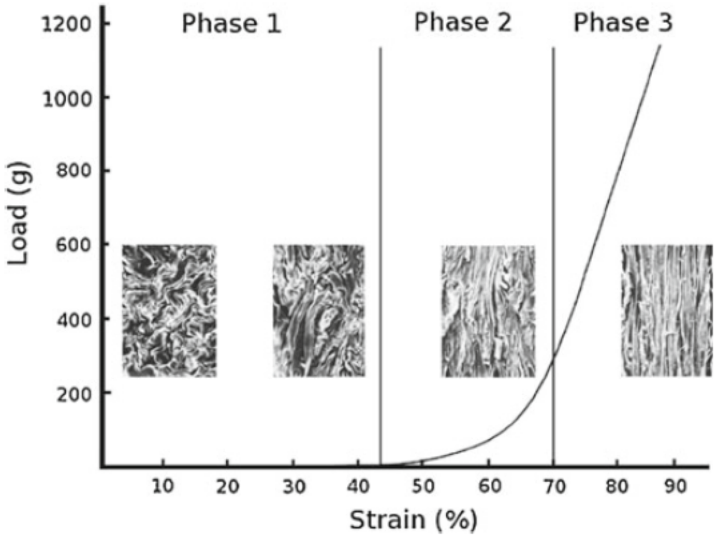

Figure I.27 – Stress/strain curve for skin, with samples observed with scanning electron microscopy at different strain levels. Figure from [32].

Microstructural models require microstructural observations, by any given method. However as mentioned before, most of the time these observations are static (the tissue is fixed in a certain deformation state) and made on different samples at different strain levels. This is ill adapted to models, which describe the evolution of a single set of parameters representing a single sample.

The idea behind our multiscale study combining simultaneous mechanical experiments and microstructural observations is to gather information to demonstrate the link between mechanical properties and microstructural evolution, rather than to infer it. The following section reviews previous multiscale work, both from the literature and from our group.

I.3 Previous multiscale works

Multiscale experiments combining optical observations and mechanical measurements are not frequent. This can be attributed to the difficulty of marking the samples appropriately for imaging, to photobleaching effects, that limit the time frame available for observation, and to the complexity of optical devices, not designed to leave space for a mechanical testing apparatus under the objective.

Notable multicale studies have been carried out using various techniques, *e.g.* polarised light imaging [84, 85, 86, 87], optical coherence tomography [88], confocal microscopy [12, 89, 90], small-angle light scattering [91], X-rays [35]. The studies were carried out on aortic valves, ligaments, joints, tendons and engineered tissues.

Multiphoton microscopy has been used recently for multiscale characterisation of fœtal membranes [92], liver capsule [41] and skin [93].

Multiscale studies combining mechanical tests and SHG microscopy imaging have been conducted at the Solids Mechanics Laboratory before, in collaboration with Marie-Claire Schanne-Klein's team at the Laboratory of Optics and Biosciences (LOB). Two tissues where tested: tendon and cornea. Cornea was investigated using a pressure test, which corresponds to physiological loading. Tendons were tested in uniaxial tensile test [94, 95].

The characterisation of tendons is presented here as it has laid down the framework we used for the investigation of skin multiscale properties, both from an experimental point of view, as our set-up is an adaptation of the one used here, and as a point of comparison for mechanical and microstructural results.

Rat tail tendons were studied, as they are one directional with a well known microstructure. The tendon is made of bundles of parallel collagen ropes, the fascicles, that lie aligned next to one another, embedded in ground substance. The main feature of the fascicles is the wavy shape they assume in rest state, called crimps. These crimps have been demonstrated to disappear as the tendon gets stretched and reappear when the tendon is relaxed, provided it was not taken too far and damaged [80].

In this study, tendon fascicles were stretched using a uniaxial tensile test machine under SHG observation. The set-up is shown in figure I.28. The chosen loading path was cyclic with increasing strain, followed by a traction up to rupture, as seen in figure I.29 a i. The stress/strain curve obtained, shown in figure I.29 a ii, follows the expected non-linear J-curve, with a notable hysteresis on the unloading path.

Using SHG, images at the scale of the micrometer were taken. Bundles of parallel wavy fibres appear, as seen in figure I.29 b i. The crimp is visible at rest state, and disappears when loading the tendon, as seen in figure I.29 b ii. The crimp evolution was tracked during the whole experiment (figure I.29 a i-v) on SHG images taken at chosen strains (figures I.29 a vi). A quantitative parameter, the crimp period, was measured on the SHG images (figures I.29 a vii and viii).

The results indicate that the crimp period evolves throughout the cyclic mechanical test. This means that the crimps are not correlated with a default in the collagen molecule arrangement, but rather with a local buckling resulting from internal stresses. Such a fine observation of crimp evolution through a mechanical stimulation had not been performed before, and provides useful information for the optimisation of multiscale modelling of tendons.

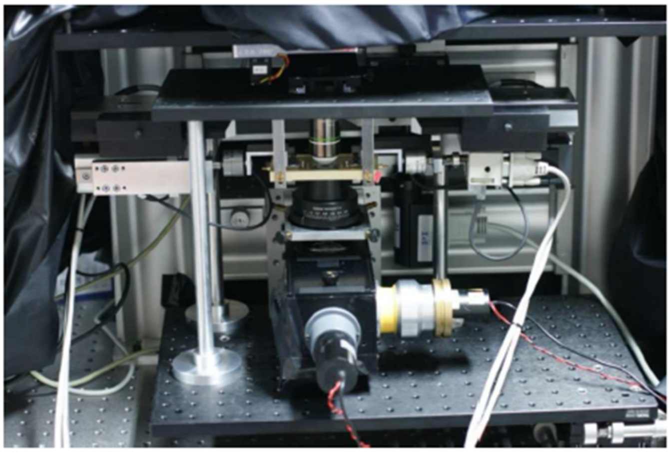

Figure I.28 – Experimental set-up for multiscale characterisation of tendon: the uniaxial traction device is inserted under the SHG microscope. Image from [94].

I.4 Aim of the thesis

The aim of this thesis is to investigate the multiscale biomechanics of skin. Our approach, summarised in figure I.30, is to combine macroscopic mechanical tests on mice skin and microscopic observations with Second Harmonic Generation imaging to investigate the interplay between material and structural properties of skin. The test protocol allows us to monitor the reorganisation of the collagen network through a mechanical tensile test. The full test protocol will be presented in Chapter II. The results of the multiscale characterisation of normal mice skin will be presented in Chapter III.

Some diseases affect the fibrillogenesis of collagen and the microstructural morphology of collagenous tissues. A classic example is Ehlers-Danlos syndrome. We used two mice lines created to investigate the mechanisms behind Ehlers-Danlos syndrome to assess the impact of a small change in the dermis' microscopic anatomy on both microstructural reorganisation during a tensile test and macroscopic mechanical properties. This study is presented in Chapter IV.

Finally, age induces great changes in the morphology and mechanical behaviour of skin. We used our multiscale method to investigate those changes, and this will be presented in Chapter V.

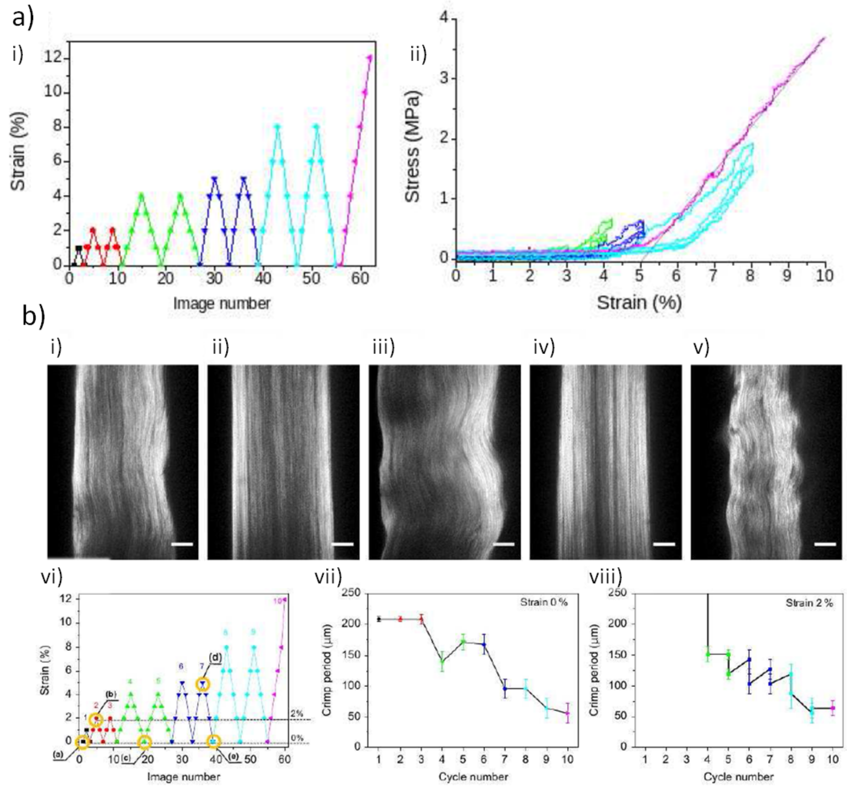

Figure I.29 – Multiscale mechanical characterisation of a tendon using SHG imaging: a) macroscopic mechanical test of a rat tail tendon using cyclic loading: i) loading path, ii) corresponding stress-strain curve and b) microscopic characterisation using SHG imaging: i-v) SHG cuts at different loading steps shown in (vi), scale bar: 50 μm, vii) and viii): quantitative evolution of a microstructural parameter, the crimp period. Figure from [94].

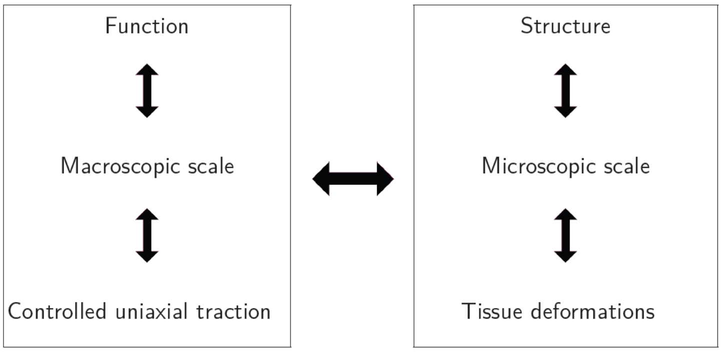

Figure I.30 – Summary of our approach: we combine macroscopic mechanical tests on mice skin and microscopic observations with Second Harmonic Generation imaging to investigate the interplay between material and structural properties of skin.

Chapter II

Experimental multiscale study of skin biomechanics

The previous chapter illustrated the need for an experimental database on the behaviour of skin's microstructure under mechanical stimulation. This PhD research work consists of a study of skin biomechanical properties using a multiscale set-up that combines macroscopic mechanical stimulation and microscopic observations.

This chapter aims at presenting in detail the material and methodological aspects of this work. The first section presents the preparation of the mice skin samples. The second section introduces our tensile test machine and the multiscale set-up, as well as the test protocols used. Finally, the third and fourth sections address data post-treatment, respectively from the mechanical and image processing points of view.

In the following sections we show histograms of mean values for the parameters considered, and the error bars stand for standard error of the mean (SEM), unless stated otherwise. Many references will be made to "statistical differences": we consider two populations statistically different with regard to one parameter if the p-factor resulting from the appropriate Student test is lower than 0.05, or 5%. Details on the statistical tools used in this work can be found in Appendix A.

II.1 Mice skin samples

Skin samples were harvested on the back of one-month-old mice. The sample preparation protocol was designed to meet three specifications. The first is obviously that the protocol should not damage the skin's microstructure. Secondly, to perform mechanical measurements, the tissue needs to be simultaneously of sufficient dimensions and strong enough to be held between jaws without damage. Finally, the hairs and epidermis need to be removed prior to the experiments with SHG imaging. This is due to the fact that the melanin contained in hairs and epidermal cells absorbs light emitted by the laser, and does not re-emit it. This energy absorption can lead to burns and

tissue damage.
Removing the epidermis has two effects on skin. First, it removes the mechanical contribution of the epidermis and of the epidermis-dermis junction. In particular the mechanical contribution of the stratum corneum, which is considered the stiffest layer of skin, is eliminated. Secondly, it degrades the natural regulation of skin's hydration by the epidermal cells. The hairs and epidermis were removed for all experiments, both with and without SHG imaging, to obtain comparable results.

The protocol described thereafter was designed by Florence Ruggiero and Christelle Bonod-Bideau at the Institut de Génomique Fonctionnelle de Lyon (IGFL) to obtain well preserved and well characterised skin samples suitable for our experiments.

All animal experiments were performed under animal care procedures and conducted in accordance with the guidelines set by the European Community Council Directives (86/609/EEC). All experimental procedures were approved by the Direction of the Veterinary Service of Rhône Department (DDSV, Lyon, France).

II.1.1 Sample preparation

The samples were prepared at the IFGL in Lyon, France. For the Wild Type (WT) mice we used black mice from the 129sv strain. For the genetically-modified mice we used specifically engineered strains described later in Chapter IV. All genetically-modified litters encompass both mutant and non-mutant mice. Although from slightly different genetic backgrounds, non-mutant mice from genetically-modified litters were equivalent in all aspects considered to true WT mice. This was tested for all parameters, the results can be found in Appendix B.

The mice were sacrificed by cervical dislocation. Right after sacrifice, the back of the mouse was first shaved with an electric trimmer. A thick layer of depilatory cream was applied on the skin, and after the recommended waiting time (usually around 6 minutes) the cream was gently removed using a scraper. This depilation procedure was repeated twice, three times if the hairs seemed to not come out easily.
This depilatory protocol is not perfect: often some hairs remained after depilation, and in any case the hair was only removed at the surface of the sample. This was found to be sufficient for our SHG observations. Additionally other depilation methods such as tweezers and waxing, in which the hair is pulled from its follicle, could damage the skin structure, especially as follicles lay deep in the dermis, often as deep as the hypodermis.
Finally, skin was cut out from the back of the mouse with surgical scissors and a dot of black ink was applied with a permanent marker on the right foreleg corner to identify head-tail direction. On mutant samples, a biopsy of ear was also collected for genotyping analysis.

To remove the epidermis, the sample was then put in a bath of 3.8% ammonium thiocyanate, epidermis side facing down, for 30 minutes at room temperature. The epidermis was removed as shown in figure II.1. The sample was observed with an optical microscope and the remaining epidermal cells were scraped away. The skin sample consists at that stage of the two deepest layers, the dermis and the hypodermis. As the hypodermis is mainly made of fat and contributes little to the mechanical properties of skin, we tried to take it off. We attempted to cut away the hypodermis from the dermis, but found that the structural integrity of the dermis was often impaired: the process left holes in the sample visible to the naked eye. The samples used in the biomechanical experiments described thereafter consist of dermis and hypodermis combined.

Figure II.1 – Epidermis removal after ammonium thiocyanate treatment. The epidermal layer (left) is detached from the dermis (right). Remaining epidermal cells were removed with a scraper.

The samples were stored in individual tubes with culture medium without phenol red (Dulbecco's Midified Eagle's Medium, Sigma-Aldrich), supplemented with 50 μg/mL penicillin/streptomycin (Sigma-Aldrich) to prevent contamination. They were sent by post to the École Polytechnique. The transport from the IGFL to the École Polytechnique took less than 24 hours. The samples were put in fresh culture medium upon arrival and kept at 6 $^\circ$C thereafter. The culture medium was changed again after two days, and the samples were tested within five days.

For mutant samples, genotyping experiments usually took place at the same time as biomechanical experiments, which were performed as blind tests.

II.1.2 Validation of preparation protocol with histological cuts

To validate the samples' preparation protocol we needed to confirm both the complete removal of the epidermis, which can alter mechanical properties and hinder imaging, and the preservation of the dermis' structure after epidermis removal. In order to do so we used histological analyses. The skin samples were examined at two different steps in the aforedescribed protocol: after hair removal but before epidermis removal and after removal of both hairs and epidermis, exactly as they were used in biomechanical experiments.

The samples were fixed in 4% paraformaldehyde and embedded in paraffin. The cutting and staining was carried out by an outside company (Novotec, Lyon, France). Sections of 5 mm thickness were cut and deparaffined, and were then stained with Masson's trichrome or Herovici's stain. Masson's trichrome stain colours collagen blue, cells' cytoplasms pink and cells' nuclei dark brown. Herovici's stain colours young collagen and reticulum blue, mature collagen red and cells' cytoplasms yellow.

The microscopy observations were carried out at the IGFL. The histological images, shown in figure II.2, provide evidence that the epidermis was correctly removed. The dermis' global structure is similar before (figures II.2 a and b) and after (figures II.2 c and d) epidermis removal, which ensures that the epidermis removal did not damage the dermis. Further observations with TEM showed that the basement membrane, the thin layer of characteristic extracellular matrix that separates the epidermis and the dermis, was preserved when we removed the epidermis and remained attached to the dermis.

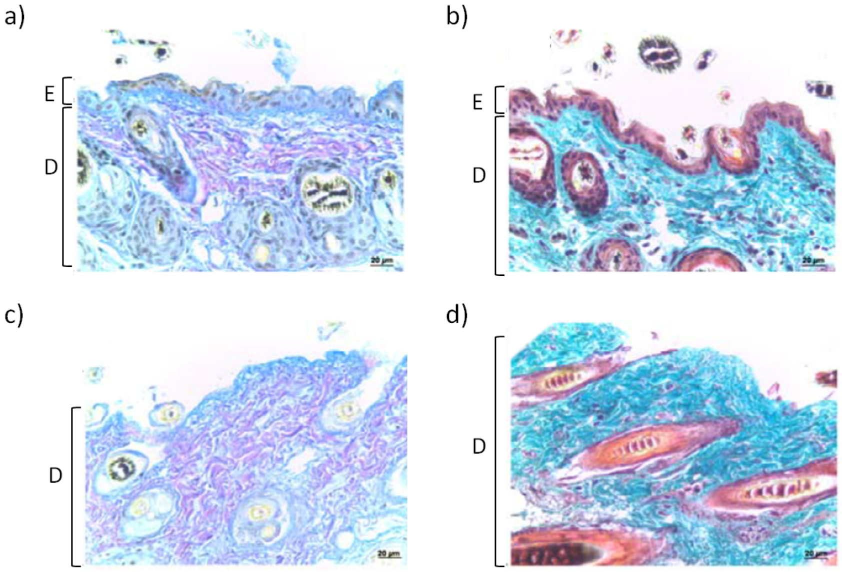

Figure II.2 – Stained histological cuts confirm epidermis removal and preservation of dermis integrity: a) and b) skin without hairs, stained with Masson's trichrome and Herovici's stains respectively, c) and d) dermis without epidermis, stained with Masson's trichrome and Herovici's stains respectively. E identifies the epidermis and D the dermis. Scale bar is 20 μm. Images made at the IGFL by C. Bonod-Bideaud.

II.1.3 Sample cutting for mechanical test

To ensure homegeneous repartition of the strain in the skin sample upon stretching, we choose to have the sample cut in the shape of a standard tensile test specimen, the dumbbell shape, also called T-bone or dog-bone shape. When the sample is the same width along its entire length, the stress concentrates where the sample is gripped. The reduction of width in the central part, and thus reduction of effective surface, allows for an equal repartition of strain and a concentration of stress in work area (central region). The rupture is expected to occur near the transition between the two widths.

Just before being installed in the traction machine, the samples were cut into a dumbbell shape following the red line shown in figure II.3. We used the dot of Indian ink arrowed in figure II.3 to locate the direction of the spine. That direction was the main axis of the dumbbell shaped sample. Cutting was made manually with curved dissection scissors, taking care to hold the samples on the outskirt parts that will not be used in mechanical test, so as to damage the sample as little as possible. The sample was maintained hydrated throughout the duration of cutting with drops of culture medium.

The typical dimension of the central region of the sample was about 20 mm in length and 8 mm in width.

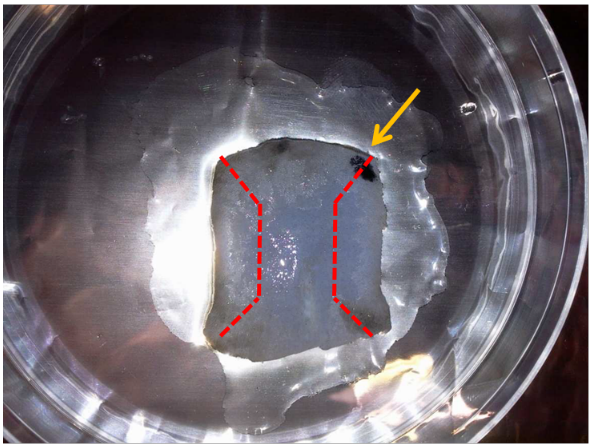

Figure II.3 – Preparation of the skin sample for mechanical test. The yellow arrow shows the black ink dot applied after dissection to indicate the right foreleg, the red mark shows the dumbbell shape the sample was cut into. Typical length of the cut sample is 30 mm from one end to the other, typical length of the central region is 20 mm, typical width of the central region is 8 mm.

II.2 Mechanical tensile tests

II.2.1 Tensile test device

The tensile test set-up was adapted from the one used previously at the LMS for tensile tests on tendons, as reported in [94].

We used a custom-built uniaxial traction device for mechanical loading. The sample was held by means of mechanical jaws that pinched the sample on either side. The skin was pressed on a rubber joint to limit damage and slippage. When removing the sample from the machine after

traction we could see that the skin was thinned down on the line of the joint but unbroken. This confirmed that the skin was grasped at this point, and not on the edge of the jaws.
Each grip was connected to a motor (drl42pa2g-04 ; Oriental Motor, Tokyo, Japan) and a load cell (Futek, LPM200, 2lb) with a force range of 9 N and a resolution of 0.03 N. The displacement of the motors was imposed and the resulting force recorded with a frequency of 1 Hz. The tensile test set-up can be seen in figure II.4.

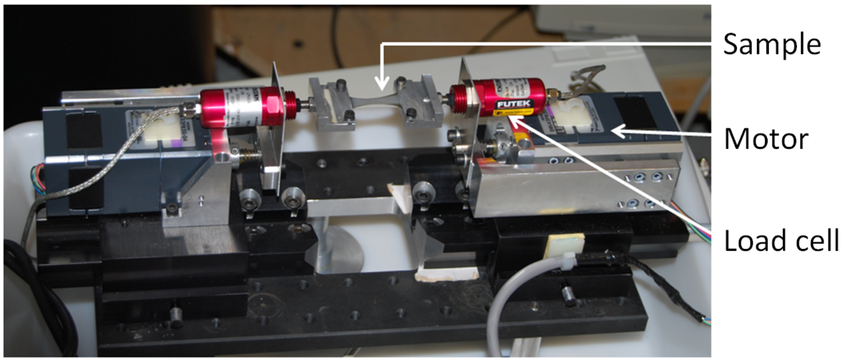

Figure II.4 – Custom-built uniaxial traction device for uniaxial tensile tests on skin.

The traction was symmetric to enable semi-continuous imaging of the same Region Of Interest (ROI). With our set-up and our samples, the range of strain rate accessible was $10^{-4}s^{-1}$ to $10^{-2}s^{-1}$. There is however a sample dehydration problem at $10^{-2}s^{-1}$, that will be discussed later.
The displacement of the motors could be controlled with an accuracy up to the micrometer. To choose the imposed traction speed when aiming for a strain rate of $10^{-4}s^{-1}$, we had to round up the length of the sample to the nearest tenth. It should be noted that this induced a discontinuity and that the strain rate differed slightly from sample to sample with regards to their length. If the sample's length was 14 mm the speed imposed was 0.001 mm/s and the strain rate $7.\ 10^{-5}s^{-1}$, whereas for a sample measuring 16 mm, as we imposed a speed of 0.002 mm/s the strain rate was $1.25.\ 10^{-4}s^{-1}$.

II.2.2 *In situ* set-up

Figure II.5 summarises the experimental set-up as used in combined biomechanical/SHG microscopy experiments. To image the skin sample semi-continuously during traction we used a custom-built multiphoton microscope from the LOB at the École Polytechnique.

The scanning protocol was designed to record optical cuts at given depths: mirrors allowed for a point-by-point scanning in focal plane, then DC motors moved the objective down by a given axial step and the scanning resumed. The scanning is summarised schematically in figure II.6. We obtained a stack of 2D images: the imaging is in semi-continuous 3D.

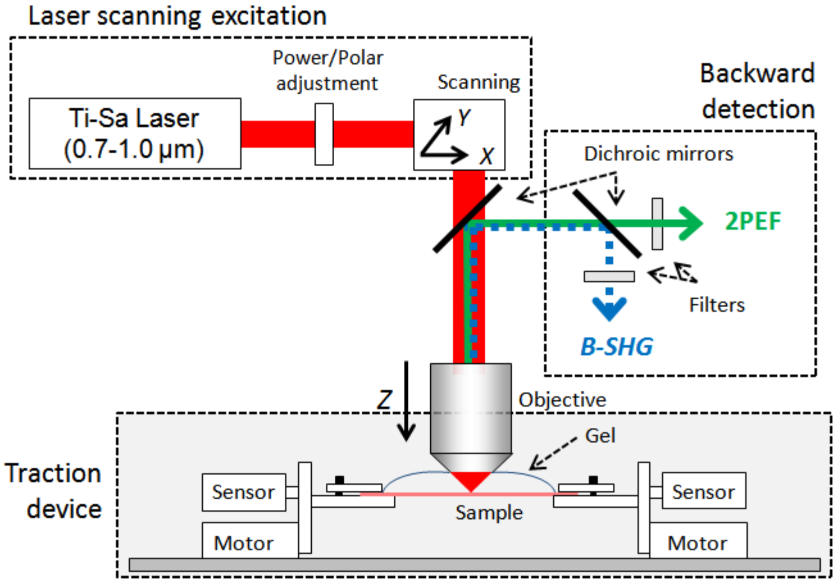

Figure II.5 – Schematic representation of the whole experimental device, with multiphoton microscope and traction device. Adapted from [94].

Backwards SHG and 2PEF signals were collected at the same time on different channels using photon-counting photomultiplier tubes. The signals can be differentiated as they conveniently come out at different wavelengths: because of the specificity of the phenomenon generating SHG, the SHG signal only comes out at exactly half the excitation wavelength λ, in a very narrow peak. On the contrary, there is energy loss in the generation of biphoton fluorescence and the 2PEF signal appears at a relatively wide range above $\frac{\lambda}{2}$ and below λ. This is summarised schematically in figure II.7.

Signals were collected with 0.5 μm pixel size and 2 μm axial steps. Typical size of image stacks was $480 \times 480 \times 50\ \mu m^3$ (corresponding to $960 \times 960 \times 25$ voxels). The typical lateral and axial resolutions were 0.4 μm × 1.6 μm near the sample surface. A stack of images took five to ten minutes to record.
It is also possible to image the sample almost continuously (an image every other second approximately) with much lower resolution. We use this faster imaging to follow the same ROI throughout the mechanical tensile test. Further details on the microscope and imaging protocol can be found in [7].
We used a quasi-circularly polarised excitation to have homogeneous imaging of fibres of any given orientation in the focal plane. Polarised excitation can also be used for a more precise analysis of local orientations, but this technique requires a much longer imaging time, as the direction of polarisation has to be rotated. Details on SHG imaging with polarised light can be found in [95] on tendon and [96] on cornea.

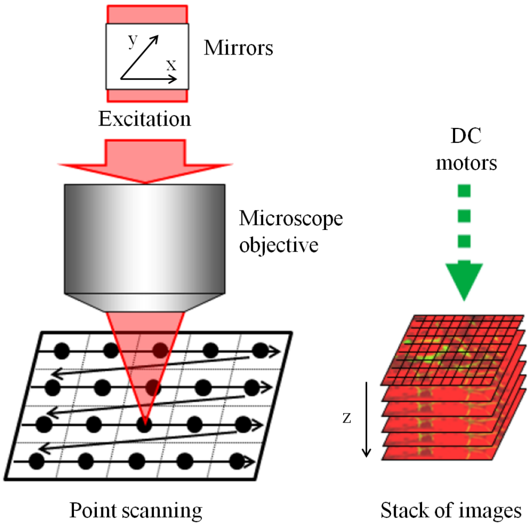

Figure II.6 – Schematic representation of SHG/2PEF imaging in 3 dimensions: the mirrors allow for a point-by-point scanning in a x-y plane, and DC motors move the objective downwards to image successive focal planes. Image from [7].

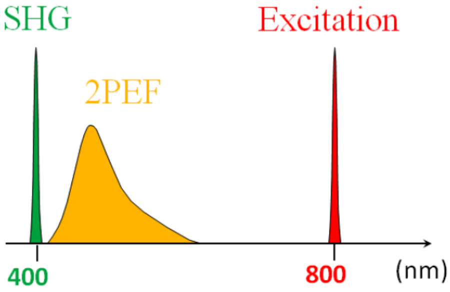

Figure II.7 – Schematic representation of wavelength distribution of excitation (red), SHG (green) and 2PEF (yellow) signals, illustrating how these three signals can be differentiated with photon-counting photomultiplier tubes. Image from [7].

The depth accessible to multiphoton imaging decreased with stretch, from 80 μm to 30 μm approximately. This is due to fibres getting closer and diffusion getting more and more significant. Yet, based on histological analyses we know that the typical thickness of the papillary dermis in rest state is about 20 μm in one-month-old mice. This means that we always image both dermises: the whole papillary dermis and the upper part of the reticular dermis.

The traction set-up was custom-built to fit *in lieu* of the microscope stage. Figure II.8 shows the traction set-up inserted under the objective. We imaged a region close to the center of the sample, both in length and width, to limit edge effects. We followed the same region for the entire duration of the test. The horizontal movements of the sample can be counter-balanced manually by using the scanning stage controlled by micrometric screws (x and y directions) to move the whole traction device. The vertical movements can be balanced by moving the objective up and down using DC motors (z direction).

At working distance, the objective was at about 2 mm above the sample surface. To provide immersion needed for imaging, water gel (Lacrygel, Europhta) was deposited between the objective and the sample. To ensure continuous hydration of the sample, the same gel was also spread all over sample surface in a relatively thick layer. It is important not to put too much gel at the beginning of the experiment: at small strains the weight of the gel makes the tissue creep, and the movements hinder microscopic imaging. During the experiment under SHG microscope we regularly checked that there was enough gel left and that it was well distributed over the surface, and added gel whenever needed. No degradation of the skin sample, neither dehydration nor burns, was observed with these imaging conditions over the course of the experiment, which lasted approximately 4 hours.
The microscope room temperature is controlled at 21 ° C for laser stability. As temperature is an important parameter for the mechanical properties of viscoelastic materials (see [42] for skin) we carried out all other experiments at the same temperature.

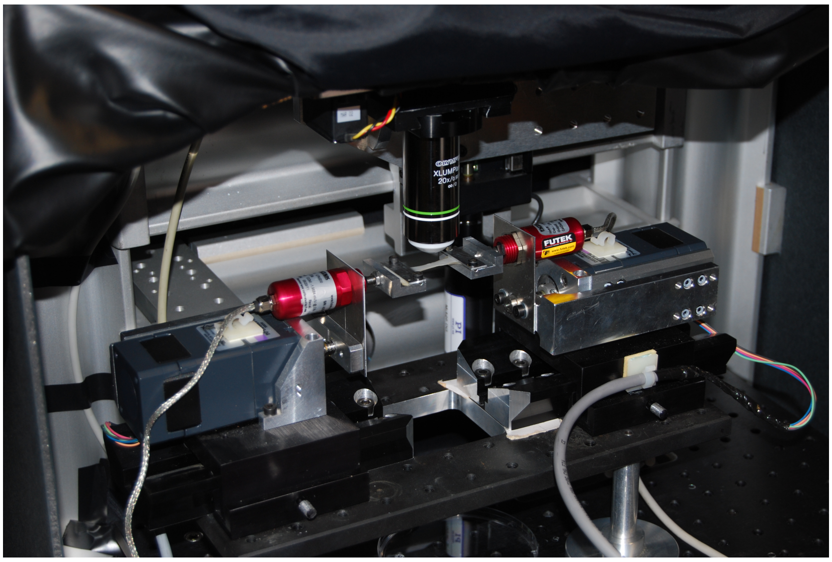

Figure II.8 – Traction device inserted under the multiphoton microscope.

II.2.3 Test procedure under the microscope

The first step of the mechanical tensile test protocol is to search for the reference configuration. This is the position in which the sample is considered to be at zero strain. This is a rather difficult thing to do with soft tissues, as their stress/strain curve starts off very slowly, as showed in the previous chapter. We used systematically the following protocol to be as reproducible as possible. We used low-resolution SHG imaging, which allows for almost continuous visualisation, to determine the reference position more easily. Making sure the force did not exceed the sensors noise level (0.03 N), the sample was stretched at relatively slow speed (10 μm/s) until no more vertical displacement and almost no more horizontal displacement was observed in microscope images. This corresponded to a recorded force of 0.02 N. This was considered the zero strain, or reference, position.

The sample was then measured using a digital calliper to get the initial length l_0 and initial width w_0, with 0.01 mm precision. The thickness being typically around 1 mm, it was more difficult to measure accurately. The initial thickness e_0 was also measured using a digital calliper ; empirically, the precision on the thickness was found to be approximately 0.1 mm.

While stretching the sample, we visualised a chosen ROI continously with low-resolution SHG imaging. We used the micrometric screws to control the x-y stage and follow the same ROI. We were able to recognise the ROI by looking for the characteristic patterns in hair follicles. This manual readjustment is difficult to carry out for displacements too large or too fast. Hence the tensile test under SHG were performed at a fixed strain rate chosen deliberately slow at $10^{-4}s^{-1}$ (for our sample, typically 0.002 - 0.003 mm/s).

Since high resolution SHG imaging takes about five minutes to complete, imaging was not possible during traction, because of skin movements. The loading path was thus chosen to be incremental: we stretched the sample by a step of 0.05 strain, recorded a SHG/2PEF stack of images while keeping the deformation constant, then resumed the stretching for another 0.05 strain. The incremental loading path is represented in figure II.9 a. The arrows indicate pauses for SHG imaging. We carried on this way until sample breakage, usually around a stretch ratio of 1.5. The total duration of each experiment was approximately 4 hours, during which the sample remained hydrated thanks to the immersion gel.

The strain rate we used is lower than in the vast majority of tensile test studies on skin [30, 43, 45, 53, 54, 55, 56, 97, 98, 99, 100, 101, 102]. For a viscoelastic material such as skin, different responses are expected at different strain rates. In particular, a slow strain rate better tests the elastic properties of the material rather than its viscous behaviour [9]. The viscous behaviour of skin could however be observed even at $10^{-4}s^{-1}$, as the skin relaxed everytime we stopped the motors.

II.2.4 Test procedure outside the microscope

Some mechanical tests were carried out outside the multiphoton microscope. This allowed us to increase the number of samples tested, firstly because we used a faster protocol and secondly because we were not subjected to restrictions of microscope availability.

Mechanical tests were faster without SHG imaging as traction was performed at the same strain rate, $10^{-4}s^{-1}$, but continuously without stopping for imaging, as shown in figure II.9 b.

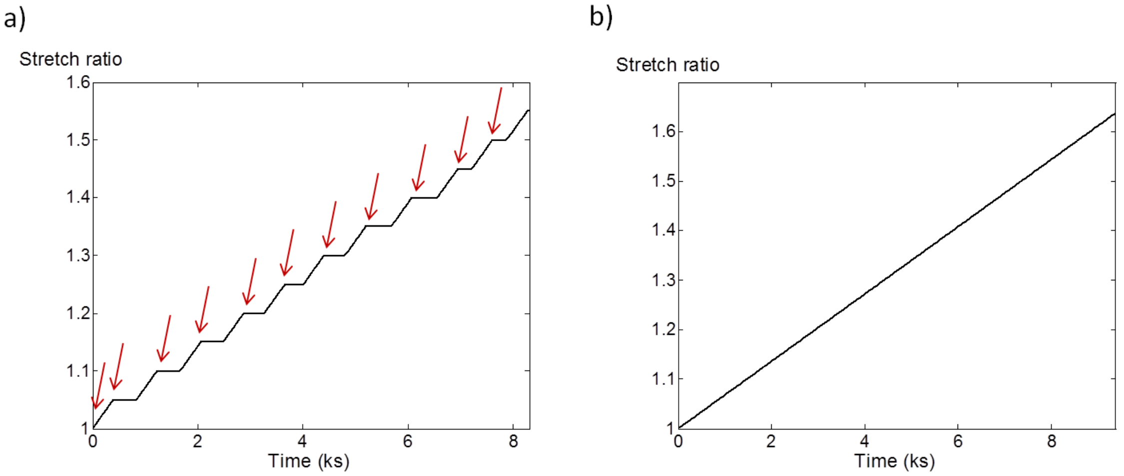

Figure II.9 – Loading paths: a) incremental loading for experiments under the multiphoton microscope, arrows indicate pauses for microscope imaging every 5% strain, b) continuous traction outside the microscope.

When testing outside the multiphoton microscope, the samples were marked on the papillary dermis side with a pattern of dots of Indian ink using a soft brush. A marked sample can be seen in figure II.10. This created the macroscopic pattern needed to analyse the experiments with Digital Image Correlation in post treatment.
Outside the multiphoton microscope, the reference position was determined with a force criterion consistent with the displacement criterion used in experiments with microscope imaging. The sample was stretched at the same slow speed (10 μm/s) until a force of 0.02 N was recorded, comparable to the force reached when no microscopic movements could be observed in continuous SHG imaging. This was considered the zero strain configuration. The sample was measured using a digital calliper exactly as described before.

Constant hydration was obtained by spraying mineral water on the sample. The spraying frequency was adjusted to the strain rate: the faster the stretching, the faster the skin dehydrated, as a consequence of water flowing out. Dehydration clearly showed on the stress/stretch curve, as a change in the slope that disappeared immediately when the sample was sprayed with water again. The hydration frequency was adapted with a trial and error protocol looking for evidences of dehydration. At $10^{-4}s^{-1}$ we sprayed the sample every 4 minutes, while at $10^{-3}s^{-1}$ we sprayed every other minute. At $10^{-2}s^{-1}$ it seemed impossible to maintain a satisfying sample hydration through water spraying. Immersing the sample in culture medium could be considered, but it is not an optimal solution: the sample swells when immersed, which changes its mechanical properties.

A digital camera (Pike, Allied Vision Technologies, with objective Tamron SP AF 90mm F/2.8 Di Macro 1:1) was used to record a picture of the sample every second. The sample was lit with white light using a LED light (Schott, KL 2500 LED), which has the advantage of reduced heating. Digital Image Correlation was performed using a software developed by M. Bornert (CorrelManuV, see [103]) to correct for possible slippage and confirm strain homogeneity.

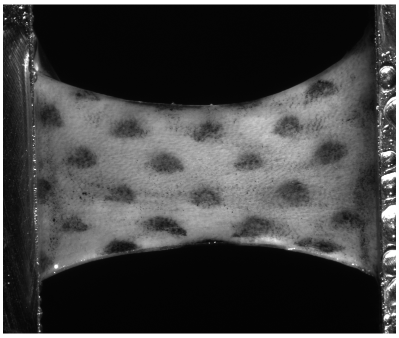

Figure II.10 – Skin sample for mechanical testing without SHG imaging. The picture was taken with a digital camera. The sample is in rest state, the length between the jaws is 28 mm. A similar picture is taken every second during the tensile test. The pattern of Indian ink dots, made with a soft brush, allows for Digital Image Correlation post-processing to correct for possible slippage and confirm strain homegeneity.

We showed that the mechanical properties of the samples were not statistically different in the two protocols, with and without SHG imaging. The corresponding statistical analysis is presented in Appendix B.

Some tests were also carried out at increased strain rate, $10^{-3}s^{-1}$ and $10^{-2}s^{-1}$. Finally, we carried out a few cycling experiments with increasing maximum stretch ratio. The results of these experiments will be discussed in the next chapter.

II.3 Mechanical analysis

This section introduces the parameters that were used to characterise the mechanical properties of our samples. Four parameters were obtained from the stress/stretch curve on the different parts of the curve described earlier: toe region, heel, linear part and rupture.

In the experiments performed under SHG microscope, every 0.05 strain the motors were stopped for imaging and skin relaxed for a short time. The second part of this section introduces the analysis that was made of these relaxations. We also carried out a few relaxation experiments on longer time scales. This study gives us an insight into the viscous behaviour of the skin, although limited, as discussed later.

II.3.1 Stress/time and stress/stretch curve

The global stretch ratio was obtained as:

$$\lambda = \frac{l_0 + \Delta l_m}{l_0}$$

where l_0 is the reference length measured in reference configuration and Δl_m is the motors displacement.

In this work, when we say "stress" we consider the nominal stress. The nominal stress was obtained as:

$$\sigma = \frac{F}{S_0} = \frac{F}{w_0 \times e_0}$$

where F is the measured force, S_0 is the initial cross section and w_0 and e_0 are respectively the initial width and thickness of the tissue.

Figure II.11 shows typical stress/time and stress/stretch ratio curves for uniaxial tensile tests until rupture with (a, b) and without (c, d) stops for SHG imaging.

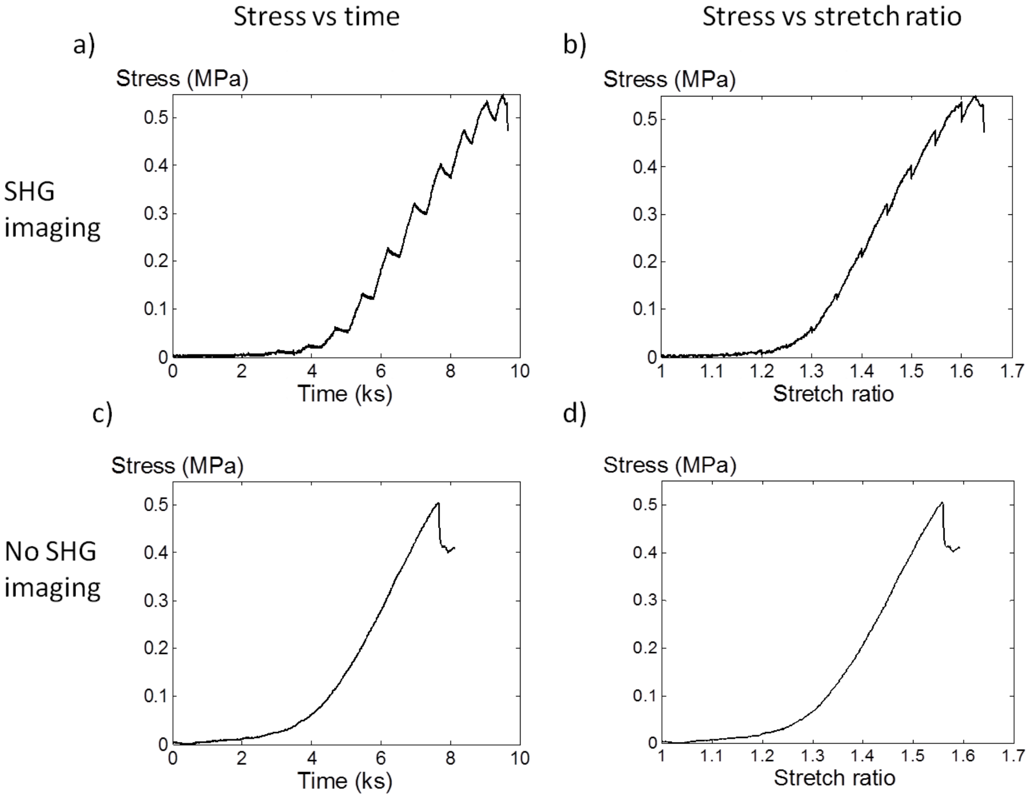

Figure II.11 – Stress/time and stress/stretch ratio curves for a typical uniaxial tensile test until rupture with stops for SHG imaging (a,b), and without stops (c,d).

The stress/stretch curve correspond to the non-linear J-curve expected for skin [9]. In the stress/time and stress/stretch curve with stops for SHG imaging we can see the skin relaxing for a short time at each strain increment.

We characterised the stress/stretch curve with four parameters summarised in figure II.12: the tangent modulus of the linear part, the heel region length and two rupture parameters, the final stress and the final stretch ratio.

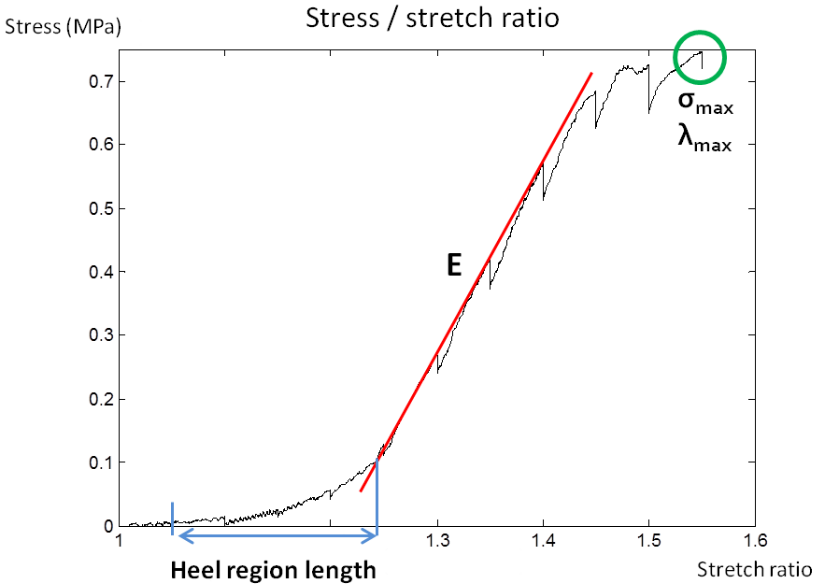

Figure II.12 – Four parameters are extracted from the stress/stretch curve: the tangent modulus E, in red, the heel region length, in blue, and the rupture parameters σ_{max} and λ_{max}, in green.

II.3.1.a Tangent modulus

The tangent modulus E corresponds to the slope of the linear part (in red in figure II.12). It characterises the stiffness of the sample.

The linear part was defined manually for each sample. For the curves with incremental loading (experiments under the microscope) the fit was carried out on the linear part leaving out the pauses made for imaging, from the beginning of the pause until the stress reached again the value it had before pausing.

The slope of the linear part is often referred to in the literature as skin's Young's modulus or stiffness, ever since the first studies on biomechanics of skin in the seventies (see [104, 105]).

II.3.1.b Heel region length

To compute the heel region length (in blue in figure II.12), the noise was first measured for each test at very small strain (a few percent). The start of the heel region was defined by the first point at which the stress stayed over twice the noise value for at least 10 seconds. We defined the end of the heel region as the point for which the stress got close enough to the linear fit of the linear part, *i.e.* when the difference became inferior to twice the noise.

The measure of the heel region length is subjected to experimental uncertainties on the determination of the reference zero strain state and on the delimination of the linear part, both being operator dependent. As a consequence, we expect the experimental noise to be quite large for this parameter.

II.3.1.c Rupture

We quantified the resistance to rupture with the rupture stretch ratio and rupture stress (in green in figure II.12).
Rupture in soft tissues can be very progressive, similar to that of a rope. The exact moment of rupture can thus be difficult to identify precisely. We considered the maximum stress of the curve to be the maximum stress σ_{max}, and the stretch ratio for which that stress was obtained was considered the maximum stretch ratio λ_{max}.
These parameters are very dependent on sample cutting: a defect can lead to a premature rupture of the sample.

Notably, another approach is possible to analyse the data. The stress/stretch curve can be fitted using a hyperelastic model, such as Fung's [9, 72] or variations. This fit yields two parameters, one that substantially controls the toe and heel regions behaviour and one responsible for the linear region's slope. This approach is fairly equivalent to our "piece by piece" approach, but we found that measuring each parameter separately was more robust in dealing with possible experimental problems and data dispersion.

II.3.2 Relaxation

For the experiments combining mechanics and microcopic observations, we stopped the traction every 5% elongation to image the sample. While we maintained the deformation constant the stress relaxed because of skin's viscoelasticity. The incremental loading protocol lets us access relaxations from the same sample at different stress levels.
Using these relaxations to investigate the viscous behaviour of the tissue is not ideal for various reasons. Firstly, the constraints of the test mean that we only get short time relaxations, approximately 5 minutes. Secondly, the relaxation time is of the same order of magnitude compared to the loading time in our experiments. To investigate the viscoelastic behaviour, the loading needs to be much faster. Finally, the tissue has a different loading history at each stress level. The sample loading history is an important parameter in viscoelasticity: this implies that strictly speaking the different relaxations of the same sample are difficult to compare.
The systematic analysis of the short time relaxations and their evolution with stretch can however offer an insight into the viscous properties of the tissue, to a certain extent.

We also completed long time relaxation experiments, with a relatively slow ($10^{-3}s^{-1}$) loading, up to a stretch ratio of 1.3 and a free relaxation for 3 to 8 hours. The force/time curve from one of these experiments is shown in figure II.13. The sample was kept hydrated during that time either with a drop of hydrogel or by regularly spraying mineral water on the sample.

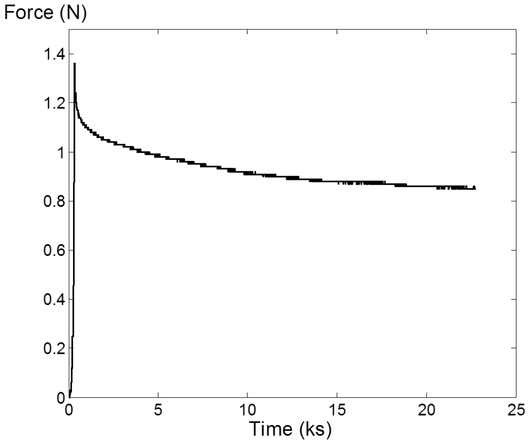

Figure II.13 – Force versus time curve for a long time relaxation: a skin sample was stretched up to a stretch ratio of 1.3 and left to relax freely for 6 hours.

To fit the relaxation curves, we used a series of exponentials with decreasing magnitude, sometimes called Prony Series, as proposed by Fung [9] for skin. One exponential was not enough to fit our data so we used a biexponential function. We fitted the relaxation curves on the force/time curve with a bi-exponential function with saturation:

$$F(t) = F_1.e^{\frac{-t}{\tau_1}} + F_2.e^{\frac{-t}{\tau_2}} + F_3$$

Finally, F_1, F_2 and F_3 were divided by the initial force before relaxation $F(0)$ to have relative proportions of force relaxed.

The relaxation analysis consisted eventually in five parameters:
- a_1: the relative amplitude for short time relaxation, $a_1 = \frac{F_1}{F(0)}$,
- a_2: the relative amplitude for long time relaxation, $a_2 = \frac{F_2}{F(0)}$,
- s_0: the relative constant for the relaxation, $s_0 = \frac{F_3}{F(0)}$,
- t_1: the short relaxation time,
- t_2: the long relaxation time.

Clearly, the three amplitudes are interdependent: $a_1 + a_2 + s_0 = 1$.

Figure II.14 shows the biexponential fit of an 8-minute long relaxation, recorded during SHG imaging. Notably, only relaxations in the linear part can be fitted with this discreet fitting protocol. The reason for this is simply the low signal-to-noise ratio in the toe and heel regions of the curve, as illustrated in figure II.15, where force/time relaxation curves in toe and linear regions of the stress/stretch curve are shown.

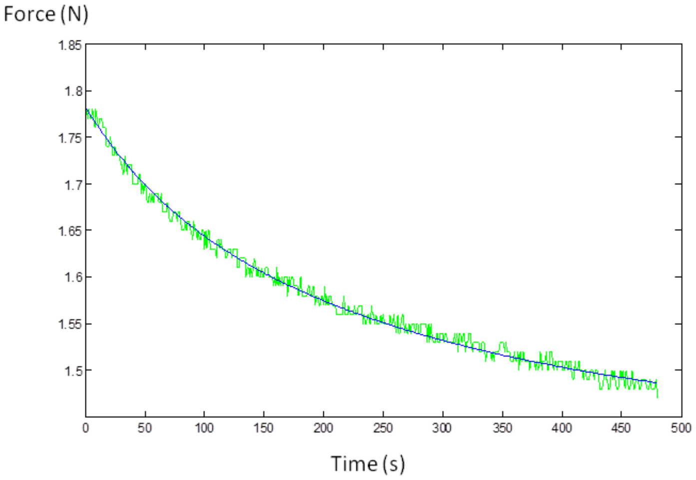

Figure II.14 – Biexponential fit on an 8-minute long relaxation.

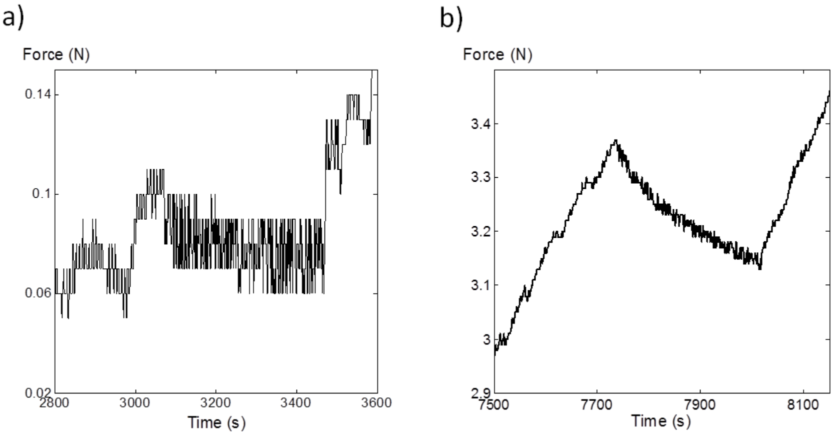

Figure II.15 – Force/time relaxation curves for a) a relaxation in the toe region of the stress/stretch curve and b) a relaxation in the linear region of the stress/stretch curve, for the same sample.

The number of characteristic relaxation times that can be identified is strongly dependent on experimental protocol. No characteristic time under a few times the data acquisition period can be identified. On the other end, no relaxation time larger than the duration of the relaxation can be identified. In the short time relaxations those limitations mean that we could single out times between a few seconds and a few hundreds of seconds. As expected, the two relaxation times found for short time relaxations were typically around 10 and 100 s.

More than two exponentials can be used to fit longer time relaxations. However, the relative amplitude of the smaller times is then very small (approximately 5%), and thus they are difficult to identify precisely.

It should be noted that a power law fit, often used in biomechanics, for instance in microrheological experiments on living cells [106], was not a satisfying fit for our data.

II.4 Optical analysis

When performing the experiments under the multiphoton microscope, we obtained at each deformation step a stack of SHG images (horizontal cuts in the depth of the tissue), as described in section II.2.

It is difficult to take images exactly at the same depth at every deformation step, because the tissue gets thinner when stretched, and the surface, used as reference, is not perfectly flat and well defined at the microscopic scale. Typical images of the same skin sample at approximately the same depth are shown in figure II.16 for 6 deformation steps. The SHG and 2PEF canals have been combined.
The collagen network can be seen in green (SHG signal) with excellent contrast. The biphotonic fluorescence canal (2PEF) appears in red. Hair shafts appear as dark holes interrupting the collagenous network. They were always observed in discontinued parallel lines. Remains of hair keratin can be seen in red in the hair shafts. We also observed on the 2PEF canal a weak and diffuse fluorescent background coming from the fibroblasts' cellular cytoplasm, and sometimes remaining epidermal cells when imaging the surface of the sample.
No elastin fibrils could be observed in any of our experiments. We did not see any elastin fibrils neither when imaging the skin with the hypodermis face facing up, through the reticular dermis, nor in aged mice skin. The reason for this is unclear: either there is no elastin fibre in mice skin, or they were too small to observe (smaller than 1 μm), or the laser power used was not large enough to reveal them.
A custom-written image processing was developed to analyse the images, with two different objectives in mind. Our first ambition was to measure the local stretches at the microscopic scale. This was done by tracking the hair shafts displacements. The second goal of image processing was to obtain quantitative parameters to characterise the level of organisation of the collagenous network throughout the test, to compare with mechanical behaviour.

The first paragraph of this section presents the local stretches computation. While assessing local stretches, we collected information on sample porosity, which is relevant to evaluate the mechanical properties of a porous material. These data are described in the second paragraph. Finally, the quantitative evaluation of fibre orientation is presented in the last paragraph.

The image processing was developed using Matlab by Stéphane Bancelin during his PhD work at the LOB. The computation of the stretches was initially developed at the LMS. Details can be found in [7]. The algorithm analysing the collagen fibres network orientation was developed by

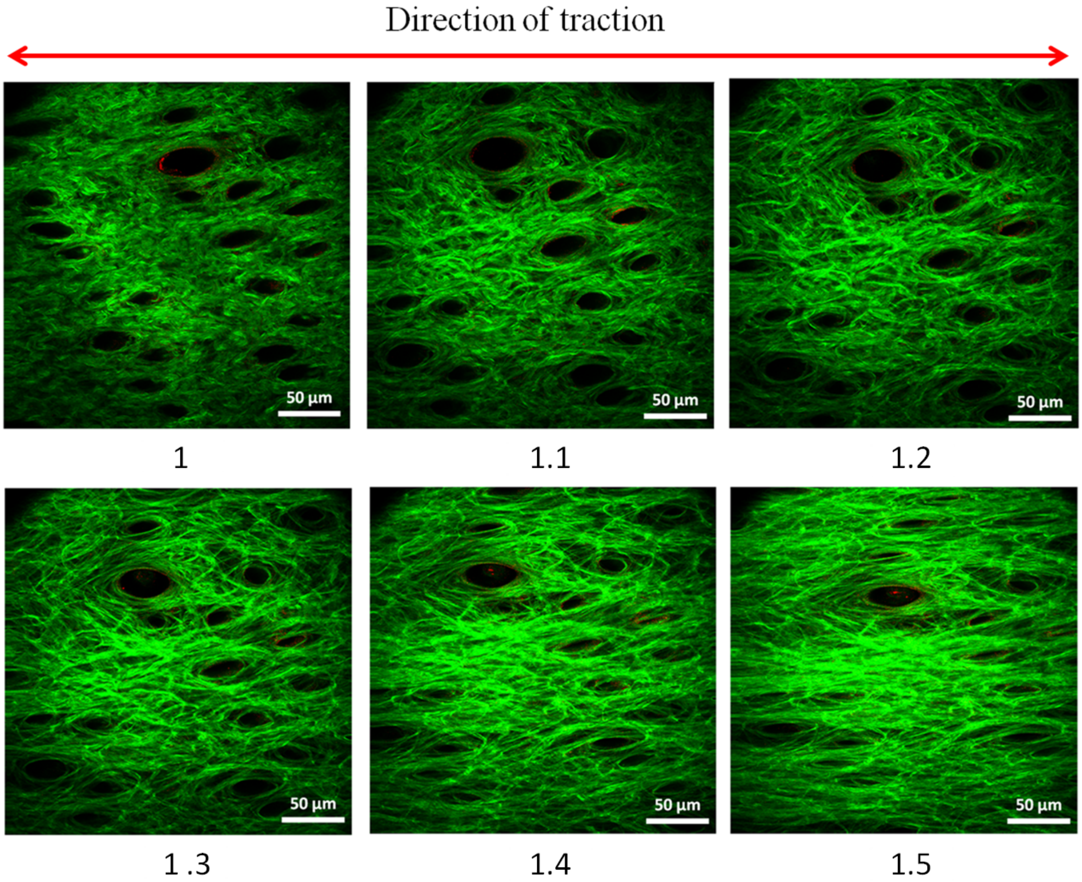

1 1.1 1.2

1 .3 1.4 1.5

Figure II.16 – Typical images combining SHG and 2PEF at different stretch ratios, at approximately the same depth, on the same ROI. Collagen appears in green on the SHG canal, and hairs in red on the 2PEF canal. Scale bar is 50 μm.

Petr Dokladal and Etienne Decencière (Centre de Morphologie Mathématiques, Fontainebleau).

II.4.1 Local stretches

Analysing the local stretches provides valuable information to validate the tensile test protocol. For one, comparing the measured local stretch to the global imposed deformation allows us to assess the overall slipping of the sample. Secondly, the homogeneity of the deformation at the scale of the image can be evaluated through the computation of local strain tensors. Finally, the deformation in y-direction, perpendicular to traction, is relevant to the mechanical behaviour: it is comparable to the Poisson's ratio in linear materials.

The processing of SHG images with a standard technique of Digital Image Correlation was made impossible by three factors: the density of the collagen network, the aforementioned difficulty to image the tissue at constant depth at different deformation steps, and the size of the vertical step used for imaging (2 μm). Spreading fluorescent beads on the sample, as has been done before in our laboratory on cornea or tendon [94] for example, allows for DIC, but only at the surface of the sample.

We chose instead to take advantage of an intrinsic pattern present in the depth of the dermis: the hair shafts network. Specifically, we obtained the local stretches by following the displacements of the hair shafts, or follicles.

Monitoring the same hair shafts throughout the tensile test was not without obstacles.

First, the follicles got farther and farther apart from each other as the sample was stretched to large elongations (up to a stretch ratio of 1.6). Yet, the field of view available to imaging remained the same. Consequently, it was not always possible at large strains to have all initial follicles in a single SHG image, were they chosen too far apart at the beginning.

Secondly, the follicles' shape changed drastically during the tensile test, as can be seen in figure II.16. They became more and more elliptic with increasing strain. Additionally, due to the depilatory cream protocol, the hair shafts were empty close to the surface of the sample, whereas it was more probable to find remaining hair material in the depth of the tissue. This is one of the reasons the follicles deformed differently at different depths, as shown in figure II.17 for two SHG images of the same sample, at the same strain level, taken at different depths. These alterations can cause the automatic tracking of the follicles to be troublesome.

To overcome these problems and identify the follicles, the following protocol was followed.

The first step of the analysis was to crop the images so that the same hair follicles could be seen at all deformation steps. When the rupture occured at a particularly large strain, we had fewer follicles to base measurement of local stretches on, less statistical data and eventually more experimental noise.

We could then isolate the hair shafts on the gray-scale images to follow their displacements and deformations. The segmenting protocol steps can be seen in figure II.18. It goes as follows:

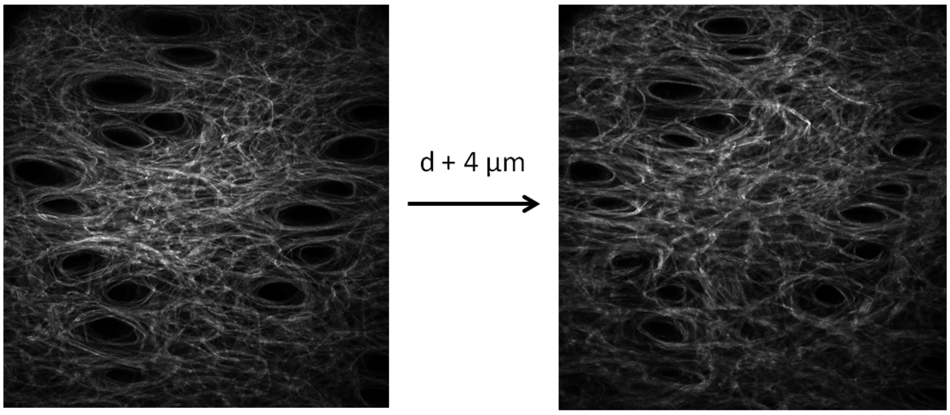

Figure II.17 – SHG images at different depths (d and d+4μm) for the same sample, at the same deformation step (λ=1.35). We can see that the hair shafts are not perpendicular to the surface, and that they deform differently at different depths.

- Noise was reduced by using a median filter (2 pixels radius). The contrast was inverted to show the follicles in white and collagen in black.
- To isolate follicles from other small structures that are not follicles, a circular opening was used to smooth the image while preserving the hair follicles edges.
- To create binary images, we used a colour threshold.
- A standard Matlab shape detection function was applied to identify the follicles. Each follicle was fitted with an ellipsis, characterised by area, position of center of mass, semi-major and semi-minor axes and angle of semi-major axis with regards to the horizontal.
- The follicles were numbered so that each follicle bears the same number at each deformation step.

Once the follicles were identified, we considered the network formed by the centers of mass of the follicles as a pattern. We used a Delaunay triangulation, and calculated for each triangle the deformation tensor components: the stretch ratio in the direction of traction λ_{xx}, the stretch ratio in the surface direction perpendicular to traction λ_{yy} and the sliding angle ω.
Figure II.19 shows an example of deformation map in the direction of traction for an imposed global stretch ratio of 1.2. We can see experimental noise on some of the triangles, due to errors in the positionning of a few follicules. The errors would generally appear between the first two images and remain on the same follicules throughout the test.

We computed the local stretches at the scale of the image by averaging the values from all triangles. We also obtained from this the standard deviation on the average value, quantifying experimental noise. A reasonable standard deviation was obtained for a sufficient number of follicles (6 to 8). With fewer follicles an error on the position of any follicle, especially one involved in more than one triangle, caused an important error.

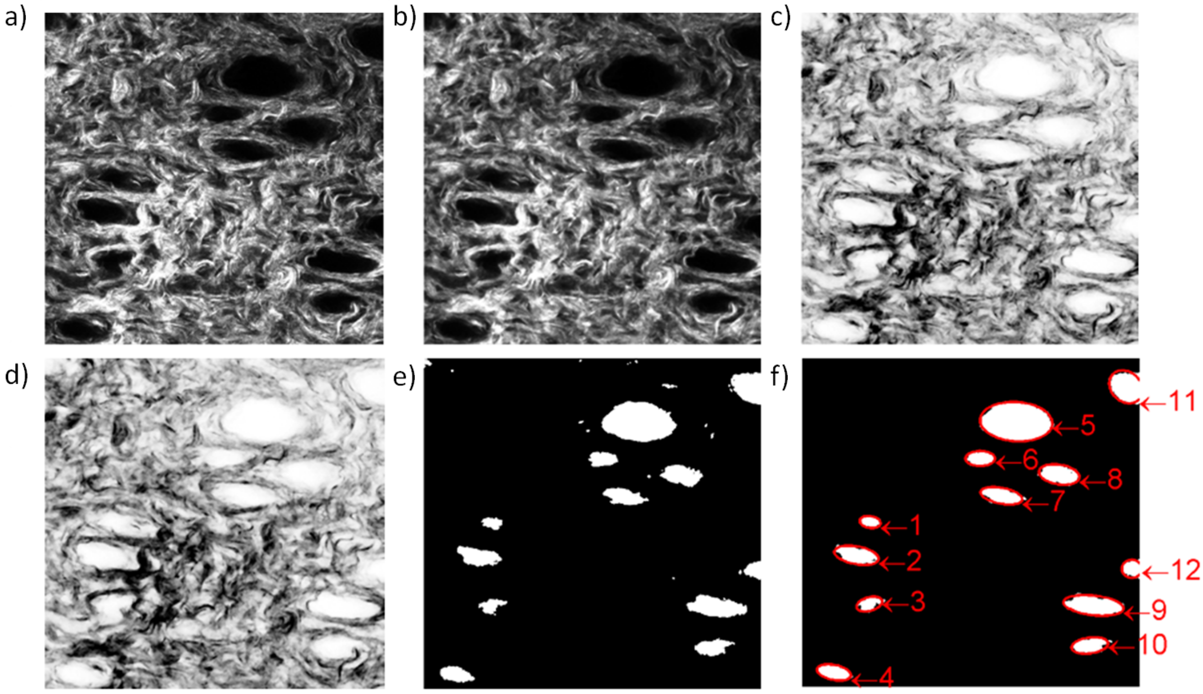

Figure II.18 – Identification and segmentation of hair follicles: a) original image, b) with a median filter of 2 pixels radius, c) contrast inversion, d) circular opening, e) binary thresholding, f) shape detection. ROI is 275.0 x 268.5 μm. Image from [7].

The choice of averaging method was discussed. An algebric mean considers all triangles' contribution to be equal, which amplifies the errors due to small triangles. An average weighted by the area of the triangles, *a priori* the right choice, solves that problem. However, it was quite common to have a triangle significantly larger than the others. An error on one of the three apexes of this triangle led to a massive error in the value of the mean. Most of the time the two means proved to be comparable. When faced with a local stretch with a large standard deviation we looked at the results of both methods and chose the most relevant one.

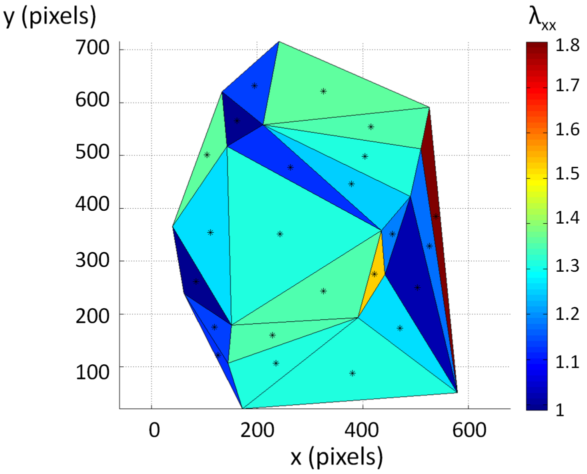

Figure II.19 – Map of the stretch ratio in the direction of traction λ_{xx} obtained from the hair follicules network deformation, for an imposed global stretch ratio of 1.2.

II.4.2 Measure of porosity

When using the shape detection algorithm on the follicles to compute local stretches, we accessed information on the hair shafts morphology. The number of hairs and their area in the image at zero strain can give us an idea of the general sample porosity. We used two parameters, computed on the initial cropped image:

- We extrapolated the number of hairs obtained from a field of view of typically 300 μm *per* 300 μm (cropped ROI) to the scale of a millimeter square to get the initial number of hairs *per* millimeter square.
- The initial relative porosity at a few micrometers below the surface was calculated as the sum of the area of all hairs divided by the size of the initial (cropped) image.

This measure of porosity is obviously flawed. The first issue is the choice of the region considered. Indeed, to measure local stretches as above, we actively looked for a region with enough hairs before imaging. Yet the density of hairs is quite inhomogeneous at the scale we are imaging. This can skew the number of hairs and relative porosity of the ROI upwards.

Another issue is the choice of the cropped image. The cropped image is chosen so that all hairs present in the initial image can be followed up to the last image. When the sample reached large deformations, the initial image had to be smaller. This is illustrated in figure II.20. The relative porosity is then artificially bigger as the initial image is cropped around the follicles.

Both of these choices also depend strongly on the operator doing the experiment and image analysis. This method is however useful to evaluate the overall hair number and porosity from different types of sample. When looking at a great number of samples, we can also evaluate if the skin's stiffness is correlated with porosity. This is presented in Appendix B.

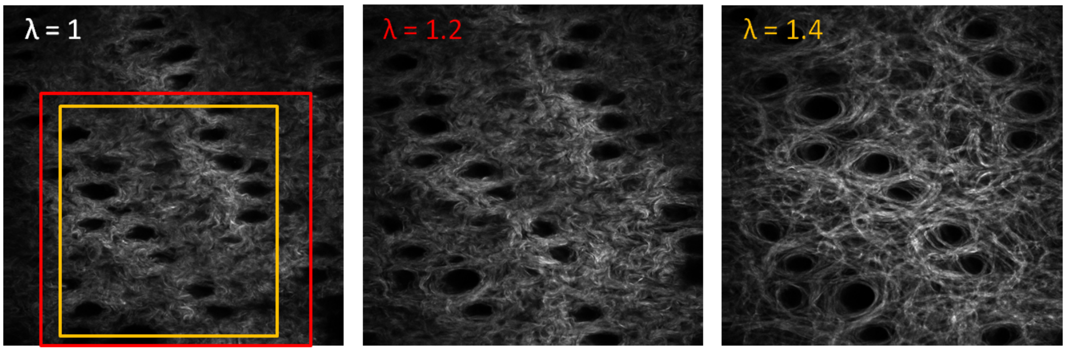

Figure II.20 – The initial image at λ=1 is cropped so that all follicles can be followed up to the last image. With a final stretch of λ=1.2, it is already necessary to cut out a big region of the initial image (red square). With a larger final stretch of λ=1.4, the initial image has to be even smaller (yellow square).

II.4.3 Fibre orientation

The second post-processing implemented on the images aimed at quantitative information on the overall fibre orientation.

The images were analysed using a rotating linear structural element to extract the fibres aligned in the direction of the element. In concrete terms, for a small linear region, typically 20 pixels long, the program searched for the direction which corresponded to the maximum of signal intensity. The element was then rotated by steps of 10°.

The output was, for each pixel of the SHG image, the local orientation of collagen fibres. The size of the linear element played an important role in the result: its choice arose from a compromise between a small element, with a large range of independent angles accessible, and a larger element, allowing precision in orientation measurements. Details can be found in [7].

The program took a long time to run on the images due to their size, and for this reason it was only applied to a restricted number of images. We selected six images to have enough statistical data, and chose the images where the SHG signal intensity was highest. These images were coincidentally always consecutive.

This analysis outputs a map of fibre orientation and corresponding histogram of normalised probability of fibre orientation, for each of the six images selected. The results are shown for one image at one deformation step in figure II.21. The global histogram for the deformation step is computed by averaging the histograms from the six images analysed.

From these results we derived three quantitative parameters describing the collagenous network organisation.

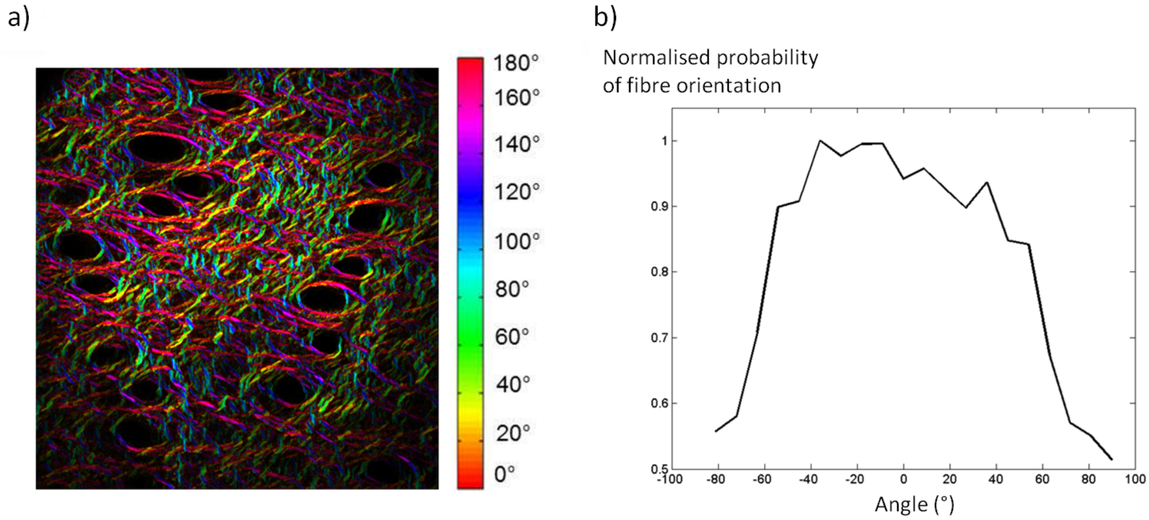

Figure II.21 – Fibre orientation for a WT sample at a stretch ratio of 1.35: a) map of orientation, b) corresponding histogram of normalised probability of fibre orientation.

The first is the angle with maximum probability of fibre orientation, θ_{max}. This was simply the maximum of the histogram of normalised probability of fibre orientation.

The second parameter is the Orientation Index (OI), computed as:

$$OI = 2 \times [\frac{\int_{\frac{-\pi}{2}}^{\frac{\pi}{2}} I(x)\cos^2(x)dx}{\int_{\frac{-\pi}{2}}^{\frac{\pi}{2}} I(x)dx} - 1].100$$

The orientation index is correlated with the inverse of the width of the fibre orientation histogram: it reaches its maximum value for a pic centered on zero, its minimum for a pic centered on 90 ° and is equal to zero for a continuous uniform distribution. In concrete terms, the OI reaches a value of 100% if all fibres are aligned in the direction of traction, -100% if they are all perpendicular to the direction of traction and 0% if the system is perfectly isotropic. The OI is calculated at a given angle, zero here, as it is the direction of traction. The OI is not adapted to a system with more than one significant orientation direction.

For systems with more than one significant orientation direction, another way to describe the tissue organisation is to use the entropy S, defined as:

$$S = \sum_{\theta=-90^\circ}^{90^\circ} p(\theta) ln[p(\theta)]$$

where

$$p(\theta) = \frac{I(\theta)}{\sum_{-90^\circ}^{90^\circ} I(\theta)}$$

is the probability to find a fibre in the direction θ. The entropy presents the advantage over the orientation index to consider the overall fibre organisation with no preferred direction.

In the uniaxial case, OI and entropy are fairly equivalent and their evolutions are connected. In this work, we will only consider the former. In biaxial traction, they would be quite different. The orientation indexes in both directions of traction would be an indication of preferential angle of reorientation, while the entropy would give an overview of the general sample disorder in the physical sense of the term.

Chapter III

Evolution of micrometer-scale collagen organisation in mice skin upon mechanical strain

The previous chapter described our experimental protocol combining macroscopic mechanical tests and microscopic SHG observations. We performed those experiments on skin samples from one-month-old control, or Wild-Type (WT), mice. This chapter presents the results of our multiscale investigation of collagen reorganisation in the dermis upon mechanical strain on control mice. We also present preliminary results on two other types of loadings: faster strain rate and cyclic loading. Then we discuss the compability of our findings with the microstructural models found in the literature.

Possible experimental bias were ruled out using statistical analyses, shown in Appendix B:

- As described in the previous chapter, we carried out mechanical tests both under a SHG microscope with short stops for imaging (25 samples with a strain rate of $10^{-4}s^{-1}$) and outside the SHG microscope with continous traction (7 samples with a strain rate of $10^{-4}s^{-1}$). We verified that these short stops had no impact on the mechanical properties of the tissue.
- The post-processing of the SHG images yields some information on hair density and relative porosity. The porosity can affect the mechanical properties of porous materials. In our case, no correlation between mechanical properties and hair density or relative porosity was found.
- Finally, we tested samples from both male and female mice. No change in mechanical properties, microstructural behaviour, hair number or relative porosity was observed between male and female mice.

All data for young WT mice can be found in Appendix C, tables C.1 (mechanical data at slow strain rate), C.3 (mechanical data at higher strain rate), C.5 (local deformation at the microscale) and C.8 (collagen organisation).

III.1 Multiscale biomechanics of mice skin

III.1.1 Stress/stretch behaviour

As reported in section II.3 of the previous chapter we obtained stress/stretch curves that agree with the J-shaped curve reported in the literature for soft collagenous tissues [9].
The tangent modulus was measured as the slope of the linear part. The average on 32 samples (one-month-old mice, back skin) was 1.6 MPa ± 0.1. This is consistent with values reported in the literature: Guan and coworkers used an unixial tensile test with a slow strain rate comparable to ours ($2.\ 10^{-4} s^{-1}$) on skin samples from the back of neonatal rat skin and found a tangent modulus of 1.6 MPa ± 0.1 [98]. Crichton and coworkers used nanoidentation tests on freshly excised 6-week-old mouse ear skin to isolate the tangent modulus of the dermis from the properties of the other layers. The values they found for the tangent modulus (7.33 - 13.48 MPa, depending on the size of the probe) are larger than ours, but comparable given the differences in experimental protocol.
The order of magnitude reported for human skin varies from a few tens of megapascals to a few hundreds of megapascals (for reviews, see [42, 46, 104, 107, 108]). As discussed in the introductory chapter, it is difficult to compare results from two biomechanical studies as many variables impact the results, *e.g.* type of animal tested, age, region and direction(s) tested and test protocol.

In our tests, the heel region lasted for approximately 15% elongation, and the rupture occured statistically for a stretch ratio just over 1.4 ± 0.01, with a average rupture stress of 0.47 MPa ± 0.03. Guan and colleagues [98] carried out uniaxial tensile tests on whole rat skin until rupture, and found a rupture stress approximately 0.35 MPa for a rupture stretch ratio approximately 1.2. The smaller extensibility of the samples in this study compared to ours may come from the age of the animals (neonatal rats, versus one-month-old mice in our study) or hydration protocol (the sample was not hydrated in their study, while the hydration was controlled with water spray or water gel in ours).

The stretches computed from SHG images showed that the local deformations at the microscale were relatively homogeneous in the tissue in our test conditions, as illustrated by the three deformation maps at different stretch ratios (1.05, 1.25 and 1.5) in figure III.1. The errors originated from the same triangles at every deformation step (for instance in figure III.1 the small triangle at x=450 and y=250 that displays a value of 1.15 for an imposed stretch of 1.05, 1.5 for imposed stretch 1.25 and 1.8 for imposed stretch 1.5). This shows that the experimental noise comes from errors in finding the position of some follicles.

Figure III.2 shows the local deformations at the microscale, measured using the follicles network deformation, versus global imposed stretch ratio.

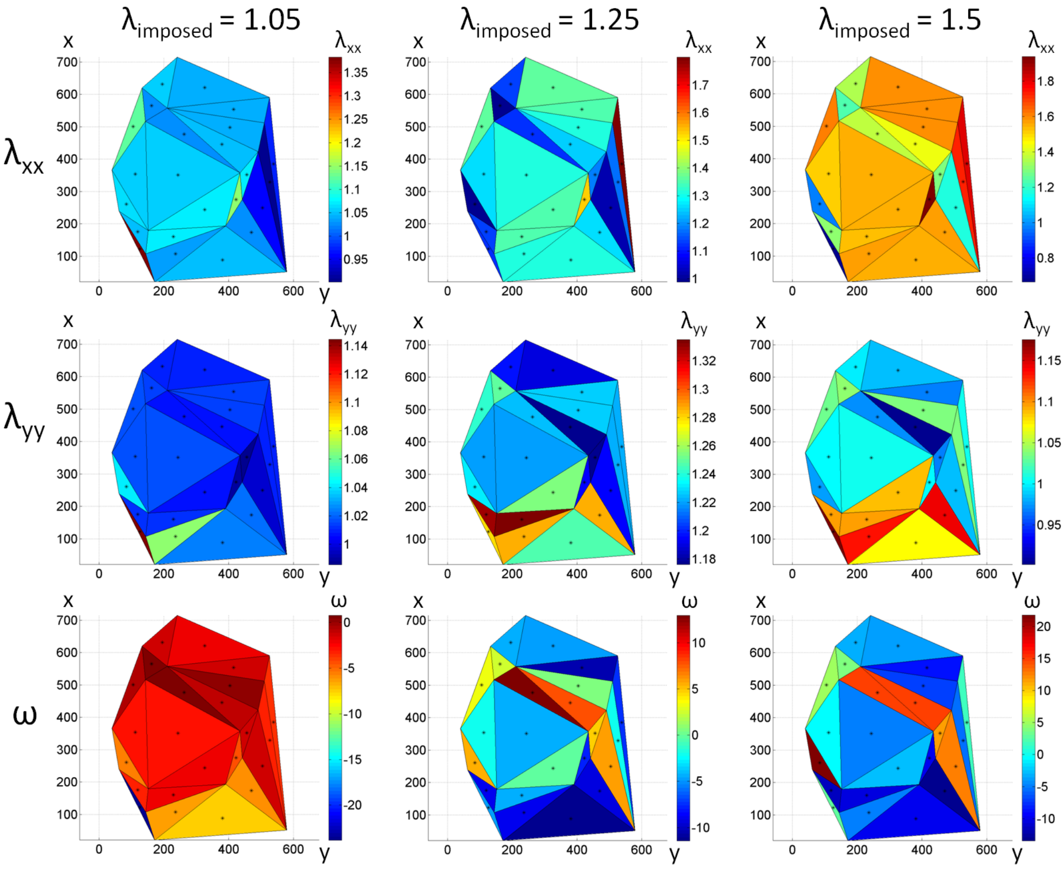

Figure III.1 – Deformation maps obtained from hair follicules displacements in the direction of traction λ_{xx} (top), direction perpendicular to traction λ_{yy} (middle) and sliding angle ω (bottom), at three different stretch ratios: 1.05 (left), 1.25 (middle) and 1.5 (right).

The local stretch ratio in the direction of traction followed the imposed strain closely. This was well verified for nearly all samples. We fitted the curves of observed stretch in direction of traction versus imposed stretch with a linear fit. The average of the slope of the linear fit over 25 samples was equal to 1.1 ± 0.08. We sometimes observed a slope different than 1, and in rare cases up to 40% difference between measured and imposed stretches. It is difficult to know for a single sample whether the difference between the two stretches came from actual strain inhomogeneity or from errors in the measurement of the follicles displacements. In particular, since the images were not taken at exactly the same depth at every deformation step and since the follicles were not perpendicular to the surface, a shifting in the z-direction resulted in misplaced follicles. Yet, one misplaced follicle can lead to large errors, especially if it is quite central in the follicle network and thus engaged in many triangles. For instance in figure III.1 the follicle at x=250 and y=550 is engaged in 7 triangles and probably slightly misplaced.

Since the imposed strain was close to the measured strain in almost all samples we considered it reasonable to keep the imposed stretch ratio as the real stretch. If other evidences pointed to sliding or strain inhomogeneity we simply did not consider the experiment valid.

The relationship between imposed global stretch and measured local stretch proved that there was no slipping of the sample. It also validated our protocol to determine the zero strain reference state.

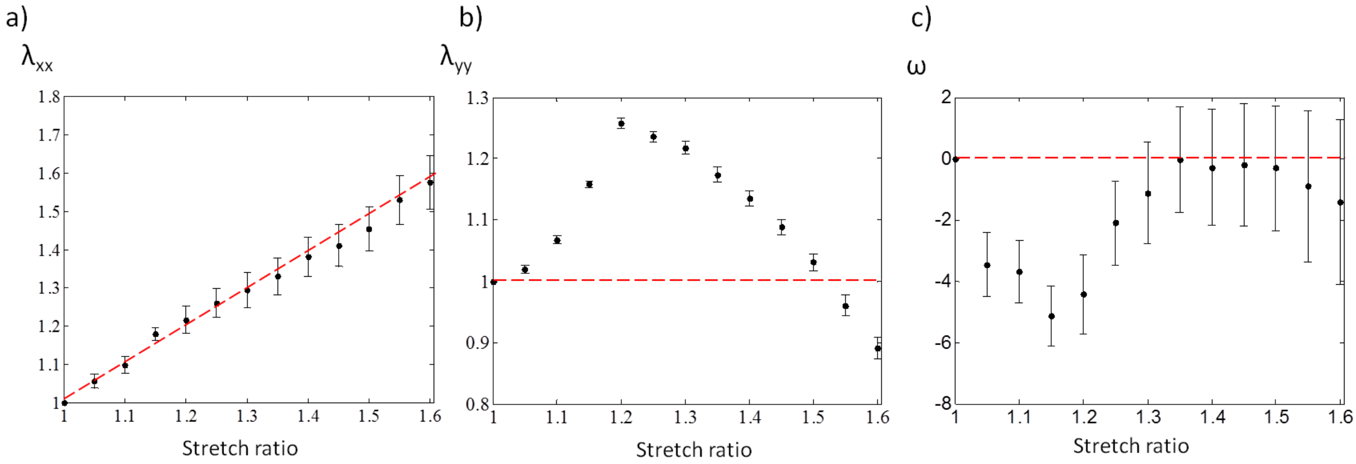

Figure III.2 – Local deformation in a) direction of traction λ_{xx}, b) direction perpendicular to traction λ_{yy} and c) sliding angle ω versus the imposed stretch, for a typical unixial tensile test under the microscope. The values are averaged over all triangles from the deformation maps shown in figure III.1. Error bars represent the standard deviation.

The behaviour in the direction perpendicular to traction was more complex to interpret. At first λ_{yy} increased, as if the surface or volume increased. This would be attributed to a negative Poisson's ratio in linear materials.

The decreasing region of λ_{yy} that followed, after 1.2 in figure III.2, was expected, and had an averaged slope of 1.5 ± 0.1 for WT mice. The transition from swelling to shrinking in the direction perpendicular to traction generally occured at the end of the heel region or at the beginning of the linear region of the stress/stretch curve.

The sliding angle versus imposed stretch curve demonstrated that the shear at the scale of the ROI remained limited throughout the experiment ($\omega < 5^\circ$).

At a larger macroscopic scale, the post-processing of the images with Digital Image Correlation based on the ink pattern drawn on the samples, gave similar deformations maps, that revealed a well distributed strain with exception of the borders of the sample. Figures III.3 a, b and c show the deformations maps obtained in the direction of traction, direction perpendicular to traction and sliding angle. Figure III.3 d shows the correction of the stress/stretch obtained from DIC analysis. The measured stretch followed the imposed stretch closely.

This is illustrated in figure III.4 a, where the measured local deformation in the direction of traction measured with DIC is shown against the imposed stretch ratio. Figure III.4 b shows the local deformation in the direction perpendicular to traction: the same initial increase was observed at the macroscopic scale than for microscopic stretches measured on SHG images. Finally, figure III.4 c shows the sliding angle, that remains small throughout the experiment.

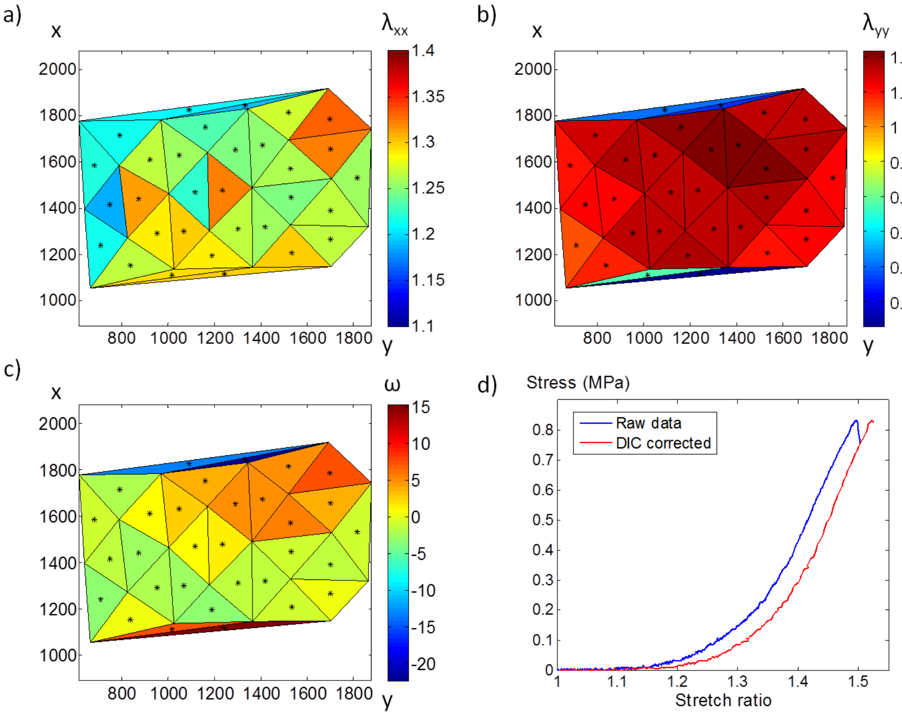

Figure III.3 – Deformation maps obtained from DIC analysis of the macroscale images, based on the ink pattern drawn on the samples: a) direction of traction λ_{xx} b) direction perpendicular to traction λ_{yy} and c) sliding angle ω, for a stretch ratio of 1.25. The correction of the stress/stretch curve with DIC analysis is shown in d.

The fact that the samples swelled in the direction perpendicular to traction in both experiments, outside and under the microscope, suggested that this phenomenon was to be attributed to the tensile test set-up.

We estimated it likely to be simply an effect of hydration, more specifically swelling of the tissue transitioning from culture medium to water (or water gel). This swelling in water has already been reported in other tissues such as the cornea [13]. In the cornea, a disfunctionnal water regulation can lead to a condition called Fuchs endothelial corneal dystrophy: water is retained in the cornea, which results in gradual decline in vision. In our case, the dysfunctional water regulation could be due to the absence of epidermis to regulate the fluid flowing in and out of the tissue.

We tested that hypothesis with a “swelling test”. We stretched the sample to a stretch ratio of 1.1 at $10^{-4}s^{-1}$, then imaged every 30 minutes, exactly as in a normal experiment, but without further stretching. No swelling in the y-direction was observed, which infirmed the static swelling hypothesis. The swelling only occured when the sample was submitted to mechanical stretch: it is likely to be a poroelastic effect.

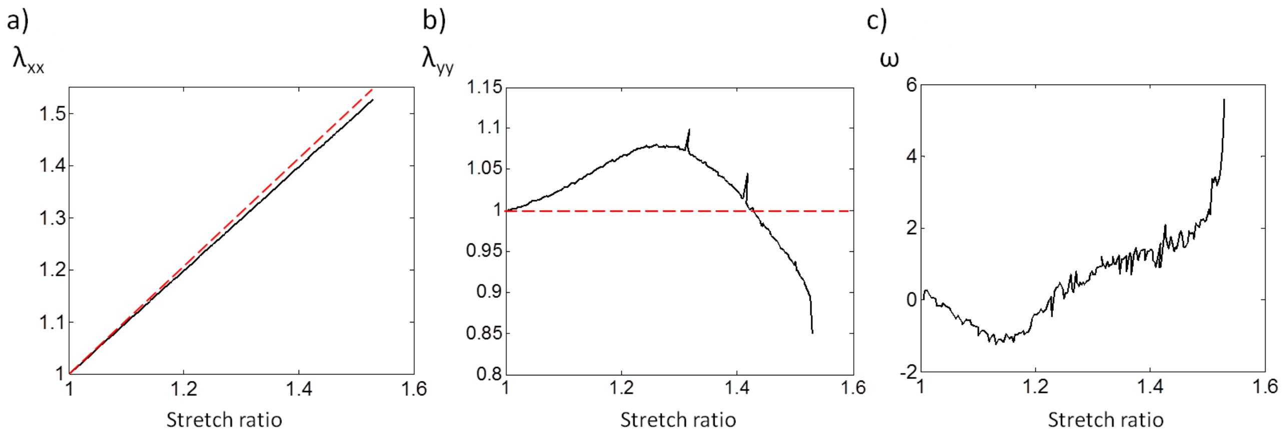

Figure III.4 – Local deformation in a) direction of traction λ_{xx} b) direction perpendicular to traction λ_{yy} and c) sliding angle ω versus the imposed stretch, for a typical macroscale unixial tensile test outside the microscope, using DIC post-processing to compute the local stretches. The sample presented is the same as in figure III.3.

To test this poroelastic hypothesis it would be useful to measure the local stretches in similar experiments, but with the epidermis still on. This is however only possible in experiments outside the microscope and would require a large number of samples dedicated only to this study to compare the results with previous findings.

Guan and coworkers [98] carried out uniaxial tensile tests with the epidermis on and measured the strain fields with DIC, but did not maintain the sample hydrated during the test. In this work the displacement fields in the surface direction perpendicular to traction are heterogeneous, with both swelling and shrinking: it is impossible to conclude.

Veronda and colleagues [48] performed uniaxial tensile tests on *ex vivo* cat skin with epidermis, also with no hydration control. Notably, the samples were frozen prior to the experiments, which may damage the microstructure. The stretch ratios in all directions, direction of traction (λ_1) and directions perpendicular to traction (λ_2 and λ_3), were measured using an optical technique. The evolutions of λ_2 and λ_3 versus λ_1 are shown in figure III.5. No swelling was observed for λ_2, corresponding to the y-direction in our experiments, however a plateau could be seen before contraction, probably as a result of the epidermis preserving the sample's hydration state. The samples also swelled in thickness (λ_3, z-direction in our experiments) all along the tensile test, but especially for large stretch ratios ($\lambda_1 \approx 1.4$ - 2.1), which were very rarely reached in our experiments.

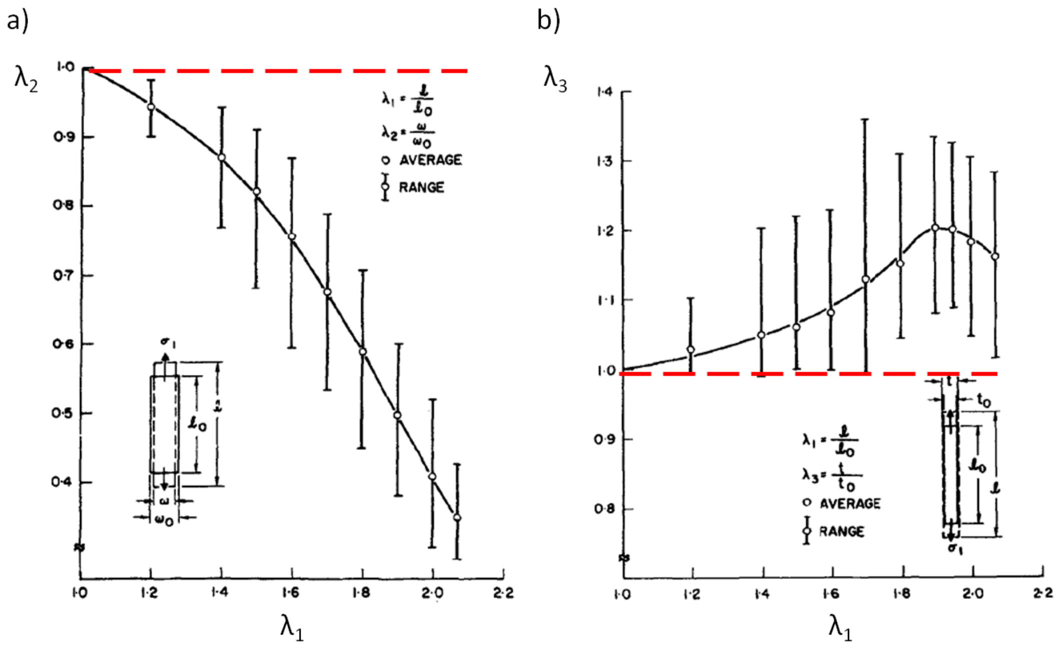

Figure III.5 – Stretch ratios in the directions perpendicular to traction: a) λ_2, in the surface of the sample and b) λ_3, perpendicular to the surface of the sample, versus λ_1, stretch ratio in the direction of traction. The stretch ratios were computed from *ex vivo* uniaxial tensile tests on cat skin and measured using an optical technique. The red dotted lines indicate $\lambda_2 = 1$ and $\lambda_3 = 1$. Figure from [48].

III.1.2 Relaxation analysis

In the experiments with microscopic observations the motors were stopped every 5% deformation for a few minutes to image the sample. As a result of skin's viscoelasticity, stress relaxed when the stretch was kept constant. By analysing the relaxation at each deformation steps we can get an overview of the viscous behaviour of skin, which we do not obtain from simple continuous tensile test.

The relaxations were fitted with a biexponential curve with saturation as described in Chapter II. The shortcomings of this method have also been discussed in the same section. The fit gave us five parameters: amplitude of force relaxed in short time relaxation, amplitude of force relaxed in long time relaxation, amplitude of the relative constant, and two characteristic times, short time and long time. Figure III.6 shows the mean of the five parameters for all WT samples observed with the SHG protocol (25 samples), versus the imposed stretch. The number of samples varied at each step, because the rupture stretch ratio varied from sample to sample, as did the heel region length (only the relaxations in the linear region of the curve could be fitted). In figure III.6, a threshold at 3 samples was applied for every point.

The parameters remained fairly constant throughout the tensile test. The relaxation behaviour

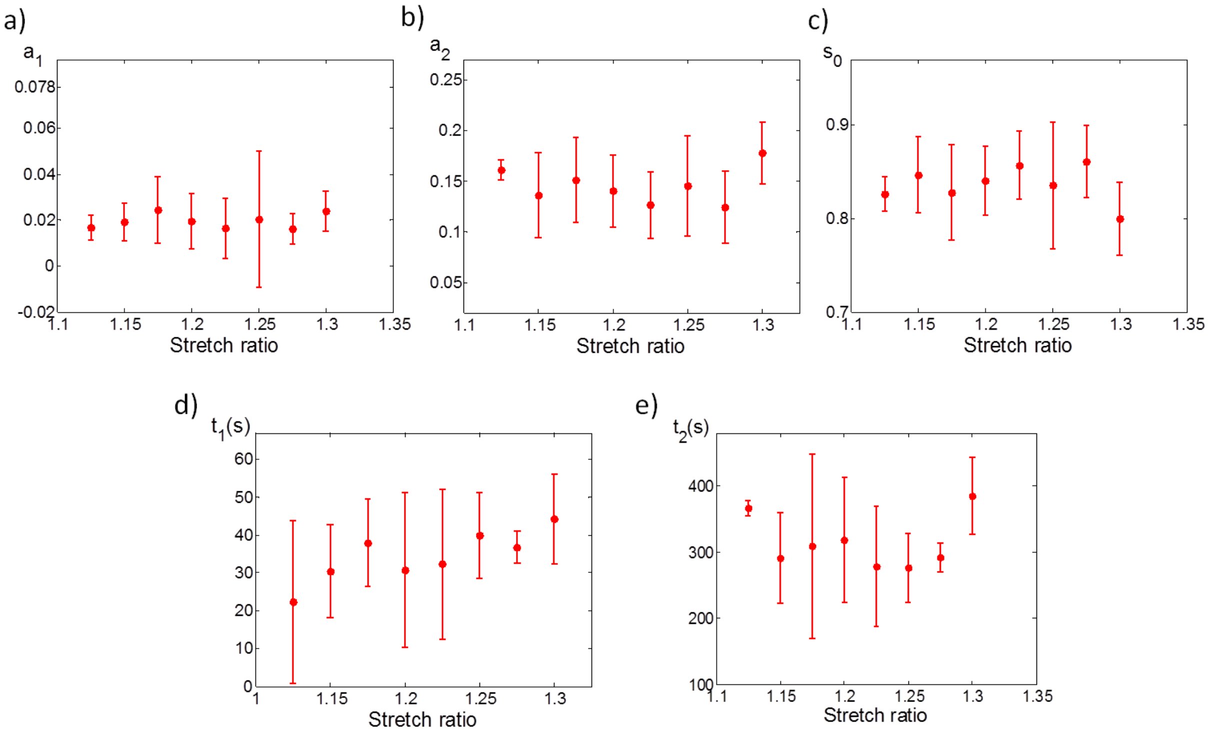

Figure III.6 – Averaged values of the five parameters describing the relaxation behaviour of WT samples, averaged over all available samples: a) amplitude of short time relaxation a_1, b) amplitude of long time relaxation a_2, c) amplitude of the relative constant s_0, d) short time t_1(s) and e) long time t_2(s). Error bars represent the standard error of the mean.

seems independent of the stress level. This is consistent with the quasi-linear viscoelastic behaviour proposed by Fung [9], in which strain effects can be isolated from time effects.

The relaxations could only be fitted with certainty in the linear region of the stress/stretch curve. In figure III.7 we plot, for a single sample, five normalised relaxations: two in the heel region and three in the linear part (all curves were processed with a moving average). The relaxations in the heel region of the stress/stretch curve were usually below, *i.e.* “more efficient”, than the relaxations in the linear part.

Furthermore, we also see in figure III.7 that, for the same sample, all normalised relaxations in the linear part (beige, orange and red curves) can be superimposed, consistently with the independence of relaxation behaviour with stress observed earlier.

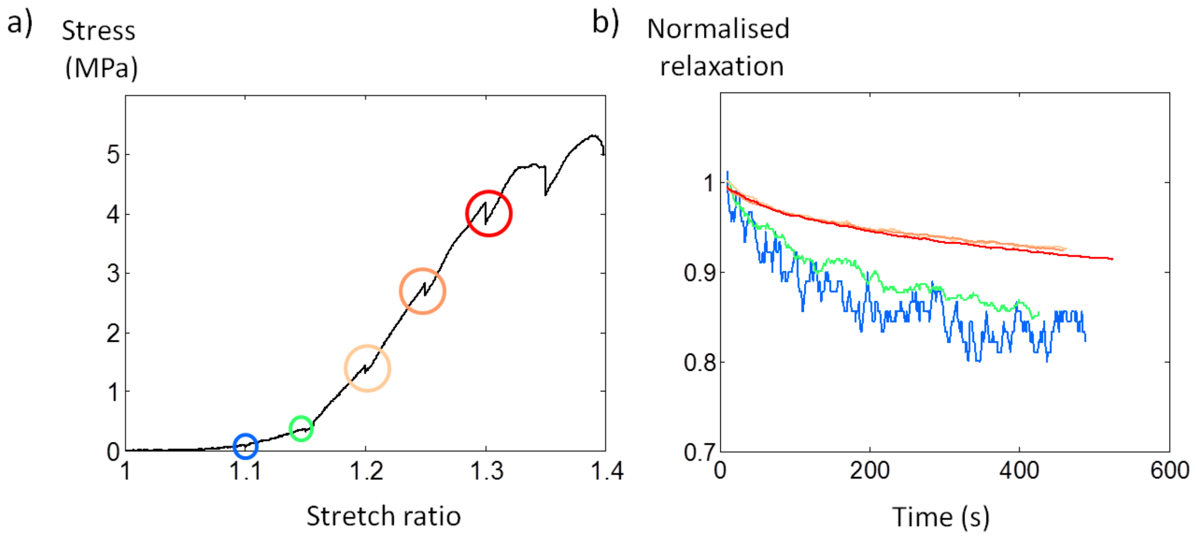

Figure III.7 – Comparison of relaxation behaviour in heel and linear regions: a) stress/stretch curve, b) corresponding normalised relaxations in the heel (blue and green) and linear (beige, orange, red) parts. All normalised force/time curves were processed with a moving average using Matlab (number of points=9). The relaxation at 1.35 was affected by the start of the rupture and is not plotted.

III.1.3 Evolution of fibre orientation

The evolution of fibre orientation was analysed as described in the last chapter. The outputs are a visual representation of the orientation of the fibres through orientation maps, and quantitative parameters: the histogram of normalised probability of fibre orientation, the Orientation Index (OI) and the entropy. In uniaxial tensile tests orientation index and entropy are fairly similar, therefore in this work only the former will be considered.

The evolution of the orientation maps with increasing imposed stretch ratio is shown in figure III.8. The direction of traction is the left-right direction. As expected, the maps show the fibres leaning progressively towards the direction of traction. The holes of the hair follicles get more and more elliptic, with the major axis aligned with the direction of traction.

The corresponding normalised histograms can be seen in figure III.9. As reported in the previous chapter, each histogram is the average of the orientation histograms from six images of the stack.

The original layout of the fibres was often found to be organised around two major directions, most of the time symmetrical with respect to the direction of the back (zero angle). The two peaks could be of the same amplitude (as in figure III.9, red curve for $\lambda = 1$) or not. The existence of two preferred directions in skin is coherent with the multiaxial stimulation that the tissue is submitted to in its natural environment: it allows the skin to resist mechanical loadings in any direction.

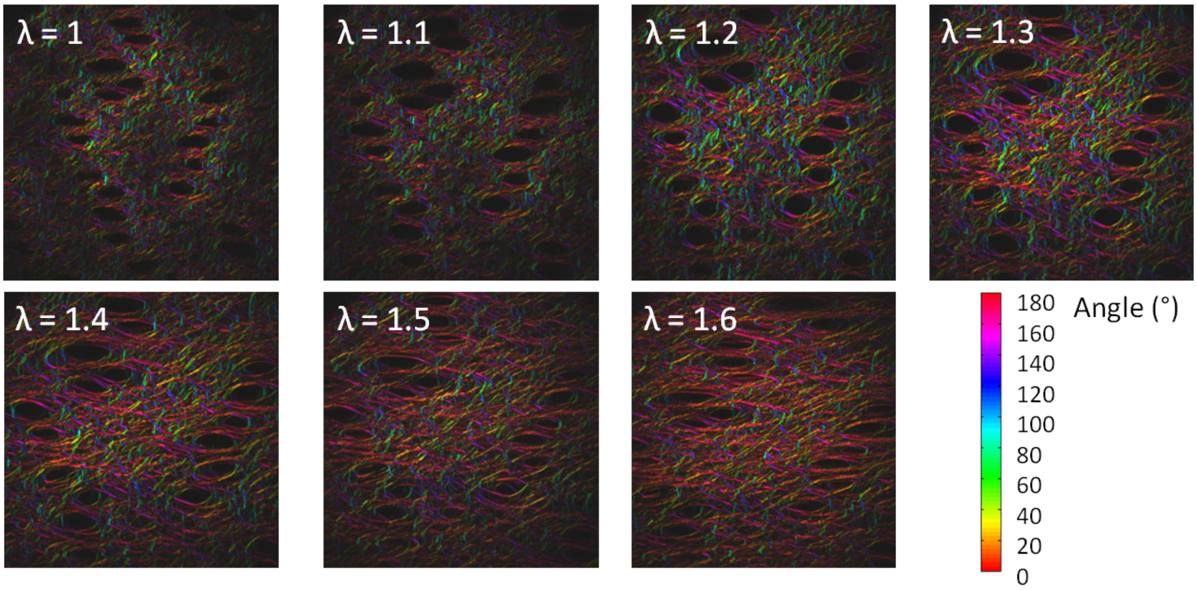

Figure III.8 – Orientation maps reveal the evolution of fibre orientation through the mechanical test from $\lambda = 1$ to $\lambda = 1.6$. The deformation maps are obtained from a single image of the stack. The size of the ROI is approximately 400 μm × 400 μm.

The angles of maximum orientation observed *ex vivo* are however difficult to relate quantitatively to the *in vivo* case, because the skin is pretensed when on the animal whereas we measured the directions in rest state with no stress.
Looking more closely at the inital orientation map, we can see local disparities: some areas of the image have preferred orientations in rest state. Specifically, a concentration of fibres oriented in the direction of traction can be seen between the hairs follicles of the same vertical line (regions in red in figure III.8 for $\lambda = 1$). This local concentration could be observed the majority of the time.

During the mechanical test, the orientation histogram evolves from the initial two peaks distribution (red curve in figure III.9) to a single peak distribution centered on the direction of traction (blue curve in figure III.9). Typically, as we impose stretch on the sample, the proportion of fibres oriented in the original directions decreases: this can be seen in figure III.9 at -40 $^\circ$ and +40 $^\circ$. Simultaneously, the proportion of fibres aligned in the direction of traction increases: in figure III.9, it corresponds to -10 $^\circ$ and +10 $^\circ$. The redistribution of fibre orientation first results in a one peak distribution with a fairly large plateau (at $\lambda = 1.3$ in figure III.9), followed by a narrowing of the central peak until the end of the test (from $\lambda = 1.4$ in figure III.9).

If we plot the maximum of the normalised orientation histogram versus imposed stretch ratio, for SHG images at approximately the same depth for each stack, we obtain the curve in red in figure III.10. For almost every sample and every depth, the angle of preferred orientation jumps from the angle associated with one of the peaks in initial distribution to a value close to zero,

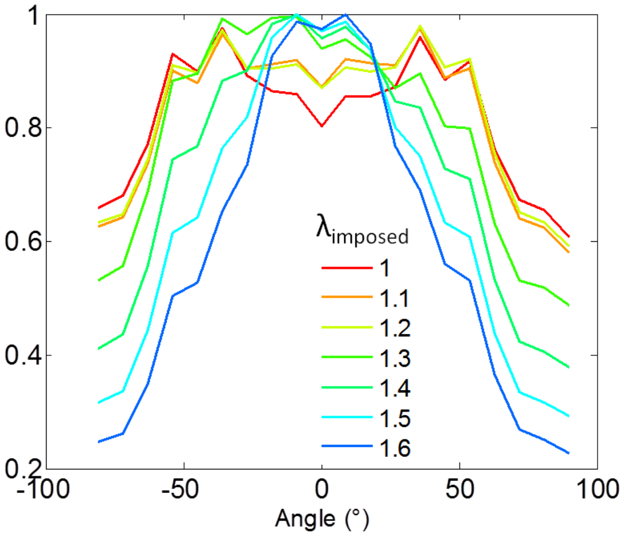

Figure III.9 – Histogram of fibre orientation throughout the mechanical test, from $\lambda = 1$ to $\lambda = 1.6$. Each histogram is the average of six histograms from images taken in the depth of the tissue.

associated with the central peak. This looks like a state transition: the whole system shifts from one configuration to another, in a seemingly abrupt fashion.

In the example in figure III.10, we can see the transition happening near the end of the heel region of the stress/stretch curve, close to the beginning of the linear part. Similarly, the transition was observed in most images within 5% strain of the end of the heel region. However, the jump did not occur exactly at the same strain level for all six images of the same sample: there is a depth variability.

It should be noted that both maximum angle of fibre orientation and stretch ratio are discrete values: the structural element is rotated by 10 ° to assess fibre orientation, and the stretch ratio is implemented by 5% at every deformation step. It is possible that if we refine one or both of these measures, the jump will be smoothed down in a continuous transition.

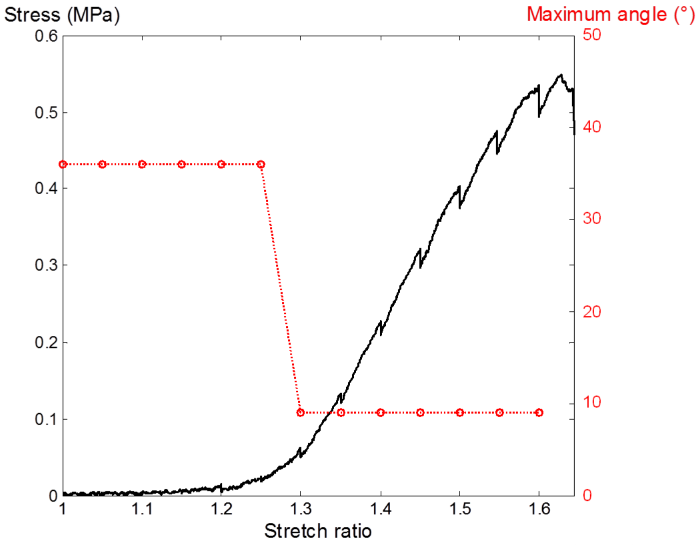

Figure III.10 – The angle of preferred orientation jumps from an angle associated with one of the peaks in initial distribution to a value close to zero, associated with the central peak. Red: maximum of the normalised histogram of fibre orientation for one SHG image versus imposed stretch ratio, black: stress versus imposed stretch ratio.

III.1.4 Correlation of OI and stress

Figure III.11 shows two superimposed curves: orientation index versus stretch and stress versus stretch. The orientation index was defined in Chapter II. During the mechanical assay, the orientation index followed a J-curve, with at least a recognisable toe region and a linear part. Other parts are more difficult to distinguish because the OI curve is discrete, with points every 5% deformation. The evolution of the OI in the toe region was occasionally a little more chaotic, but the slope of the linear part of the OI could always be adjusted to fit the linear part of the stress/stretch curve.

The collagen alignment followed exactly the stress curve. In other words, the stress was proportional to the proportion of fibres aligned. The linear part of the OI/stretch curve was measured for each sample, and this parameter was used to assess how easily the collagen fibres rearranged themselves during the tensile test.

This correlation between OI and stress was true for all samples, regardless of mutation or age. As such, this seems to be an intrinsic property of mice skin. It is probable that the same result will hold for human skin, although some microstructural differences, for instance the presence of elastin, may affect the microstructural behaviour.

This result is surprising as it is not in agreement with the commonly accepted microstructural explanation for the J-shape of skin's stress/stretch curve, as will be discussed in section III.3.

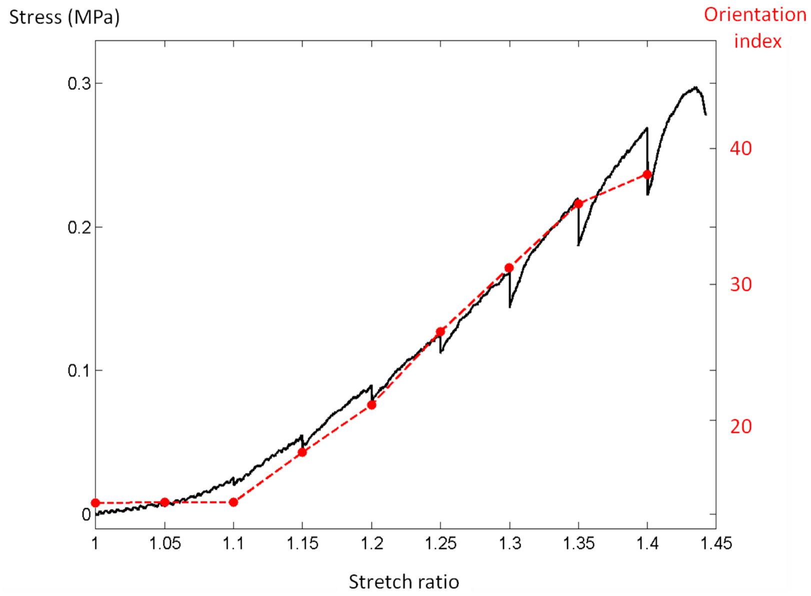

Figure III.11 – Stress (in black) and orientation index (in red) versus global imposed stretch ratio.

III.1.5 Strain rate dependency

Experiments with different strain rates were carried out outside the microscope. At $10^{-3}s^{-1}$ the set-up was fit for the experiment with no modification needed, whereas at $10^{-2}s^{-1}$ the skin dehydrated too quickly and the mechanical behaviour was altered. The results at $10^{-2}s^{-1}$ are shown here as mere indications and need to be considered with caution.

The values for tangent modulus, heel region length, maximum stress and maximum stretch ratio for the three different strain rates are shown in figure III.12.

The tangent modulus, heel region length and maximum stress increased significantly with increasing strain rate, while the rupture stretch ratio remained unchanged. Figure III.13 summarises schematically the average mechanical behaviour of WT skin at slow ($10^{-4}s^{-1}$) and medium ($10^{-3}s^{-1}$) strain rates.

These results will be discussed as part of our microstructural interpretation in the next section.

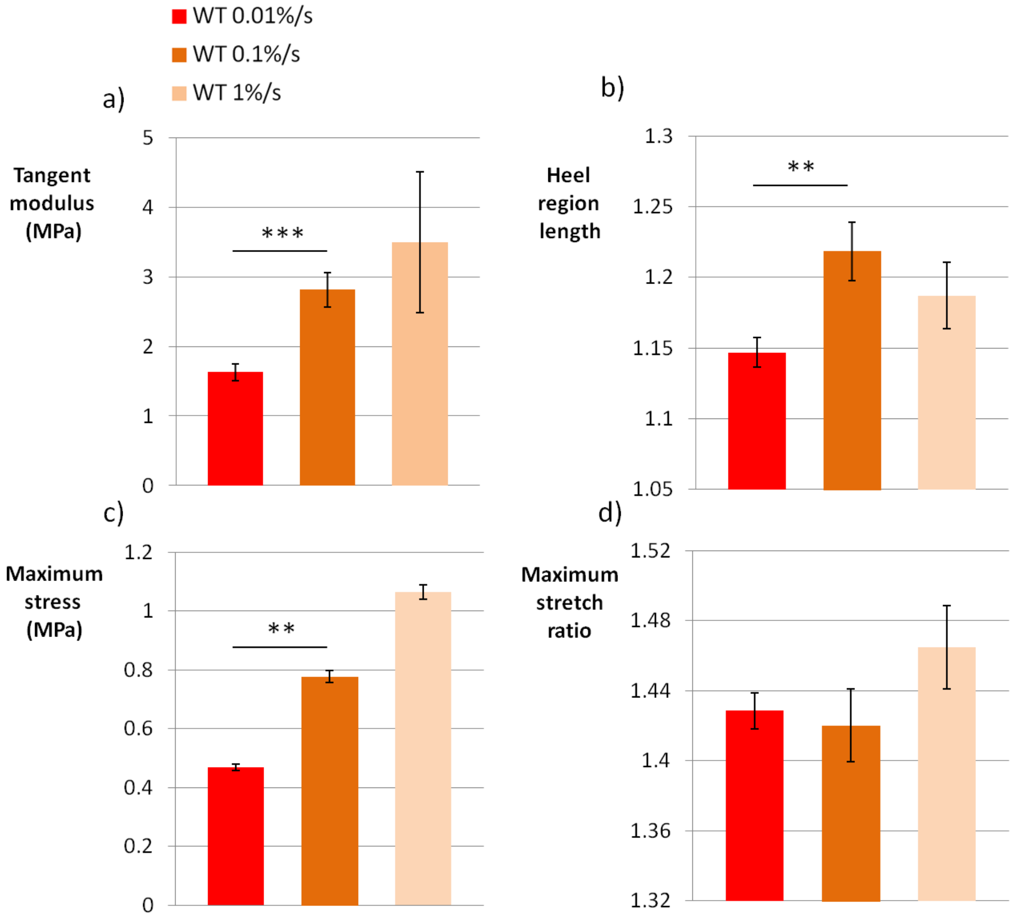

Figure III.12 – Evolution with increasing strain rate of a) tangent modulus, b) heel region length, c) maximum stress and d) maximum stretch ratio. Red corresponds to a strain rate of $10^{-4}s^{-1}$ (number of samples n = 32), orange to $10^{-3}s^{-1}$ (n = 16) and beige to $10^{-2}s^{-1}$ (n = 5). ** indicates $p \leq 1\%$, *** $p \leq 0.1\%$. The samples at $10^{-2}s^{-1}$ were not included in statistical analysis due to strong experimental incertitudes.

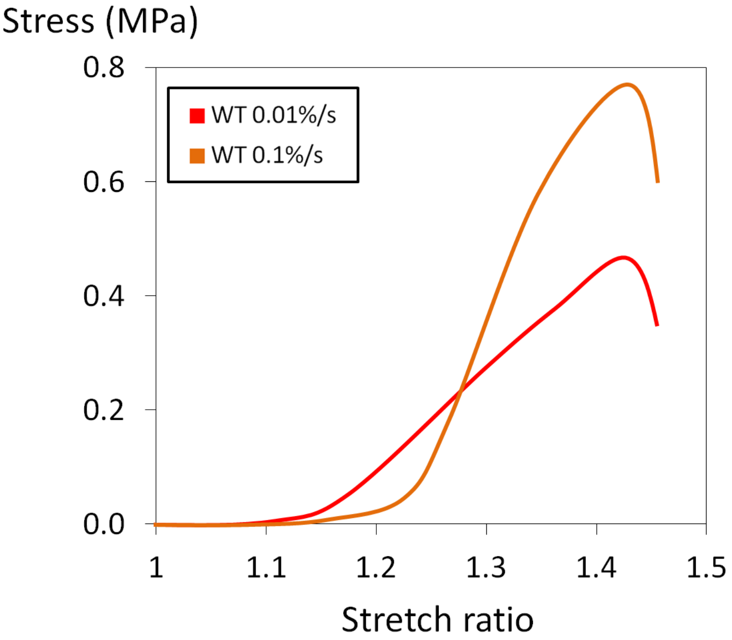

Figure III.13 – Schematic representation of typical WT stress/stretch curves tested in uniaxial tensile test with a strain rate of $10^{-4}s^{-1}$ (red) and $10^{-3}s^{-1}$ (orange).

III.1.6 Cycling experiments

Finally, cycling experiments were performed without SHG observation. Six samples were tested with a cyclic loading path with increasing maximum imposed stretch ratio: we imposed 2 complete cycles at a maximum stretch ratio of $\lambda = 1.05$, 2 cycles at $\lambda = 1.1$, 2 at $\lambda = 1.2$, 2 at $\lambda = 1.3$, and then stretched the sample up to rupture. The loading path is summarised in figure III.14 a. The strain rate was $10^{-3} s^{-1}$. The corresponding typical stress/stretch curve is shown in figure III.14 b. The statistics on these experiments were too small to have reliable quantitative results.

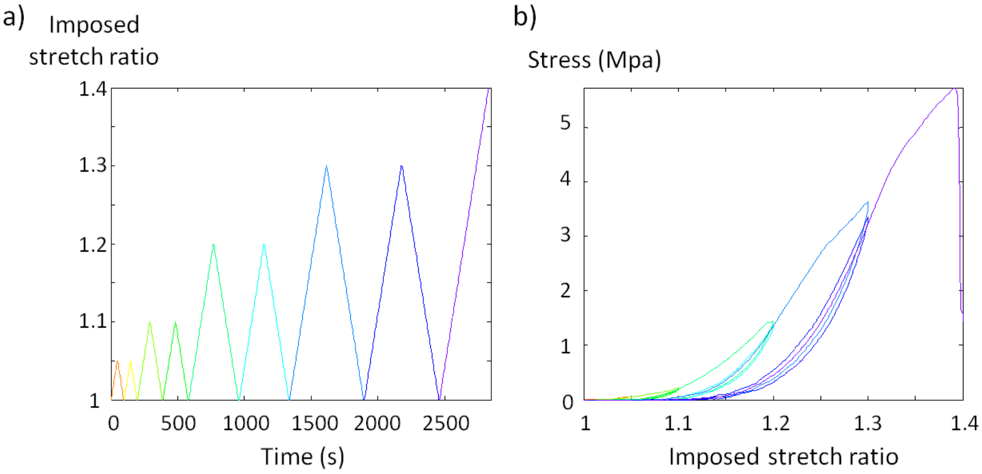

Figure III.14 – Typical cycling experiment with no SHG observation: a) loading path, b) stress/stretch curve.

The hysteresis observed between the loading and unloading curves illustrated skin's viscoelastic behaviour. When unloading the first cycle of a given stretch ratio, we generally reached zero stress at approximately half the maximum stretch ratio imposed. This can be visualised by plotting for each cycle the minimum stretch ratio for which the force exceeded the sensor's noise level, versus maximum imposed stretch. This plot is shown in figure III.15 for the same sample as in figure III.14.

When reloading, the stress went up again following very closely the unloading curve of the previous cycle, with only a small shift to the left. The maximum stress of the second cycle at a given imposed stretch ratio was only slightly shorter than the maximum reached on the first cycle.

These results will be discussed as part of our microstructural interpretation in the next section. Notably, the same experiments on tendons seem to indicate much less elastic effects, see [94].

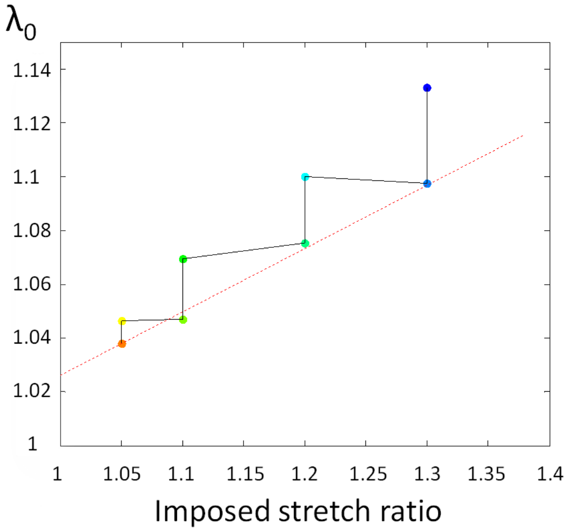

Figure III.15 – Stretch ratio for which the force first exceeded the sensor's noise level, versus maximum imposed stretch ratio, for the same sample as in figure III.14.

III.2 Discussion

III.2.1 Incompatibility with conventional models

All soft collagenous tissues exhibit a non-linear stress/stretch response, that is illustrated by the J-shaped stress/stretch curve. One could imagine that this similarity in the mechanical response arises from the similarities in microstructural components. The role of the microstructure, that changes considerably from one tissue to another, is however not trivial.

The conventional microstructural interpretation for the non-linear mechanical response of soft collagenous tissues is derived from microscopic observations of tendons. Diamant and colleagues [15] established from polarised light observations that the collagen fibres within tendons are crimped, with a periodic planar wave structure. This structure can be observed in the first image in figure III.16. The crimp wave length follows a distribution that can be characterised experimentally.
When stretched, the collagen fibres in the tendon get gradually straighter, begin to bear load and start contributing to the general stress. The disappearance of crimps in the toe region can be directly observed using polarised light [15], as observed in figure III.16 for small strains. The progressive recruitment of crimped collagen fibres was proposed as the mechanism responsible for the non-linear stiffening in the heel region of the stress/stretch curve. Kastelic and coworkers [81] developed a model for this interpretation as early as 1980, the "Sequential Straightening and Loading" model.

In this perspective, the linear part of the stress/stretch curve is interpreted as the elongation of

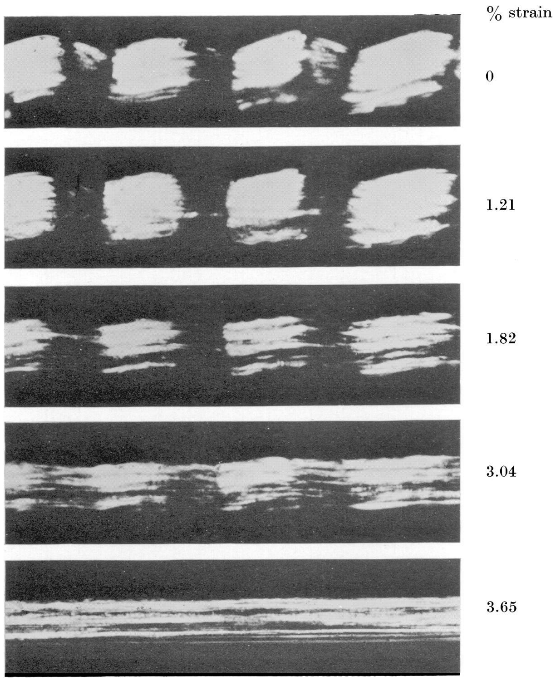

Figure III.16 – Observation of a rat tail tendon's fascicle with polarised light microscopy by Diamant and coworkers in 1972. The wavy structure of the fibres is revealed in rest state (top image). The gradual disappearance of crimps with strain can be observed: the fibres get taut and are completely straight by a strain of 3.65%. Figure from [15].

the collagen fibres. Consequently, all microstructural reorganisation must occur in the toe and heel regions. Indeed, if some fibres were to reorganise and align in the direction of traction during the linear part, the addition of their mechanical contribution would lead to an increase in the stress. The linear part would not be linear anymore, but faster than linear. As the linear part is, actually, linear, an hypothetical orientation index for this model would necessarily increase in the toe and heel regions and then encounter a plateau in the linear region of the stress/stretch curve. This hypothetical OI is drawn schematically in figure III.17. It should be noted that the start of this OI versus stretch curve could present a toe region. However the linear part of the stress/stretch curve needs to correspond to a plateau in the OI.

This interpretation has been adapted to skin, a tissue that presents a very different microstructure, with a complex 3D network of curly, wavy and interwoven collagen fibres [33, 38, 48, 109, 110]. Typically the toe region is interpreted as the unwinding of fibres at the mesoscopic scale. Elastin is generally considered to play a role at this stage as the main reinforcement of the ground matrix surrounding the collagen I fibres [110]. It is often discarded nonetheless due to its very low stiffness [33, 38]. The heel region corresponds to fibre unwinding, aligning and uncrimping at the microscopic scale. Finally, when all collagen fibres are aligned in the pulling direction, the extension of the fibres results in a linear part, attributed to an elastic behaviour of collagen fibres, followed by rupture. The microstructural behaviour during a tensile test as interpreted by this

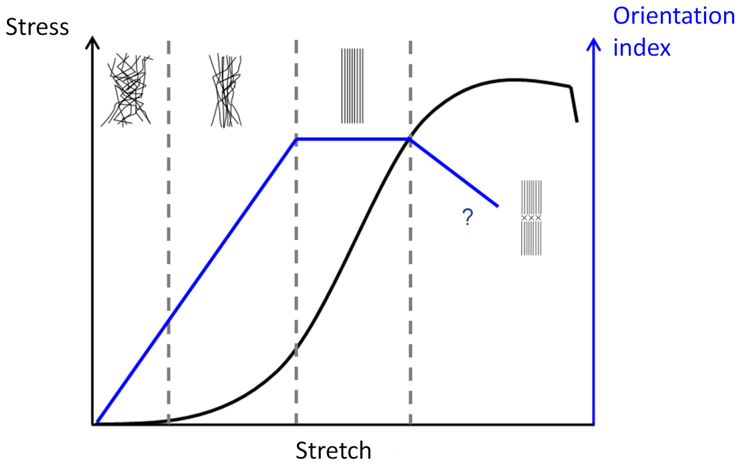

Figure III.17 – Hypothetical OI/stretch curve for the conventional microstructural model adapted to skin. The hypothetical fibre orientation in skin is represented schematically (in blue) for each region of the stress/stretch curve (in black). The microstructure is represented schematically for each region of the stress/stretch curve.

conventional model for skin is represented schematically for each region of the stress/stretch curve in figure III.17.

Many skin models take this general interpretation as a basis and add various nuances, *e.g.* properties of the fibres, properties of the extrafibrillar matrix, cross-links.

One main experimental study provides evidence to support the conventional microstructural model in skin. Brown [32] observed human skin samples with scanning electron microscopy at every stage of the stress/stretch curve, and obtained results concordant with the "sequential straightening" theory. However, due to the technique used they had to take a different sample for every observation. Additionally, the microstructural observations were purely qualitative.

On the other hand, in a recent study, Nesbitt and coworkers used SHG imaging to quantify the collagen reorganisation in the toe and heel regions of the stress/stretch curve. They showed, consistently with our results, that the fibres align in the direction of traction with strain [93]. This study was limited to small stretch ratios and the behaviour in the linear part was not investigated.

The evolution of the OI with stretch we measured on mice skin (figure III.11) does not match the hypothetical OI associated with the commonly accepted microstructural interpretation.

A possible way to reconcile our observations and this theory would be to imagine that some regions in skin act like "collagen cables", similar to tendons. The collagen fibres would uncrimp and realign in those areas in the toe and heel regions, and we would pull directly on the aligned fibres during the linear part. The progressive increase of the orientation index in the linear part could be attributed to fibres rotating to settle "close to" the pulling direction, hence narrowing the distribution of fibre, which results in a larger orientation index. The fibres possessing only

axial tensile stiffness, these “almost aligned” fibres would be unable to contribute to the global stress increase, for the reason that they would not be aligned or straightened enough.
This interpretation is an extension of some models of complex networks, such as engineered collagen gels, that can be found in the literature. MacKinstosh *et al.* developed such a model for semiflexible biopolymers, collagen being a prime example, in which the non-linear elastic properties of the network arose from straightening of intermittent chains between entanglements [111].

However, the orientation maps obtained from SHG images, see figure III.8, do not show these “collagen cables”. From the initially well aligned regions between hair shafts, it first looks like the realignment is indeed progressive and spatially delimited. However the lining up in the pulling direction becomes generalised in the whole ROI during the linear region of the stress/stretch curve, with no distinguishable spatial preference. Furthermore, the collagen cables interpretation would not explain why the orientation index slope follows the linear part of the stress/stretch curve so closely. It seems unlikely for it to be a random effect, as it is very reproducible: we observed it in more than 100 samples.

Overall, it seems difficult to believe that the collagen fibres could be elastic considering the adequation between the evolutions of orientation index and stress. With elastic fibres aligning progressively, the constant addition of elastic contributions would indeed make the linear part non-linear. Hypothesis on possible microstructural mechanisms that could account for our observations are advanced in the following section.

Finally, the evolution of the histogram of fibre orientation presented in figure III.9 seems to indicate that the modelisation of the matrix as an elastic material, commonly found in the literature, is not adequate. Indeed, with an elastic matrix the fibres would not rotate, but would only be driven by the deformation of the bulk material they are embedded in. The histogram of fibre orientation in a deformed state would then merely correspond to a narrowed version of the initial distribution. To actually modify the shape of the fibre orientation histogram, the fibres need a viscous environment.

III.2.2 Hypothesis on possible microstructural mechanisms

Considering the inadequacy of the usual interpretation of skin’s non-linear mechanical behaviour with our observations, we suggest other mechanisms that can account for our experimental data.

First, we need to make sense of the linear part of the stress/stretch region. In this region of the curve, we know that the fibres align progressively in the direction of traction while the stress increases linearly with stretch. Recent observations of sliding between collagen units in tendons inspired us to suggest a model of sliding within fibres.

Screen *et al.* [12] demonstrated that a considerable amount of sliding occured between fibres when stretching a tendon's fascicle. Using a confocal microscope they were able to obtain the displacements of stained cell nuclei, used as local discrete markers, in real time during a mechanical tensile test. As cells adhere to fibres, their displacements can be used to compute the actual strain the fibre is subjected to. Figure III.18 a shows images obtained at 0%, 3% and 6% strain, with groups of nuclei identified. Figures III.18 b and c respectively show the averaged within-group strain and between group displacement (expressed as a percentage of imposed displacement) versus applied strain. This study showed that the actual strain within the fibre, expressed *via* within group strains, never exceeded 15% of the strain imposed to the fascicle. The remaining strain was distributed between sliding between fibres and deformation in the matrix.

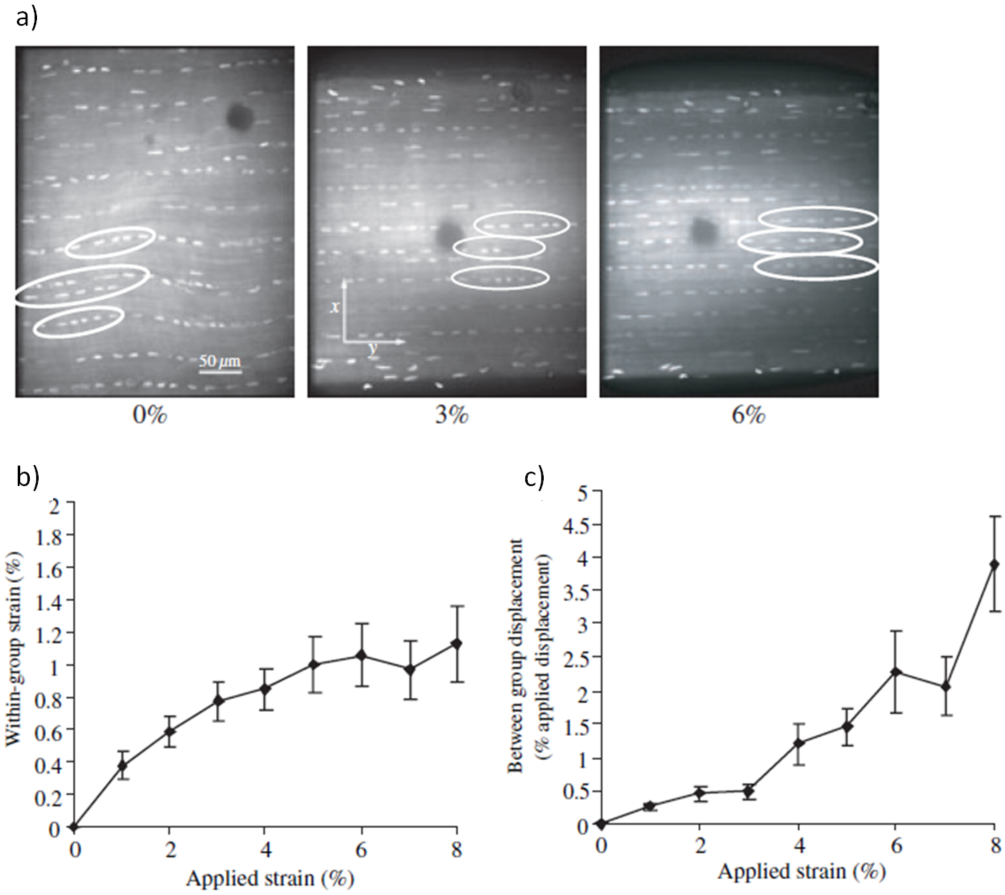

Figure III.18 – Confocal microscope images to track the displacements of stained cell nuclei in real time during a mechanical tensile test: a) images obtained at 0%, 3% and 6% strain, with groups of nuclei identified, b) average within-group strain versus applied strain and c) average between group displacement (expressed as a percentage of imposed displacement) versus applied strain. Figure from [12].

Puxkandl *et al.* [35] observed the same phenomenon, also with tendons. They carried out tensile tests and X-ray scattering observations simultaneously, and measured the elongation of collagen fibres using X-ray diffraction patterns. They were able to compare the microscopic strain in the fibre and the macroscopic strain in the whole tendon. They concluded that the overall strain in the tendon was always larger than the strain in individual fibres, and showed that the ratio of fibre strain to tendon strain depended strongly on the applied strain rate.

To explain this behaviour they suggested a simple structural model, presented schematically in figure III.19. In this model, the collagen fibres are linked together by proteoglycans, connected to collagen fibres and extending from one to the other. This is coherent with the structural organisation of soft collagenous tissues observed in TEM images with proteoglycans stained, see [8]. When the tendon is stretched, Puxkandl and coworkers postulate that the strain is distributed between the collagen fibres and the proteoglycan-rich matrix, which is mainly sheared. Fibres and matrix are considered as viscoelastic systems arranged in series. All qualitative features observed in their study can be reproduced with this model.

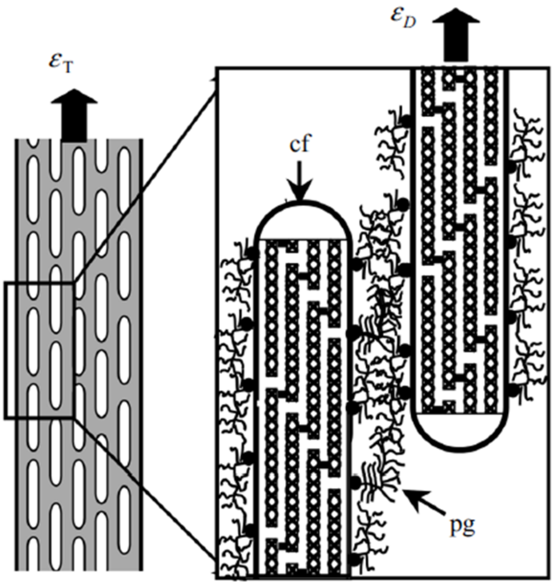

Figure III.19 – Schematic representation of the hierarchical structure of a tendon according to Puxkandl's model. When the tendon is stretched by an amount ϵ_T, the strain is distributed between the collagen fibres (cf), exhibiting a tensile strain ϵ_D, and the proteoglycan-rich matrix (pg), which is mainly sheared. Covalent cross-links between molecules are drawn schematically within the collagen fibres. Figure from [35].

A structural model based on internal sliding of collagen subunits, or fibrils, within fibres could explain the linear part in our experiments. The proteoglycans bridges between fibrils would sustain the stretch imposed on the fibre by being locally sheared, until rupture.

The stress/stretch relationship for individual fibres would be that of a perfectly plastic material, as represented in figure III.20. The initial elastic part could be attributed to the response of the proteoglycan bonds, locally under shear loading. The plateau could constitute an equilibrium between bonds breaking and possibly reattaching. For further reference, the equilibrium plateau stress level will be called σ_f. From the mechanical perspective, the fibre - proteoglycan matrix - fibre ensemble could schematically be represented by a string, a dashport and another string, in series. Incidentally, this interpretation means that the actual collagenous part of the fibre sustain little to no axial strain, which is rather counterintuitive as collagen is generally regarded as the structural scaffold of soft collagenous tissues.

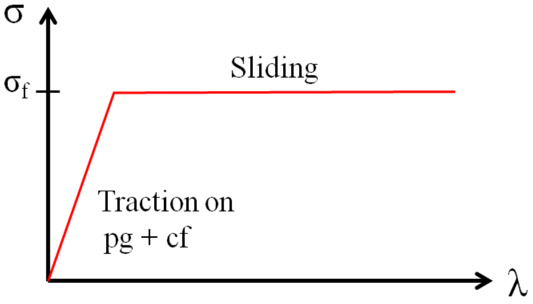

Figure III.20 – Proposed stress/stretch relationship for the collagen fibres in the context of "inner sliding". After a short elastic domain, attributed to tensile loading on proteoglycans, that are locally sheared, an equilibrium state of sliding and shearing is reached, corresponding to a plastic deformation. The plateau stress is σ_f.

A model close to this "sliding friction" interpretation has recently been developed by Sens for a moving filament detaching from a substrate to which it is linked by stochastic linkers [112]. Figure III.21 a summarises the principle of this model: a filament is sliding over a substrate covered with hookean molecular bonds, with binding and unbinding rates k_{on} and k_{off}. The linkers are stretched by the moving filament and exercise a restoring force linear with their extension. Figure III.21 b shows the corresponding energy diagrams for a single bond, with (red) and without (black) external load. The unbinding corresponds to the passage of an energy barrier, which is lowered in the presence of the filament pulling the linkers.

This "sliding friction" model predicts in particular that the cohesive force increases with strain rate until a critical strain rate value depending on the system parameters, after which the cohesive force does not evolve anymore. In skin, this would mean an increase in the plateau stress σ_f. This is coherent with the increase in tangent modulus we observed for increasing strain rates (section III.1.5). To investigate the existence of a critical strain rate it would however be necessary to carry out experiments with higher strain rates.

The mechanism of inner sliding resulting in perfectly plastic fibres would explain the linear region of the stress/stretch curve. However, this mechanism does not account for the non-linear stiffening of skin in the heel region. This could be an inherent effect of the network organisation: in the toe and heel regions, the fibres perpendicular to the direction of traction need to buckle and bend before reorientation can occur. Recent results on engineered networks, such as low density collagen gels, support this interpretation [113, 114]. Vader and coworkers [113] in particular des-

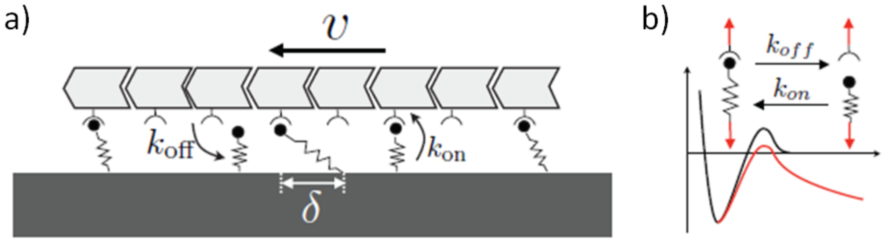

Figure III.21 – Model of a moving filament detaching from a substrate to which is is linked by stochastic linkers: a) Filament sliding over a substrate covered with hookean molecular bonds with binding and unbinding rates k_{on} and k_{off}. Linkers are stretched and exercice a restoring force linear with their extension. b) Energy diagrams: the unbinding corresponds to the passage of an energy barrier, which is lowered in the presence of an external load (red). Figure from [112].

cribed collagen gels that exhibit properties close to those of our skin samples, including non-linear stress/stretch behaviour. It should be noted however that these engineered materials differ from skin by a number of microstructural features crucial to skin's mechanics, in particular collagen density, which is much higher in skin, and absence of extrafibrillar matrix.

In the study reported in [113] two imaging techniques were combined: confocal microscopy to visualise directly the collagen fibres, and wide-field fluorescence imaging to visualise fluorescent beads embedded in the gel at a larger scale. The fluorescence images at 0%, 4%, 8%, 12% and 16% strain are shown in figure III.22 a, while the corresponding confocal microscopy images are shown in figure III.22 b.
The local strains in the three directions were computed using the fluorescent beads and an image cross-correlation technique. The evolution of the local strains in the two directions perpendicular to traction, ϵ_{yy} and ϵ_{zz}, are represented in figure III.22 d as a function of the local strain in direction of traction ϵ_{xx}. A "non linear Poisson effect" can be observed. In particular, no surface deformation in the direction perpendicular to traction (ϵ_{yy}) can be seen for small strains. This is close to the evolution of the local stretch ratio in the y-direction λ_{yy} in our experiments, although without actual swelling, and very similar to the results of uniaxial tensile tests on cat skin carried out by Veronda and coworkers, discussed in section III.1.1 [48]. Vader and colleagues attributed this phenomenon to the buckling and bending of fibres normal to the stretch direction, which preceded the collapse of the material in the normal directions.

An order parameter, comparable to our orientation index, was derived from the confocal images of the fibres. Its evolution with imposed strain is reproduced in figure III.22 c. The non-linear order parameter/strain relationship resembles the J-shaped curve we observe for OI with SHG imaging. It should be noted however that the strain levels considered, lower than 0.20, correspond to the toe and heel regions in our experiments. Furthermore, in this study, Vader and coworkers could not measure precisely the order parameter for strains higher than 0.15 due to high fibre density preventing proper detection of the fibres (grey curve in figure III.22 c). The results seem however to indicate a plateau in the order parameter/strain curve, similar to what is expected in a tendon-like model, which we do not observe in skin.

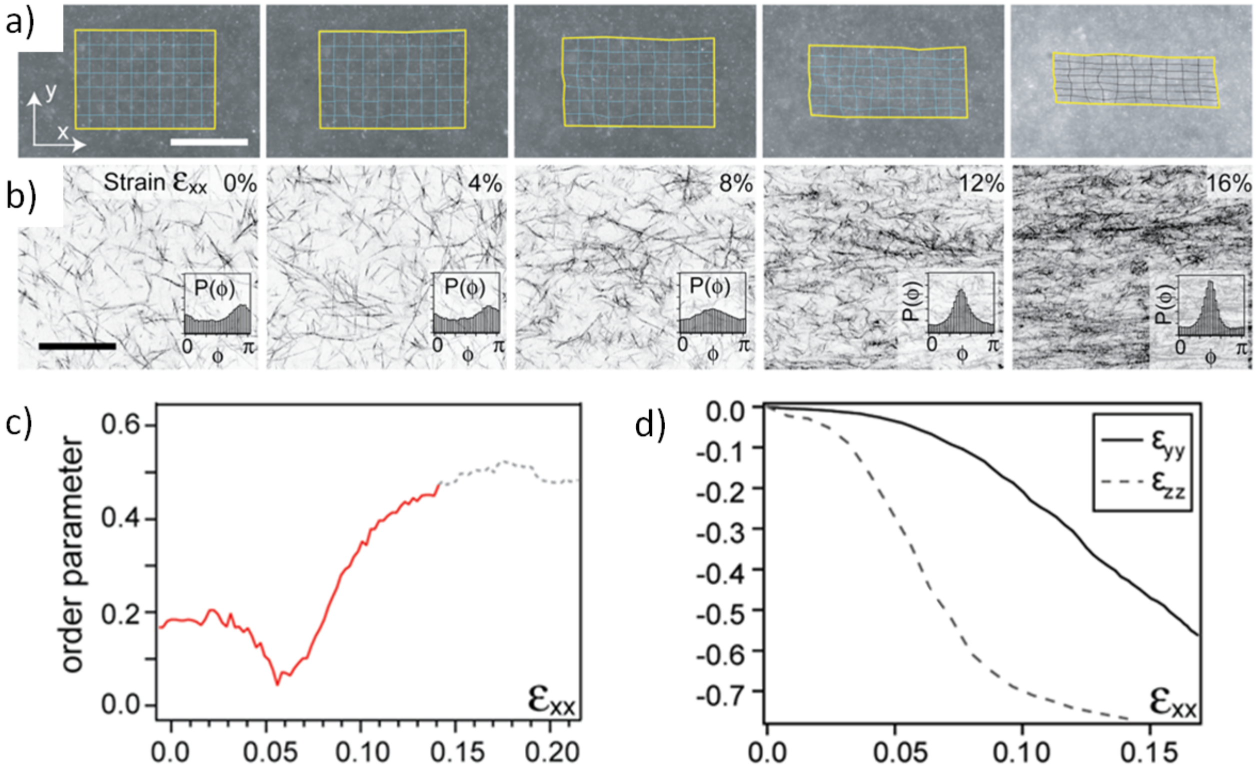

Figure III.22 – Multiscale investigation of the mechanical properties of low density collagen gels with embedded fluorescent beads: a) Fluorescence images at 0%, 4%, 8%, 12% and 16% strain. Scale bar is 500 μm. b) Confocal microscopy images at the same strains. Scale bar is 50 μm. c) Order parameter derived from the confocal images throughout the test. The curve beyond 15% stretch is grayed out due to the lack of confidence in the measure. d) Local strains ϵ_{yy} and ϵ_{zz} as a function of the local strain in the direction of traction ϵ_{xx}. Local strains were computed from the fluorescent beads using an image cross-correlation technique. Figure from [113].

Vader and colleagues also carried out repeated cyclic loadings on cross-linked gels (treated with glutaraldehyde, a cross-linking agent) and untreated gels. The order parameter as a function of cycle number is shown in figures III.23 a and b respectively, for untreated and treated gels. The gels that were not cross-linked never returned to their initial configurations. On the contrary, when the collagen gels were cross-linked with an external agent, they exhibited near reversibility at the microscale, along with no evidence of preconditioning. The authors concluded that the strain-induced alignment was primarily an elastic effect, and that fibre plasticity could occur, but at a much larger timescale. They however pointed out that the lack of fibre plasticity could be a side effect of the cross-linking agent used, that strengthened the fibril to fibril junctions and reduced the amount of plastic deformation at this level.

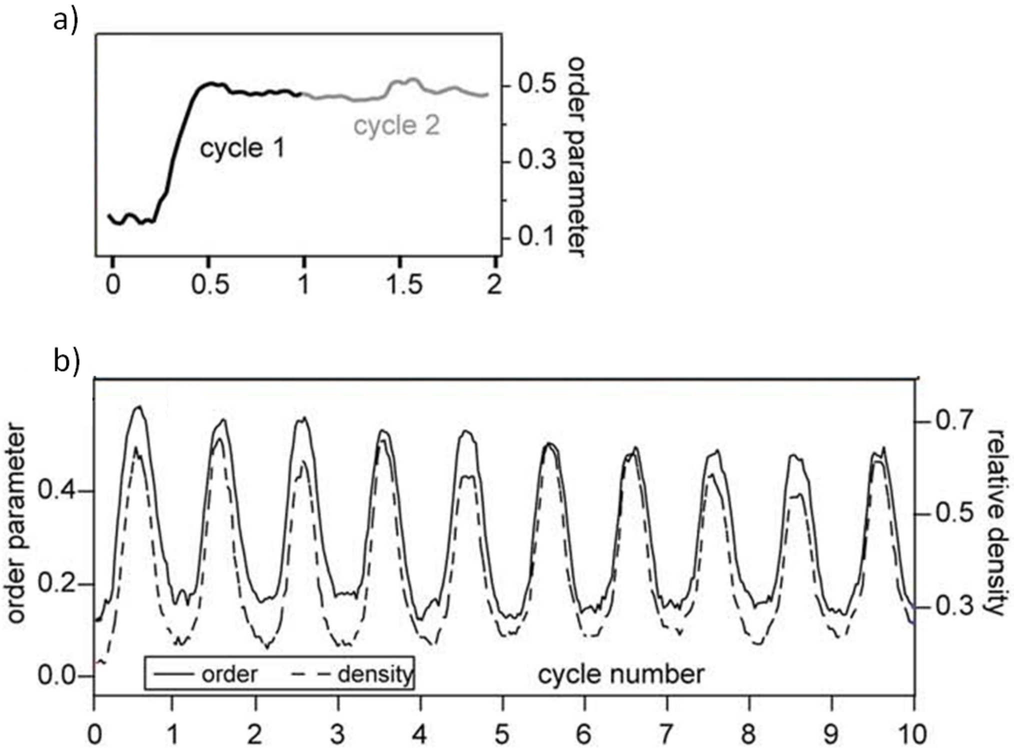

Figure III.23 – Order parameter as a function of cycle number respectively for a) untreated collagen gels and b) collagen gels treated with a cross-linking agent. Figure from [113].

Stein and coworkers [114] used numerical calculations to model the collagen gels from Vader and coworkers. The fibres are modelled as elastic beams that resist stretching and bending, and the cross-links are modeled as torsional springs. The modelled collagen gels can be seen in figure III.24 a. The deformed gels in tension and shear are shown in figures III.24 b and c respectively. By varying the parameters of the system, the authors demonstrated that the stiffening of the collagen gels originated directly from the geometric reorganisation of the network, and not from some intrinsic properties of the fibres.

The toe region can be attributed to bending of reticulation points and buckling of transversal fibres. The heel region is interpreted as the transition from a bending dominated elasticity to a stretching dominated elasticity, this transition being induced by shear.

In our case, a clue to that shift in predominant mechanism could be the change in the relaxation behaviour between heel and linear regions reported earlier in this chapter. Relaxations in the toe and heel regions involve mainly the extrafibrillar matrix, while in the linear region the relaxation of the fibrillar network through cross-links and reticulation points also plays a role. This could affect the characteristic times of relaxation.

Overall, these mechanisms at different scales of the collagen fibre network contribute to a com-

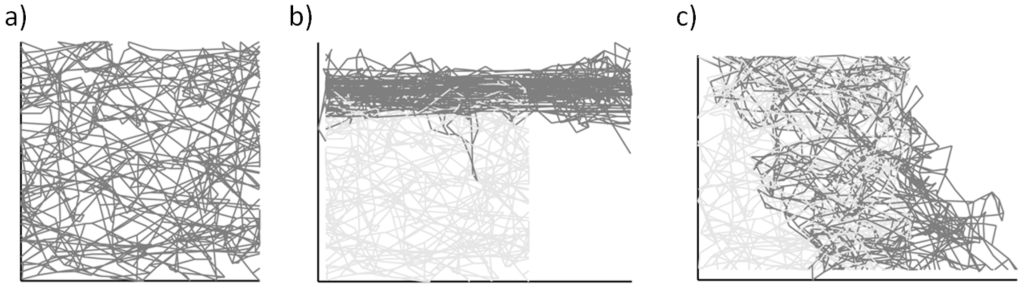

Figure III.24 – Numerical model of collagen gels: a) the fibres are modelled as elastic beams that resist stretching and bending, and the cross-links are modeled as torsional springs, b) deformation after 50% tension c) deformation after 50% shear. Figure from [114].

prehensive overview of a possible explanation for our observations.
Specifically, the mechanical properties of skin could rely on mechanisms at three different scales:

1. Inside the fibres, at the scale of the fibril to fibril junction, viscoelastic proteoglycan bonds with a stochastic probability of breaking under stress could explain why the linear part remains linear while the orientation index increases continuously. This mechanism is based on experimental observations in tendon by Screen *et al.* [12] and Puxkandl *et al.* [35], and modelisation by Sens *et al.* [112].
2. At the scale of the collagenous network, a bending dominated elasticity as evidenced in collagen gels by Vader *et al.* [113] and modelled by Stein *et al.* [114], could explain simultaneously the non-linear Poisson effect, the non-linear stiffening and the J-shaped curve of the orientation index versus imposed strain curve.
3. Finally, what we could call "the extrafibrillar matrix", the ensemble of components other than fibrillar collagen type I, *e.g.* other collagens, elastin, water, outer proteoglycans, plays a role in the mechanical behaviour of the dermis. The collagen I fibres reorganisation in the tissue, and specifically the evolution of orientation histograms, indicates that the extrafibrillar matrix is necessarily a viscous material. The extrafibrillar matrix contains in particular cross-linking bonds that can detach and reattach. The extrafibrillar matrix contributes to the global mechanical behaviour, affects collagen fibre mobility, and has an impact on the sample's viscoelastic behaviour.

The three mechanisms proposed are summarised schematically in figure III.25.

In the context of the hypotheses detailed above we can attempt to interpret the cycling experiments carried out. In particular, we observe both elastic and non-elastic effects. The elastic effects could be linked to the initial elastic elongation of the proteoglycans. When unloading the skin sample, we could imagine that the fibril to fibril proteoglycan bonds are reformed in a less stressed state. However, it seems unprobable that this reattachment could be possible after a critical strain, when the fibres are permanently damaged. The partial recovery of the network's initial

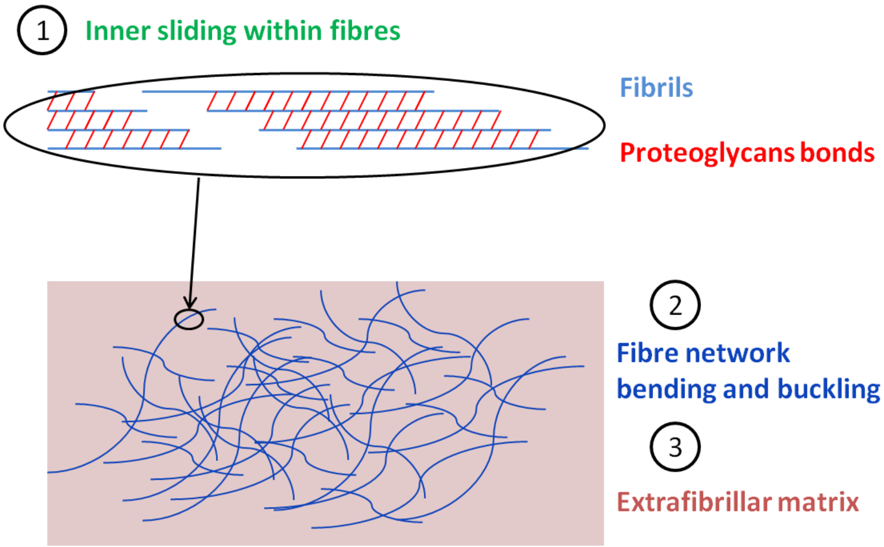

Figure III.25 – Schematic representation of the three microstructural mechanisms proposed for our interpretation: 1- at the scale of the fibre, sliding between fibrils connected by with proteoglycan bonds, 2- at the scale of the collagenous network, bending of reticulation points and fibre buckling, 3- the mechanical properties of the extrafibrillar matrix contribute to the general mechanical behaviour of skin.

organisation, based on reticular points and entanglements, similar to the mechanism described for polymerised collagen gels in [113], seems to be the most probable mechanism. Experiments with cyclic loadings under SHG observation are required to conclude on this mechanism.

The independence of the relaxation behaviour with regards to the stress reported earlier in this chapter suggests that the same components and mechanisms are involved at each step. The model described above attributes the relaxation to the proteoglycans, either between fibrils or in the extrafibrillar matrix. It is thus consistent with the experimental conclusions.

The identification of multiple characteristic relaxation times reveals that there are multiple scales, or mechanisms, involved. Screen and coworkers used the same method described before with stained cell nuclei and fluorescence microscopy to investigate precisely the relaxation behaviour in tendons [115]. This study showed that relaxation in tendons occurs predominantly through sliding between fibres, associated with some fibre reorganisation and fibrillar level relaxation.

Our interpretation of skin's microstructural behaviour includes three mechanisms implicated in the relaxation behaviour: the reorganisation of the network through fibre sliding and cross-linking bonds relaxing, an inner fibre relaxation *via* proteoglycans bonds relaxing and reattaching, and the viscous behaviour of the extrafibrillar matrix. Each of these mechanisms can incidentally be associated with more than one relaxation time.

Remarkably, the tentative model presented above is not transposable to tendons, as there is almost no fibre reorientation in tendon: in most tendons the fibres are aligned in the main direction from the start. Consequently the orientation index is the same throughout the test. The presence of a toe and heel regions in the stress/stretch curve for tendons is not compatible with the buckling and bending interpretation given above. The linear part of the stress/stretch curve in tendons corresponds to the elongation of collagen fibres, associated with important sliding between fibres and matrix deformation [12].

This could imply that despite the similarities in the basic components of soft collagenous tissues and in their stress/stretch behaviour, they actually have different microstructural responses to mechanical stimulation. In other words, knowing both the properties of the basic constitutive blocks and the microstructure could be insufficient to compute the mechanical properties of any given tissue through a common mechanism.

The careful analysis of our experimental results on WT mice skin showed that the underlying microstructural mechanisms cannot be accounted for with a simple model and that multiple mechanisms and scales are involved.

To test the plausibility of the hypothetical mechanisms we put forward, we conducted the same experiments on skin of mutant mice with alterations of the microstructural organisation of the dermis. These experiments are reviewed in the next chapter. Age also affects the structural properties of all of skin's components at the microscale. Experiments on aged mice skin have also been carried out, and will be reported in Chapter V.

Chapter IV

Biomechanics of mice skin with genetic mutations affecting the microstructure

The previous chapter described our investigation of skin's microstructural adaptation when subjected to strain. The results suggest that the usual interpretation of skin's non-linear elasticity, attributing the linear part to fibre elongation, is not verified. A simple model is not sufficient to explain all experimental features we observed. We presented possible microstructural mechanisms to account for our results.

To further investigate the multiscale biomechanics of skin, we carried out multiscale experiments on mice presenting a genetic modification affecting skin's microstructure. Two types of mutant mice were tested. Both strains were created in the context of studying a human condition affecting all collagen-rich tissues, Ehlers-Danlos Syndrome (EDS). Besides the relevance of this study from the medical and biological points of view, these mutations allowed us to explore the repercussions of modifying the dermis' microstructure from a fundamentally mechanical perspective.

The first part of this chapter introduces the pathology, its microstructural origin, and presents the two types of mutants we tested in this work. Then, for each mutant we review the multiscale results we obtained, and discuss them in the framework established in the previous chapter.

All data for young genetically-modified mice can be found in Appendix C, tables C.2 (mechanical data at slow strain rate), C.3 (mechanical data at higher strain rate), C.6 (local deformation at the microscale) and C.9 (collagen organisation).

IV.1 Ehlers-Danlos Syndrome

Ehlers-Danlos Syndrome (EDS) is a human genetic disease affecting all collagenous tissues. 90% of classical Ehlers-Danlos syndrome cases originate from a mutation on a gene coding for collagen type V, that results in a defective synthesis of collagen-rich tissues.

In this section, we first review the role played by collagen V in the dermis. Then we introduce the context of Ehlers-Danlos syndrome, from its microstructural origin to the pathology. Finally, we present the concepts behind the creation of the two genetically-modified mice strains used in this study.

IV.1.1 Role of collagen V in collagen I fibrillogenesis

Collagen V is a minor component of soft collagenous tissues, including skin. It is generally found co-distributed with collagen I and plays a major role in the fibrillogenesis of collagen I fibres.

Collagen V tropocollagen is a triple helix, in which each chain can be either of three amino acids chains: $\alpha_1(V)$, $\alpha_2(V)$, $\alpha_3(V)$, coded in humans by 3 genes, respectively COL5A1, COL5A2, COL5A3. There are several collagen V isoforms, among which three principal forms, summarised in figure IV.1 with their relative distribution and known functional properties.

Further information on the helical structure of collagen and different collagen types can be found in Chapter I.

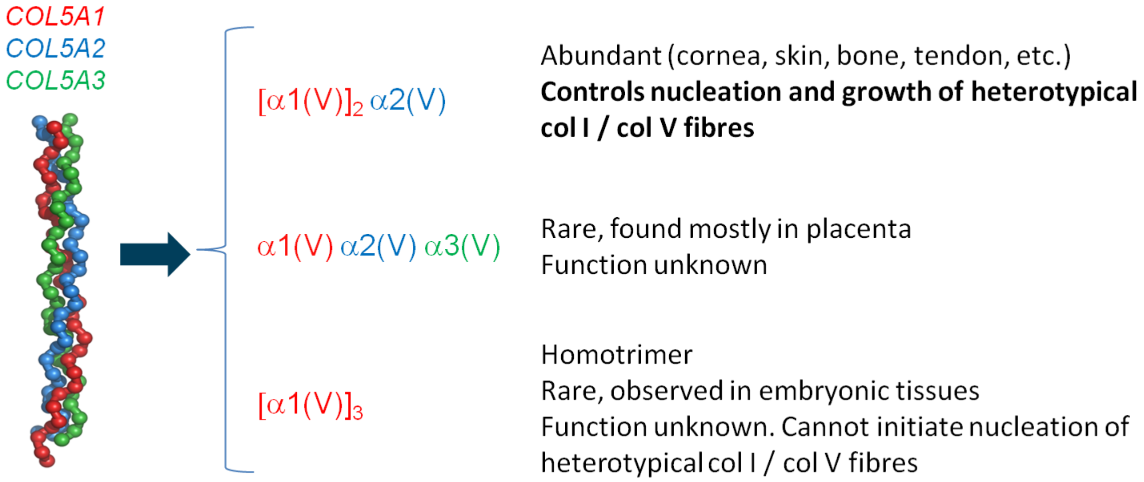

Figure IV.1 – The three principal forms of collagen V, their relative distribution and known functional properties.

The most common collagen V subtype is the heterotrimeric form $[\alpha_1(V)]_2\alpha_2(V)$. This subtype is present in most connective tissues, such as cornea, tendon, bone and skin. It interacts with collagen I to form what we call improperly collagen I fibres, which are actually heterotypical collagen I/III/V fibres in skin.

The $[\alpha_1(V)]_2\alpha_2(V)$ tropocollagen assumes a bended shape in 3D, as represented schematically in figure IV.2 a. It has been shown that this collagen V subtype controls the growth of collagen I fibres and in particular regulates their diameter [116, 117]. This fibre growth control process is summarised schematically in figure IV.2 b. The underlying mechanism is simply of steric nature:

the bended regions of the collagen V tropocollagens obstruct the fibre surroundings and prevent new collagen I subunits from aggregating. In tissues containing a high proportion of collagen V, such as the cornea, the collagen V tropocollagens block the radial growth of the collagen I fibres, which results in small fibres. On the other hand, in tissues low in collagen V, such as tendon, less steric effects are generated and the collagen I fibres can continue to grow in the radial direction: this results in large fibres. TEM cuts of tendon and cornea are shown for comparison in figure IV.2 c.

The other heterotrimeric form of collagen V, subtype $\alpha_1(V)\alpha_2(V)\alpha_3(V)$, is rare and mostly found in the placenta. Its functional significance is unknown. Similarly, the homotrimeric form of collagen V, subtype $[\alpha_1(V)]_3$, has been observed only in cell cultures and embryonic tissues in small quantities. Its role and interactions with other collagens are still unclear and have been little studied up to now [52].

The mutation responsible for 90% of classical Ehlers-Danlos syndrome cases affects one of the genes coding for collagen V (most of the time COL5A1, sometimes COL5A2, coding respectively for the α-chains $\alpha_1(V)$ and $\alpha_2(V)$). This mutation leads to structurally abnormal collagen V synthesis, which in turn results in abnormal collagen I fibrillogenesis. The microstructure of the collagen I fibres is pathologically altered.

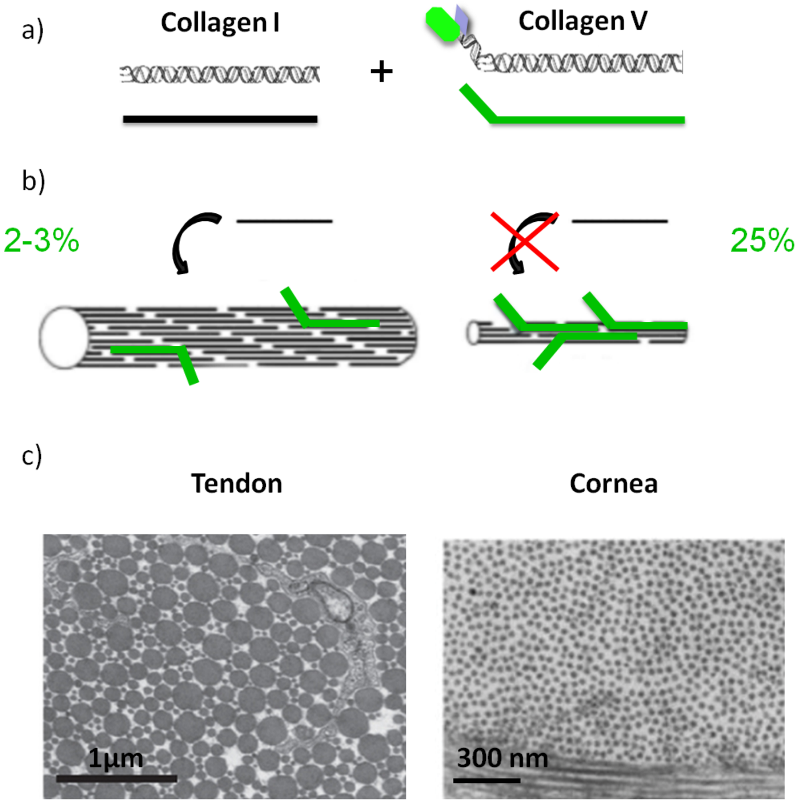

Figure IV.2 – Schematic representation of the role of normal heterotrimetric collagen V in collagen I fibre diameter regulation through steric effects: a) normal collagen V tropocollagen assumes a bended shape in space (not to scale), b) steric effects allow collagen V to control the growth of collagen I fibres in the radial direction, c) TEM cuts of tendon (image from [118]) and cornea (image from [13]). Tissues with a low proportion of collagen V such as tendons grow large collagen I fibres while tissues with more collagen V, such as cornea, grow thin collagen I fibres. Figure modified from [117] and [119].

IV.1.2 Microstructural modifications

Figure IV.3 shows a TEM image of skin biopsy from a patient with EDS, along with normal skin biopsy. Collagen I fibres can be seen cut in the radial direction.

Several changes attributable to the genetic mutation can be identified [52]:

- The fibre density is reduced.
- Some fibres, indicated by arrows in figure IV.3, show morphological irregularities. They do not have a regular round shape and are abnormally large in diameter. These fibres are called "cauliflower" fibres because of their irregular radial shape.
- Some fibres, as indicated by brackets in figure IV.3, fuse together.

Only about 5% of collagen I fibres are affected by microstructural abnormalities. Surprinsigly, these scarce modifications at the microscale lead to drastic modifications of the mechanical properties at the scale of the whole tissue.

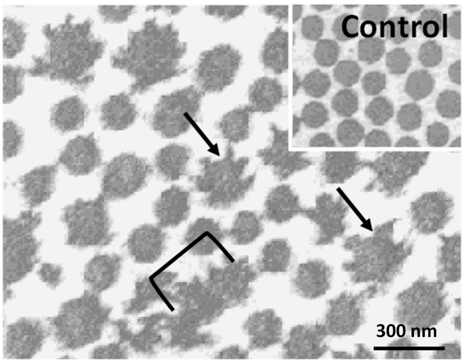

Figure IV.3 – TEM images of EDS suffering patient skin and control skin (inset). Skin affected by EDS shows a reduction in fibre density, larger fibres, structurally abnormal ("cauliflower") fibres (arrows) and fibres that are fused together (brackets). Image courtesy of F. Ruggiero.

IV.1.3 Ehlers-Danlos Syndrome

Ehlers-Danlos syndrome (EDS) is a genetic condition that can present various clinical symptoms. It is the third most common pathology of collagenous tissues. There is no cure to the pathology and the medical support has to be adapted to each patient's symptoms. Ehlers-Danlos syndrome patients suffer from very acute pain, particularly during crises that can extend from days to months.

The pathology has been classified in 6 different forms [120]:
- Hypermobile (1 person over 10 to 15 000).
- Classical form (1 person over 20 to 50 000).
- Vascular type (1 person over 100 to 250 000).
- Kyphoscoliosis (less than 60 cases reported).
- Arthrochalasia (approximately 30 cases reported).
- Dermatosparaxis (approximately 10 cases reported).

Only the classical form will be considered in this work. The generic symptoms for the classical form of EDS include:
- Thin, soft, hyperextensible and highly fragile skin.
- Joint hypermobility and frequent dislocations.
- Fragile blood vessels.
- Abnormal wound healing process and abnormal looking scars.
- Numerous and spontaneous hematomes, without deffective coagulation.
- Premature rupture of membranes in pregnant patients.

Figure IV.4 shows a dog affected by the canine equivalent of EDS with hyperextensible skin that can extend way beyond normal range.
Studies characterising specifically the mechanics of EDS affected tissues are fairly rare in the li-

Figure IV.4 – Dog affected by the canine equivalent of EDS presenting hyperextensible skin.

terature. This comes partly from the fact that it is difficult to get EDS affected tissue samples, especially large enough to perform mechanical experiments. Nielsen and coworkers [121] reported a lower tendon stiffness in patients with classical form of EDS than in patients affected from benign joint hypermobility syndrome. On the other hand, Sonesson and coworkers [122] could not demonstrate any alteration in wall mechanics as a sign of disturbed vessel wall integrity of elastic arteries in *in vivo* experiments on individuals with EDS.

This highlights the benefit of accurate murine models to reproduce the EDS pathology, as it is possible to have large statistical data sets on mice samples. The precise identification of the mechanisms involved in EDS in mice models is valuable to drive the experiments on humans, more difficult to implement, in the right direction. The work reported in this chapter falls in that general context. The objective is to clarify how the microstructural changes we reviewed can result in the altered mechanical behaviour observed. To study precisely the link between microstructure and mechanical properties two mice models were used.

IV.1.4 Mice models for the investigation of EDS

Two strains of genetically-modified mice were tested in this work: the peK strain and the pN strain. This section aims at presenting the general idea behind each model and mutation, and will leave the description of the impact of the mutation on microstructure and mechanical properties to the appropriate sections later in this chapter.

The pN mutant mice model (also called Col5a2pN/+) was the first to be created. It was designed by Andrikopoulos *et al.* [123] to replicate the physiopathology of EDS. The pN mutation consists in the removal of the DNA domain coding for the α_2(V) chain.
The production of the collagen V α_2(V) chain is no longer ensured. The normal heterotrimeric collagen V subtype $[\alpha_1(V)]_2\alpha_2(V)$ cannot be synthetised. To compensate, there is an upregulation in the production of $\alpha_1(V)$ chains, produced in excessive numbers. The supernumerary $\alpha_1(V)$ chains associate in triple helices to form the homotrimeric subtype of collagen V, $\alpha_1(V)_3$. This form does not associate with collagen I to form heterotypical fibres, for reasons that remain unclear, and

does not control the collagen I fibres growth [124]. The homotrimetric form of collagen V $[\alpha_1(V)]_3$ is secreted in the dermis, and the tropocollagens assemble into small, collagen V only, fibrils [124]. The homotrimeric collagen V fibrils are less than 10 nm in diameter.

The homozygous pN/pN phenotype is shown in figure IV.5. It presents similarities with the human EDS, specifically evidences of connective tissue disorder: spinal abnormalities (back hunching), locomotion trouble, substantial respiratory problems (major cause of premature death). Skin is fragile and more stretchable.

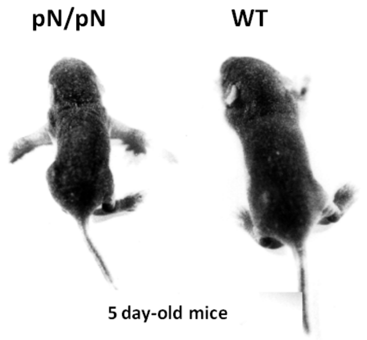

Figure IV.5 – 5-day-old homozygous pN/pN and WT mice [123].

Most homozygous pN/pN mice died within 5 days post-partum. Reproducing mice were thus always heterozygous pN/- mice. Statistically, in the same litter, 25% of mice are -/-, these mice don't have the mutation and are supposed to be exactly identical to normal mice of the same strain, 25% are homozygous pN/pN mice, which die rapidly, and 50% are pN/- mice.

Homozygous pN/pN mice were designed to reproduce the EDS pathological presentation. In particular, their skin presents the same macroscopic hyperextensibility: when pinched, their back skin elongates more than in control mice, and seems to take a longer time to return to normal configuration when let go [123]. Yet, as pN/pN mice die very quickly, the experiments have to be carried out on perinatal skin, which proved to be too small and fragile.

The experiments were carried out on one-month-old heterozygous pN/- mice, that have a life span close to normal. The heterozygous pN/- mice can not be differentiated from WT mice macroscopically, and neither can their skin once it has been dissected. As mechanical experiments were carried out at the same time as genetic characterisation (from a piece of ear taken from the mouse after sacrifice), the experiments were performed in complete double blind.

The other genetically-modified strain we used, historically the first tested, is called peK (or K14-COL5A1) strain. PeK mice were designed by our collaborators Florence Ruggiero and Christelle Bonod-Bidaud in the IGFL to study EDS [52]. They chose a different approach than the pN strain, which replicates the pathology. The idea is that in EDS patients the normal heterotypic form of collagen V is not produced: only the homotrimeric form is synthetised. Yet, we know very little of this collagen V isoform, its interaction with other components and possible functions. The idea behind the peK mice was to investigate the role of the homotrimetric collagen V by forcing the transgenic skin to overexpress that component.

For that purpose the human gene COL5A1, coding for the $\alpha_1(V)$ chain, was introduced into mice cells along with an epidermis-specific promoter (K14 promoter). The gene was then only expressed in the epidermis. Cells at the epidermis-dermis junction, that did not express collagen V at all before the mutation, did after the mutation. The overabundance of $\alpha_1(V)$ chains led to the formation at the epidermis-dermis junction of small collagen V fibrils made of homotrimeric collagen V, that diffused in the dermis and especially around hairs [52].
Figure IV.6 shows microscopic images of cross-sections of 5-day-old WT and peK mice skin, in which collagen V, both endogeneous and transgene-derived, has been stained brown using a specific antibody (the monoclonal 18G5 antibody). In both WT and peK mice the collagen V signal is weak and diffuse, but it is substantially more intense at the epidermis-dermis junction zone in peK mice, as shown in figure IV.6 b. A strong signal, undetectable in WT, can be seen in peK skin around hair follicles in figure IV.6, d.

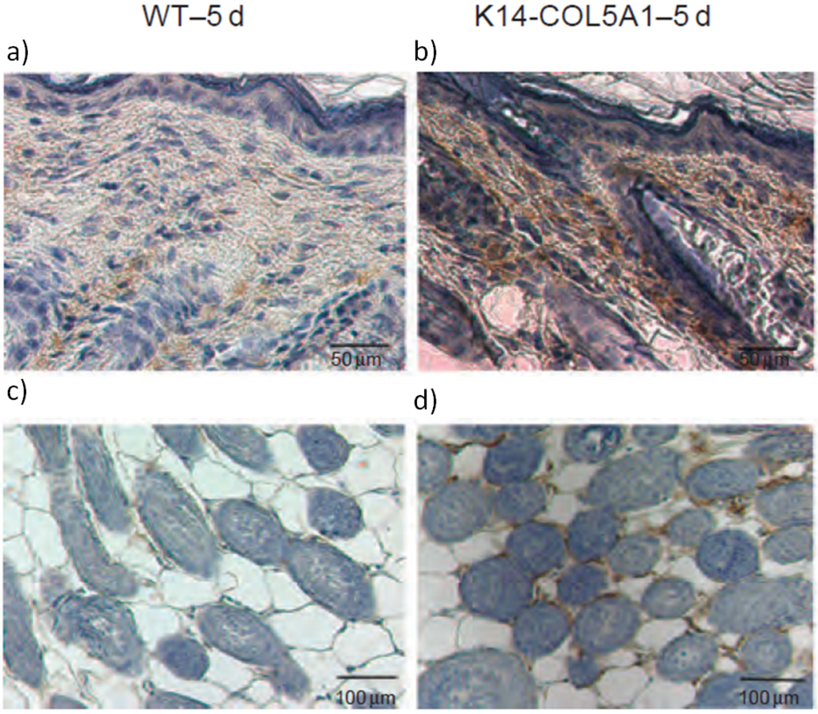

Figure IV.6 – Microscopic observation of cross-sections of 5-day-old WT (a, c) and peK (b, d) mice skin with collagen V stained in brown using a specific antibody (the monoclonal 18G5 antibody). The signal is more intense at the epidermis-dermis junction zone in transgenic skin (b). A strong signal, undetectable in WT, can be seen in mutants around hair follicles (d). Figure from [52].

The normal subtype of collagen V is also synthetised in the dermis, and the fibrillogenesis of collagen I fibres is thus supposed to be unaffected. The only alteration is the addition of small homotrimeric collagen V fibrils. In a peK litter, the mutation was successful in about half the mice, the non-mutant mice are normally similar to WT mice of the same strain.

The peK mice were not designed to reproduce the EDS physiopathology, but to decipher collagen V functions in skin. From a mechanical perspective it allowed us to study the influence of a simple microstructural change on skin mechanics.

Th peK mice are not strictly speaking mutant animals like pN mice (*i.e.* with a genetic change which may have occurred through natural environmental factors), but transgenic organisms.

It should be noted that, for both pN and peK strains, all litters have both mutant and non-mutant animals. Thus, we can compare the mutants with their control littermates. The genetic analysis of a piece of ear using PCR gave us the genotype of each individual.

Non-mutant animals theoretically have the same properties as control mice of the same strain. In this work, the "true" WT, the pN mice and the peK mice were from different genetic backgrounds. Nevertheless, all control mice, whether non-mutant or "true" WT , had statistically the same behaviour for the properties measured, as shown in Appendix B. They will all be regrouped as a single category, called WT, in the following sections.

The peK mutation is much simpler than the pN, because it affects less components of the dermis. Consequently, we will start by presenting the results of our multiscale experiments on peK mice in the following section, and will consider pN mice in section IV.3.

IV.2 peK mice: Results and Discussion

The transgenic peK mice were designed to elucidate the role of collagen V in skin, to eventually understand pathologies like EDS better. It involved a fairly simple change in skin microstructure: the synthesis of small collagen V fibrils at the epidermis-dermis junction, that diffused in the dermis. This chapter presents our results on how this simple modification affects skin's mechanical properties and microstructural behaviour, then discusses it in the context of the findings of the last chapter.

A total of 16 peK mutant mice were tested, including 9 with SHG imaging.

IV.2.1 Genetic mutation and microstructural changes

IV.2.1.a Literature review

Details on the microstructural characterisation of the peK (or K14-COL5A1) line can be found for fœtal (right before birth) and 5-day-old mice in [52]. A mechanical characterisation of one-month-old peK mice is also reported in this paper, and will be discussed in relation with our results later in this chapter.

PeK mice overexpress the human gene coding for the α_1(V) chain in the epidermal cell. The supernumerary collagen V subunits assemble in fibrils, made exclusively of homotrimeric collagen V. These fibrils are deposited as thin unstriated fibrillar material underneath the epidermal basement membrane, shown in TEM images of the dermis in figure IV.7. Accumulation of $[\alpha_1(V)]_3$ fibrils leads to ultrastructural modifications, mostly at the interface between the epidermis and the dermis, such as small lacunae. Collagen fibre density and organisation in the transgenic dermis appeared normal in histological cuts and TEM images [52].

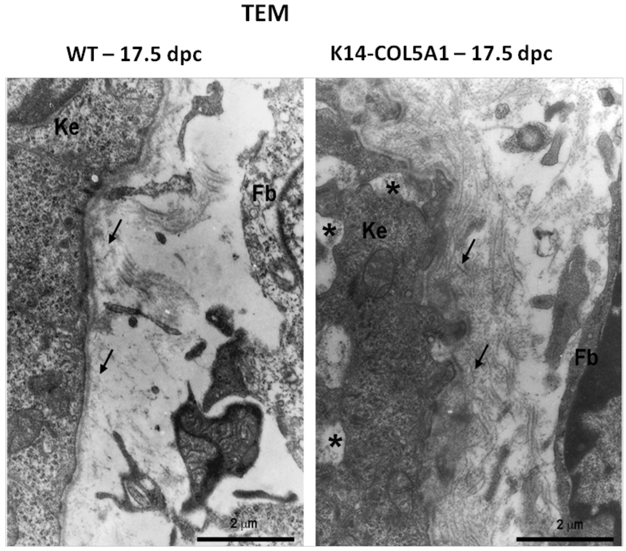

Figure IV.7 – TEM images of fœtal (17.5 days post coitum, gestation period in mice is 18-21 days) WT (left) and peK (right) mouse skin. Arrows show the accumulation of dense unstriated fibrillar material underneath the basement membrane in peK skin compared with WT. Asterisks indicate lacunae in the basal layer of the transgenic epidermis. Fb indicates fibroblasts, Ke keratinocytes. Scale bar is 2 μm. Figure reproduced from [52].

The characterisation reported in [52] pointed to three main differences between WT and peK:

- The number of hairs appeared significantly higher in transgenic mice.
- The number of junction proteins between epidermal cells and extracellular matrix of the dermis, called hemidesmosomes, was significantly higher in transgenic mice.
- The mechanical properties were not statistically different between transgenic and control mice. The authors noticed a tendency towards lower stiffness and rupture stress for transgenic mice.

The mechanical changes were interpreted in this study as a result of a higher stiffness of the epidermis-dermis junction in transgenic skin due to the higher number of hemidesmosomes, resulting in rupture at site of lower stiffness, *i.e.* the dermis.

The mechanical characterisation protocol the authors used differed from ours by a number of slight but significant changes. First, they kept all layers of skin while we removed the epidermis. The epidermis is a very thin layer compared to the dermis, and indentation experiments have demonstrated that it has a smaller elastic modulus than the dermis [125]. The removal of the epidermis is not expected to change skin's mechanical properties *per se*. Nevertheless, the absence of the epidermis deprives the skin from its natural hydration control, and, in this particular case, also removes the contribution of the increased number of hemidesmosomes between epidermal cells and dermal fibres.

The experiments were also performed at a strain rate higher than ours ($1.7.\ 10^{-3}\ s^{-1}$). Finally, the samples were immersed in saline solution, whereas we hydrated it from the outside, with either gel or water spraying, which does not induce sample overswelling. This has to be kept in mind when comparing the results from this study and the present work.

IV.2.1.b Measured characteristics

We found the thickness to be the same for peK and WT mice. The hair density *per* mm^2 and relative porosity, calculated when implementing the hair follicles displacements tracking, was equivalent for peK and WT mice. The corresponding histograms are shown in Appendix B.

The hair density was also measured in [52], but with different results: the hair density was found to be almost 20% higher in peK mice than in WT mice. The authors suggested that this demonstrated an unexpected role of the collagen V homotrimer in hair cycling. The hair density was however assessed with a completely different experimental protocol than the follicle detection on SHG images we followed (described in Chapter II).

First, the hair density evaluation was carried out on 5-day-old mice in [52], while we performed the experiments on one-month-old mice. Depilation was obtained through depilatory cream in both protocols, but we applied fresh cream 3 times and removed it every 6 minutes, while in [52] it was left on for 20 minutes. Finally, the hairs were counted manually with a stereomicroscope at low magnification on a random area approximately 500 μm per 500 μm in [52], on 7 peK and 4 WT mice, on 4 different areas for each sample. In our study, we detected automatically the hair follicles (a hair follicle can contain more than one hair), in a single area approximately 400 μm per 400 μm, chosen specifically to have enough hairs to be able to compute the local stretches. We assessed the hair density on 24 WT and 9 peK samples.

The difference in hair density between the two studies can probably be ascribed to these variations in protocol. In the present study we consider that the hair density is equivalent for peK and WT mice, and that consequently the differences in mechanical behaviour can not be attributed to variations in hair distribution.

In the next section we report the mechanical differences observed for transgenic peK mice. Then we review the differences observed at the microscale with SHG images analysis. Finally we evaluate the adequacy between the observed modifications and the model proposed for WT mice in the previous chapter.

IV.2.2 Mechanical behaviour under stretch

IV.2.2.a Stress/stretch behaviour

Qualitatively, the mechanical behaviour of genetically-modified peK skin was close to the control, reported in the previous chapter. The stress/stretch relationship followed a J-shaped curve with toe, heel, linear and rupture regions. In experiments under SHG observation, the sample relaxed when we stopped the motors for SHG imaging every 5%.
The local deformations were again homogeneous inside the ROI, both when measured at the microscale on SHG images and with DIC at the macroscale. At both scales, the measured local deformation in the direction of traction followed the imposed stretch closely, and the deformation in the direction perpendicular to traction also had an initial increase before the expected shrinking.

Differences in mechanical behaviour can be observed when examining the stress/stretch curves more closely. Figure IV.8 summarises the differences observed between WT and peK samples, for the four mechanical parameters described in Chapter II: tangent modulus, heel region length, maximum stress and maximum stretch ratio.

Significant differences could be observed between WT and peK mice. The skin appeared to be stiffer in genetically-modified mice: the tangent modulus, *i.e.* the slope of the linear part, increased by approximately 60%. The heel region was significantly longer for peK mice: it went from approximately 0.15 to 0.22. The maximum stretch ratio remained the same, around 1.4, while the maximum stress was higher for transgenic peK mice. Figure IV.9 summarises schematically the average mechanical behaviour of peK skin with regards to control skin.

IV.2.2.b Relaxation analysis

The short relaxations that occur every 5% strain when we stop the motors for SHG imaging were analysed for peK mice. As for WT mice, the relaxations could be fitted well with a biexponential curve with saturation. The relaxation analysis is summarised in figure IV.10 for the parameters described in Chapter II. The number of samples varied at each step, as the rupture stretch ratio changed sample to sample as did the heel region length. In figure IV.10 the data points were not plotted if the sample number was lower than 3. As the heel region was longer for peK mice than for WT, this means in particular that there is no data point for stretch ratios of 1.15 and 1.2.

The differences with the relaxation parameters from WT samples were not significant, but there seemed to be a tendency for the peK mice to relax less than WT mice for the same relaxation

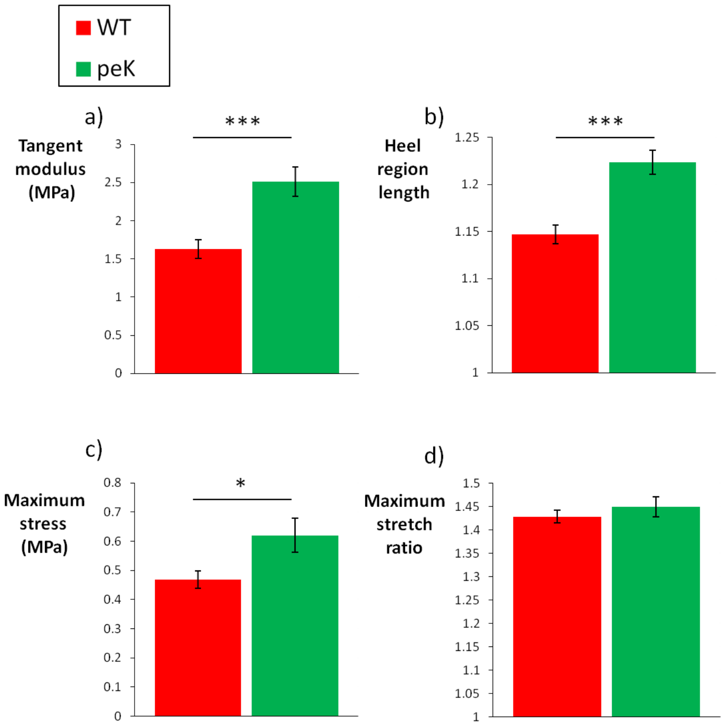

Figure IV.8 – Mechanical behaviour of peK mice compared to WT mice: a) Tangent modulus, b) Heel region length, c) Maximum stress, d) Maximum stretch ratio. Error bars represent the standard error of the mean. n=30 for WT mice, n=16 for peK mice. * indicates $p < 5\%$, ** indicates $p < 1\%$, *** indicates $p < 0.1\%$.

time. The amplitude of the constant s_0, shown in figure IV.10 c, was larger for peK mice, while the amplitude of short time relaxation a_1 remained constant and a_2, the amplitude of long time relaxation, was smaller for transgenic mice than for control mice. This tendency needs to be validated with a higher number of samples, but could mean that peK mice skin relax slower than control skin, as summarised schematically in figure IV.11.

IV.2.2.c Strain rate dependency

Experiments were carried out at a higher strain rate ($10^{-3}s^{-1}$) on 6 peK samples. The results on mechanical behaviour are shown in figure IV.12.

Similarly to WT mice, the tangent modulus increased with a higher strain rate, but the difference was not significant with the number of sample tested. The maximum stress also increased, significantly. Contrary to WT samples however, the heel region length remained completely unchanged, and the maximum stretch ratio increased.

Figure IV.13 summarises schematically the average mechanical behaviour of peK skin for the two strain rates considered.

The typical stress/stretch curve reported in [52] was recorded with a strain rate of 1.7. $10^{-3}s^{-1}$,

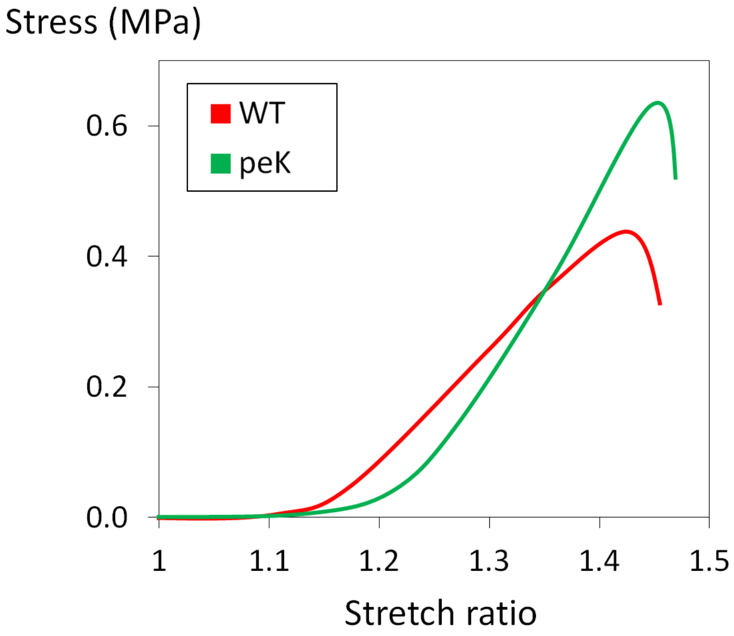

Figure IV.9 – Schematic representation of typical WT (red) and peK (green) stress/stretch curves.

comparable to what is considered the "faster" strain rate in the present study. The average tangent modulus of peK mice was reported at ≈ 0.6 MPa, the heel region length ≈ 1.35, maximum stress ≈ 0.16 MPa and maximum stretch ≈ 1.7, on a relatively low sample number (6 peK mice). The skin was found to be much more stretchable (both in heel region and overall) than in our study, but also a lot less stiff.

This disagreement between the two characterisations could be ascribed to the differences in experimental protocols reported earlier in this chapter (presence of the epidermis and hydration protocol, mainly). It is however unclear how these variations in protocol resulted in the observed differences in mechanical behaviour.

Notably, the WT mice used in [52] were also found to be less stiff and more extensible than the WT mice we tested with a strain rate of $10^{-3}s^{-1}$ (the tangent modulus was found to be ≈ 0.9 MPa, heel region length ≈ 1.35, maximum stress ≈ 0.22 MPa and maximum stretch ratio ≈ 1.7). This could be evidence that the variations in observed behaviour arise indeed from differences in evaluation protocols. The alteration of mechanical behaviour between WT and peK skin was not found to be statistically significant in [52].

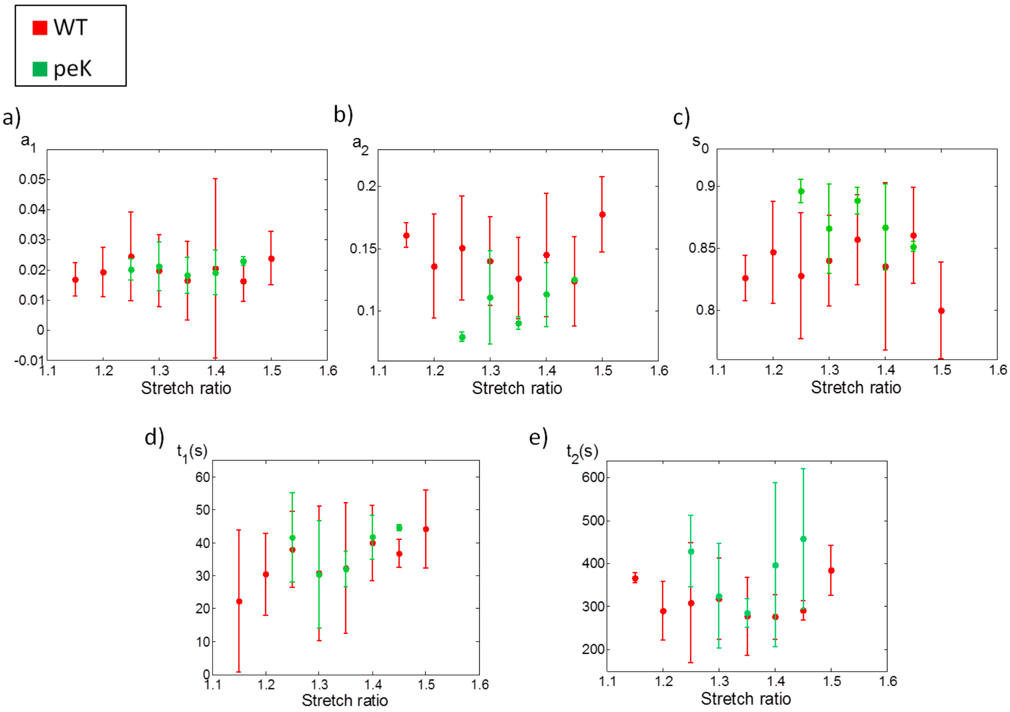

Figure IV.10 – Averaged values of the five parameters describing the relaxation behaviour of peK mice compared to WT mice: a) amplitude of short time relaxation a_1, b) amplitude of long time relaxation a_2, c) amplitude of the relative constant s_0, d) short time t_1 (s) and e) long time t_2 (s). Error bars represent the standard error of the mean.

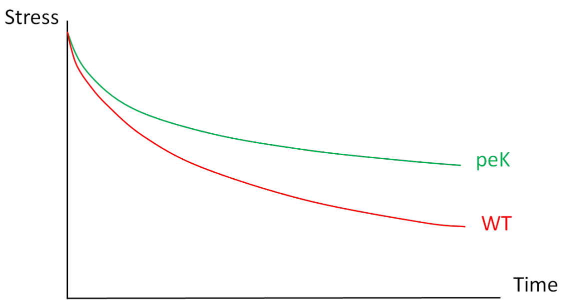

Figure IV.11 – Schematical comparison of the relaxation behaviour between peK and WT mice.

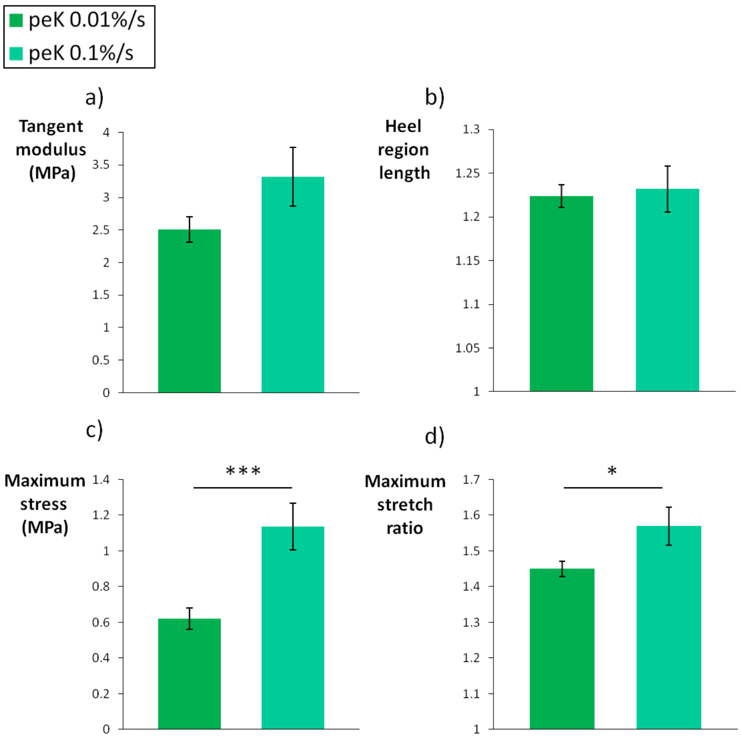

Figure IV.12 – Evolution with increasing strain rate of a) Tangent modulus, b) Heel region length, c) Maximum stress and d) Maximum stretch ratio for peK mice. Left corresponds to a strain rate of $10^{-4}s^{-1}$ (number of samples n = 16), right to $10^{-3}s^{-1}$ (n = 6). Error bars represent the standard error of the mean. * indicates $p < 5\%$, ** indicates $p < 1\%$, *** indicates $p < 0.1\%$.

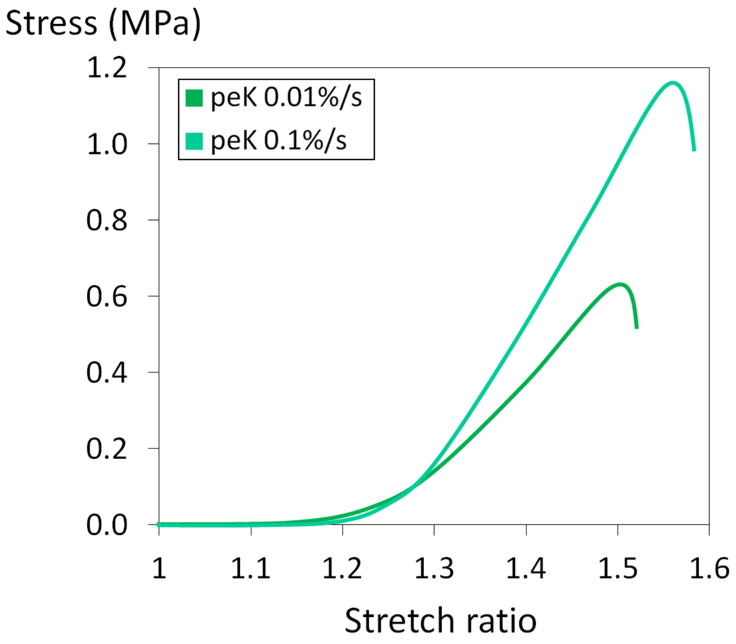

Figure IV.13 – Schematic representation of typical peK stress/stretch curve for a strain rate of $10^{-4}s^{-1}$ (green) and $10^{-3}s^{-1}$ (blue).

IV.2.3 Microstructural behaviour under stretch

In the same manner as mechanical behaviour, the microstructural observations for transgenic peK mice were qualitatively the same as for WT mice. The fibres oriented gradually in the direction of traction when the sample was stretched, while hair follicles became more and more elliptic. The initial distribution of fibres was still usually in two peaks, that evolved in a single peak distribution after the heel region, similarly to what was described for WT samples in Chapter III. Finally, the orientation index always followed exactly the stress curve.

Significant differences can be observed in the quantitative parameters used to assess microstructural behaviour. Figure IV.14 summarises the differences observed between WT and peK samples for three parameters, measured as described in Chapter II.

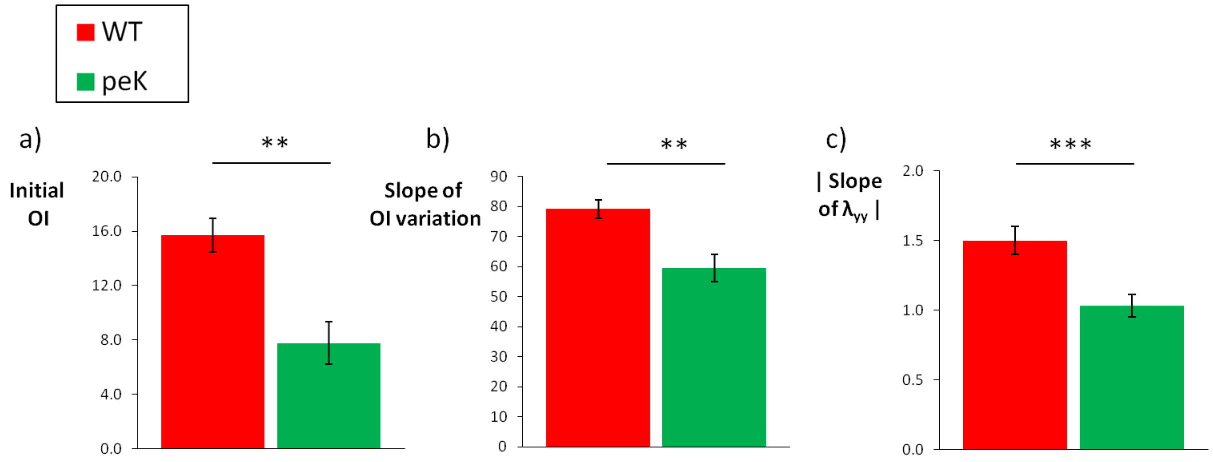

Figure IV.14 – Microstructural parameters derived from SHG images for peK and WT mice: a) initial orientation index, b) slope of the orientation index variation, c) absolute value of the slope of the final region of the λ_{yy} versus imposed stretch curve. Error bars represent the standard error of the mean. n=23 for WT mice, n=9 for peK mice. * indicates $p < 5\%$, ** indicates $p < 1\%$, *** indicates $p < 0.1\%$.

First, the initial orientation index, illustrating microstructural differences in rest state, is much smaller for genetically-modified peK mice. It should be noted that in any case the initial value does not correspond to an isotropic distribution, which is consistent with skin's natural anisotropy. The absolute value of the slope of the final region of λ_{yy} (local deformation in direction perpendicular to traction) versus imposed stretch curve is smaller for peK mice. The local contraction in the direction perpendicular to traction is slower for genetically-modified peK mice than for WT. Finally, the slope of the orientation index variation, expressing differences in adaptation to strain, is smaller for peK mice than for WT mice. When stretching the skin sample, fibres in peK mice reorganise less easily than fibres from WT skin. The heel region length is another indicator of how easily the fibres align in the direction of traction: consistently with OI variation, it was demonstrated to be longer for peK mice than for control skin.

IV.2.4 Interpretation

In this section, we discuss the multiscale results for transgenic peK mice in the context of the framework we developed in Chapter III. Three mechanisms were suggested to account for all features observed on WT mice:

1. Viscoelastic proteoglycans bond fibre subunits together and slide when the fibre is stretched. The fibres have a nearly perfectly plastic mechanical behaviour, with a stress plateau (named σ_f), after a short elastic period.
2. At the scale of the fibre network, the toe and heel regions are dominated by the bending of reticulation points and buckling of fibres perpendicular to the direction of traction. The linear region is dominated by the stretching of fibres aligned with the direction of traction.
3. Finally, the "extrafibrillar matrix", which encompasses anything that is not collagen I fibres (other collagens, elastin, water, proteoglycans, etc.) contributes to the mechanical response as a viscoelastic material.

The addition of small collagen V fibrils can intervene in each of these three mechanisms.

Notably, only the cells at the epidermis-dermis junction were modified to overexpress collagen V. The microscopic observations at 5 days in [52] confirmed a concentration of collagen V mostly at the epidermis-dermis junction, with a strong signal around hair follicles. In the one-month-old transgenic peK mice we tested, the collagen V fibrils had time to diffuse farther in the dermis from the epidermis-dermis junction, in particular around hairs.

The collagen V fibrils are very small in diameter (< 10 nm). It is possible that they are able to play a role at the scale of fibre inner sliding. Specifically, we would expect them to make the sliding more difficult, both by steric effect and by increasing local shears. The collagen I fibres could withstand the deformation more efficiently. This means that the plateau stress σ_f of each affected collagen I fibre would be higher than for control fibres. Yet, the collagen I fibre density was found to be normal in transgenic peK mice (as judged by histology and TEM in [52]). An increased mechanical contribution of each individual fibre would result in an increase of the stress in the whole tissue. This is consistent with the higher tangent modulus observed for peK mice.

At the scale of the extrafibrillar matrix, the presence of collagen V fibrils is expected to increase the viscosity, which could impede the fibres' movements. This could have several consequences. Following the timeline of a typical tensile test assay, the first one would be that the fibres perpendicular to the traction direction could resist buckling more easily. The collagen V fibrils would indeed act like props for collagen I fibres, and the bending would be slowed down. This could be an explanation for the lengthened heel region in transgenic mice.

Secondly, we know that the collagen I fibres align in the direction of traction during the linear region of the stress/stretch curve, causing the stress to rise. Yet, if the collagen I fibres movements are obstructed by collagen V fibrils, the realignement would be more difficult. This would lead to a decreased slope of the orientation index/stretch curve, as observed.
Finally, the increase in matrix viscosity in peK mice could prevent water from flowing out as easily as in WT dermis, which is crucial for volume conservation. This would explain the decreased slope of λ_{yy} versus strain final linear region: the peK mice dermis is less compressible than unaltered dermis.

The lower initial orientation index observed in genetically-modified peK mice could be related to the presence of collagen V homotrimeric fibrils during the dermis embryogenesis. We know that the collagen V fibrils are deposited near the epidermis and diffuse in the dermis in particular around hairs. Yet we observed a concentration of fibres oriented in the direction of the back around the edges of hairs in SHG images in rest state (see section III.1.3). The collagen V fibrils near the hairs could prevent the collagen I fibres from aligning in their normal preferred direction during embryogenesis. The mechanism for this phenomenon remains rather unclear.

The relaxation behaviour of peK mice was not found statistically different from WT mice with our sample number. There seem however to be a tendency for a slower relaxation in peK mice: less force is relaxed in a given amount of time than for control skin. In our interpretation, the relaxation is a combined effect of extrafibrillar matrix relaxation, cross-links reattaching in a less stressed state and fibre network rearranging thanks to reticulation and/or entanglements points. It is possible that the collagen V fibrils interfere with cross-links attachment and collagen I fibres reorganisation, thus slowing down the whole relaxation process.

Finally, the mechanical properties were affected in comparable ways for WT and peK mice when increasing the strain rate tenfold. It seemed however that the tangent modulus was not modified as much for peK mice as in controls, and this was also the case for the heel region length. It is possible that this is an effect of the collagen V fibrils hampering force transmission in peK mice. To conclude on the influence of strain rate on the mechanical properties of both control and transgenic mice, it would be valuable to carry out experiments at a third strain rate, for instance lower than $10^{-4}s^{-1}$ (which is not possible with our actuators) or higher than $10^{-3}s^{-1}$ (which causes hydration problems).

Overall, the peK dermis is similar to the control with one microstructural difference: the presence of small collagen V only fibrils in the extrafibrillar matrix, in particular at the epidermis-dermis junction, and possibly much deeper in the dermis through diffusion. We can see however that this very small change has drastic effects on the microstructural and mechanical properties of the mouse's dermis. This underlines the fact that every component of the dermis may be important,

independently of abundance, location in the scaffold, whether or not it interacts directly with cells, etc. Working out the functions and interplays of the many components of soft collagenous tissues proves to be a challenging task.
Our first instinct for peK mice was to think that, if the tissue followed a simple composite model, the slowed alignment of fibres, namely the smaller slope of OI variation, would likely result in a lower tangent modulus. This was not the case. The careful analysis of the peK multiscale biomechanics reinforces the idea developed in the previous chapter that a simple model is not sufficient to accurately describe the dermis.

The interpretation of skin's multiscale behaviour developed in the last chapter can be extended successfully to a simple modification of skin's microstructure. In particular, the hampering of fibre sub-units sliding by collagen V fibrils could explain the higher tangent modulus observed for peK mice. At a larger scale, the collagen V fibrils could also obstruct collagen I fibres movements and account for both the smaller variation of orientation index and the lengthened heel region in genetically-modified mice.
The following section reviews our results for the pN mice strain, which replicates a real life pathology: Ehlers-Danlos syndrome. We discuss the validity of the mechanisms suggested for a mutation both more complex and closer to an existing pathology.

IV.3 pN mice: Results and Discussion

The pN mutant mice strain was created by Andrikopoulos *et al.* [123]. The pN strain is believed to be a good murine model for reproducing the EDS pathology. For details on the biological characterisation, see [124].

This section presents our results on how a modification closer to an actual collagenous tissue disorder affects skin's mechanical properties and microstructural behaviour. As for the peK mice, these will then be discussed in the context of our interpretation of skin's multiscale mechanics.
A total of 18 pN mutant mice were tested, all of them with SHG imaging.

IV.3.1 Genetic modification and microstructural changes

IV.3.1.a Literature review

The pN mice belong to the group of knockout mice. Knockout mice are genetically modified mice in which an existing gene has been inactivated, or "knocked out", by replacing or disrupting it with an artifical piece of DNA.
In pN mice, there is a deletion of the gene coding for the $\alpha_2(V)$ chain, that is no longer synthetised. This results in the modifications of the physiological and biomechanical properties of several collagen-rich tissues with a relatively poor collagen V content, such as cornea, ligaments, bone,

blood vessels and skin [123, 124].

The targeted deletion affects the dermis matrix through a complex sequence of events [124]. The assembly/secretion of the heterotrimeric $[\alpha_1(V)]_2\alpha_2(V)$ is impaired, and thus the homotrimeric form $[\alpha_1(V)]_3$ is predominantly deposited in the matrix. The $[\alpha_1(V)]_3$ collagen is excluded from incorporating into heterotypical fibres formed with collagen I, for unclear reasons.
The mutant matrix stimulates an upregulation of the gene coding for the $\alpha_1(V)$ chain, which leads to further deposition of $[\alpha_1(V)]_3$. These assemble into small (diameter $<$ 10 nm) fibrils formed only by homotrimeric collagen V. The mutation is summarised schematically in figure IV.15.

In pN mice the small collagen V fibrils are deposited everywhere in the dermis by the cells that produce the dermal extracelullar matrix, the fibroblasts. This is a notable difference with previously characterised peK mice, where only the cells at the epidermis-dermis junction were modified to overexpress collagen V.

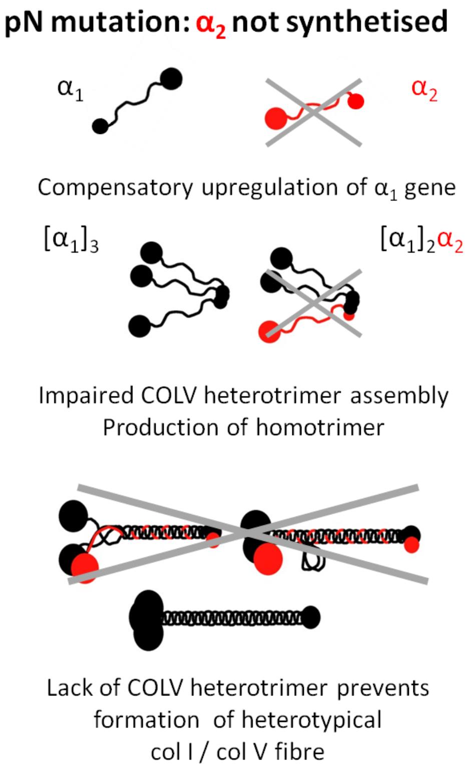

Figure IV.15 – Schematic representation of pN mutation mechanism: the deletion of the gene coding for the $\alpha_2(V)$ chain hinders the production of the normal heterotrimeric collagen V $[\alpha_1(V)]_2\alpha_2(V)$ and blocks the control of collagen I fibre growth by collagen V. The upregulation of $\alpha_1(V)$ chains leads to deposition of small homotrimeric $[\alpha_1(V)_3]$ fibrils. Image courtesy of F. Ruggiero.

The pN mutation is close to the EDS clinical presentation: the macroscopic phenotype of homozygous pN/pN mice shows similarities with the human EDS. Biomechanical experiments were carried out on a very small number of samples (3 pN/pN mutants) in [123], and showed that the pN/pN mice skin was more stretchable and failed under less stress than the WT.
Since most homozygous pN/pN mice died within 5 days post-partum, we used heterozygous pN/- mice for our experiments. Most EDS patient have a heterozygous mutation, and thus the mechanical properties from pN/- mice are expected to be different enough from WT mice to be observed, although not as remarkable as for homozygous mice. No characterisation on pN/- mice has been reported.

The microstructural changes in pN/pN mice have been characterised with TEM images, reproduced in figure IV.16 [124]. The microstucture of heterozygous pN/- was not characterised, but is expected to be somewhere between pN and WT.
The pN/pN mutation resulted in severe modifications of the matrix structure, including:

- a significant reduction in collagen I fibril density,
- collagen I fibrils abnormally small in diameter,
- degraded proteoglycans, assembling in dense aggregates in the matrix,
- disorganised matrix, with holes.

Further microstructural changes have been observed, such as reduction of the thickness of basement membranes underlying the epidermis and increased apoptosis (cell death) of stromal fibroblasts [124].

In pN mice, most components of the extracellular matrix of the dermis are affected, contrary to peK mice. In particular, the collagen I fibrils are altered, in a manner comparable to EDS skin: there are expected to be less densely packed and with probable structural defects. The fibrils were found to be smaller in pN/pN mice whereas large irregular fibres were observed in TEM images of EDS skin (figure IV.3). The extrafibrillar matrix is also modified, with degraded proteoglycans, holes, fragile cells and general disorganisation. Finally, small homotrimeric collagen V fibrils are deposited everywhere in the dermis.

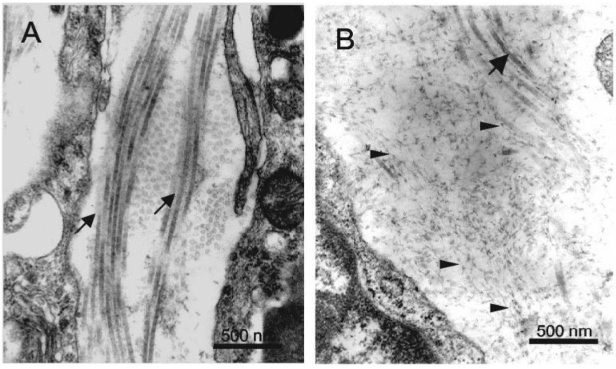

Figure IV.16 – TEM images of skin biopsy from WT (left) and pN/pN mutant (right). Bundles of banded collagen I fibrils can be seen in the wild-type (A, arrows), whereas only rare fibrils are observed in the mutant (B, arrow). The proteoglycans are disorganised in the mutant and form abnormal dense aggregates (B, arrowheads). Figure from [124].

IV.3.1.b Measured characteristics

We measured the thickness of the samples with a digital calliper before the tensile test, and it was found to be the same for pN mutants and WT. The relative porosity, computed when tracking the hair follicles displacements, was equivalent for mutants and controls. A statistical difference was found in hair density between pN and WT, with 20% less hair in pN mutants for the same surface. This should not impact the mechanical properties significantly as the relative porosity is the most important parameter for the mechanical behaviour of a porous material.
The histograms for thickness, hair density and relative porosity can be found in Appendix B.

In the next section we report the mechanical differences observed for pN mutant mice. Then we review the differences observed at the microscale with SHG images analysis. Finally we try to link the observed modifications and the model proposed for WT mice in Chapter III.

IV.3.2 Mechanical behaviour under stretch

IV.3.2.a Stress/stretch behaviour

The mechanical behaviour of pN mutant skin was qualitatively identical to the control, reported in Chapter III. The stress/stretch relationship followed a J-shaped curve with toe, heel, linear and rupture regions, with force relaxations when we stopped the motors every 5% strain in experiments under SHG observation.
The local stretches were homogeneous at the scale of the ROI in SHG images. The microscopic local deformation in the direction of traction followed the imposed macroscopic stretch closely, and the microscopic deformation in the direction perpendicular to traction also had an initial increase before shrinking. No experiment was performed at the macroscale only with DIC post-processing

for pN mutant mice.

Figure IV.17 summarises the mechanical behaviours of WT and pN samples, for the 4 parameters described in Chapter II: tangent modulus, heel region length, maximum stress and maximum stretch ratio. The parameters for peK mice are also plotted for comparison.

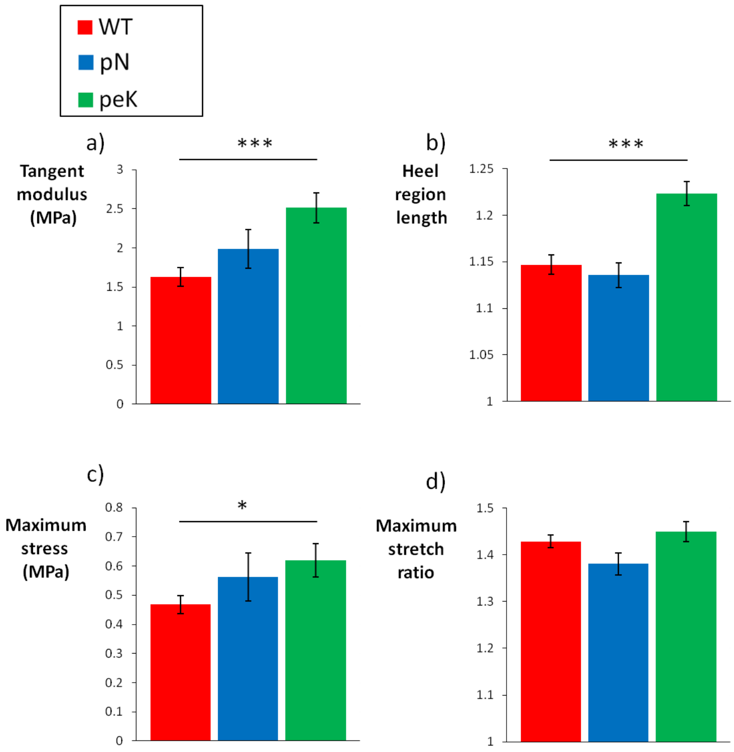

Figure IV.17 – Mechanical behaviour of pN mice (blue) compared to WT (red) and peK (green) mice: a) Tangent modulus, b) Heel region length, c) Maximum stress, d) Maximum stretch ratio. Error bars represent the standard error of the mean. n=30 for WT mice, n=16 for pN mice, n=16 for peK mice. * indicates $p < 5\%$, ** indicates $p < 1\%$, *** indicates $p < 0.1\%$.

As the pN mice are supposed to reproduce the phenotype from EDS, one could expect a smaller tangent modulus, longer heel region or higher rupture strain, possibly combined. This was however not observed. No statistically significant difference was found between WT and pN mice for the 4 mechanical parameters considered.

The mechanical behaviour of heterozygous pN/- skin was not characterised before in the literature. The homozygous pN/pN mice skin were tested with an extensiometry test in [123], with a very small sample number (3 mutant mice). The skin was found to break at a higher stretch but lower stress than control mice. The experimental protocol was not detailed and it is not clear whether the differences were statistically significant, which makes it difficult to compare with the results of the present study.

IV.3.2.b Relaxation analysis

The relaxation analysis is summarised in figure IV.18 for the 5 parameters described in Chapter II. Similarly to WT and peK mice, the number of samples varied at each step, as the rupture stretch ratio changed from sample to sample, as did the heel region length. In figure IV.18 the data points were not plotted if the sample number was lower than 3, and this is the reason why there is no data point at 1.45 and 1.5. The pN mice show a relaxation behaviour similar to WT mice.

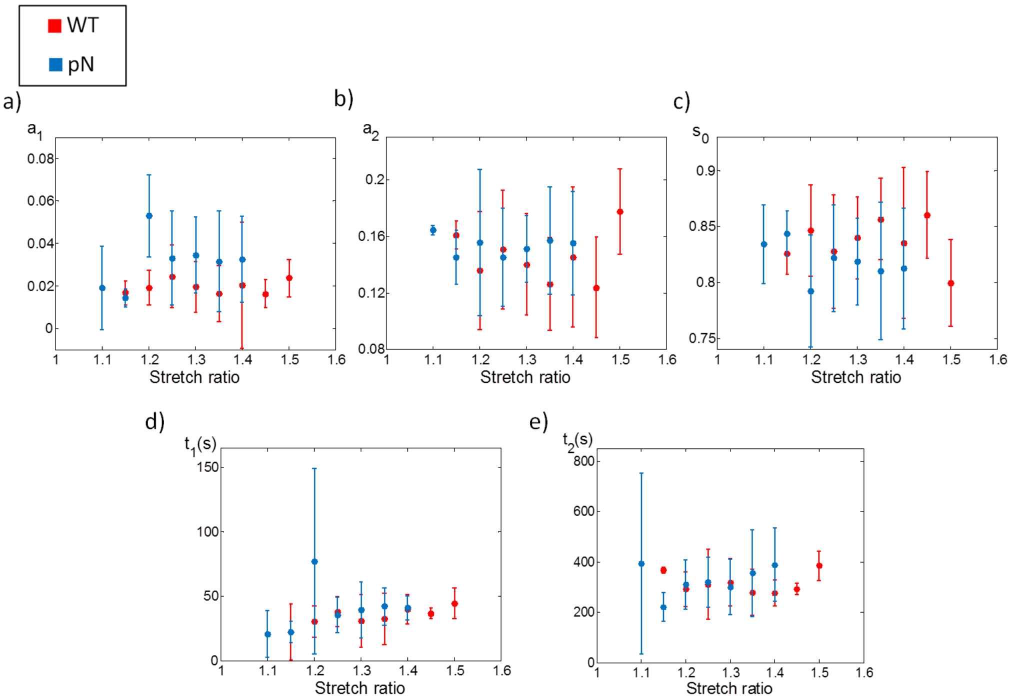

Figure IV.18 – Averaged values of the five parameters describing the relaxation behaviour of pN mice compared to WT mice: a) amplitude of short time relaxation a_1, b) amplitude of long time relaxation a_2, c) amplitude of the relative constant s_0, d) short time t_1 (s) and e) long time t_2 (s). Error bars represent the standard error of the mean.

From the macroscopic mechanical point of view, the pN mice are extremely similar to the WT mice. This is surprising, as they are supposed to model a pathology that severely affects skin mechanics, and as the changes in the dermis structural organisation are supposed to be deep and ubiquitous.

In section IV.3.4 we try to interpret the lack of mechanical differences between WT and pN mice in the light of the microstructural mechanisms proposed earlier.

IV.3.3 Microstructural behaviour under stretch

In the same manner as mechanical behaviour, the microstructural observations for pN mutant mice were qualitatively the same as for WT mice. The fibres oriented gradually in the direction of traction when the sample was stretched, while the hair follicles became more and more elliptic. The initial fibre distribution was usually in two peaks, that evolved in a single peak distribution after the heel region, similarly to what was described for WT samples in Chapter III. Finally, the orientation index always followed exactly the stress curve.

Figure IV.19 summarises the differences observed in the microstructural behaviour between WT and pN samples, with peK samples for comparison. The same three parameters as for peK mice are shown.

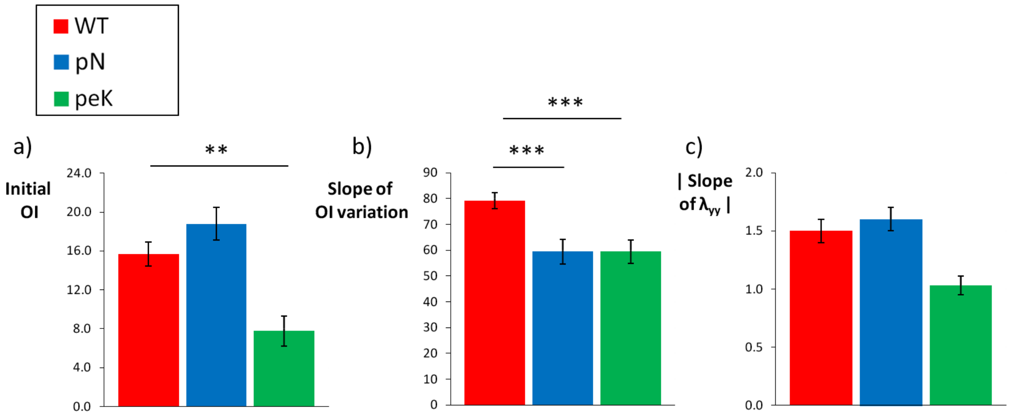

Figure IV.19 – Parameters derived from the SHG images for pN (blue) mutants versus WT (red) and peK (green) mice: a) initial orientation index, b) slope of the orientation index variation, c) absolute value of the slope of the final region of the λ_{yy} versus imposed strain curve. Error bars represent the standard error of the mean. n=23 for WT mice, n=18 for pN mice, n=9 for peK mice. * indicates $p < 5\%$, ** indicates $p < 1\%$, *** indicates $p < 0.1\%$.

The hair density was found earlier to be lower in pN mutant mice. Yet we reported in Chapter III our observation that the fibres organise differently around hairs in rest state: there is a concentration of fibres oriented in the direction of the back on the edges of hair shafts, which could change the initial distribution. The measured initial distribution of fibres in pN mice is however not statistically different from the control. The local contraction in the direction perpendicular to traction is also unchanged.

The only parameter for which a statistical difference can be found between pN and WT mice is the slope of the orientation index, a parameter illustrating how easily the fibres reorganise during the tensile test. As for peK mice, the fibres reorganise less easily in the genetically-modified mice than in controls. The value of the slope of the orientation index is remarkably similar between peK and pN mice.

IV.3.4 Interpretation

Except for the slope of the orientation index, the pN mice are statistically equivalent to the WT during a mechanical tensile test for the parameters considered. This result was verified with a significant number of pN samples (n = 18, all with SHG).

One could argue that this absence of difference is a consequence of the use of heterozygous pN/- mice, in which the mutation is expressed less drastically than in homozygous pN/pN mice. EDS patients however usually have a heterozygous mutation and strongly affected collagenous tissues. Another possible explanation would be the use of one-month-old mice: this is fairly early in the mice growth cycle. The mice are not yet fully grown at this stage and the pathology could grow in scale with age. In pN/pN mice however, the mutation can be seen very early on, from birth, and it seems unlikely that the mutation would not show at all in pN/- mice after one month.
In the end, the fact that the orientation index variation is strongly affected by the pN mutation proves that the mutation does develop in heterozygous pN/- mice at some level. In this section we try to see how the interpretation developed for WT mice in Chapter III and expanded to genetically-modified peK mice in the previous section can explain the absence of significant difference between pN and WT mice for all but one parameter measured.
In pN mutants, small homotrimeric collagen V fibrils are synthetised and deposited throughout the whole dermis. On the other hand the extrafibrillar matrix is disorganised and the proteoglycans are degraded. Those two phenomena have contradictory effects on the viscosity of the extracellular matrix. It is thus difficult to predict the outcome *a priori*.

Similarly to peK mice, the addition of small collagen V fibrils should slow down the sliding between sub-units within collagen I fibres. Hence it is possible that the contribution of each fibre to the general stress is greater in pN than in WT mice. Yet, TEM analysis of pN/pN mice skin revealed that the fibrils are smaller in diameter, and that the fibril density is considerably reduced with regards to the control (figure IV.16, [124]). This is probably also the case in pN/- mice to some extent, and these morphological characteristics lead to a decrease in skin's stiffness. These two effects seem to compensate each other to result in an unmodified tangent modulus.

In the same way, the addition of small collagen V fibrils should, as for peK mutants, impede the bending and buckling of fibres perpendicular to traction during the toe and heel regions. This would point to a longer heel region for pN mutants. However, as the extrafibrillar matrix is less dense and with degraded mechanical properties, and as the collagen I fibres are smaller in diameter, the bending and buckling are facilitated. This makes up for the hampering mentioned before, and results in an unchanged heel region length compared to WT.

All in all, as both the matrix density and viscosity are enhanced by small collagen V fibrils, but lessened at a larger scale by degraded proteoglycans and lack of organisation, the extrafibrillar matrix surrounding the collagen I fibres in the pN dermis seems to be globally equivalent to the control. The similarities in original distribution of fibres and behaviour in the direction perpendicular to traction, related to water flow through the matrix, supports that hypothesis. In that context it also seems logical that the relaxation behaviour is unmodified between WT and pN mice.

In the end the most surprising result for pN mice is the modification of the OI/stretch slope, related to how easily the collagen I fibres can migrate in the extrafibrillar matrix. The value of the OI variation in pN mice is affected in a very significant manner, as much as for peK mice. Yet, if the matrix is equivalent for WT and pN mice, as the other unchanged parameters suggest, it is difficult to see why the OI variation would change. The alteration of the OI slope indicates that the small collagen V fibrils are numerous and large enough to hinder the collagen I fibres mobility. The exact reason why this interference does not impact the heel region length or relaxation behaviour, two other indicators of microstructural reorganisation, is quite uncertain.

General conclusion

Overall, the interpretative model developed in Chapter III with 3 different mechanisms holds for genetically-modified mice with a mutation affecting skin's microstructural organisation. For a simple enough change, like the peK mice, the alteration of the parameters we measure can be correctly predicted in a qualitative way. A mutation mimicking a real pathology, such as the pN mutation, is more complex, with all components affected in different, sometimes contradictory, ways. Foreseeing the outcome proved to be much more difficult in this case and precise numerical modelling seems necessary to explain all experimental observations.

Similarly to EDS, age modifies all aspects of skin's microstructure. Multiscale experiments were also carried out on aged mice. We will review in the next chapter our results on the impact of age on skin's multiscale biomechanical properties.

Chapter V

Biomechanics of aged mice skin

In the same way as appearance, the mechanical properties of skin undergo drastic modifications with age. Age affects all layers of skin, but while changes in cells can be observed, the major functional alterations occur as a result of compositional and structural changes in the extracelullar matrix of the dermis. Other collagen and elastin-rich tissues, such as arteries and lungs, are affected in similar ways.

We performed multiscale experiments on skin samples from mice aged 15 and 19 months. This is a fairly advanced stage in the mice life, as their expected lifespan is less than 24 months.
The first experiments were performed on 19-month-old mice, but as they regularly died from old age before the experiments could be conducted we switched to 15-month-old mice. No correlation between age and multiscale properties was found between 15 and 19 months.

The first part of this chapter reviews the impact of age on human skin, especially structural and mechanical aspects. Similarly to the preceding chapter, we then report the multiscale results for aged mice and discuss how they relate to the model developed in Chapter III.

A total of 19 old WT mice were tested, including 14 with SHG imaging. 7 pN mice were tested, all with SHG. The age of each mice can be found in Appendix C, table C.11. All data for old mice, WT and pN, can be found in Appendix C, tables C.4 (mechanical data), C.7 (local deformation at the microscale) and C.10 (collagen organisation).

V.1 Effect of age on human skin

The effect of age on mice skin has been studied very little up to now. This section reviews studies on the effect of age on human skin, a topic which has been investigated rather extensively recently. We will suppose that the impact of age is the same on human and mice skin.

Ageing of skin results from both the passage of time (called intrinsic or chronological ageing) and from cumulative exposure to external factors, such as UV light and smoking (extrinsic ageing, also called photoageing in the case of UVs). Both intrisincally and extrinsically aged skin are affected in similar ways: they become wrinkled, stiffer and loose some ability to recoil. The severity of these changes, age of onset and rate of alteration are however exacerbated in extrinsically aged skin [126].
This is illustrated in figure V.1, which shows a man who has been driving a truck for 28 years with always the same side of his face facing the sun. The skin on his right side, not exposed, appears much younger than the skin on his left side, exposed to the sun radiations.
In this section we review the structural aspects of skin ageing, then describe the mechanical characterisation of aged skin reported in the literature.

Figure V.1 – Chronologically aged and photoaged skin: photo of a man who has been driving a truck for 28 years with always the same side facing the sun. The skin on his right side, not exposed, appears much younger than the skin on his left side, exposed to the sun radiations. Image from [127].

V.1.1 Structural changes

The most noticeable manifestation of age in skin is obviously the appearance of wrinkles. Aged skin also looks thinner and more fragile in appearance than young skin. These are the results of multiple structural changes in the dermis that inevitably occur with age.

All dermal proteins, collagen, elastin and proteoglycans alike, have a remarkably long lifespan compared to intracellular proteins [126]. For instance, fibrillar collagen I has a half life of 15 years and proteoglycans have a half life of 11 to 23 years, while intracellular proteins' half lives are measured in hours. Elastin on the other hand is predominantly synthetised during the foetal and early postnatal development, and the elastin stock acquired then is required to last a life time.
This extreme longevity means that the skin's proteins are likely to accumulate damage over the years and eventually become degraded. The damage can ensue from various events, such as glucose-

mediated cross-linking, calcium and lipid accumulation, time-dependent modification of acid residues, etc.

The structural changes in collagen, elastin and glycoaminoglycans are summarised in figure V.2 for both intrinsically and extrinsically aged skin, along with histological cuts. As a reminder, a proteoglycan consists of a core protein with one or more attached long-chain glycoaminoglycans. The microstructural damage induces a general disorganisation of the collagen network, as shown in figure V.2 on the far left panel, for both intrinsic and extrinsic ageing (collagen is stained red by picrosirius red).
The damage inflicted to the dermis by various phenomena also results in a general loss in collagen content. This is illustrated in figure V.3, which shows histological cuts of human skin from a young subject, below 30 years old, and an aged subject, over 80 years old [128]. The loss of global collagen content results in a thinned down dermis [129]. The fibroblasts synthetise less collagen in aged skin than in young skin. The mechanism behind this production loss is believed to be of mechanical origin. The fibroblasts are usually stimulated into collagen production by mechanical signalling from the dense fibrillar network. In ageing skin, as the network is scattered the cells are less stimulated and produce less collagen [128]. The fibroblasts environment in young and aged skin can be seen in insets in figure V.3.

Additionally to the loss of structural collagen fibres, there is a degradation of collagen VII fibrils that anchor the epidermis to the dermis and ensure the cohesion of the two layers.
Finally, the glucose mediated cross-linking results in more cross-links within and between collagen fibres. This phenomenon is particularly pronounced in photoaged skin.

In young skin, the elastic fibre network, composed mainly of two types of proteins (elastin and fibrillin) is believed to adopt a characteristic highly ordered architecture. Fibrillin-rich microfibrils are oriented perpendicularly to the epidermis-dermis junction in the papillary dermis, while elastin fibres lay parallel to the surface in the reticular dermis [126]. This is illustrated schematically in the central panel of figure V.2, middle picture, along with an histological cut of young dermis coloured with Miller's elastin stain, that colours elastin purple and collagen red.
Similarly to collagen, elastin is degraded in aged skin. The fibrils become smaller and the debris accumulate in disorganised aggregates. This is also shown in figure V.2 for intrinsic and extrinsic ageing in the central panel, top and bottom pictures.

Finally, the proteoglycans show drastic age-related changes: they are replaced by smaller proteoglycans, more loosely arranged [130]. Yet, the cross-linked network of proteoglycans usually acts like superabsorbent polymers in a water gel: it swells and traps water. With smaller and less organised proteoglycans, one of the most crucial function of the dermis is impaired: the ability to retain water. This is held as one of the main reason for the "deflated" aspect of aged skin, as opposed to the plump and full impression that a young face gives. In figure V.2, far right panel, the dermis cuts are stained with periodic acid stain, that colours in particular proteoglycans pink.

The epidermis is also modified in aged skin. The outermost layer of dead cells, the stratum-corneum, becomes thicker. The epidermis on the other hand thins down. The finger-like projections at the epidermis-dermis junction get smoothed down [131]. Brown spots often appear on sun-exposed skin, particularly on the hands and face, as pigmentation gets defective.
Finally, changes in subcutaneous tissues are also responsible for giving an ageing face its characteristic features. This includes reduction of the underlying lipidic tissues and facial bone loss, that deprive the skin from underlying support.

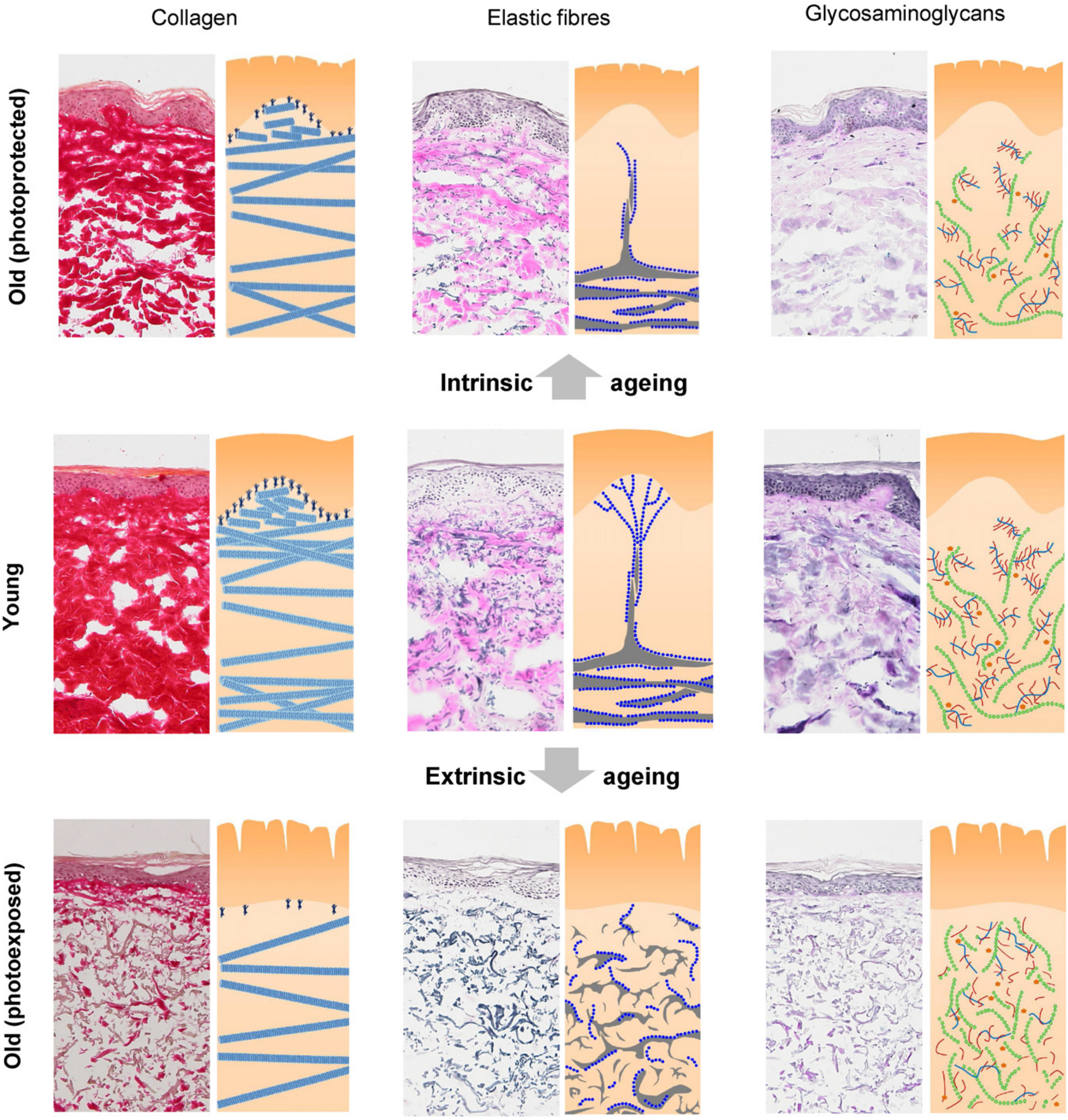

Figure V.2 – Dermal collagen, elastic fibres and glycoaminoglycans in young (middle), intrinsically aged (top) and extrinsically aged (bottom) skin. Histological cuts on human skin (stained respectively with picrosirius red, Miller's elastin and periodic acid) and schematical representation. All proteins appear less dense and less structured with age. The changes are dramatically exacerbated in extrinsically aged skin compared to intrinsically aged skin. Image from [126].

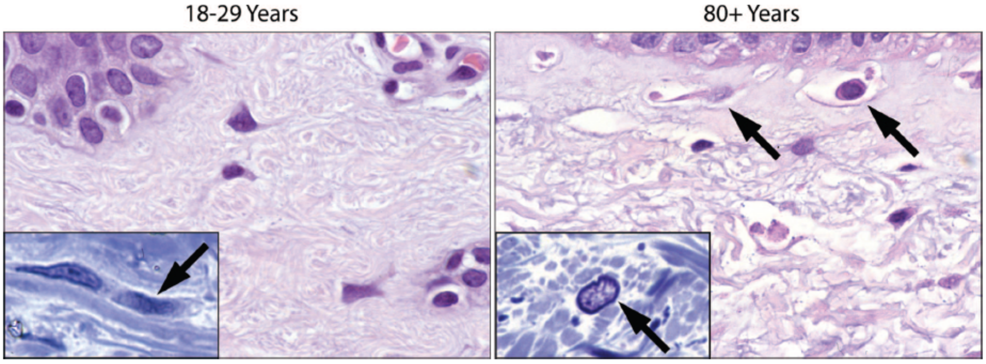

Figure V.3 – Histological cuts of sun-protected skin from young and old individuals, stained with hematoxylin and eosin. The collagen fibres are organised in thick bundles in young skin, whereas in aged skin only thin disorganised fibres can be observed. Insets: histological cuts focusing on fibroblasts, stained with toluidine blue. The fibroblasts are oriented in the same direction as the fibre bundles in young skin, whereas in aged skin they are surrounded by open space and no orientation can be seen. This is believed to be the reason for the fibroblasts' decreased collagen production in aged skin. Image from [128].

V.1.2 Mechanical changes

From a macroscopic point of view, the age-induced alteration of skin's mechanical properties are rather obvious. Besides from wrinkles, the skin looks thinner, softer, more fragile. It is less extensible when pinched between two fingers, and maintains a deformed shape much longer. Aged skin is often compared to cigarette paper.

Most experimental studies on the age-related changes in the mechanical properties of skin have been carried out *in vivo* on human skin, using torsion or suction devices [104, 105, 107, 129]. *Ex vivo* experiments up to rupture are practically nonexistent [105].
Most authors observed that skin's Young's modulus increased with age, especially after puberty. This is illustrated in figure V.4, which shows the evolution of skin's Young's modulus with age [129]. A factor 2 can be observed between young and aged skin, in agreement with other studies [104].

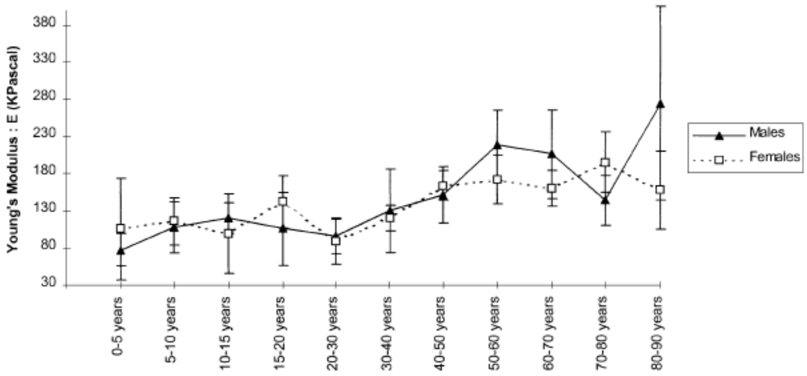

Figure V.4 – Evolution of human skin's Young's Modulus as a function of age for males and females, as measured with *in vivo* suction experiments. The skin's stiffness increases steadily after puberty. No differences were found between male and female skin. Figure from [129].

The retention of an imposed deformed shape is associated with an impaired recovery ability. This property has been investigated quite early on with *in vivo* torsion experiments on aged human skin, for instance by Escoffier and coworkers in 1989 [107]. When they applied a torque on the skin, they observed an immediate deformation (UE) followed by a slower one. When the torque was removed, the skin returned to a point almost at its initial position, recovering a part (UR) of its initial deformation (UE), and thereafter very slowly returning to its original state. The ratio UR/UE represents the ability of skin to recover from a deformation. Figure V.5 shows the evolution with age of this ratio [107]. The constant decrease of this parameter illustrates that ageing skin recovers less and less easily from an initial deformation. Notably, this parameter depends little on the deformation applied (high or low torque), which is close to our results on young WT mice skin regarding the independence of the relaxation parameters to applied stress.

Using different parameters to characterise this property, several studies highlighted an increase in the non-elastic behaviour of skin with age [107, 129].

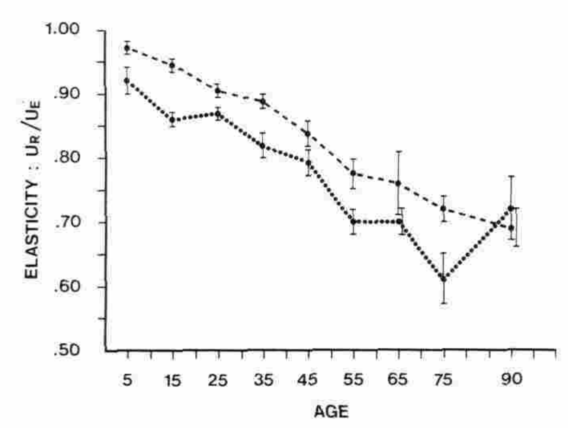

Figure V.5 – Evolution with age of the ratio of immediate recovered deformation (UR) over initial imposed deformation (UE), as measured with *in vivo* torsion experiments on human skin with a high (dashed line) and low (dotted line) torque. The ability to recover from deformation is impaired in aged skin. Figure from [107].

Daly and coworkers reported from *ex vivo* uniaxial tensile tests on human skin that the initial deformation for which stress could be measured was shorter for aged skin than for young skin [105]. This is illustrated in figure V.6. They attributed this result to the gradual fragmentation of the elastin network in the dermis with age. The linear region of the curve was found to be similar in young and aged skin, as well as rupture strain and stress.
The authors also noticed that aged skin deformed much more under its own weight than young skin, and attributed this observation to the progressive relieve of skin's pretension *in vivo* with age, resulting in the formation of wrinkles. Skin was also observed to be less tense in its natural environment in other *in vivo* studies [129].

The increased stiffness and loss in ability to recoil are the two main age-induced modifications in skin's mechanical behaviour reported in the literature. Additionally, the modifications of skin's mechanical properties with age were found to be uncorrelated with gender in all studies consulted. Due to a lack of appropriate micro-mechanical experiments on aged skin, the link between microstructural and mechanical changes are often inferred rather than experimentally demonstrated [126].

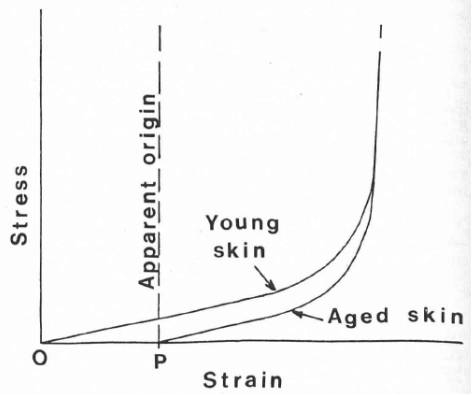

Figure V.6 – Effect of age on the mechanical response of young and aged human skin, measured with *ex vivo* uniaxial tests. The linear region of the curve was found to be similar in young and aged skin, as well as rupture strain and stress. The initial deformation for which stress could be measured was shorter for aged skin than for young skin. Figure from [105].

V.2 Aged mice: Results

We performed multiscale experiments on skin samples from mice aged 15 and 19 months, at a fairly advanced stage in their life expectancy.
In this section we report the changes observed in old mice skin compared to young mice skin at the microstructural and mechanical levels, and then discuss the extension of the model developed in Chapter III to these results.

A total of 19 old WT mice were tested, including 14 with SHG imaging. 7 pN mice were tested, all with SHG. These mice were either 15 or 19 months old. The age of each mouse can be found in Appendix C. No correlation between age and mechanical or microstructural properties was found between 15 and 19 months.

V.2.1 Tissue morphology changes

The figures for thickness, hair density and relative porosity for aged WT mice and aged pN mice can be found in Appendix B.
The loss in collagen content in aged skin was reported to result in a thinned down dermis [129]. This was verified for the aged mice skin we tested. The average thickness for all old mice was 0.8 mm ± 0.03, while it was 1.0 mm ± 0.03 for young mice. We observed no difference between control and mutant old mice in terms of thickness for the number of samples tested.
However, because of protein degradation, the thinning down of the tissue is not correlated with a higher density. Holes in the extracellular matrix have even been observed in human skin [126, 128]. Consistently, we did not observe a decrease in the tissue thickness available to SHG imaging.
Since the dermis got thinner and the imaging continued to go as deep as before, the proportion of

dermis imaged with SHG in old mice was larger than in young mice. Specifically, in young mice, we imaged the papillary dermis and the upper part of the reticular dermis, while in old mice we observed the papillary dermis and a bigger proportion of the reticular dermis. As the structural properties of the papillary and reticular dermis are known to be different, this has to be kept in mind when comparing the microstructural results from young and old mice.

The hair density and relative porosity was modified with age. This is logical as the number of hair shafts remains roughly the same from birth to death, while the global skin surface of the mouse increases with age. Consequently, the hairs get larger in diameter. Yet, the field of view we measured with the SHG microscope remained the same, *i.e.* 400 × 400 μm: we imaged a smaller proportion of the mouse's global skin surface.

These two phenomena combined resulted in a lower measured hair density, computed from hair shafts counting at the scale of the region imaged. The mean number of hair *per* mm^2 was found to be 35% lower in old WT compared to young WT and 20% lower between old pN and young pN. A modified hair shafts network distribution could have an effect on the original fibre distribution measured.

The relative porosity however was remarkably similar between young and old, whether we considered the WT or the pN. This means that the hair shafts and the rest of the dermis grew at similar rates. Since the relative porosity did not change, modifications of mechanical properties can not be attributed to the hair distribution.

As the observed region remained the same size, but the components observed got bigger, it is possible that the microscale Region Of Interest (ROI) no longer was a representative elementary volume.

V.2.2 Mechanical behaviour under stretch

V.2.2.a Stress/stretch behaviour

Qualitatively, the mechanical behaviour of aged mice skin was close to the response of young mice, reported in Chapter III. The stress/stretch relationship followed a J-shaped curve with toe, heel, linear and rupture regions. In experiments under SHG observation, the sample relaxed when we stopped the motors for SHG imaging every 5% strain.

Due to the decreased number of hair on the ROI, the local stretches could not always be computed on SHG images. When they could be computed, there were again homogeneous inside the ROI. This was also the case for the 4 aged WT skin samples tested outside the SHG microscope when analysing the images with DIC. At both scales, the measured local deformation in the direction of traction followed the imposed stretch closely, and the deformation in the direction perpendicular to traction also had an initial increase before the expected shrinking.

Figure V.7 summarises the differences observed in mechanical behaviour between young and old

WT and pN samples, for the 4 parameters described in Chapter II: tangent modulus, heel region length, maximum stress and maximum stretch ratio. The 4 parameters considered evolved with age in similar ways for WT and pN mice. However the differences were not always statistically significant for pN mice because of insufficient sample number.
Figure V.8 summarises schematically the average mechanical behaviour of old WT skin with regards to young WT skin.

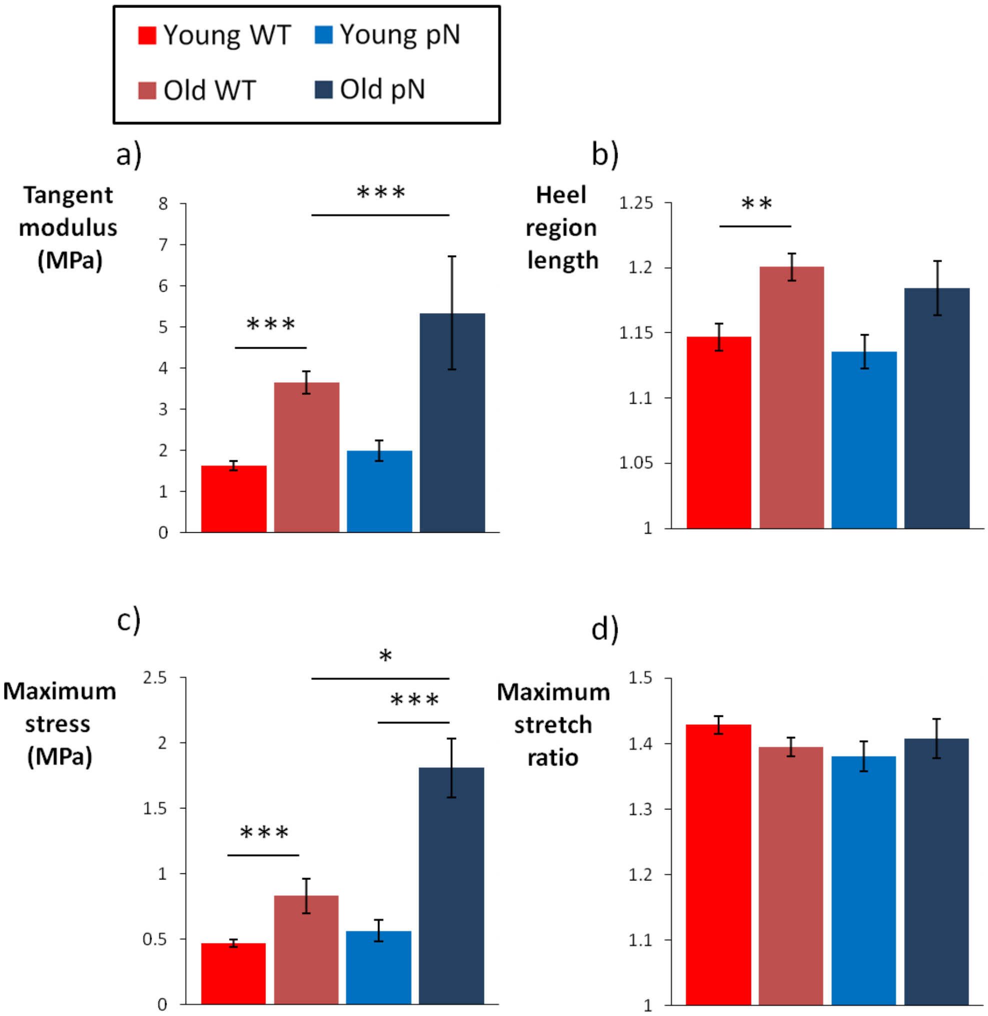

Figure V.7 – Mechanical behaviour of young and old WT and pN mice: a) Tangent modulus, b) Heel region length, c) Maximum stress, d) Maximum stretch ratio. Error bars represent the standard error of the mean. n=30 for young WT mice, n=19 for old WT mice, n=16 for young pN mice, n=7 for old pN mice. * indicates $p < 5\%$, ** indicates $p < 1\%$, *** indicates $p < 0.1\%$.

As expected from the literature review, the tangent modulus increased considerably with age: it was twice as big in old mice than in young mice. This result is quantitatively close to others studies [104, 129]. The skin stiffening was particularly statistically significant for WT mice, and a similar tendency can be observed in pN mice.
Additionally, the tangent modulus was significantly bigger for old pN than for old WT mice. Age

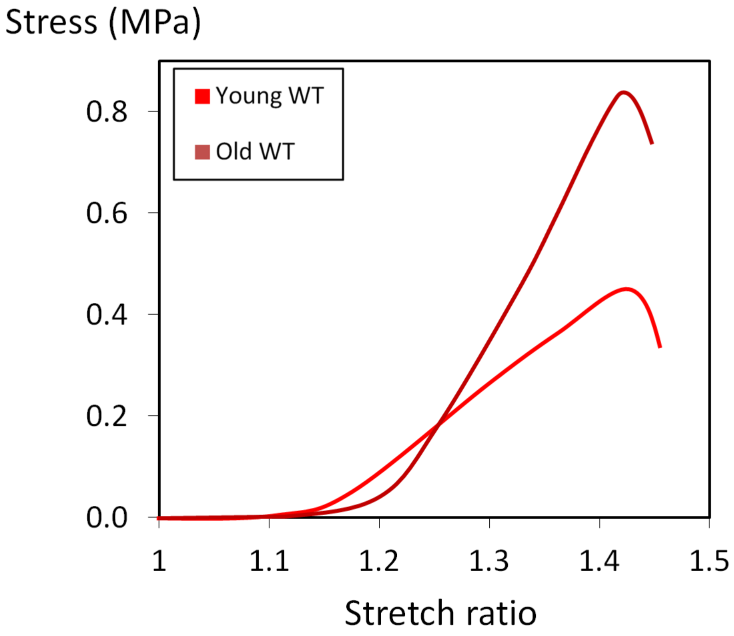

Figure V.8 – Schematic representation of typical young (red) and old (dark red) WT stress/stretch curves.

seems to reveal a difference between WT and pN that we were not able to see at one month.

The heel region was significantly longer for aged WT skin than for young WT skin. The same tendency could be observed for pN mice. This result is not consistent with the observation of Daly and coworkers [105]. This could be attributed to differences in experimental protocol. Even if no strain rate was specified in [105], it is unlikely that the authors used a strain rate much slower than ours, technically difficult to obtain. Yet, we observed in Chapter III that a higher strain rate resulted in a longer heel region in young mice. Another possibility is actual microstructural variations between human and mouse skin: in [105] the authors attributed the shortening of the heel region to the gradual framentation of the elastin network, yet we did not observe elastin fibrils in mice skin, neither young nor old. It is possible that this microstructural difference results here in a difference in macroscopic mechanical behaviour.
The heel region length was similar in old WT and old pN mice, as it was for young mice of the same strains.

The maximum stretch ratio remained unchanged in old mice with regards to young mice, both for WT and pN mice: the averaged maximum strain was still 1.4. This is surprising as our first intuition would have been to expect old skin to be less extensible than young skin. The maximum stress increased considerably between young and old mice of the same type, and it was significantly bigger for old pN mice with regards to old WT.

V.2.2.b Relaxation analysis

Figure V.9 shows the evolution of the relaxation behaviour for old WT for the 5 parameters described in Chapter II. Figure V.10 shows the same parameters for the old pN mice.
We observed a tendency, especially visible when comparing old and young WT mice, for the skin to relax more and more efficiently with increasing stretch, as the relative constant for the relaxation s_0 got smaller through the test. The characteristic relaxation times also seemed to become larger with increasing stretch. Only relaxations in the linear part of the stress/stretch curve were fitted: the number of samples varies at each step, but is higher than 3 for every point plotted.

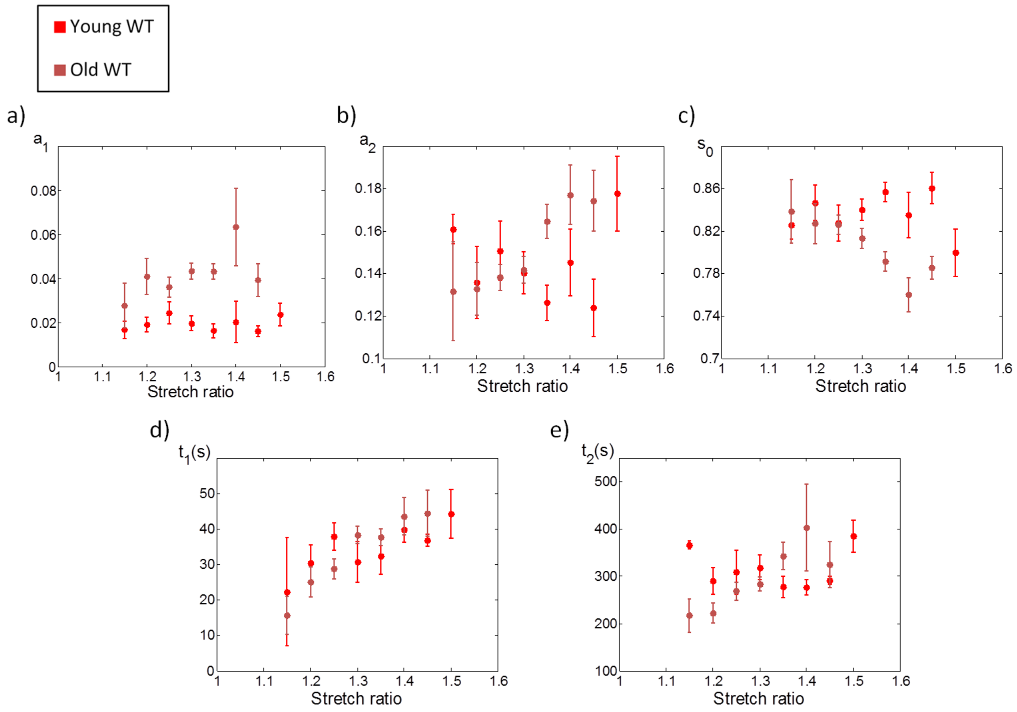

Figure V.9 – Averaged values of the five parameters describing the relaxation behaviour of old WT mice compared to young WT mice: a) amplitude of short time relaxation a_1, b) amplitude of long time relaxation a_2, c) amplitude of the relative constant s_0, d) short time t_1 (s) and e) long time t_2 (s). Error bars represent the standard error of the mean.

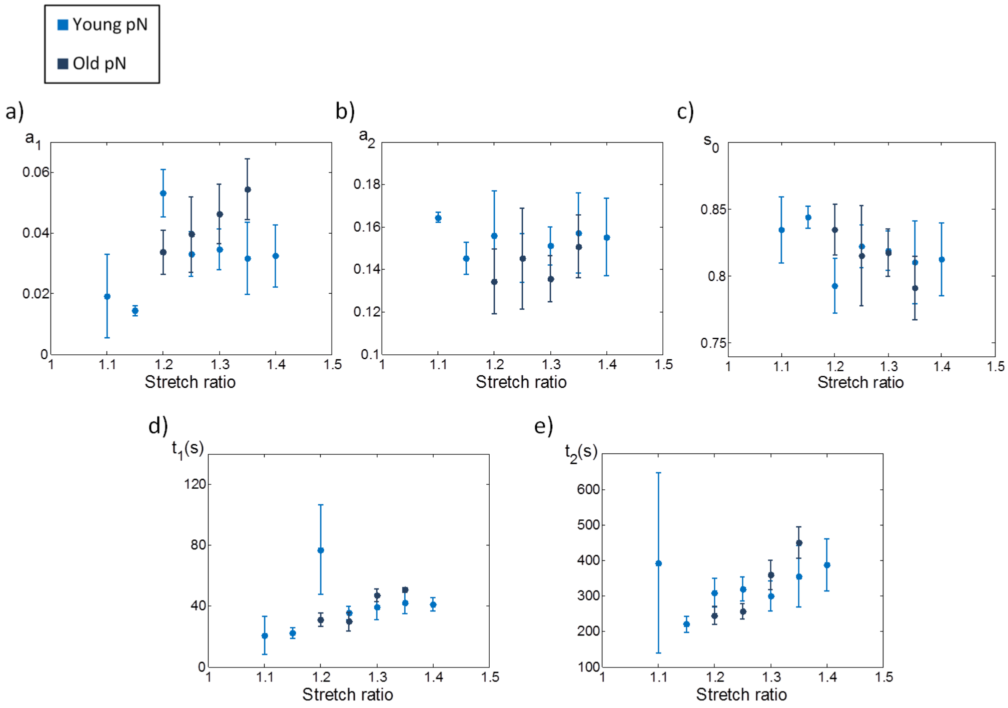

Figure V.10 – Averaged values of the five parameters describing the relaxation behaviour of old pN mice compared to young pN mice: a) amplitude of short time relaxation a_1, b) amplitude of long time relaxation a_2, c) amplitude of the relative constant s_0, d) short time t_1 (s) and e) long time t_2 (s). Error bars represent the standard error of the mean.

V.2.3 Microstructural behaviour under stretch

The microstructural behaviour for old mice, WT and pN, was qualitatively the same as for young mice. The fibres oriented gradually in the direction of traction when the sample was stretched, while the hair follicles became more and more elliptic. The initial distribution of fibres was still usually in two peaks, that evolved in a single peak distribution after the heel region, similarly to what was described for young samples in the previous chapters. Finally, the orientation index always followed exactly the stress curve.

Figure V.11 summarises the differences observed in the microstructural behaviour between young and old WT and pN mice, for the same 3 parameters as in the last chapter: initial orientation index, slope of the orientation index variation and absolute value of the slope of the final region of λ_{yy} versus imposed stretch curve.

In the same way as for mechanical parameters, the microstructural parameters considered here evolved with age similarly for WT and pN mice, yet the differences were only significant for the former as a result of sample number.

The initial orientation index measured was higher for the old mice than for the young ones, both

for WT and pN. It was also quantitatively the same in old WT and old pN mice. More than 20% of the fibres were already initially aligned in the direction of traction in old mice.
The contraction in the direction perpendicular to traction occured significantly faster for old mice. This was particularly true for WT mice,less easily observed for the pN strain.
Finally, the parameter linking mechanical properties and microstructural reorganisation, the slope of the orientation index, remained the same for young and old mice. This was the case for WT and pN mice alike. The modification of this parameter with the pN mutation we observed at one month remained the same at an advanced age. Accordingly, the slope of the OI was significantly smaller for old pN than for old WT.

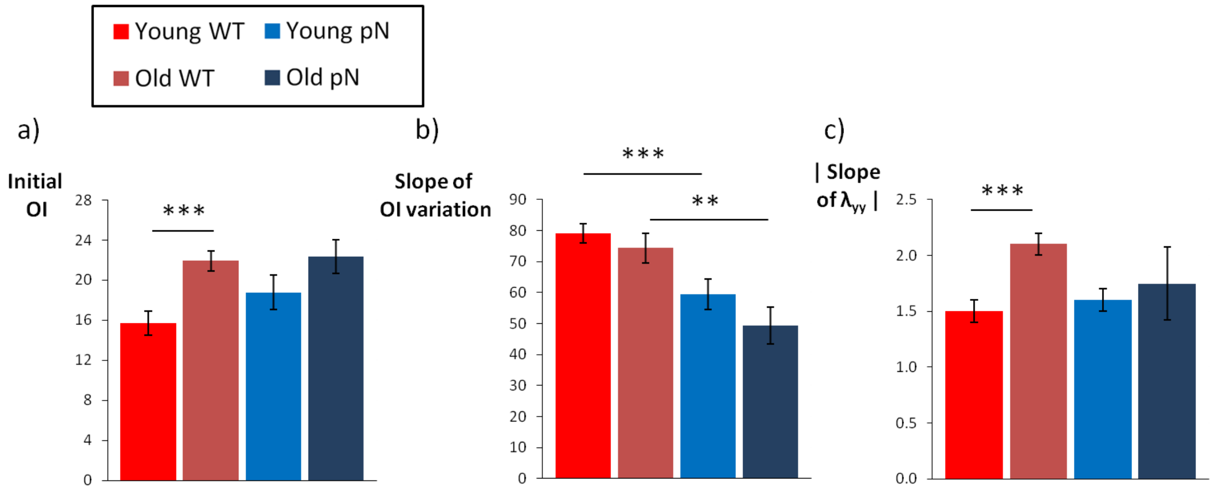

Figure V.11 – Parameters derived from SHG images for young and old WT and pN mice: a) initial orientation index, b) slope of the orientation index variation, c) absolute value of the slope of the final region of λ_{yy} versus imposed stretch curve. Error bars represent the standard error of the mean. n=23 for young WT mice, n=14 for old WT mice, n=16 for young pN mice, n=7 for old pN mice. * indicates $p < 5\%$, ** indicates $p < 1\%$, *** indicates $p < 0.1\%$.

These results will now be discussed in the light of the framework developed in Chapter III.

V.2.4 Interpretation

Age-related microstructural changes in the dermis affect collagen I fibres and extrafibrillar matrix alike [126]. There is a decrease in the collagen content, but on the other hand the collagenous network becomes more interconnected and reticulated. The collagen fibres themselves are modified: there are more inner cross-links. The extrafibrillar matrix, encompassing everything that is not collagen I fibres, is degraded and disorganised. Specifically, there is a loss in elastin and proteoglycans contents. The remaining proteins are smaller, fragmented and with little spatial structure. The dermis is thinner, and presents microscopic holes.

The age-related microstructural changes in mice skin have not yet been properly characterised. We supposed that they were equivalent to the changes observed for human skin. This hypothesis is supported by the fact that, in mice skin, the tangent modulus increased with age in proportions quantitatively comparable to what is reported in the literature for human skin.

The age-induced structural changes are ubiquitous, complex, and affect all three mechanisms suggested in Chapter III to explain the multiscale behaviour of skin.
As a reminder, these mechanisms are:

1. Inside the fibres, the sliding of viscoelastic proteoglycan bonds results in perfectly plastic fibres with a stress plateau (named σ_f) after a short elastic period.
2. The bending of reticulation points and buckling of fibres perpendicular to direction of traction are responsible for the toe and heel regions. The linear region is dominated by the stretching of fibres aligned with the direction of traction.
3. The extrafibrillar matrix contributes to the mechanical response as a viscoelastic material.

The impaired collagen structure and general loss of collagen content would induce a decreased tissue stiffness. The effect of the degradation of the proteoglycans is more difficult to predict. On one hand, the loss of spatial organisation between collagen fibrils inside fibres could facilitate sliding, and thus each fibre would have a smaller σ_f. On the other hand, smaller proteoglycans induce more shear, less sliding, and a larger σ_f for each individual fibre. The predominant effect here seems to be at a larger scale: the higher reticulation and cross-linking rate between fibres also participates in a higher stiffness of the whole tissue. The very high tangent modulus observed for old mice skin, both WT and pN, can be attributed to these two phenonema: increased shear between collagen fibre sub-units and increased reticulation and cross-linking between fibres.

The extrafibrillar matrix loses structural organisation with age. The degraded proteins of the dermis form small fragmented aggregates, that induce an increased shear compared to bigger bundles. Similarly to the small collagen V fibrils in peK mice, these small components act like props and make the buckling of the fibres initially oriented perpendicularly to traction more difficult. The reticulation points are also expected to be more difficult to bend due to increased glycation. These two structural modifications are responsible for the lengthening of the heel region.

The general overcrowding of the dermis, with smaller proteins and protein debris, could impair the mobility through the matrix. This would result in a smaller slope of λ_{yy}, as water would flow out less easily, and a smaller slope of the orientation index, as the fibres' movements would be hindered.
The exact opposite is observed for the slope of λ_{yy}. The collapse in the direction perpendicular to traction is much faster for aged skin than for young skin. The reason for this is most likely the loss of the ability to retain water by the proteoglycans, reported in previous studies in the

literature [126]. One of the main functional purpose of the proteoglycans is indeed to retain water in a mesh-like network, exactly like cross-linked polymers in water gels. Smaller, fragmented and less organised proteoglycans lose their ability to retain water.
The slope of the OI, on the other hand, is unmodified with age. This is probably to be attributed to the reduction of the collagen fibre density, which facilitate the fibres' movements. This compensates the general overcrowding of the dermis to result in an average fibre mobility equivalent to the young mice.

The increased efficiency of relaxation with strain in aged mice could be attributed to a secondary network, composed here of degraded proteins, orienting in the direction of traction throughout the mechanical test and making the displacements of the collagen I fibres less and less difficult. This would however impact the evolution of orientation index with strain: as the fibres would move around more easily, the orientation index versus strain curve would not be linear anymore, but faster than linear. It was not the case: the orientation index always followed closely the stress/stretch curve in the linear region. The increased relaxation could also be an effect of microstructural damage.
In any case, we do not observe clearly the age-induced increase in skin's non-elastic behaviour reported in the literature [107, 129]. The main explanation for this could be that the time scales involved are too short, as we only consider relaxation over the course of 5 minutes for young and old mice alike. Longer experiments, such as cyclic loadings or longer time relaxations, are needed to further investigate the viscoelasticity of aged mice skin.

Finally, even with a relatively low sample number for old pN mice, a very statistically significant difference was found in the tangent modulus between old WT and old pN mice ($p < 0.01\%$). No statistical difference was found between pN and WT mice at one month of age.
The microstructure of pN/- mice was not characterised, contrary to pN/pN mice, for which the mutation was important and ubiquitous. However, the modification of the slope of the orientation index proved that the mutation was expressed at the microscale level at one month even for heterozygous pN/- mice, see Chapter IV.
The pN mutation results in a lower density of collagen fibres, abnormal morphology of fibres, degraded proteoglycans and disorganised extrafibrillar matrix presenting lacunae. Age on the other hand results in a loss of collagen, smaller proteoglycans, degraded elastin and a disorganised extrafibrillar matrix with holes. Both pN mutation and age work in the same direction, and it follows that the aged pN mice, even heterozygous, are particularly affected, which shows in their skin's mechanical properties.
However, the loss of collagen content had us expect a lower tangent modulus for old pN than old WT mice. Furthermore, the pN mice strain were created to mimic the Ehlers-Danlos syndrome, in which skin is hyper-extensible. We would then expect a lower tangent modulus, a longer heel region lenth or a higher maximum stretch ratio. In this context the results of old pN mice with

regards to old WT mice are rather surprising. The smaller proteins present in the dermis in aged pN mice, whether degraded collagen, degraded elastin or smaller proteoglycans, seem to increase considerably the shear in the matrix. The reduced sliding inside the fibres and the facilitated force transmission between fibres then result in a higher stress in the tissue. This result highlights once more the crucial role of the extrafibrillar matrix in the mechanical properties of the dermis.

General conclusion

The experiments carried out on aged mice skin revealed an age-related increase in the tangent modulus, which doubled from one month to old age in the WT mice, in good agreement with the literature. The increase in the viscous behaviour of skin could not be observed in the short time scales analysed. Further experiments are needed to evaluate this property.

The evolution of the mechanical and microstructural behaviour could be interpreted in the context of the framework developed for young WT mice skin in Chapter III. Our observations demonstrate the crucial role of the extrafibrillar matrix in the mechanical properties of soft collagenous tissue, including features commonly attributed to collagen such as stiffness.

Visualising the extrafibrillar matrix evolution during a mechanical assay is not possible through SHG imaging. The cross examination of results from diverse mechanical loadings, such as biaxial loadings and different strain rates, will however allow for a better comprehension of the extrafibrillar matrix behaviour. For that purpose we could also carry out experiments on other mice with a targeted mutation of the extrafibrillar matrix, affecting the proteoglycans for instance, or use chemicals to degrade specific components of the dermis, collagenase for example (an enzyme which degrades collagen).

Conclusion and perspectives

In this dissertation we have presented the results of our work on multiscale mechanics of skin. The rationale of this project was to understand the link between microstructure and macroscopic mechanical properties. Precise information on skin mechanical properties can be useful in a number of domains: tissue engineering, medical applications, cosmetics, etc.
For this purpose we developed, optimised and validated a multiscale protocol to carry out mechanical experiments while simultaneously quantifying microstructural remodelling. Using uniaxial tensile tests *in situ* under a Second Harmonic Generation microscope, we were able to visualise the collagen fibres, the main component of the dermis, aligning in the direction of traction during the test. Quantitative parameters were developed and validated both at the macroscopic scale, to measure mechanical properties, and at the microscopic scale, to assess microstructural evolution. The multiphysics protocol presented was developed in collaboration with Marie-Claire Schanne-Klein's team at the LOB for multiphoton imaging and Florence Ruggiero's team at the IGFL for biological characterisation.

The experiments carried out on young mice demonstrated that a simple model inspired by a tendon-like model, in which the linear part of the J-shaped stress/stretch curve is attributed to the extension of aligned collagen fibres, was not appropriate for mice skin.
We were able to measure on SHG images the fraction of fibres aligned in the direction of traction. This parameter, called orientation index, increased non-linearly with stretch and followed exactly the stress/stretch curve. This unexpected result was found to be true for all mice skin tested, whether young, old or affected by a mutation of the dermis' microstructure.
We demonstrated that a simple model can not account for all of skin's complex multiscale properties. We suggested three mechanisms at different scales that can account for our experimental observations, based on microscopic sliding, specific behaviour of fibre networks and considerations on the role of the extrafibrillar network. The conclusion that follows is that, even though all soft collagenous tissues have similar components and resembling mechanical characteristics, the microstructural specificity of each tissue involves different microscoscopic mechanisms in response to mechanical stimulation.

Two genetically-modified mice strains created in the context of the study of a genetic disease affecting skin's mechanical properties, Ehlers-Danlos syndrome, were investigated with our multiscale

protocol. In both these mice models, the microstructure is modified, either in a simple way, with the addition of one component, or in a complex and ubiquitous manner. Aged skin samples were also tested to assess the impact of age on mechanical and microstructural properties of skin.
The common conclusion of these studies is that the mechanisms we put forward for control mice can account for simple changes in the microstructure. When handling bigger and more complicated transformations, our results will be valuable to guide future quantitative models. Additionally, we demonstrated that even small alterations can have drastic effects on the microstructural and mechanical properties of the dermis. This underlines the fact that every component of soft collagenous tissues is important, independently of abundance.

Our experiments were performed on *ex vivo* skin with neither hairs nor epidermis. This deprives the skin from both its natural prestress and hydration system. Furthermore, the mechanics of *in vivo* skin is expected to depend on the other components of skin (glands, blood vessels) and underlying support system (muscles and bones). Finally, the cells present in the dermis may react to apoptosis with signalling that could for instance damage microstructural organisation.
All experiments have been carried out on mice skin. One must exercise caution when considering the validity of this study's results for human skin. Indeed, we found at least one main structural difference that could affect the microstructural behaviour: the absence of clearly identified elastin fibres in mice skin. Furthermore, it is obvious that variations in human skin with a number of intrinsic (age, gender, race) and extrinsic (sun exposure, smoking, hydration level) factors will result in a much greater dispersity in the result.

The unique tool we developed can be easily generalised to characterise other tissues. Experiments have been carried out on tendon [94] and cornea in the past. The mechanical characterisation was also successfully applied to collagen gels designed to be corneal subtitutes for transplant [132].
The multiscale protocol could be used to study other pathologies of soft collagenous tissues, as well as the effect of external factors, such as scars or chemicals. Experiments on cutaneous scar tissue resulting from wound healing are currently being implemented.
The mechanical testing apparatus was recently modified to perform biaxial traction. This new device, bigger than the unixial apparatus, was optimised so that it could also be inserted *in situ* under the SHG microscope. Biaxial loading will allow us to test the skin with a mechanical stimulation closer to actual *in vivo* conditions. The diversification of mechanical tests, *e.g.* multiaxial testing, cyclic testing, relaxation, will provide new information on skin's mechanical properties, including viscoelasticity.
Other observation techniques, such as OCT, could also be used to complement our SHG observations with the advantages of a larger field of view and much shorter imaging time. Finally, experiments are planned at the IGFL to study cell signalling during a tensile test using ribonucleic acid (RNA) analysis.
All these experiments will eventually constitute a valuable data base for the identification of rele-

vant microscale parameters and implementation of accurate and effective microstructural models for soft collagenous tissues mechanics.

Appendices

Appendix A

Statistical analysis

Data dispersion is expected with biological samples: an animal will never be the exact copy of another. To limit dispersion as much as possible, our mice came from controlled strains and were bred in animal houses, where light, temperature and food was controlled.

The intrinsic nature of experimental testing means that we can not test every animal: we only test a "sample" of a population. "Sample" must be understood here in the statistical sense, as an ensemble of elements observed, taken from a "population", that encompasses all elements. In concrete terms, the population of WT mice encompasses all mice from the C57black6 strain, and the sample corresponds to the 32 samples we tested.
Statistical analysis is needed to determine if a difference between two samples is enough to confirm a difference between the corresponding populations. This paragraph is not intented as a course in statistical analysis, but merely presents the statistical package we have been using for this study and what we mean in the context of this work when we say that differences are statistically significant. Details on the test used and statistical analysis can be found in [133].

A.1 Normal distribution

Before using statistical tests, we need to verify whether the data are normally distributed: most statistical tests require a normal data distribution. Additionally, most "biologically driven" quantities are expected to follow normal distributions. It would be surprising and possibly the evidence of unseen experimental bias if most of the recorded data were not to follow a normal distribution.
To test for normal ditribution we plot a normal probability plot. This method is easier to interpret than the usual frequency histogram. We first compute the cumulative frequency of our data distribution (using the Excel function RANK), then obtain the standard normal distribution that would hypothetically correspond to that cumulative distribution (using the Excel function NORMSINV). We get an hypothetical idealised distribution of data, called t, with a mean of zero and a standard

deviation of one. If the experimental data is normally distributed, that hypothetical distribution t is correlated to the actual distribution x through an affine function:

$$t = \frac{x - m}{\sigma} = \frac{x}{\sigma} - \frac{m}{\sigma}$$

Thus if the data are normally distributed, the normal probability plot, idealised standard normal distribution versus actual data, should be a straight line, with a slope of $\frac{1}{\sigma}$ and a y-intercept of $-\frac{m}{\sigma}$.

Figure A.1 shows an example of normal probability plot for the distribution of thickness in young WT samples. In this example the distribution is very normal, as the normal probability plot can be very well fitted by a straight line. For all quantitative parameters described in this work the distribution was normal (linear fit residual minimum $R^2 > 0.8$), provided that the number of sample was sufficient (7 to 15). This means that statistical tests can be applied.

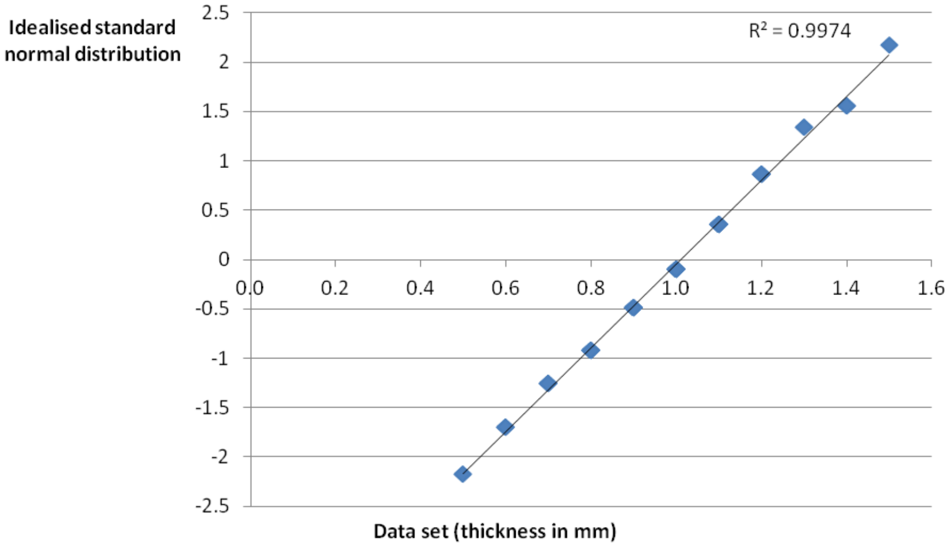

Figure A.1 – Normal probability plot for thickness in young WT samples.

A.2 Mean, SEM and p-factor

In every histogram presented in this work, the values shown are averaged over the whole data set. The error bars correspond to Standard Error of the Mean (SEM) unless stated otherwise (in which case they correspond to the standard deviation). The standard error of the mean represents the error between the sample's mean and the "true" mean of the whole population. It is calculated as:

$$SEM = \frac{s}{\sqrt{n}}$$

where s is the standard deviation of the sample (*i.e.* an estimate of the "true" standard deviation of the population from the selected sample) and n is the number of elements in the sample (number of mice in our case).

To determine whether two populations are truly different with regards to one parameter, we use the free software R [133].
First we test whether the variances of two data sets are statistically different with a Fisher test (R function var.test, $p > 0.05$ means the variances are statistically equivalent). We then test for significant differences with a Student test if the variances are equivalent, and with the alternative Welsh test if not (function t.test with the input TRUE if the variances are equivalent, FALSE if not).
These tests output a value called p-value, or p-factor. This number is interpreted in comparison with a chosen threshold, under which the two populations sampled can be considered significantly different. This threshold represents how confident we are in the statistical difference: the smaller the threshold, the less probable it is for the difference between populations to be only coincidental. A commonly used threshold is 0.05: if $p > 0.05$, we cannot confidently reject the hypothesis that the two populations are actually the same, and that the difference is a coincidence attributable to the sampling process. We also use the thresholds 0.01 and 0.001 in this work.
Obviously, the bigger the sample, the easier it gets to distinguish differences between populations with confidence. A large sample number is preferable to discriminate between two types of sample precisely.

Appendix B

Possible experimental bias

B.1 Tests under and outside the microscope

Two experimental protocols were used, depending whether we imaged the sample with SHG or not (mechanical analysis only). Two features vary from one protocol to the other and can lead to changes in the results: the hydration protocol (with SHG we used hydrogel, without SHG water spraying) and the loading path (with SHG we stopped every 5% strain for SHG imaging and let the skin relax for approximately 5 minutes, without SHG we performed a continuous traction). The mechanical behaviour was not statistically different between samples tested with or without SHG imaging.

Figure B.1 shows the mechanical parameters (tangent modulus, heel region length and rupture parameters) for WT samples tested with SHG imaging and WT samples only characterised mechanically.
Figure B.2 shows the mechanical parameters (tangent modulus, heel region length and rupture parameters) for peK samples tested with SHG imaging and peK samples only characterised mechanically.

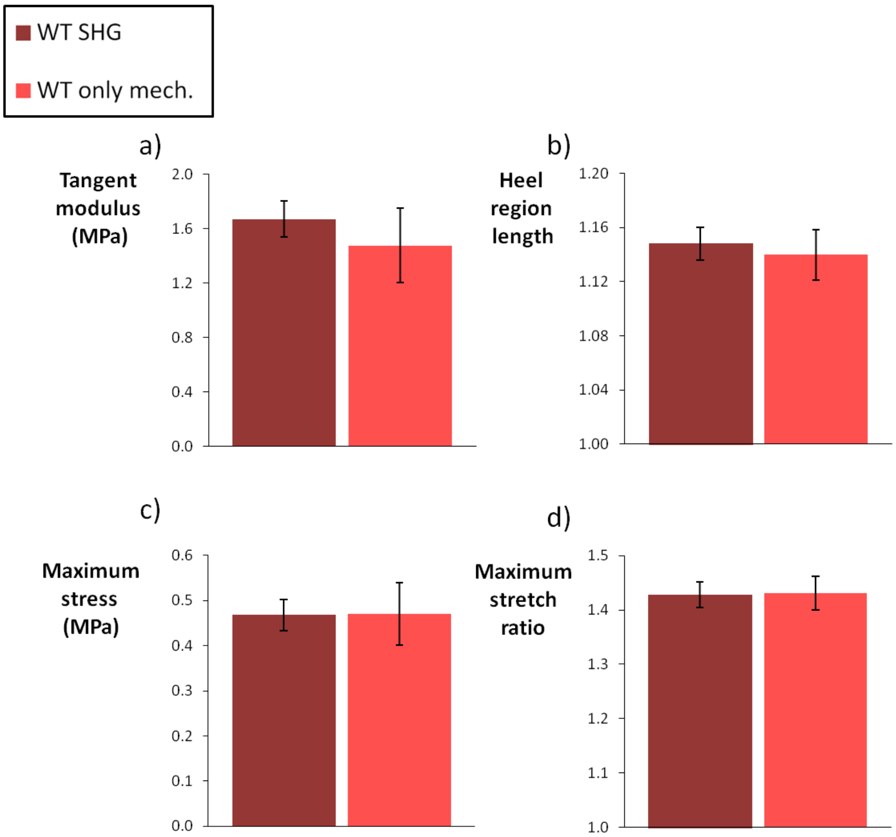

Figure B.1 – The mechanical behaviour was identical for experiments with and without stops for WT mice: a) Tangent modulus, b) Heel region length, c) Maximum stress, d) Maximum stretch ratio. Error bars represent the standard error of the mean. n=25 for WT with SHG, n=7 for WT with only mechanical analysis.

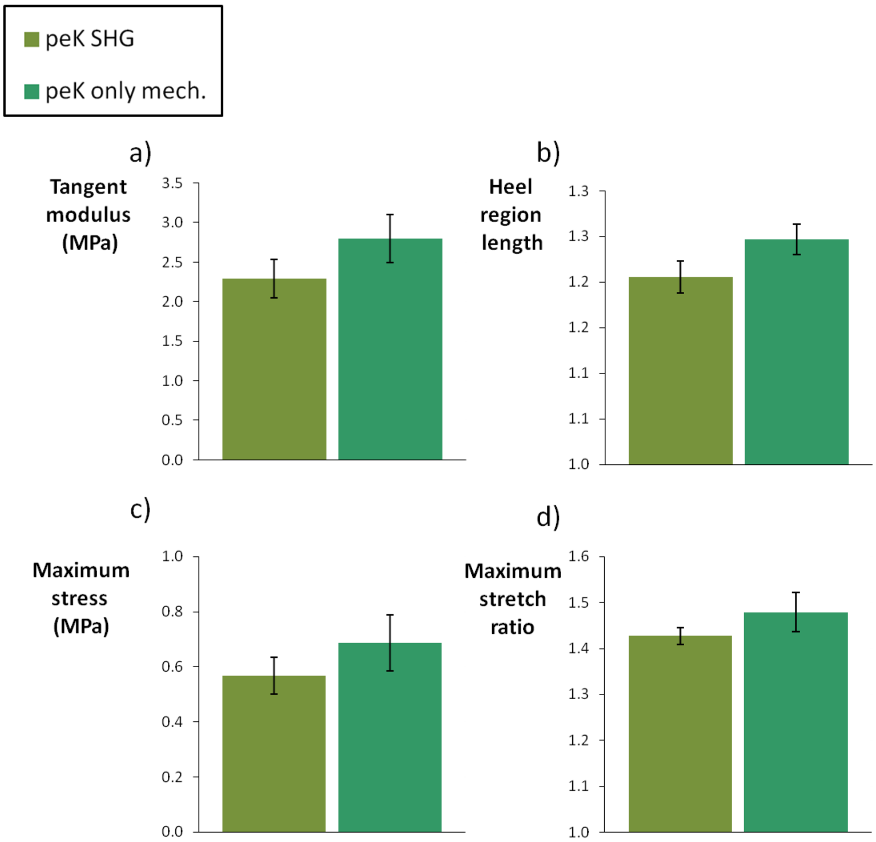

Figure B.2 – The mechanical behaviour was identical for experiments with and without stops for peK mice: a) Tangent modulus, b) Heel region length, c) Maximum stress, d) Maximum stretch ratio. Error bars represent the standard error of the mean. n=9 for peK with SHG, n=7 for peK with only mechanical analysis.

B.2 WT mice and non-mutant peK and pN mice

In this work, true WT mice are from the C57black6 strain. Both peK and pN mice come from specifically engineered strains. For both types, genetically-modified litters comprise both mutant and non-mutant animals. Non-mutants animals are supposed to be similar to normal mice of the same strain. We verified that the non-mutants pN and peK were similar to the true WT mice, although not from the same genetical background, for both mechanical parameters (see figure B.3) and microstructural parameters (see figure B.4).

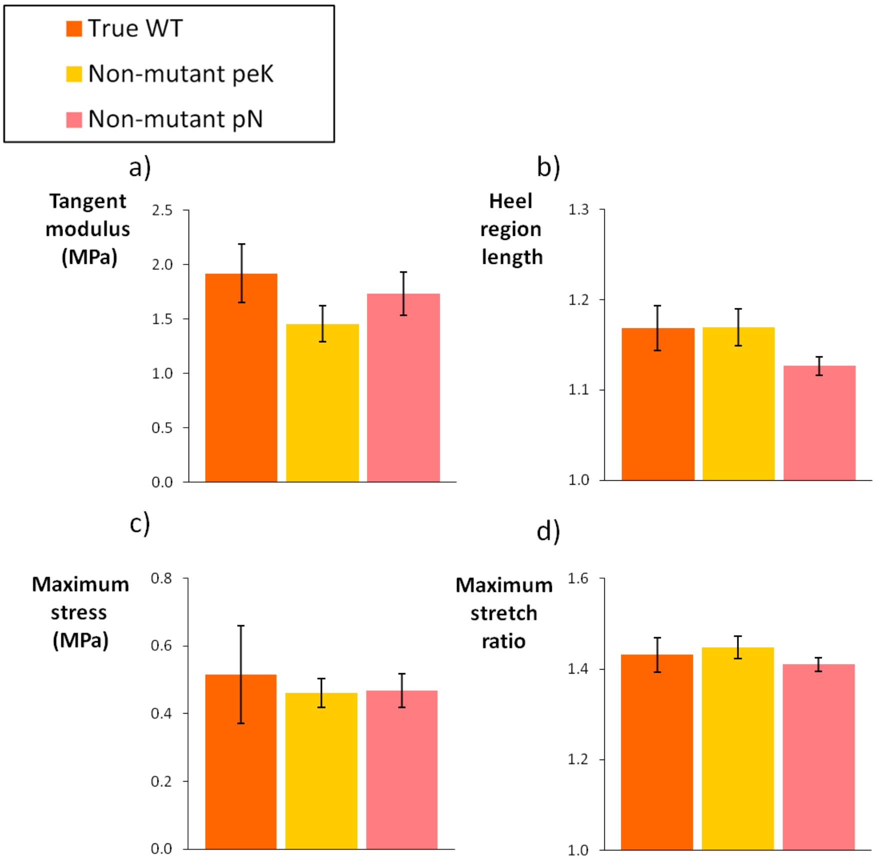

Figure B.3 – The mechanical behaviour was identical for true WT and non-mutants peK and pN mice: a) Tangent modulus, b) Heel region length, c) Maximum stress and d) Maximum stretch ratio. Error bars represent the standard error of the mean. n=3 for true WT, n=14 for non-mutant peK and n=15 for non-mutant pN.

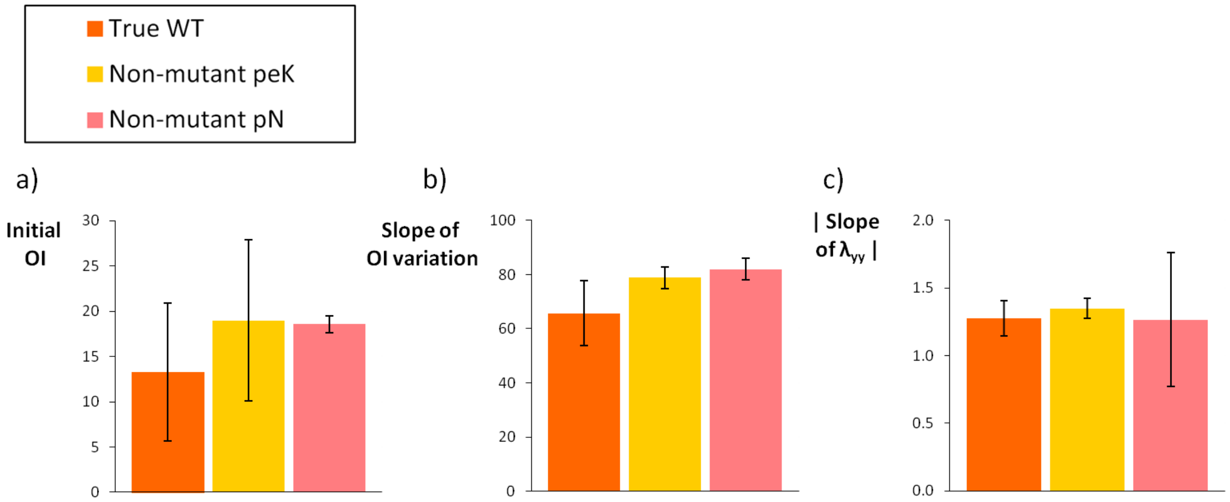

Figure B.4 – The microstructural behaviour was identical for true WT and non-mutants peK and pN mice: a) Initial orientation index, b) Slope of the orientation index variation, c) Absolute value of the slope of the final region of λ_{yy} versus imposed stretch curve. Error bars represent the standard error of the mean. n=3 for true WT, n=7 for non-mutant peK and n=15 for non-mutant pN.

B.3 Thickness

Figure B.5 shows the mean thickness for WT, peK, pN, old WT and old pN mice, along with the mean for all young skin and all old skin. The thickness was the same for WT and genetically-modified mice. Aged mice skin was statistically thinner than young mice skin. The reason for this is discussed in Chapter V.

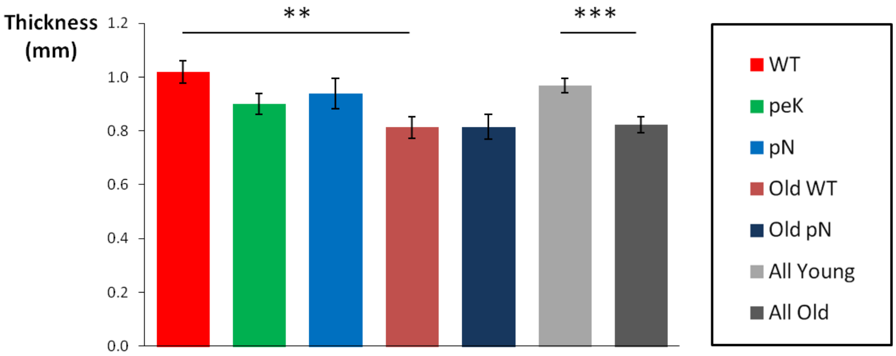

Figure B.5 – Mean thickness for WT, mutant mice peK and pN, old WT, old pN, all young mice together and all old mice together. Error bars represent the standard error of the mean. n=25 for WT, n=16 for peK, n=16 for pN, n=19 for old WT, n=7 for old pN. * indicates $p < 5\%$, ** indicates $p < 1\%$, *** indicates $p < 0.1\%$.

B.4 Hair density and relative porosity

B.4.1 Correlation with mechanical properties

Skin is a porous structure: hair follicles are disseminated in the dermis. Hair follicles are mostly empty in surface due to the depilation protocol, and often filled with keratin in the depth of the tissue. We verified that no correlation could be made between the parameters measured for skin's hair distribution and the mechanical properties. Figure B.6 shows for all young WT samples tested with SHG protocol (n=24) the tangent modulus versus number of hairs (extrapolated to the millimeter square) and tangent modulus versus surface porosity. No correlation was found between tissue stiffness and hair distribution.

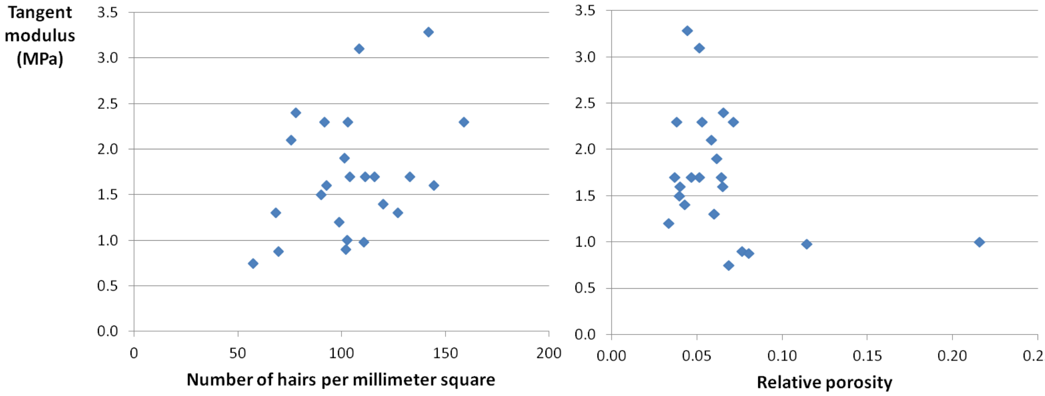

Figure B.6 – Correlation between tissue stiffness and hair distribution for all young WT samples tested with SHG protocol (n=24): left, tangent modulus versus number of hair extrapolated to the mm^2 ; right: tangent modulus versus surface relative porosity.

B.4.2 Effect of mutation and age

Figure B.7 shows the number of hair extrapolated to the mm^2 and the relative porosity for WT mice and genetically-modified mice peK and pN. No statistical difference was found between WT and peK mice in hair distribution. The number of hair per mm^2 was statistically smaller in pN mice than in WT mice: this is discussed in Chapter IV. The relative porosity was similar for WT and pN mice.

Figure B.8 shows the number of hair extrapolated to the mm^2 and the relative porosity for young and old WT mice and young and old pN mice. The number of hair is statistically smaller for old WT mice than for young WT mice, while the relative porosity does not change. Further details can be found on this subject in Chapter V. With the number of samples tested no difference was found between young and old pN in terms of hair distribution.

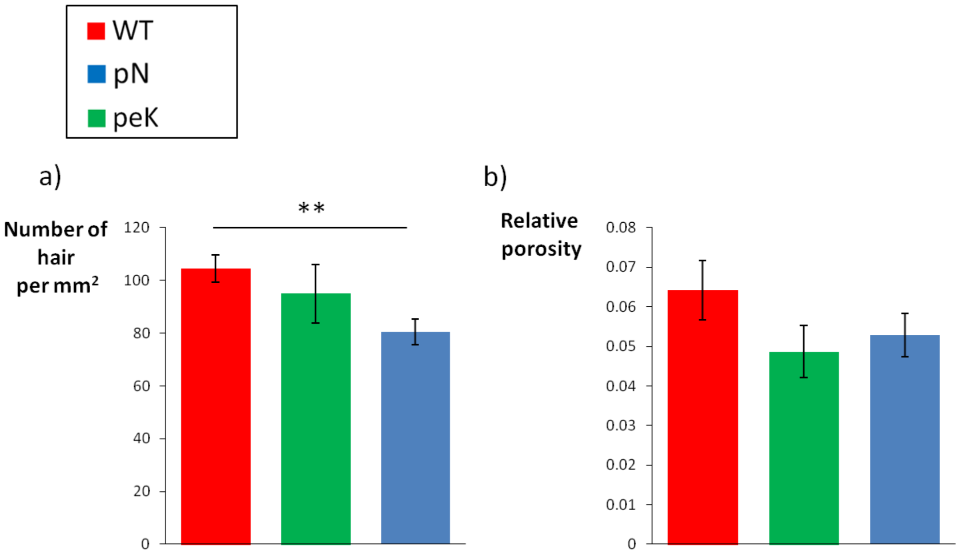

Figure B.7 – Impact of genetic mutation on hair distribution: a) Number of hair extrapolated to the mm^2, b) Surface relative porosity. Error bars represent the standard error of the mean. n=23 for WT, n=9 for peK, n=15 for pN. * indicates p < 5%, ** indicates p < 1%, *** indicates p < 0.1%.

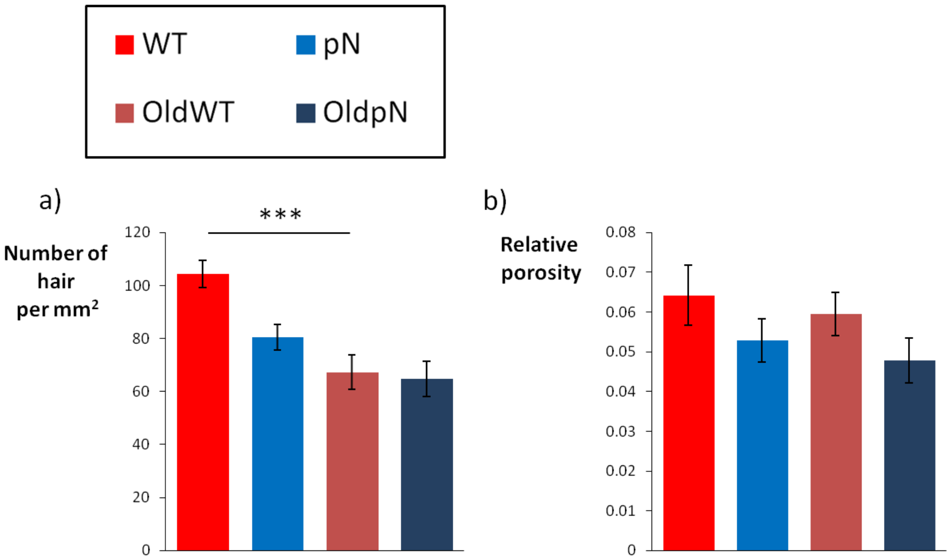

Figure B.8 – Impact of age on hair distribution: a) Number of hair extrapolated to the mm^2, b) Surface relative porosity. Error bars represent the standard error of the mean. n=23 for young WT, n=14 for old WT, n=15 for young pN and n=7 for old pN. * indicates p < 5%, ** indicates p < 1%, *** indicates p < 0.1%.

B.5 Male and female mice

We did not realise from the beginning of the study that the mouse's gender might be a relevant parameter. Thus, we only have access to this information for approximately half of the samples. Based on the data we have, we observed no difference between males and females in mechanical (see figure B.3) or microstructural behaviour (see figure B.4), whether WT or pN mice. Coincidentally, all but one peK samples for which gender had been documented were female, so no comparison could be made.

It should be noted that about half of the data base is not accounted for in the figures below, as we did not have their gender documented. This is the reason why the values can be different from values found elsewhere in this work. This section only aims at demonstrating that there was no statistical difference between males and females of the same strain for any parameter considered.

No mechanical difference between male and female human skin was found in various studies of the literature [107, 129].

No differences in hair distribution was found between males and females, as shown in figure B.11.

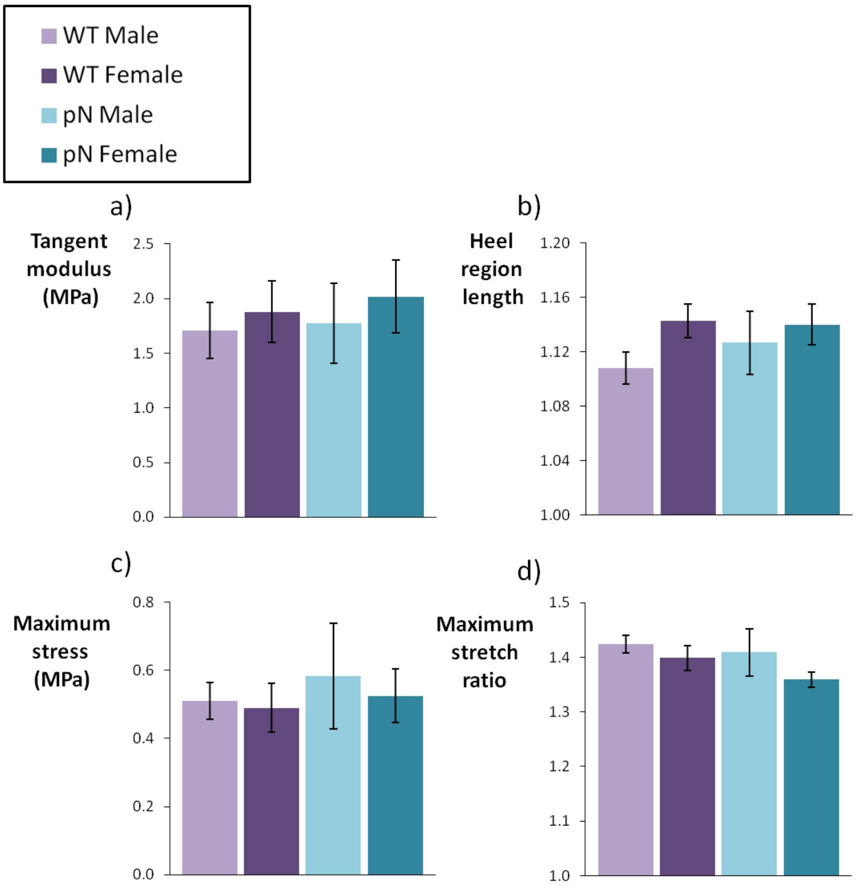

Figure B.9 – The mechanical behaviour was identical for males and females, whether WT or pN: a) Tangent modulus, b) Heel region length, c) Maximum stress and d) Maximum stretch ratio. Error bars represent the standard error of the mean. n=8 for male WT, n=9 for female WT, n=8 for male pN and n=7 for female pN.

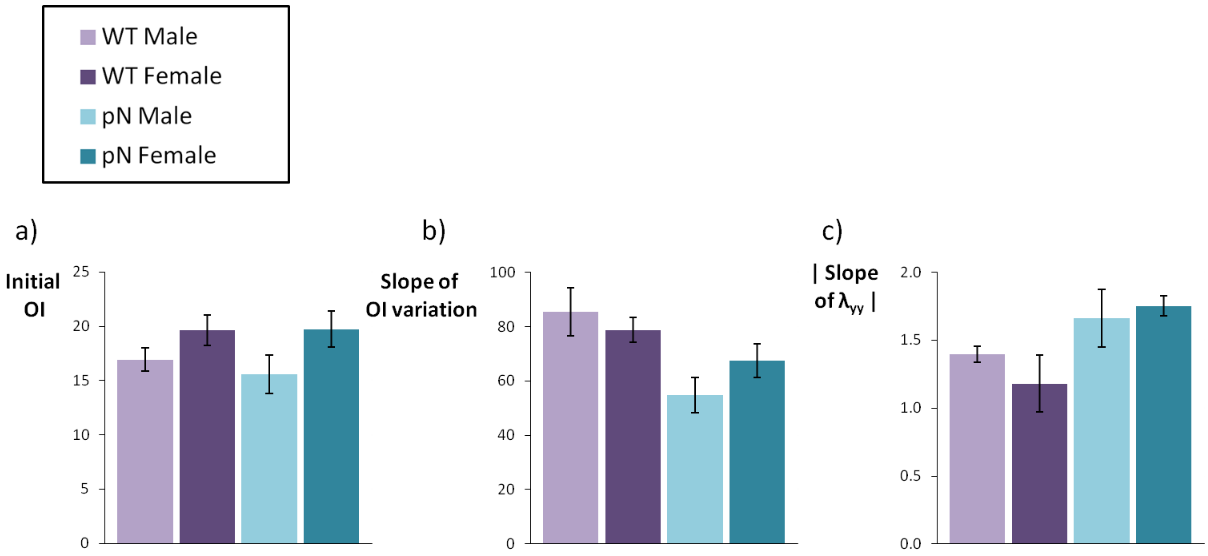

Figure B.10 – The microstructural behaviour was identical for males and females, whether WT or pN: a) Initial orientation index, b) Slope of the orientation index variation, c) Absolute value of the slope of the final region of λ_{yy} versus imposed stretch curve. Error bars represent the standard error of the mean. n=5 for male WT, n=9 for female WT, n=7 for male pN and n=6 for female pN.

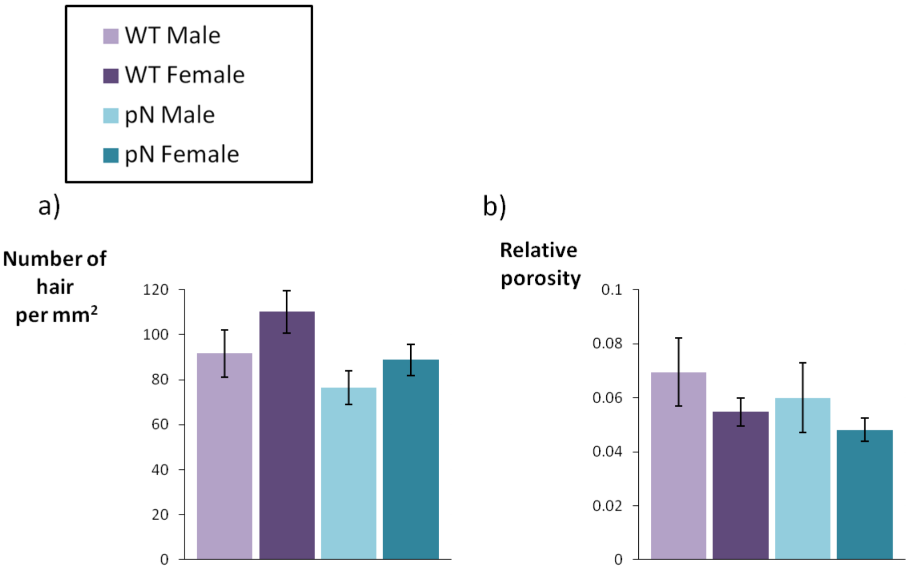

Figure B.11 – The hair distribution was identical for males and females, whether WT or pN: a) Number of hair extrapolated to the mm^2, b) Relative porosity. Error bars represent the standard error of the mean. n=5 for male WT, n=9 for female WT, n=7 for male pN and n=6 for female pN.

Appendix C

Data tables

Type	No	Sample size (mm)			Stress/stretch			
		Length	Width	Thickness	Heel region length	Final stretch ratio	Final stress (MPa)	Tangent modulus (MPa)
WT $10^{-4}s^{-1}$	peK 92	22.1	10.7	0.9	1.28	1.49	0.26	0.90
	peK 93	19.9	11.1	1.1	1.24	1.48	0.36	1.00
	pN 82-12	17.2	10.1	1.1	NA	1.44	0.31	0.75
	WT 4	15.0	10.0	1.0	1.13	NA	NA	2.27
	WT 5	16.3	8.5	1.0	1.16	1.39	0.37	1.39
	WT6	18.7	8.1	0.8	1.22	1.47	0.66	2.09
	peK 21	19.1	7.5	1.0	NA	1.46	0.58	1.60
	peK 22	17.9	7.9	0.8	1.14	1.41	0.57	2.28
	peK 25	16.7	8.2	1.0	1.18	1.54	0.56	1.71
	peK 26	25.0	7.5	1.2	1.11	1.39	0.55	1.70
	peK 35	18.0	9.9	1.2	NA	1.47	0.30	0.86
	pN 74	25.5	7.0	1.4	1.12	1.45	0.56	1.71
	pN 76	28.8	9.1	1.5	1.14	1.42	0.30	0.98
	pN 78	25.1	6.8	1.0	1.08	1.40	0.68	2.38
	pN 70	18.9	5.8	1.1	1.20	1.28	0.47	3.29
	pN 72	25.2	8.7	1.3	1.16	1.41	0.46	1.59
	pN 77	25.8	8.3	1.4	1.16	1.41	0.31	1.26
	pN 79	26.5	7.0	1.3	1.08	1.38	0.45	1.94
	pN 80	21.9	8.1	1.1	1.09	1.33	0.18	8.76
	pN 84 - 13	23.6	10.1	1.0	1.09	1.47	0.32	1.27
	pN 85	17.4	7.6	1.2	1.15	1.49	0.40	1.22
	pN 86	23.4	7.3	0.9	1.14	1.44	0.49	1.67
	pN 87	26.1	4.9	0.8	1.10	1.42	0.90	2.34
	pN 88	21.6	6.5	1.1	1.13	1.46	0.42	1.55
	pN 90	16.2	4.8	0.9	NA	1.34	0.76	3.11
	peK 36 #	16.6	8.3	0.8	1.18	1.61	0.55	0.92
	peK 51 #	13.7	7.5	0.5	NA	1.43	0.49	1.48
	peK 52 #	17.1	6.1	0.9	NA	1.41	0.45	2.72
	peK 53 #	17.5	7.2	0.7	NA	1.38	0.67	2.20
	peK 54 #	14.1	9.1	0.5	1.13	1.52	0.66	1.00
	peK 63 #	22.7	6.7	0.7	1.16	1.22	0.16	1.25
	peK 95 #	25.2	10.9	1.2	1.10	1.45	0.32	0.76
Average		20.6 ± 0.7	8.0 ± 0.3	1.0 ± 0.04	1.15 ± 0.01	1.43 ± 0.01	0.47 ± 0.03	1.6 ± 0.1

Table C.1 – Mechanical data for WT skin samples at slow strain rate (10^{-4} s^{-1})
The stress/stretch response is characterised by 4 parameters: heel region length, final stretch ratio, final stress and tangent modulus. These parameters are averaged over the WT population (± SEM). Wild-Type specimens are either from true WT strains, or non-mutants peK and pN mice.
stands for: no complete SHG analysis.

Type	No	Sample size (mm)			Stress/stretch			
		Length	Width	Thickness	Heel region length	Final stretch ratio	Final stress (MPa)	Tangent modulus (MPa)
peK 10^{-4} s^{-1}	peK 91	17.2	9.1	1.1	1.24	1.46	0.38	1.22
	peK 94	19.4	9.0	1.1	1.24	1.41	0.24	1.14
	peK 24	16.2	4.8	1.1	1.30	1.45	0.43	2.31
	peK 29	17.0	9.6	1.0	1.14	1.41	0.47	2.19
	peK 30	15.7	9.1	0.7	1.20	1.50	0.75	2.84
	peK 32	15.4	8.1	0.9	1.21	1.48	0.88	2.91
	peK 37	15.1	9.7	1.0	1.21	1.42	0.62	2.33
	peK 38	16.2	9.3	0.9	1.12	1.41	0.60	2.31
	peK 39	15.3	9.4	0.8	1.18	1.32	0.73	3.36
	peK 44 #	12.3	6.1	0.9	1.27	1.52	0.75	2.40
	peK 45 #	14.7	5.7	1.0	1.17	1.46	0.91	2.67
	peK 46 #	12.4	6.1	0.7	1.26	1.43	0.68	3.32
	peK 48 #	15.9	5.2	1.0	1.25	1.67	0.44	1.85
	peK 49 #	12.6	10.5	0.8	1.32	1.54	0.55	2.36
	peK 50 #	13.5	5.5	0.6	1.23	1.43	1.12	4.30
	peK 55 #	18.0	9.2	0.8	1.23	1.30	0.36	2.67
Average		15.4 ± 0.5	7.9 ± 0.5	0.9 ± 0.04	1.22 ± 0.01	1.45 ± 0.02	0.62 ± 0.06	2.5 ± 0.2
pN $10^{-4}s^{-1}$	pN 81-12	17.8	8.9	1.1	1.13	1.58	0.60	1.56
	pN 84 -12 *	19.9	10.7	1.2	/	/	/	/
	pN 73	19.8	7.2	1.1	1.12	1.47	1.40	2.75
	pN 71	24.5	8.1	1.4	1.10	1.40	0.31	0.98
	pN 81-13	16.1	6.8	1.2	1.17	1.51	0.41	1.10
	pN 75	19.7	8.8	1.2	1.14	1.41	0.32	1.15
	pN 82-13	23.6	8.8	1.1	1.13	1.41	0.32	1.02
	pN 83	26.1	7.5	1.2	1.26	1.41	0.25	1.14
	pN 33	29.6	6.2	1.0	1.10	1.37	0.66	1.15
	pN 38	31.2	5.1	0.6	1.15	1.37	0.39	3.12
	pN 39	23.3	4.6	0.7	1.14	1.31	0.79	2.05
	pN 40	27.8	4.6	0.9	1.15	1.34	0.54	1.97
	pN 42	28.2	4.1	0.6	1.09	1.32	0.53	3.20
	pN 45	32.6	7.9	0.9	1.05	1.16	0.80	1.57
	pN 48	30.0	3.3	0.6	1.06	1.36	0.19	3.90
	pN 49 *	28.0	7.4	0.8	/	/	/	/
	pN 51	21.2	4.4	0.8	1.21	1.36	1.11	1.66
	pN 92	17.0	7.6	0.7	1.18	1.30	0.39	3.51
Average		24.2 ± 1.2	6.8 ± 0.5	1.0 ± 0.1	1.14 ± 0.01	1.38 ± 0.02	0.58 ± 0.08	2.0 ± 0.25

Table C.2 – Mechanical data for peK and pN skin samples at slow strain rate (10^{-4} s^{-1})
The stress/stretch response is characterised by 4 parameters: heel region length, final stretch ratio, final stress and tangent modulus. These parameters are averaged over the peK and pN populations (± SEM). # stands for: no complete SHG analysis. * stands for: no mechanical analysis.

Type	**No**	**Sample size (mm)**			**Stress/stretch**			
		Length	**Width**	**Thickness**	**Heel region length**	**Final stretch ratio**	**Final stress (MPa)**	**Tangent modulus (MPa)**
WT $10^{-3}s^{-1}$	peK20 #	13.8	8.2	1.0	1.37	1.63	0.51	1.97
	peK66 #	18.5	8.1	0.6	1.20	1.60	0.93	2.23
	peK70 #	16.1	7.8	0.8	1.22	1.51	1.30	3.29
	peK73 #	15.6	7.7	0.5	1.17	1.47	1.40	3.57
	pN91 #	17.8	6.7	0.9	1.18	1.50	0.58	1.68
	pN93 #	28.4	7.4	1.2	1.16	1.28	0.28	1.65
	WT5_01_2014 #	22.3	8.3	0.8	1.15	1.20	0.29	2.23
	pek24_2014 #	20.5	9.4	0.9	1.23	1.43	0.47	1.98
	pek26_2014 #	20.0	12.3	0.9	1.32	1.41	0.61	2.92
	WT1_04_2014 #	20.7	9.6	0.8	1.32	1.35	0.73	3.29
	WT3_04_2014 #	19.7	8.3	0.7	1.28	1.38	1.01	4.91
	WT2_04_2014 #	20.2	8.5	0.8	1.32	1.33	0.64	3.86
	WT4_04_2014 #	28.0	3.7	0.8	1.23	1.31	0.92	3.90
	peK24_05_2014 #	25.5	5.9	1.2	1.10	1.54	0.82	1.82
	peK25_05_2014 #	27.2	4.3	0.8	1.18	1.35	1.16	3.55
	peK27_05_2014 #	26.9	8.3	1.0	1.09	1.45	0.78	2.15
Average		21.3 ± 1.2	7.8 ± 0.5	0.9 ± 0.05	1.22 ± 0.02	1.42 ± 0.03	0.77 ± 0.08	2.8 ± 0.25
WT $10^{-2}s^{-1}$	pN41#	26.0	8.0	1.0	1.19	1.52	0.79	1.70
	pN43#	21.4	5.3	0.5	1.27	1.46	0.57	7.13
	pN44#	24.6	6.0	1.0	1.14	1.60	0.86	1.86
	pN46#	22.2	4.8	1.1	1.19	1.40	1.53	2.31
	pN47#	27.6	5.3	0.6	1.14	1.35	1.58	4.30
Average		24.4 ± 1.2	5.9 ± 0.6	0.8 ± 0.12	1.19 ± 0.02	1.46 ± 0.04	1.06 ± 0.21	3.46 ± 1.03
peK $10^{-3}s^{-1}$	peK64_2013 #	13.5	7.5	0.6	1.33	1.57	0.99	3.07
	peK72 #	12.1	7.3	0.4	1.25	1.50	1.30	4.45
	peK74 #	13.0	5.6	0.4	1.18	1.80	1.58	3.95
	peK75 #	12.8	7.0	0.6	1.25	1.49	1.25	3.56
	peK25_2014 #	19.5	8.5	0.9	1.24	1.61	0.64	1.24
	peK27_2014 #	24.2	6.8	0.8	1.14	1.44	1.05	3.64
Average		15.9 ± 2.0	7.1 ± 0.4	0.6 ± 0.08	1.23 ± 0.02	1.57 ± 0.05	1.13 ± 0.13	3.32 ± 0.46

Table C.3 – Mechanical data for WT and peK skin samples at higher strain rates (10^{-3} s^{-1} and 10^{-2} s^{-1})
The stress/stretch response is characterised by 4 parameters: heel region length, final stretch ratio, final stress and tangent modulus. These parameters are averaged over the WT and peK populations for the strain rate considered (± SEM).
stands for: no complete SHG analysis.

Type	No	Sample size (mm)			Stress/stretch			
		Length	Width	Thickness	Heel region length	Final stretch ratio	Final stress (MPa)	Tangent modulus (MPa)
Old WT	OldpN85	28.7	5.3	0.6	1.15	1.42	1.52	3.95
	OldpN86	27.9	7.0	0.6	1.23	1.37	0.85	3.41
	OldpN87	39.0	9.3	1.0	1.00	1.45	0.56	1.93
	OldpN89	30.6	8.9	0.9	1.19	1.40	0.57	2.14
	OldpN93	35.9	7.0	0.9	1.19	1.35	0.59	2.21
	OldpN94	36.2	8.7	0.9	1.25	1.45	0.92	2.99
	OldpN97	35.0	7.2	0.8	1.29	1.38	0.78	3.80
	WT1_10_2014 #	26.2	2.9	0.6	1.15	1.40	NA	NA
	WT2_10_2014 #	27.5	6.8	1.1	1.23	1.35	0.69	4.26
	WT3_10_2014 #	33.1	6.7	0.9	1.18	1.35	0.97	4.98
	WT4_10_2014 #	28.0	8.3	0.9	1.18	1.48	0.86	3.56
	WT1old_11_2014	26.0	5.3	0.9	1.18	1.43	0.65	3.15
	WT3old_11_2014	31.1	7.8	0.6	1.15	1.29	0.81	4.63
	WT4old_11_2014	32.2	6.2	0.7	1.19	1.33	0.84	4.55
	WT5old_11_2014	34.0	7.4	0.6	1.13	1.32	0.67	3.40
	WT6old_11_2014	29.7	4.7	0.6	1.26	1.52	1.42	5.01
	WT7old_11_2014#	27.3	8.3	1.1	1.26	1.33	0.28	2.04
	OldpN64	30.6	2.8	0.9	1.19	1.45	1.12	3.46
	OldpN69	23.9	3.4	0.9	1.20	1.43	1.23	6.18
Average		30.7 ± 0.9	6.5 ± 0.4	0.8 ± 0.04	1.20 ± 0.01	1.39 ± 0.01	0.83 ± 0.13	3.65 ± 0.27
Old pN	OldpN1	23.5	6.8	0.9	1.18	1.32	1.47	6.66
	OldpN95	24.3	8.7	0.6	1.25	1.35	1.72	9.62
	OldpN98	32.6	5.8	0.8	1.19	1.34	2.24	10.71
	OldpN60	30.9	4.9	0.8	1.11	1.42	0.83	2.86
	OldpN68	26.3	4.4	0.8	1.13	1.40	0.82	3.35
	OldpN62	30.4	4.1	1.0	1.19	1.54	1.07	2.13
	OldpN54	28.4	5.9	0.8	1.26	1.49	0.81	2.05
Average		28.1 ± 1.3	5.8 ± 0.6	0.8 ± 0.05	1.18 ± 0.02	1.41 ± 0.03	1.28 ± 0.23	5.34 ± 0.14

Table C.4 – Mechanical data for old WT and old pN skin samples
The stress/stretch response is characterised by 4 parameters: heel region length, final stretch ratio, final stress and tangent modulus. These parameters are averaged over the old WT and old pN populations (± SEM). The strain rate was always $10^{-4}s^{-1}$ for old mice.
stands for: no complete SHG analysis.

Type	No	λ_{xx}			λ_{yy}		
		$\lambda_{xx,1}$	A_{xx}	R^2	$\lambda_{yy,1}$	A_{yy}	R^2
WT $10^{-4}s^{-1}$	peK 92	1.00 ± 0.01	1.0 ± 0.1	0.89	1.46 ± 0.03	-1.46 ± 0.07	0.99
	peK 93	0.89 ± 0.02	0.78 ± 0.06	0.94	1.06 ± 0.02	-0.90 ± 0.06	0.96
	pN 82-12	1.09 ± 0.01	1.97 ± 0.05	0.99	1.51 ± 0.05	-1.65 ± 0.01	0.95
	WT 4	0.992 ± 0.004	1.13 ± 0.03	0.99	1.018 ± 0.002	-0.55 ± 0.02	0.99
	WT 5	0.975 ± 0.008	1.04 ± 0.03	0.99	1.42 ± 0.03	-0.97 ± 0.08	0.97
	WT6	0.91 ± 0.01	0.89 ± 0.04	0.98	1.39 ± 0.09	-0.9 ± 0.3	0.75
	peK 21	0.97 ± 0.01	1.17 ± 0.04	0.99	1.54 ± 0.04	-1.8 ± 0.1	0.98
	peK 22	0.985 ± 0.004	1.11 ± 0.02	0.99	1.32 ± 0.01	-1.33 ± 0.05	0.99
	peK 25	1.023 ± 0.008	0.90 ± 0.02	0.99	1.48 ± 0.03	-0.92 ± 0.07	0.96
	peK 26	1.00 ± 0.02	0.7 ± 0.1	0.88	1.22 ± 0.02	-1.6 ± 0.1	0.98
	peK 35 #	/	/	/	/	/	/
	pN 74	1.02 ± 0.02	1.06 ± 0.07	0.97	1.55 ± 0.06	-1.9 ± 0.2	0.95
	pN 76	0.97 ± 0.01	1.17 ± 0.06	0.98	1.35 ± 0.01	-1.77 ± 0.05	0.99
	pN 78	1.05 ± 0.02	1.37 ± 0.08	0.97	1.31 ± 0.03	-2.0 ± 0.1	0.98
	pN 70	1.01 ± 0.01	0.99 ± 0.03	0.99	1.80 ± 0.08	-1.1 ± 0.1	0.93
	pN 72	0.96 ± 0.02	1.26 ± 0.08	0.97	1.26 ± 0.01	-1.61 ± 0.04	0.99
	pN 77	0.97 ± 0.01	1.33 ± 0.07	0.98	1.50 ± 0.02	-1.9 ± 0.1	0.99
	pN 79	0.80 ± 0.03	2.1 ± 0.1	0.98	1.26 ± 0.03	-2.2 ± 0.1	0.99
	pN 80	0.96 ± 0.07	1.8 ± 0.4	0.79	1.15 ± 0.02	-1.74 ± 0.09	0.99
	pN 84 -13	0.94 ± 0.03	0.7 ± 0.1	0.86	1.38 ± 0.04	-1.6 ± 0.1	0.97
	pN 85	1.01 ± 0.01	0.86 ± 0.06	0.97	1.08 ± 0.01	-0.86 ± 0.08	0.96
	pN 86	0.97 ± 0.02	0.76 ± 0.07	0.94	1.53 ± 0.04	-2.0 ± 0.1	0.98
	pN 87	0.97 ± 0.02	0.9 ± 0.1	0.91	1.43 ± 0.02	-2.37 ± 0.09	0.99
	pN 88	1.03 ± 0.02	0.51 ± 0.07	0.84	1.28 ± 0.03	-1.77 ± 0.08	0.99
	pN 90	1.01 ± 0.05	1.00 ± 0.04	0.99	-0.4 ± 0.1	-1.7 ± 0.1	0.97
Average		0.98 ± 0.01	1.10 ± 0.08		1.29 ± 0.08	-1.5 ± 0.1	

Table C.5 – Relationship between local and global stretch ratio for WT skin samples at slow strain rate (10^{-4} s^{-1})
The linear fitting of the variation of the local deformation tensor as a function of imposed stretch ratio provides 2 parameters: the intercept $\lambda_{ii,1}$ and the slope A_{ii}, with squared correlation coefficient R^2.
These parameters are averaged over the WT population (± SEM). Wild-Type specimens are either from true WT strains, or non-mutants peK and pN mice.
stands for: no complete SHG analysis.

Type	**No**	**λ_{xx}**			**λ_{yy}**		
		$\lambda_{xx,1}$	**A_{xx}**	**R^2**	**$\lambda_{yy,1}$**	**A_{yy}**	**R^2**
peK **10^{-4} s^{-1}**	peK 91	1.00 ± 0.02	1.06 ± 0.04	0.99	1.270 ± 0.004	-0.90 ± 0.01	0.99
	peK 94	1.00 ± 0.01	1.1 ± 0.2	0.85	1.32 ± 0.03	-1.2 ± 0.1	0.97
	peK 24	0.982 ± 0.006	0.85 ± 0.02	0.99	1.28 ± 0.03	-0.71 ± 0.09	0.94
	peK 29	1.02 ± 0.02	0.98 ± 0.06	0.97	1.47 ± 0.06	-1.5 ± 0.2	0.94
	peK 30	1.00 ± 0.01	1.11 ± 0.04	0.99	1.40 ± 0.04	-1.2 ± 0.1	0.96
	peK 32	0.98 ± 0.01	1.06 ± 0.03	0.99	1.36 ± 0.02	-0.89 ± 0.05	0.99
	peK 37	1.00 ± 0.01	1.29 ± 0.06	0.99	1.30 ± 0.01	-0.88 ± 0.05	0.99
	peK 38	1.059 ± 0.006	1.14 ± 0.02	0.99	1.42 ± 0.04	-1.1 ± 0.1	0.95
	peK 39	0.95 ± 0.01	1.53 ± 0.07	0.99	1.36 ± 0.06	-0.9 ± 0.2	0.87
Average		1.00 ± 0.010	1.12 ± 0.06		1.35 ± 0.02	-1.03 ± 0.08	
pN **$10^{-4}s^{-1}$**	pN 81-12	1.04 ± 0.007	1.05 ± 0.02	0.99	1.25 ± 0.02	-1.00 ± 0.05	0.99
	pN 84 -12 *	1.0 ± 0.1	1.34 ± 0.04	0.99	1.11 ± 0.02	-0.46 ± 0.04	0.93
	pN 73	0.95 ± 0.02	1.37 ± 0.09	0.97	1.31 ± 0.03	-2.0 ± 0.1	0.98
	pN 71	0.96 ± 0.03	1.1 ± 0.1	0.90	1.28 ± 0.01	-2.12 ± 0.06	0.99
	pN 81-13	1.04 ± 0.05	0.6 ± 0.2	0.54	1.88 ± 0.07	-2.0 ± 0.1	0.97
	pN 75	0.99 ± 0.01	0.71 ± 0.04	0.98	1.26 ± 0.01	-1.58 ± 0.04	0.99
	pN 82-13	0.96 ± 0.02	1.0 ± 0.1	0.91	1.24 ± 0.06	-1.3 ± 0.3	0.88
	pN 83 #	/	/	/	1.58 ± 0.03	-1.57 ± 0.09	0.98
	pN 33 #	/	/	/	/	/	/
	pN 38	0.9 ± 0.1	1.2 ± 0.1	0.98	1.06 ± 0.02	-1.85 ± 0.02	0.99
	pN 39	1.0 ± 0.1	0.9 ± 0.1	0.95	1.08 ± 0.07	-1.71 ± 0.06	0.96
	pN 40	1.0 ± 0.2	0.8 ± 0.2	0.99	1.06 ± 0.03	-1.55 ± 0.03	0.99
	pN 42	0.9 ± 0.3	1.2 ± 0.2	0.97	1.14 ± 0.06	-1.76 ± 0.05	0.93
	pN 45	/	/	/	/	/	/
	pN 48	0.9 ± 0.2	1.4 ± 0.2	0.89	1.15 ± 0.05	-2.00 ± 0.04	0.97
	pN 49 *	1.0 ± 0.1	1.4 ± 0.1	0.99	1.06 ± 0.09	-1.90 ± 0.08	1.00
	pN 51	1.0 ± 0.1	1.13 ± 0.08	0.99	1.18 ± 0.10	-1.69 ± 0.08	0.93
	pN 92	1.00 ± 0.03	0.84 ± 0.03	1.00	1.02 ± 0.02	-0.97 ± 0.02	1.00
Average		0.97 ± 0.01	1.07 ± 0.06		1.23 ± 0.06	-1.6 ± 0.1	

Table C.6 – Relationship between local and global stretch ratio for peK and pN skin samples at slow strain rate (10^{-4} s^{-1})
The linear fitting of the variation of the local deformation tensor as a function of imposed stretch ratio provides 2 parameters: the intercept $\lambda_{ii,1}$ and the slope A_{ii}, with squared correlation coefficient R^2.
These parameters are averaged over the peK and pN populations (± SEM).
stands for: no complete SHG analysis, * stand for: no mechanical analysis.

Type	No	λ_{xx}			λ_{yy}		
		$\lambda_{xx,1}$	A_{xx}	R^2	$\lambda_{yy,1}$	A_{yy}	R^2
Old WT	OldpN85	0.97 ± 0.32	1.1 ± 0.3	0.93	1.36 ± 0.15	-2.65 ± 0.13	0.98
	OldpN86	0.82 ± 0.08	0.92 ± 0.06	0.98	1.28 ± 0.06	-1.82 ± 0.04	1.00
	OldpN87	0.92 ± 0.10	1.24 ± 0.08	0.96	1.40 ± 0.15	-1.94 ± 0.12	0.95
	OldpN89	0.948 ± 0.063	0.86 ± 0.05	0.99	1.611 ± 0.095	-2.59 ± 0.07	1.00
	OldpN93	0.971 ± 0.079	0.86 ± 0.07	0.98	1.45 ± 0.23	-2.58 ± 0.19	0.98
	OldpN94	0.98 ± 0.04	0.88 ± 0.03	0.99	1.25 ± 0.10	-2.0 ± 0.1	0.99
	OldpN97	0.97 ± 0.04	1.18 ± 0.03	0.99	1.29 ± 0.10	-2.0 ± 0.1	0.99
	WT1old_11_2014	0.98 ± 0.05	0.89 ± 0.04	0.99	1.69 ± 0.27	-2.1 ± 0.2	0.91
	WT3old_11_2014	0.88 ± 1.93	1.11 ± 1.69	0.98	1.63 ± 0.34	-1.76 ± 0.27	0.95
	WT4old_11_2014	0.84 ± 0.23	1.27 ± 0.19	0.91	1.72 ± 0.39	-1.8 ± 0.3	0.99
	WT5old_11_2014 #	0.97 ± 0.05	0.64 ± 0.04	0.88	/	/	/
	WT6old_11_2014	0.81 ± 0.24	0.96 ± 0.19	0.93	1.66 ± 0.10	-1.53 ± 0.07	0.93
	OldpN64	1.02 ± 0.08	1.24 ± 0.07	0.98	1.59 ± 0.27	-2.2 ± 0.20	0.96
	OldpN69	0.96 ± 0.05	0.88 ± 0.04	0.99	1.26 ± 0.04	-2.3 ± 0.0	0.99
Average		0.93 ± 0.02	1.00 ± 0.05		1.48 ± 0.05	-2.1 ± 0.1	
Old pN	OldpN1	0.99 ± 0.06	0.79 ± 0.06	0.98	1.28 ± 0.06	-1.82 ± 0.05	1.00
	OldpN95	-0.03 ± 0.01	0.01 ± 0.00	0.99	0.21 ± 0.02	-0.01 ± 0.0	0.99
	OldpN98	0.99 ± 0.04	1.02 ± 0.04	0.99	1.07 ± 0.12	-1.9 ± 0.1	0.99
	OldpN60	0.81 ± 0.18	0.89 ± 0.15	0.91	1.95 ± 0.83	-2.74 ± 0.59	1.00
	OldpN68	0.93 ± 0.18	1.31 ± 0.16	1.00	1.82 ± 0.31	-2.4 ± 0.2	1.00
	OldpN62	1.00 ± 0.14	1.3 ± 0.1	0.94	1.88 ± 0.43	-1.5 ± 0.3	0.99
	OldpN54	0.86 ± 0.80	1.0 ± 0.6	0.97	1.51 ± 0.17	-1.89 ± 0.13	0.98
Average		0.79 ± 0.14	0.91 ± 0.17		1.39 ± 0.23	-1.7 ± 0.3	

Table C.7 – Relationship between local and global stretch ratio for old WT and old pN skin samples
The linear fitting of the variation of the local deformation tensor as a function of imposed stretch ratio provides 2 parameters: the intercept $\lambda_{ii,1}$ and the slope A_{ii}, with squared correlation coefficient R^2. These parameters are averaged over the old WT and old pN populations (± SEM). The strain rate was always $10^{-4}s^{-1}$ for old mice.
stands for: no complete SHG analysis

Type	No	OI			Initial OI
		OI(1)	A_{OI}	R^2	
WT $10^{-4}s^{-1}$	peK 92	-3 ± 2	85 ± 4	0.98	8.7
	peK 93	8.2 ± 0.8	88 ± 3	0.94	12.7
	pN 82-12	16.40 ± 0.07	61 ± 4	0.97	14.0
	WT 4	5.9 ± 0.7	88 ± 6	0.98	5.5
	WT 5	-5 ± 2	62 ± 5	0.96	5.8
	WT6	15.7 ± 0.9	47 ± 2	0.99	28.5
	peK 21	-4.9 ± 0.9	90 ± 3	0.99	7.9
	peK 22	4.8 ± 0.7	82 ± 3	0.99	12.2
	peK 25	-3.1 ± 0.5	60 ± 1	0.99	6.8
	peK 26	8.8 ± 0.8	75 ± 3	0.99	12.5
	peK 35	1 ± 2	72 ± 6	0.96	13.1
	pN 74	8.4 ± 0.9	70 ± 3	0.99	20.1
	pN 76	7.5 ± 0.7	87 ± 3	0.99	17.0
	pN 78	5 ± 2	108 ± 6	0.99	15.2
	pN 70	-11.0 ± 0.9	65 ± 2	0.99	10.7
	pN 72	14.9 ± 0.4	76 ± 2	0.99	21.9
	pN 77	12 ± 1	75 ± 4	0.99	24.9
	pN 79	3 ± 2	101 ± 7	0.97	18.5
	pN 80	18.1 ± 0.4	75 ± 2	0.99	18.6
	pN 84	-2 ± 1	94 ± 4	0.99	17.0
	pN 85	15.4 ± 0.3	70 ± 1	1.00	21.3
	pN 86	-1.40 ± 0.05	113 ± 2	1.00	17.3
	pN 87	14.30 ± 0.08	75 ± 3	1.00	23.1
	pN 88	13 ± 1	77 ± 4	0.98	18.4
	pN 90	20 ± 4	83 ± 3	0.99	20.5
Average		6 ± 2	79 ± 3		16 ± 1

Table C.8 – Collagen organisation for WT skin samples at slow strain rate (10^{-4} s^{-1})
The linear fitting of the OI variation as a function of imposed stretch ratio provides 2 parameters: the intercept OI(1) and the slope A_{OI}, with squared correlation coefficient R^2. The initial OI is the value of the OI in the initial rest state.

These parameters are averaged over the WT population (± SEM). Wild-Type specimens are either from true WT strains, or non-mutants peK and pN mice.

Type	No	OI			Initial OI
		OI(1)	A_{OI}	R^2	
peK **10^{-4} s^{-1}**	peK 91	13.5 ± 0.5	52 ± 1	0.99	11.9
	peK 94	4 ± 1	80 ± 3	0.99	16.5
	peK 24	7.2 ± 0.8	58 ± 2	0.98	7.9
	peK 29	0 ± 3	64 ± 9	0.89	6.3
	peK 30	-1.1 ± 0.8	57 ± 2	0.99	10.2
	peK 32	-4.4 ± 0.03	64 ± 1	0.99	3.0
	peK 37	0.8 ± 0.5	63 ± 2	0.99	5.0
	peK 38	-7 ± 1	67 ± 1	0.98	1.4
	peK 39	7.9 ± 0.9	30 ± 4	0.86	7.7
Average		2 ± 2	59 ± 5		8 ± 2
pN **$10^{-4}s^{-1}$**	pN 81-12	8.1 ± 0.5	52 ± 2	0.99	7.5
	pN 84 *	16.3 ± 0.7	47 ± 1	0.99	/
	pN 73	5 ± 2	81 ± 5	0.98	16.3
	pN 71	17.4 ± 0.9	79 ± 4	0.98	20.3
	pN 81-13	9 ± 2	44 ± 4	0.90	13.7
	pN 75	14.2 ± 0.6	67 ± 2	0.99	15.4
	pN 82-13	10.8 ± 0.9	71 ± 5	0.98	15.5
	pN 83	3.6 ± 0.5	29 ± 2	0.98	12.2
	pN 33	16 ± 5	52 ± 4	0.96	15.8
	pN 38	26 ± 2	45 ± 2	0.99	25.7
	pN 39	22 ± 5	84 ± 5	0.98	21.5
	pN 40	10 ± 5	76 ± 4	0.99	13.1
	pN 42 #	/	/	/	22.9
	pN 45 #	/	/	/	24.9
	pN 48	23 ± 8	54 ± 7	0.91	18.6
	pN 49 *	18 ± 8	89 ± 7	0.97	17.9
	pN 51	19 ± 3	54 ± 3	0.98	19.3
	pN 92	39 ± 4	27 ± 3	0.91	38.6
Average		16 ± 2	60 ± 5		19 ± 2

Table C.9 – Collagen organisation for peK and pN skin samples at slow strain rate (10^{-4} s^{-1})
The linear fitting of the OI variation as a function of imposed stretch ratio provides 2 parameters: the intercept OI(1) and the slope A_{OI}, with squared correlation coefficient R^2. The initial OI is the value of the OI in the initial rest state.
These parameters are averaged over the peK and pN populations (± SEM).
stands for: no complete SHG analysis, * stand for: no mechanical analysis.

Type	**No**	**OI**			**Initial OI**
		OI(1)	**A_{OI}**	**R^2**	
Old WT	OldpN85	23 ± 0.8	65 ± 4	0.98	26.1
	OldpN86	16 ± 1.1	59 ± 5	0.97	23.2
	OldpN87	14 ± 1.0	69 ± 4	0.99	26.3
	OldpN89	-0.6 ± 3.6	108 ± 12	0.95	17.1
	OldpN93	12 ± 1.4	92 ± 5	0.99	26.4
	OldpN94	18 ± 0.4	72 ± 3	0.99	22.2
	OldpN97	17 ± 0.4	85 ± 2	1.00	17.9
	WT1old_11_2014	-59 ± 2.9	72 ± 2	0.97	24.3
	WT3old_11_2014	-61 ± 3.6	71 ± 3	0.91	22.5
	WT4old_11_2014	-56 ± 5.8	60 ± 4	0.98	22.4
	WT5old_11_2014	-74 ± 2.0	74 ± 2	0.93	20.0
	WT6old_11_2014	-53 ± 1.6	63 ± 1	0.93	25.1
	OldpN64	-114 ± 18.2	99 ± 13	0.93	14.2
	OldpN69	-24 ± 1.4	43 ± 1	0.99	19.3
Average		-24 ± 12	74 ± 5		22 ± 1
Old pN	OldpN1	21 ± 0.8	55 ± 3.5	0.98	26.1
	OldpN95	13 ± 1.0	66 ± 5.9	0.96	19.6
	OldpN98	25 ± 0.4	62 ± 3.8	0.98	24.8
	OldpN60	-6 ± 3.0	28 ± 2.3	0.97	26.7
	OldpN68	-23 ± 1.6	41 ± 1.4	0.96	15.4
	OldpN62	/	/	/	18.4
	OldpN54	-28 ± 1.7	44 ± 1.3	0.96	25.5
Average		0.3 ± 9	49 ± 6		22 ± 2

Table C.10 – Collagen organisation for old WT and old pN skin samples
The linear fitting of the OI variation as a function of imposed stretch ratio provides 2 parameters: the intercept OI(1) and the slope A_{OI}, with squared correlation coefficient R^2. The initial OI is the value of the OI in the initial rest state.
These parameters are averaged over the old WT and old pN populations (± SEM). The strain rate was always $10^{-4}s^{-1}$ for old mice.
stands for: no complete SHG analysis. * stands for: no mechanical analysis

Type	No	Age (months)
Old WT	OldpN85	19
	OldpN86	19
	OldpN87	19
	OldpN89	19
	OldpN93	19
	OldpN94	19
	OldpN97	19
	WT1_10_2014 #	15
	WT2_10_2014 #	15
	WT3_10_2014 #	15
	WT4_10_2014 #	15
	WT1old_11_2014	15
	WT3old_11_2014	15
	WT4old_11_2014	15
	WT5old_11_2014	15
	WT6old_11_2014	15
	WT7old_11_2014#	15
	OldpN64	19
	OldpN69	19
Old pN	OldpN1	19
	OldpN95	19
	OldpN98	19
	OldpN60	19
	OldpN68	19
	OldpN62	19
	OldpN54	19

Table C.11 – Age of the old WT and old pN mice, in months.
stands for: no complete SHG analysis.

Bibliography

[1] K.E. Kadler, C. Baldock, J. Bella, and R.P. Boot-Handford. Collagens at a glance. *Journal of Cell Science*, 120(12):1955–1958, 2007.

[2] P. Fratzl. Cellulose and collagen: from fibres to tissues. *Current Opinion In Colloid & Interface Science*, 8(1):32–39, 2003.

[3] P. Fratzl and R. Weinkamer. Nature's hierarchical materials. *Progress In Materials Science*, 52(8):1263–1334, 2007.

[4] D.J.S. Hulmes. Building collagen molecules, fibrils, and suprafibrillar structures. *Journal of Structural Biology*, 137(1-2):2–10, 2002.

[5] A. Gautieri, S. Vesentini, A. Redaelli, and M.J. Buehler. Hierarchical structure and nanomechanics of collagen microfibrils from the atomistic scale up. *Nano Letters*, 11(2):757–766, 2011.

[6] D.E. Birk, M.V. Nurminskaya, and E.I. Zycband. Collagen fibrillogenesis in situ: fibril segments undergo post-depositional modifications resulting in linear and lateral growth during matrix development. *Developmental Dynamics*, 202(3):229–243, 1995.

[7] S. Bancelin. *Imagerie quantitative du collagène par génération de seconde harmonique*. PhD thesis, École Polytechnique, 2013.

[8] A.M. Cribb and J.E. Scott. Tendon response to tensile-stress - an ultrastructural investigation of collagen - proteoglycans interactions in stressed tendon. *Journal of Anatomy*, 187(2):423–428, 1995.

[9] Y.C. Fung. *Biomechanics. Mechanical Properties of Living Tissues*. Springer-Verlag, Second edition, 1993.

[10] D.R. Eyre, M.A. Paz, and P.M. Gallop. Cross-linking in collagen and elastin. *Annual Review of Biochemistry*, 53:717–748, 1984.

[11] M. Kjaer. Role of extracellular matrix in adaptation of tendon and skeletal muscle to mechanical loading. *Physiological Reviews*, 84:649–698, 2003.

[12] H.R.C. Screen, D.L. Bader, D.A. Lee, and J.C. Shelton. Local strain measurement within tendon. *Strain*, 40(4):157–163, 2004.

[13] C. Crotti. *Chirurgie du segment antérieur de l'oeil et traitement du glaucome par laser femtoseconde et imagerie de tomographie par cohérence optique.* PhD thesis, École Polytechnique, 2011.

[14] M. Franchi, M. Fini, M. Quaranta, V. De Pasquale, M. Raspanti, G. Giavaresi, V. Ottani, and A. Ruggeri. Crimp morphology in relaxed and stretched rat achilles tendon. *Journal of Anatomy*, 210(1):1–7, 2007.

[15] J. Diamant, R.G.C. Arridge, E. Baer, M. Litt, and A. Keller. Collagen - ultrastructure and its relation to mechanical properties as a function of aging. *Proceedings of the Royal Society Series B-biological Sciences*, 180(1060):293–315, 1972.

[16] Y. Komai and T. Ushiki. The three-dimensional organization of collagen fibrils in the human cornea and sclera. *Investigative ophthalmology & visual science*, 32(8):2244–2258, 1991.

[17] T. Ushiki. Collagen fibers, reticular fibers and elastic fibers. a comprehensive understanding from a morphological viewpoint. *Archives of histology and cytology*, 65(2):109–126, 2002.

[18] D.A.D. Parry. The molecular and fibrillar structure of collagen and its relationship to the mechanical-properties of connective-tissue. *Biophysical Chemistry*, 29(1-2):195–209, 1988.

[19] Z.L. Shen, M. Reza Dodge, H. Kahn, R. Ballarini, and S.J. Eppell. Stress-strain experiments on individual collagen fibrils. *Biophysical Journal*, 95(8):3956–3963, 2008.

[20] M.P.E. Wenger, L. Bozec, M.A. Horton, and P. Mesquida. Mechanical properties of collagen fibrils. *Biophysical Journal*, 93(4):1255–1263, 2007.

[21] J.A.J Van der Rijt. *Micromechanical testing of single collagen type I fibrils.* PhD thesis, University of Twente, Enschede, The Netherlands, 2004.

[22] Y.L. Sun, Z.P. Luo, A. Fertala, and K.N. An. Direct quantification of the flexibility of type I collagen monomer. *Biochemical and Biophysical Research Communications*, 295(2):382–386, 1996.

[23] A. Khademhosseini and R. Langer. Microengineered hydrogels for tissue engineering. *Biomaterials*, 28(34):5087–5092, 2007.

[24] A. Khademhosseini, J.P. Vacanti, and R. Langer. Progress in tissue. *Scientific American*, pages 64–71, 2009.

[25] S.L. Moschella and H.J. Hurley. *Dermatology, Third Edition.* Saunders, 1992.

[26] R. Garrone, C. Lethias, and D. LeGuellec. Distribution of minor collagens during skin development. *Microscopy Research and Technique*, 38(4):407–412, 1997.

[27] J.E. Scott. Proteoglycan - collagen interactions in connective tissues - ultrastructural, biochemical, functional and evolutionary aspects. *International Journal of Biological Macromolecules*, 13(3):157–161, 1991.

[28] J.E. Scott. Elasticity in extracellular matrix 'shape modules' of tendon, cartilage, etc. a sliding proteoglycan-filament model. *Journal of Physiology-london*, 553(2):335–343, 2003.

[29] M. Ventre, F. Mollica, and P.A. Netti. The effect of composition and microstructure on the viscoelastic properties of dermis. *Journal of Biomechanics*, 42(4):430–435, 2009.

[30] C. Edwards and R. Marks. Evaluation of biomechanical properties of human skin. *Clinics In Dermatology*, 13(4):375–380, 1995.

[31] O. Lokshin and Y. Lanir. Viscoelasticity and preconditioning of rat skin under uniaxial stretch: Microstructural constitutive characterization. *Journal of Biomechanical Engineering-transactions of the Asme*, 131(3):031009, 2009.

[32] I.A. Brown. Scanning electron-microscope study of effects of uniaxial tension on human skin. *British Journal of Dermatology*, 89(4):383–393, 1973.

[33] S.M. Belkoff and R.C. Haut. A structural model used to evaluate the changing microstructure of maturing rat skin. *Journal of Biomechanics*, 24(8):711–720, 1991.

[34] J.C. Ginefri, L. Darrasse, and P. Crozat. High-temperature superconducting surface coil for in vivo microimaging of the human skin. *Magnetic resonance in medicine*, 45(3):376–382, 2001.

[35] R. Puxkandl, I. Zizak, O. Paris, J. Keckes, W. Tesch, S. Bernstorff, P. Purslow, and P. Fratzl. Viscoelastic properties of collagen: synchrotron radiation investigations and structural model. *Philosophical Transactions of the Royal Society of London Series B-biological Sciences*, 357(1418):191–197, 2002.

[36] H. Aghamohammadzadeh, R.H. Newton, and K.M. Meek. X-ray scattering used to map the preferred collagen orientation in the human cornea and limbus. *Structure*, 12(2):249–256, 2004.

[37] E. Bordenave, E. Abraham, G. Jonusauskas, J. Oberle, and C. Rulliere. Longitudinal imaging in biological tissues with a single laser shot correlation system. *Optics Express*, 10(1):35–40, 2002.

[38] J.W.Y. Jor, M.P. Nash, P.M.F. Nielsen, and P.J. Hunter. Estimating material parameters of a structurally based constitutive relation for skin mechanics. *Biomechanics and Modeling In Mechanobiology*, 10(5):767–778, 2011.

[39] D. Huang, E.A. Swanson, C.P. Lin, J.S. Schuman, W.G. Stinson, W. Chang, M.R. Hee, T. Flotte, K. Gregory, and C.A. Puliafito. Optical coherence tomography. *Science*, 254:1178–1181, 1991.

[40] H. Chen, Y. Liu, M.N. Slipchenko, X.F. Zhao, J.X. Cheng, and G.S. Kassab. The layered structure of coronary adventitia under mechanical load. *Biophysical Journal*, 101(11):2555–2562, 2011.

[41] C. Jayyosi, G. Fargier, M. Coret, and K. Bruyere-Garnier. Photobleaching as a tool to measure the local strain field in fibrous membranes of connective tissues. *Acta Biomaterialia*, 10(6):2591–2601, 2014.

[42] F. Xu, T.J. Lu, and K.A. Seffen. Biothermomechanical behavior of skin tissue. *Acta Mechanica Sinica*, 24(1):1–23, 2008.

[43] Z. Del Prete, S. Antoniucci, A.H. Hoffman, and P. Grigg. Viscoelastic properties of skin in Mov-13 and Tsk mice. *Journal of Biomechanics*, 37(10):1491–1497, 2004.

[44] H. Oxlund, J. Manschot, and A. Viidik. The role of elastin in the mechanical properties of skin. *Journal of Biomechanics*, 21(3):213–218, 1988.

[45] H. Eshel and Y. Lanir. Effects of strain level and proteoglycan depletion on preconditioning and viscoelastic responses of rat dorsal skin. *Annals of Biomedical Engineering*, 29(2):164–172, 2001.

[46] W.F. Larrabee. A finite-element model of skin deformation .1. Biomechanics of skin and soft-tissue - a review. *Laryngoscope*, 96(4):399–405, 1986.

[47] H.G. Vogel. Mechanical measurements of skin. *Acta Dermato-Venereologica*, 185:39–43, 1994.

[48] D.R. Veronda and R.A. Westmann. Mechanical characterization of skin-finite deformations. *Journal of Biomechanics*, 3(1):111–124, 1970.

[49] Y. Lanir and Y.C. Fung. 2-dimensional mechanical-properties of rabbit skin .2. Experimental results. *Journal of Biomechanics*, 7(2):175–182, 1974.

[50] L.E. Edsberg, J.R. Natiella, R.E. Baier, and J. Earle. Microstructural characteristics of human skin subjected to static versus cyclic pressures. *Journal of Rehabilitation Research and Development*, 38(5):477–486, 2001.

[51] M. Hollenstein, A.E. Ehret, M. Itskov, and E. Mazza. A novel experimental procedure based on pure shear testing of dermatome-cut samples applied to porcine skin. *Biomechanics and Modeling In Mechanobiology*, 10(5):651–661, 2011.

[52] C. Bonod-Bidaud, M. Roulet, U. Hansen, A. Elsheikh, M. Malbouyres, S. Ricard-Blum, C. Faye, E. Vaganay, P. Rousselle, and F. Ruggiero. In vivo evidence for a bridging role of a collagen V subtype at the epidermis-dermis interface. *Journal of Investigative Dermatology*, 132(7):1841–1849, 2012.

[53] C. Jacquemoud, K. Bruyere-Garnier, and M. Coret. Methodology to determine failure characteristics of planar soft tissues using a dynamic tensile test. *Journal of Biomechanics*, 40(2):468–475, 2007.

[54] Y.J. Zeng, Y.H. Liu, C.Q. Xu, X.H. Xu, H. Xu, and G.C. Sun. Biomechanical properties of skin in vitro for different expansion methods. *Clinical Biomechanics*, 19(8):853–857, 2004.

[55] O.A. Shergold, N.A. Fleck, and D. Radford. The uniaxial stress versus strain response of pig skin and silicone rubber at low and high strain rates. *International Journal of Impact Engineering*, 32(9):1384–1402, 2006.

[56] Z. Liu and K. Yeung. The preconditioning and stress relaxation of skin tissue. *Journal of Biomedical & Pharmaceutical Engineering*, 2:1:22–28, 2008.

[57] D.S. Zhang and D.D. Arola. Applications of digital image correlation to biological tissues. *Journal of biomedical optics*, 9(4):691–699, 2004.

[58] M.A. Sutton, J.J. Orteu, and H.W. Schreier. *Image Correlation for Shape, Motion and Deformation Measurements - Basic Concepts, Theory and Applications.* Springer, 2009.

[59] B. Pan, K. Qian, H. Xie, and A. Asundi. Two-dimensional digital image correlation for in-plane displacement and strain measurement: a review. *Measurement science & technology*, 20(6), 2009.

[60] G.E. Pierard. Eemco guidance to the in vivo assessment of tensile functional properties of the skin—part 1: Relevance to the structures and ageing of the skin and subcutaneous tissues. *Skin Pharmacology and Applied Skin Physiology*, 12(6):352–362, 1999.

[61] R.B. Groves. *Quantifying the mechanical properties of skin in vivo and ex vivo to optimise microneedle device design.* PhD thesis, Cardiff University, 2011.

[62] Y.A. Kvistedal and P.M.F. Nielsen. Estimating material parameters of human skin in vivo. *Biomechanics and Modeling In Mechanobiology*, 8(1):1–8, 2009.

[63] C. Pailler-Mattei and H. Zahouani. Analysis of adhesive behaviour of human skin in vivo by an indentation test. *Tribology International*, 39(1):12–21, 2006.

[64] F.M. Hendriks, D. Brokken, C.W.J. Oomens, and F.P.T. Baaijens. Influence of hydration and experimental length scale on the mechanical response of human skin in vivo, using optical coherence tomography. *Skin Research and Technology*, 10:231–241, 2004.

[65] C.H. Daly. *The Biomechanical Characteristics of Human Skin.* PhD thesis, University of Strathclyde, 1966.

[66] R.B. Groves, S.A. Coulman, J.C. Birchall, and S.L. Evans. An anisotropic, hyperelastic model for skin: Experimental measurements, finite element modelling and identification of parameters for human and murine skin. *Journal of the Mechanical Behavior of Biomedical Materials*, 18:167–180, 2013.

[67] J.E. Bischoff, E.M. Arruda, and K. Grosh. Finite element modeling of human skin using an isotropic, nonlinear elastic constitutive model. *Journal of Biomechanics*, 33(6):645–652, 2000.

[68] Y. Lanir. Structural theory for the homogeneous biaxial stress-strain relationships in flat collagenous tissues. *Journal of Biomechanics*, 12(6):423–436, 1979.

[69] Y. Lanir. Constitutive-equations for fibrous connective tissues. *Journal of Biomechanics*, 16(1):1–12, 1983.

[70] W.F. Decraemer, M.A. Maes, V.J. Vanhuyse, and P. Vanpeperstraete. A non-linear viscoelastic constitutive equation for soft biological tissues, based upon a structural model. *Journal of Biomechanics*, 13(7):559–564, 1980.

[71] A. Rauber. *Rauber's Lehrbuch der Anatomie des Menschen.* Leipzig: Verlag von Georg Thieme, 1908.

[72] P. Tong and Y.C. Fung. Stress-strain relationship for skin. *Journal of Biomechanics*, 9(10):649–657, 1976.

[73] J.G. Liu and H.T. Qi. Dissipated energy function, hysteresis and precondition of a viscoelastic solid model. *Nonlinear Analysis - Real World Applications*, 11(2):907–912, 2010.

[74] J. Diani, B. Fayolle, and P. Gilormini. A review on the Mullins effect. *European Polymer Journal*, 45(3):601–612, 2009.

[75] J. Summerscales. *Microstructural Characterisation of Fibre-Reinforced Composites.* Woodhead Publishing, 1998.

[76] J.D. Humphrey. Continuum biomechanics of soft biological tissues. *Proceedings of the Royal Society A-mathematical Physical and Engineering Sciences*, 459(2029):3–46, 2003.

[77] Y. Lanir and Y.C. Fung. 2-dimensional mechanical-properties of rabbit skin .1. Experimental system. *Journal of Biomechanics*, 7(1):29–34, 1974.

[78] R. De Pascalis. *The Semi-Inverse Method in solid mechanics: Theoretical underpinnings and novel applications. Chapter 2: Strain energy functions.* PhD thesis, Université Pierre et Marie Curie, 2010.

[79] S.P. Pearce, J.R. King, and Holdsworth M.J. Axisymmetric indentation of curved elastic membranes by a convex rigid indenter. *International Journal of Non-Linear Mechanics*, 46(9):1128–1138, 2011.

[80] B.J. Rigby, N. Hirai, J.D. Spikes, and H. Eyring. The mechanical properties of rat tail tendon. *Journal of General Physiology*, 43(2):265–283, 1959.

[81] J. Kastelic, I. Palley, and E. Baer. A structural mechanical model for tendon crimping. *Journal of Biomechanics*, 13(10):887–893, 1980.

[82] M.A. Zulliger, P. Fridez, K. Hayashi, and N. Stergiopulos. A strain energy function for arteries accounting for wall composition and structure. *Journal of Biomechanics*, 37(7):989–1000, 2004.

[83] M. Kroon and G.A. Holzapfel. A new constitutive model for multi-layered collagenous tissues. *Journal of Biomechanics*, 41(12):2766–2771, 2008.

[84] T.T. Tower, M.R. Neidert, and R.T. Tranquillo. Fiber alignment imaging during mechanical testing of soft tissues. *Annals of Biomedical Engineering*, 30(10):1221–1233, 2002.

[85] K.P. Quinn and B.A. Winkelstein. Vector correlation technique for pixel-wise detection of collagen fiber realignment during injurious tensile loading. *Journal of Biomedical Optics*, 14(5):054010, 2009.

[86] K.P. Quinn and B.A. Winkelstein. Preconditioning is correlated with altered collagen fiber alignment in ligament. *Journal of Biomechanical Engineering-transactions of the Asme*, 133(6):064506, 2011.

[87] K.P. Quinn and B.A. Winkelstein. Detection of altered collagen fiber alignment in the cervical facet capsule after whiplash-like joint retraction. *Annals of Biomedical Engineering*, 39(8):2163–2173, 2011.

[88] K.A. Hansen, J.A. Weiss, and J.K. Barton. Recruitment of tendon crimp with applied tensile strain. *Journal of Biomechanical Engineering-transactions of the Asme*, 124(1):72–77, 2002.

[89] J.G. Snedeker, G. Pelled, Y. Zilberman, F. Gerhard, R. Muller, and D. Gazit. Endoscopic cellular microscopy for in vivo biomechanical assessment of tendon function. *Journal of biomedical optics*, 11(6):064010–064010, 2006.

[90] J.G. Snedeker, G. Pelled, Y. Zilberman, A. Ben Arav, E. Huber, R. Mueller, and D. Gazit. An analytical model for elucidating tendon tissue structure and biomechanical function from in vivo cellular confocal microscopy images. *Cells Tissues Organs*, 190(2):111–119, 2009.

[91] K.L. Billiar and M.S. Sacks. A method to quantify the fiber kinematics of planar tissues under biaxial stretch. *Journal of Biomechanics*, 30(7):753–756, 1997.

[92] A. Mauri, M. Perrini, J.M. Mateos, C. Maake, N. Ochsenbein-Koelble, R. Zimmermann, M. Ehrbar, and E. Mazza. Second harmonic generation microscopy of fetal membranes under deformation: normal and altered morphology. *Placenta*, 34:1020–1026, 2013.

[93] S. Nesbitt, W. Scott, J. Macione, and S. Kotha. Collagen fibrils in skin orient in the direction of applied uniaxial load in proportion to stress while exhibiting differential strains around hair follicles. *Materials*, 8:1841–1857, 2015.

[94] Y.G. Houssen, I. Gusachenko, M.C. Schanne-Klein, and J.M. Allain. Monitoring micrometer-scale collagen organization in rat-tail tendon upon mechanical strain using second harmonic microscopy. *Journal of Biomechanics*, 44(11):2047–2052, 2011.

[95] I. Gusachenko, V. Tran, Y.G. Houssen, J.M. Allain, and M.C. Schanne-Klein. Polarization-resolved second-harmonic generation in tendon upon mechanical stretching. *Biophysical Journal*, 102(9):2220–2229, 2012.

[96] G. Latour, I. Gusachenko, L. Kowalczuk, I. Lamarre, and M.C. Schanne-Klein. In vivo structural imaging of the cornea by polarization-resolved second harmonic microscopy. *Biomedical Optics Express*, 3(1):1–15, 2012.

[97] A.E. Ehret, M. Hollenstein, E. Mazza, and M. Itskov. Porcine dermis in uniaxial cyclic loading: Sample preparation, experimental results and modeling. *Journal of Mechanics of Materials and Structures*, 6(7-8):1125–1135, 2011.

[98] E. Guan, S. Smilow, M. Rafailovich, and J. Sokolov. Determining the mechanical properties of rat skin with digital image speckle correlation. *Dermatology*, 208(2):112–119, 2004.

[99] J. Lim, J. Hong, W.W. Chen, and T. Weerasooriya. Mechanical response of pig skin under dynamic tensile loading. *International Journal of Impact Engineering*, 38(2-3):130–135, 2011.

[100] M. Lin, X. Zhai, S. Wang, Z. Wang, F. Xu, and T.J. Lu. Influences of supra-physiological temperatures on microstructure and mechanical properties of skin tissue. *Medical Engineering & Physics*, 34(8):1149–1156, 2012.

[101] M J. Munoz, J.A. Bea, J.F. Rodriguez, I. Ochoa, J. Grasa, A. Perez del Palomar, P. Zaragoza, R. Osta, and M. Doblare. An experimental study of the mouse skin behaviour: Damage and inelastic aspects. *Journal of Biomechanics*, 41(1):93–99, 2008.

[102] A. Ni Annaidh, K. Bruyere, M. Destrade, M.D. Gilchrist, and M. Ottenio. Characterization of the anisotropic mechanical properties of excised human skin. *Journal of the mechanical behavior of biomedical materials*, 5(1):139–48, 2012.

[103] M. Bornert, F. Vales, H. Gharbi, and D. Nguyen Minh. Multiscale full-field strain measurements for micromechanical investigations of the hydromechanical behaviour of clayey rocks. *Strain*, 46:33–46, 2010.

[104] P.G. Agache, C. Monneur, J.L. Leveque, and J. Derigal. Mechanical properties and Young's modulus of human skin in vivo. *Archives of Dermatological Research*, 269(3):221–232, 1980.

[105] C.H. Daly and G.F. Odland. Age-related-changes in the mechanical-properties of human-skin. *Journal of Investigative Dermatology*, 73(1):84–87, 1979.

[106] M. Balland, N. Desprat, D. Icard, S. Féréol, A. Asnacios, J. Browaeys, S. Hénon, and F. Gallet. Power laws in microrheology experiments on living cells: Comparative analysis and modeling. *Physical Review*, 74:021911, 2006.

[107] C. Escoffier, J. Derigal, A. Rochefort, R. Vasselet, J.L. Leveque, and P.G. Agache. Age-related mechanical-properties of human-skin - an in vivo study. *Journal of Investigative Dermatology*, 93(3):353–357, 1989.

[108] F.H. Silver, J.W. Freeman, and D. DeVore. Viscoelastic properties of human skin and processed dermis. *Skin Research and Technology*, 7:18–23, 2001.

[109] X. Markenscoff and I.V. Yannas. Stress-strain relation for skin. *Journal of Biomechanics*, 12(2):127–129, 1979.

[110] O. Lokshin and Y. Lanir. Micro and macro rheology of planar tissues. *Biomaterials*, 30(17):3118–3127, 2009.

[111] F.C. Mackintosh, J. Kas, and P.A. Janmey. Elasticity of semiflexible biopolymer networks. *Physical Review Letters*, 75(24):4425–4428, 1995.

[112] P. Sens. Rigidity sensing by stochastic sliding friction. *EPL*, 104(3):38003, 2013.

[113] D. Vader, A. Kabla, D. Weitz, and L. Mahadevan. Strain-induced alignment in collagen gels. *Plos One*, 4(6):e5902, 2009.

[114] A. Stein, D. Vader, D. Weitz, and L. Sander. The micromechanics of three-dimensional collagen-I gels. *Complexity*, 16:22–28, 2010.

[115] H.R.C. Screen, S. Toorani, and J.C. Shelton. Microstructural stress relaxation mechanics in functionally different tendons. *Medical Engineering & Physics*, 35(1):96–102, 2013.

[116] D.E. Birk, J.M. Fitch, J.P. Babiarz, K.J. Doane, and Linsenmayer T.F. Collagen fibrillogenesis in vitro: interaction of types I and V collagen regulates fibril diameter. *Journal of Cell Science*, 95:649–657, 1990.

[117] M.K. Gordon and R.A. Hahn. Collagens. *Cell and tissue research*, 339(1):247–257, 2010.

[118] T. Starborg, N.S. Kalson, Y. Lu, A. Mironov, T.F. Cootes, D.F. Holmes, and K.E. Kadler. Using transmission electron microscopy and 3View to determine collagen fibril size and three-dimensional organization. *Nature Protocols*, 8:1433–1448, 2013.

[119] P. Marchand, M. Volkmann, and J.S. Bond. Cysteine mutations in the mam domain result in monomeric meprin and alter stability and activity of the proteinase. *Journal of biological chemistry*, 271(39):24236–24241, 1996.

[120] A. Fichard, H. Chanut-Delalande, and F. Ruggiero. Le syndrome d'Ehlers-Danlos : l'architecture matricielle en question. *Medecine/Sciences*, 19:443–452, 2003.

[121] R.H. Nielsen, C. Couppe, J.K. Jensen, M.R. Olsen, K.M. Heinemeier, F. Malfait, S. Symoens, A. De Paepe, P. Schjerling, S.P. Magnusson, L. Remvig, and M. Kjaer. Low tendon stiffness and abnormal ultrastructure distinguish classic Ehlers-Danlos syndrome from benign joint hypermobility syndrome in patients. *Faseb Journal*, 28-11:4668–4676, 2014.

[122] B. Sonesson, F. Hansen, and T. Lanne. The mechanical properties of elastic arteries in Ehlers-Danlos syndrome. *European Journal of Vascular and Endovascular Surgery*, 14(4):258–264, 1997.

[123] K. Andrikopoulos, X. Liu, D.R. Keene, R. Jaenisch, and F. Ramirez. Targeted mutation in the col5a2 gene reveals a regulatory role for type V collagen during matrix assembly. *Nature Genetics*, 9(1):31–36, 1995.

[124] H. Chanut-Delalande, C. Bonod-Bidaud, S. Cogne, M. Malbouyres, F. Ramirez, A. Fichard, and F. Ruggiero. Development of a functional skin matrix requires deposition of collagen V heterotrimers. *Molecular and cellular biology*, 24(13):6049–6057, 2004.

[125] M.L. Crichton, B.C. Donose, X.F. Chen, A.P. Raphael, H. Huang, and M.A.F. Kendall. The viscoelastic, hyperelastic and scale dependent behaviour of freshly excised individual skin layers. *Biomaterials*, 32(20):4670–4681, 2011.

[126] E. Naylor, R. Watson, and M. Sherratt. Molecular aspects of skin ageing. *Maturitas*, 69:249–256, 2011.

[127] J.R.S. Gordon and J.C. Brieva. Unilateral dermatoheliosis. *The New England Journal of Medicine*, 366(16):e25, 2012.

[128] J. Varani, M.K. Dame, L. Rittie, S.E.G. Fligiel, S. Kang, G.J. Fisher, and J.J. Voorhees. Decreased collagen production in chronologically aged skin - roles of age-dependent alteration in fibroblast function and defective mechanical stimulation. *American Journal of Pathology*, 168(6):1861–1868, 2006.

[129] S. Diridollou, V. Vabre, M. Berson, L. Vaillant, D. Black, J.M. Lagarde, J.M. Gregoire, Y. Gall, and F. Patat. Skin ageing: changes of physical properties of human skin in vivo. *International journal of cosmetic science*, 23(6):353–62, 2001.

[130] D.A. Carrino, J.M. Sorrell, and A.I. Caplan. Age-related changes in the proteoglycans of human skin. *Archives of Biochemistry and Biophysics*, 373(1):91–101, 2000.

[131] K. Subramanyan, M. Misra, S. Mukherjee, and K.P. Ananthapadmanabhan. Advances in the materials science of skin: A composite structure with multiple functions. *Mrs Bulletin*, 32(10):770–778, 2007.

[132] A. Tidu, D. Ghoubay-Benallaoua, B. Lynch, B. Hayes, C. Illoul, J.M. Allain, V.M. Borderie, and G. Mosser. Development of human corneal epithelium on organized fibrillated transparent collagen matrices synthesized at high concentration. *Acta Biomaterialia*, 2015.

[133] R Core Team. *R: A Language and Environment for Statistical Computing.* R Foundation for Statistical Computing, Vienna, Austria, 2012. ISBN 3-900051-07-0.